



Ermes Rizzi

## **Role of timber in the seismic resilience of existing URM buildings**







University of Trento

Ph.D. program in Civil, Environmental and Mechanical Engineering

XXXII Cycle

Final Examination: April 24, 2020

Board of Examiners:

Prof. Marco Ballerini, University of Trento, Trento, Italy

Dr. Francesco Graziotti, University of Pavia, Pavia, Italy

Dr. Igor Gavric, InnoRenew CoE Research Institute, Izola, Slovenia

UNIVERSITY OF TRENTO - Italy  
Department of Civil, Environmental  
and Mechanical Engineering



Doctoral School in Civil, Environmental and Mechanical Engineering  
Topic 1. Civil and Environmental Engineering - 32<sup>nd</sup> cycle 2016/2019

Doctoral Thesis - April 2020

Ermes Rizzi

# **Role Of Timber In The Seismic Resiliende Of Existing URM Buildings**

## **Supervisors**

Prof. Maurizio Piazza, DICAM - University of Trento

Dr. Ivan Giongo, DICAM - University of Trento

Credits of the cover image: Dr. Eng. Ivan Giongo, Ermes Rizzi

All Rights Reserved

University of Trento  
Doctoral School in Civil, Environmental and Mechanical Engineering  
*<http://web.unitn.it/en/dricam>*  
Via Mesiano 77, I-38123 Trento  
Tel. +39 0461 282670 / 2611 - *[dicamphd@unitn.it](mailto:dicamphd@unitn.it)*

---

# ABSTRACT

The main topic of the thesis is the role of timber in the seismic resilience of unreinforced masonry (URM) buildings. The research addressed both existing timber components that can be encountered in URM buildings and timber-based retrofit solutions. The work presented herein can be split into two main phases.

In the first part of the research, the in-plane behavior of traditional wooden floors was analyzed by means of numerical static and dynamic simulations. Modelling strategies with different refinement levels were proposed and implemented to assess diaphragm in-plane strength and flexibility. Modelling was undertaken considering as-built diaphragms first and was then extended to diaphragms retrofitted by means of timber-based techniques. The influence of diaphragm construction details on their in-plane response was evaluated and timber-based retrofitting solutions were observed to be effective in mitigating in-plane diaphragm flexibility and in increasing in-plane diaphragm strength.

The second part of the PhD work was dedicated to investigate new retrofit solutions for URM buildings based on the use of engineered timber panels mechanically connected to the masonry. The first step saw the experimental testing of different types of timber-to-masonry connections considering both screw-type fasteners and adhesive anchors. In the second stage, full-scale masonry walls were tested in the as-built, retrofitted and repaired configurations, highlighting the benefits of the proposed technique on the in-plane response of the masonry walls.

---

---

# INDEX

1	Introduction .....	1
1.1	Thesis outline .....	4
1.1.1	Part 1.....	4
1.1.2	Part 2.....	6
1.2	References .....	8
PART 1.....		11
2	Timber Diaphragms - State of the Art.....	13
2.1	Literature review .....	13
2.1.1	Influence of flexible diaphragms on building performance .....	13
2.1.2	Diaphragm in-plane behavior idealization .....	18
2.1.3	Experimental testing of diaphragms .....	19
2.1.4	Modeling of diaphragms.....	28
2.1.5	General remarks.....	32
2.2	Standard frameworks.....	34
2.2.1	American Standard ASCE 41-17.....	34
2.2.2	New Zealand Standard NZSEE 2017 .....	39
2.2.3	Further remarks on default stiffness and strength values .....	42
2.3	References .....	44
3	As-built straight sheathed timber diaphragms .....	47
3.1	Introduction .....	47
3.2	Finite element model definition.....	47
3.2.1	Modeling approach 1 (M1).....	48
3.2.2	Modeling approach 2 (M2).....	49
3.3	Validation of the modeling approaches .....	50
3.3.1	M1 validation process.....	50
3.3.2	M2 validation process.....	56
3.4	Parametric analyses .....	65

---

3.4.1	Analysis results.....	67
3.4.2	Remarks on traditional timber floors found in Mediterranean countries. .....	70
3.5	Results fitting relations.....	71
3.6	Conclusions .....	72
3.7	References .....	74
4	Timber diaphragms retrofitted with plywood sheathing overlay.....	77
4.1	Introduction .....	77
4.2	Experimental campaign .....	77
4.2.1	General description.....	77
4.2.2	Test setup.....	78
4.2.3	Diaphragm improvement techniques.....	79
4.3	Test results.....	81
4.3.1	Re-nailing of board-to-joist connections .....	81
4.3.2	Fire-rated ceiling.....	83
4.3.3	Steel chords.....	84
4.3.4	Plywood sheet overlay.....	85
4.4	Finite element modeling .....	87
4.4.1	FE modeling details .....	87
4.4.2	FE model validation.....	89
4.4.3	Chord influence .....	91
4.5	Parametric study on Diaphragms with plywood overlays .....	93
4.5.1	Influence of plywood sheet layout.....	97
4.5.2	Sheet-to-sheet contact influence .....	99
4.5.3	Plywood sheet thickness influence .....	100
4.5.4	Plywood-to-solidwood connection influence .....	101
4.5.5	Observations on diaphragm lateral capacity.....	102
4.5.6	Observations on traditional wooden floors typical of Mediterranean countries .....	103

---

4.6	Analysis of diaphragms with re-nailed floorboard-to-joist connections ....	104
4.7	Simplified analytical model.....	106
4.8	Final remarks.....	106
4.9	References .....	109
5	Modeling of timber diaphragms retrofitted with Diagonal sheathing overlay ...	111
5.1	Introduction .....	111
5.2	Modeling approaches .....	111
5.2.1	M1 modeling approach.....	111
5.2.2	M2 modeling approach.....	112
5.2.3	Finite element model validation .....	113
5.3	Parametric analyses .....	114
5.4	Analyses results.....	116
5.4.1	Effectiveness of diagonal sheathing overlay .....	118
5.4.2	Influence of connection backbone curves .....	118
5.5	Conclusions .....	119
5.6	References .....	120
6	Timber diaphragms retrofitted with CLT panels.....	121
6.1	Introduction .....	121
6.2	Modeling approaches .....	121
6.3	Finite element model validation .....	122
6.4	Parametric analyses .....	123
6.4.1	Analyses overview.....	123
6.4.2	Retrofit details .....	124
6.4.3	Analyses results.....	128
6.5	Simplified analytical model proposal.....	135
6.5.1	Parallel-to-joists loading direction .....	135
6.5.2	Perpendicular-to-joists loading direction.....	139
6.6	Conclusions .....	140
6.7	References .....	141

---

---

7	Non-linear dynamic modeling of diaphragm in-plane behavior.....	143
7.1	Introduction .....	143
7.2	Finite element model details.....	144
7.3	Finite element model validation .....	144
7.4	Parametric study .....	147
7.4.1	Diaphragm geometries.....	147
7.4.2	Diaphragm configurations .....	147
7.4.3	Dynamic inputs.....	151
7.4.4	Boundary conditions and common assumptions .....	152
7.5	Results and discussion.....	153
7.6	Standard comparison .....	157
7.7	Conclusions .....	157
7.8	References .....	159
PART 2	.....	161
8	Use of timber for URM wall retrofit.....	163
8.1	Literature review.....	163
8.2	Research presented in Giongo et al. (2017).....	167
8.3	Conclusions .....	170
8.4	References .....	171
9	Experimental shear testing of timber-masonry connection systems.....	173
9.1	Introduction .....	173
9.2	Test configuration.....	173
9.2.1	Materials .....	174
9.2.2	Test set-up.....	177
9.2.3	Testing procedure .....	178
9.3	Results – dry connections .....	181
9.3.1	Observed failure modes .....	181
9.3.2	Monotonic testing.....	186
9.3.3	Cyclic testing .....	188

---

9.4	Results – grouted connections .....	200
9.4.1	Observed failure mechanisms.....	200
9.4.2	Envelope backbone characterization .....	201
9.4.3	Cyclic behavior.....	203
9.5	Comparisons between connection types.....	206
9.6	Simplified analytical model.....	208
9.7	Conclusions .....	210
9.8	Annex .....	213
9.9	References .....	218
10	Onsite testing of masonry shear walls strengthened with timber panels .....	221
10.1	Introduction .....	221
10.2	Experimental program.....	221
10.2.1	Materials .....	222
10.2.2	Specimen preparation .....	223
10.2.3	Test setup and instrumentation.....	225
10.2.4	Test protocol.....	228
10.2.5	Results and discussion.....	228
10.3	General remarks .....	233
10.4	Conclusions .....	235
10.5	References .....	237
11	Shear testing of retrofitted masonry wallets .....	239
11.1	Introduction .....	239
11.2	Materials.....	240
11.3	Specimen preparation .....	241
11.4	Setup and instrumentation .....	242
11.5	Test protocol.....	243
11.6	Test results.....	244
11.6.1	Failure mechanisms .....	244
11.6.2	Shear strength.....	245

---

11.6.3	Out of plane behavior .....	245
11.6.4	Backbone curve idealization.....	247
11.6.5	Comments on post-peak behavior .....	247
11.7	Conclusions .....	249
11.8	References .....	250
	Conclusions .....	251
	Acknowledgements .....	253

# 1 INTRODUCTION

Unreinforced Masonry (URM) buildings with flexible timber floor diaphragms constitute a significant portion of the global building stock in many countries around the World. This construction type has frequently exhibited an intrinsic vulnerability to earthquake-induced shaking [Augenti and Parisi (2010), Ingham and Griffith (2016), Penna et al. (2013), Binda et al. (1999) and Dizhur et al. (2016)], with building response being strongly influenced by the in-plane deformability of the timber floor and roof diaphragms [Tena-Colunga and Abrams (1996), Raggett and Rojahn (1991), Keller et al. (2019)]. URM building failures during earthquakes are frequently attributable to out-of-plane wall failures, which may be exacerbated by inadequate out-of-plane restraints offered by floor diaphragms. Inertia loads related to floors and out-of-plane loaded masonry elements are transferred to the load bearing walls oriented parallel to the earthquake direction by the diaphragms themselves. Depending on the diaphragm in-plane stiffness, the building behavior can be idealized according to alternative assumptions. In the case of flexible diaphragms, in-plane loaded walls are regarded as rigid and all deformations are concentrated in the diaphragms [ASCE (2017), NZSEE (2017)]. According to such assumptions, the building dynamic response is uniquely defined by diaphragm flexibility and tributary masses. In the case of excessively flexible floor diaphragms, inter-story drifts may exceed the displacement capacity of out-of-plane loaded walls leading to building failure. If the presence of effective diaphragm-to-wall connections is assumed, the inadequate stiffness and/or strength of flexible timber diaphragms, being often straight-sheathed, has frequently been identified as the leading cause of URM building failure [Penna et al. (2013), Dizhur et al. (2016) and Dizhur et al. (2011)] (see Figure 1.1).

Straight sheathed diaphragms consist of a layer of timber floorboards nailed perpendicularly to timber joists. According to ASCE 41-17 “*The sheathing serves the dual purpose of supporting gravity loads and resisting shear forces in the diaphragm. Most often, 1-in. (25mm) sheathing is nailed with 8d or 10d nails, with two or more*

---

*nails per sheathing board at each support. Shear forces perpendicular to the direction of the sheathing are resisted by the nail couple”.*

As reported by Wilson (2012) and Schiro et al. (2018) shear strength and stiffness of nail connections typical of straight sheathed diaphragms are relatively small, especially in the case of aged components. Therefore, when dealing with straight sheathed diaphragms in URM buildings, retrofit techniques aimed at maximizing diaphragm in-plane stiffness and strength are often implemented. Possible undesirable side effects such as the introduction of large additional masses and excessively stiff constraints between masonry walls should be carefully evaluated. When such aspects are disregarded or not adequately accounted for, interventions may prove to be detrimental, inducing the activation of failure mechanisms such as those shown in Figure 1.2-a [Borri (2011), Binda et al. (1999)]. Furthermore, due to the intrinsic duality of the seismic problem, stiffer structures might be subjected to smaller displacements and higher force demands. Therefore, if on one hand the stiffening of floor diaphragms could probably prevent the wall out-of-plane collapse, it could also imply higher horizontal forces on the in-plane loaded masonry piers, which may require to be strengthened in order to be able to bear the increased horizontal loads.



*Figure 1.1 Out-of-plane wall failure due to excessive diaphragm flexibility, 2011 Christchurch earthquake, New Zealand [Dizhur et al. (2011)]: a) Side view of building; b) Aerial view*

In such context, several retrofit techniques aimed at improving in-plane behavior of URM piers have been proposed in literature. Also in this case, effects of interventions on overall building response should be carefully evaluated. It is well acknowledged that concrete-based strengthening solutions (e.g. reinforced plaster) enable significant strength increases with remarkable stiffness increments. This might result in

unfavorable horizontal load distribution among masonry piers, especially in the case of selective interventions, with the retrofitted walls being subjected to higher loads.



*Figure 1.2: URM building failures: a) Rigid floor and RC tie beam, 1997 Umbria earthquake, Italy [Binda et al. (1999)]; b) Local collapse due to out-of-plane bending of slender URM wall, 2012 Emilia earthquake, Italy [Penna et al. (2012)]*

With reference to the above mentioned “seismic duality”, the increased global stiffness ensuing from the implementation of concrete-based retrofit solutions, combined with the significant mass increments, imply larger seismic forces to be transferred to the ground. Moreover, inconsistent material mechanical properties and inadequate detailing have repeatedly been reported to significantly reduce the effectiveness of such techniques [Binda et al, (1999)] (see Figure 1.3).

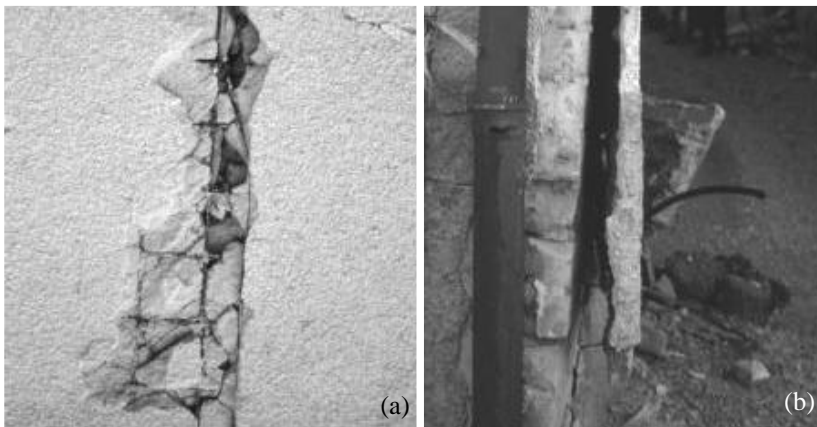


*Figure 1.3: Failure in masonry retrofitted with reinforced concrete plaster, 1997 Umbria earthquake, Italy [Binda et al. (1999)]: a) Insufficient steel mesh overlapping; b) Plaster detachment*

---

## 1.1 THESIS OUTLINE

The research work presented in this thesis addressed both the assessment of existing timber components that can be encountered in traditional URM buildings and the analysis of timber-based retrofit solutions, for timber diaphragms (Part 1) and for URM piers (Part 2).

### 1.1.1 PART 1

In Part 1 the in-plane assessment of existing timber diaphragms was considered first. Experimental studies investigating the in-plane response of timber diaphragms having commonly observed characteristics (e.g. floorboard cross-section, joist spacing and nail properties) were previously reported [ABK (1981), Wilson (2012), Wilson et al. (2014), Brignola et al. (2012), Peralta et al. (2003), Giongo et al. (2015) and Baldessari et al. (2009)]. However, the mentioned experimental tests differed from each other in terms of diaphragm size, construction details, aspect ratio and condition. Some specimens were newly constructed with the sole purpose of being tested [ABK (1981), Wilson et al. (2014), Brignola et al. (2012), Peralta et al. (2003), Baldessari et al. (2008)], whilst other diaphragms were tested after many decades of service [Wilson (2012), Giongo et al. (2015), Rizzi et al. (2019)]. In some cases, comparisons between experimental results related to consistent diaphragm constructions led to partially inconsistent conclusions.

Similar conclusions can be drawn if the literature concerning diaphragm modeling is analyzed. From such point of view, several research studies were undertaken by various Authors. In some cases, the adopted modeling strategies were found to provide satisfactory results when compared with experimental results [Wilson (2012), Brignola et al. (2012), Peralta et al. (2003) and Baldessari et al. (2009)], while in some other cases models substantially failed to reproduce diaphragm in-plane behavior [Peralta et al. (2003), Wilson (2012)]. Inconsistencies were attributed to phenomena such as board-to-board contact and friction, but the actual effects of such parameters have never been demonstrated. In addition, the influence of parameters such as diaphragm plan geometry and construction details have never been investigated and is completely disregarded by Standard assessment procedures.

In-plane behavior of timber diaphragms was analyzed by means of an extensive numerical study considering as built timber diaphragms and timber-based retrofit strategies for timber diaphragms. The study outcomes, comprising non-linear static and non-linear dynamic analyses were used to calibrate an assessment procedure for flexible timber diaphragms. Such procedure is currently being discussed within the CEN/TC250/SC8/WG3 working group as possible addition to the new “timber chapter”

in the update of Eurocode 8 – Part 3: “*Design of structures for earthquake resistance; Assessment and retrofitting of buildings and bridges*”. Part 1 is divided in the following Chapters.

### ***Chapter 2 – Timber diaphragms – State of the Art***

In Chapter 2 the subject of timber floor diaphragms is introduced. A literature review related to experimental and numerical studies on timber diaphragms is reported. Subsequently, assessment procedures proposed by the American ASCE 41-17 [ASCE (2017)] and New-Zealand NZSEE 2017 [NZSEE (2017)] are reported and discussed.

### ***Chapter 3 – As-built straight sheathed timber diaphragms***

Two modelling approaches with different levels of refinement were employed to numerically investigate the influence of different parameters on the response of straight sheathed timber diaphragms when subject to in-plane loading. The investigated parameters included diaphragm aspect ratio, scale factor (i.e. diaphragm size), impact of board-to-board contact phenomena, and the effects of floorboard friction. These parameters were specifically investigated because they were postulated to explain the notable differences that are encountered when comparing the findings from experimental studies that have influenced relevant provisions in recent standards for the seismic assessment of timber diaphragms. The modelling strategies were validated considering a wide range of available experimental data on newly constructed and vintage timber floor specimens found in literature. Analysis results confirmed that the in-plane behavior of straight sheathed diaphragms is significantly influenced by parameters that are often neglected by numerical studies and assessment procedures.

### ***Chapter 4 – Timber diaphragms retrofitted with plywood sheathing overlay***

In the first part of Chapter 4 a previously reported in-situ experimental campaign investigating the in-plane behavior of diaphragms retrofitted with plywood sheathing overlay is summarized as it served as validation reference for the numerical study that represents the core of Chapter 4. The modeling strategies presented in Chapter 3 were extended so as to represent the behavior of the selected retrofit solutions and validated with respect to the experimental results. The influence of a series of retrofit parameters, not considered in the reported experimental campaign, was subsequently assessed via a detailed parametric study.

### ***Chapter 5 – Modeling of timber diaphragms retrofitted with diagonal sheathing overlay***

The application of an additional layer of timber boards that are nailed to the original flooring at a 45° inclination to the joists is frequently referred to as a significantly

---

effective strategy for the improvement of diaphragm in-plane behavior. This retrofit solution is cost-effective and it is also welcomed by heritage agencies because of its aesthetic consistency with the original diaphragm condition. The outcomes of a parametric study based on the modelling approaches proposed in the previous Chapters are presented herein. Models were firstly validated on experimental data found in literature. The subsequent study assessed the effectiveness of such retrofit intervention and also considered the influence of various construction details such as diaphragm size and aspect ratio and geometrical and mechanical properties of the sub-components.

### ***Chapter 6 – Timber diaphragms retrofitted with CLT panels***

It is not rare that existing wooden floor structures need to be improved in order to satisfy serviceability and ultimate limit states criteria, as concerns their behavior both under out-of-plane and in-plane loading. A possible retrofit technique, mainly aimed at improving out-of-plane floor performances, consists in the application of a layer of cross-laminated timber (CLT) panels laid over the existing floorboards and oriented parallel to the joists. Appropriate panel-to-joist shear connection determines a joist-slab composite behavior that results in a significant improvement of both the out-of-plane strength and stiffness with limited mass increment. In addition, if adequate connections between adjacent panels are provided, CLT elements can also increase diaphragm in-plane strength/stiffness. Modeling strategies proposed in the previous Chapters were implemented to assess the effectiveness of the above-mentioned retrofit strategy on the diaphragm behavior, also accounting for the influence of a series of retrofit construction details.

### ***Chapter 7 – Non-linear dynamic modeling of timber diaphragm in-plane behavior***

Chapters 3 to 6 focused on the static in-plane behavior of diaphragms considering either the as-built condition and several retrofitted configurations. The study presented in this Chapter was aimed at defining seismic force and displacement demands acting on diaphragms considering the several configurations previously studied from the static point of view. The modelling strategies proposed in the previous Chapters were adopted for the undertake of an extensive series of non-linear dynamic analyses. Investigated parameters comprised seismic hazard (defined by the expected PGA value), shaking direction and diaphragm configuration.

#### **1.1.2 PART 2**

An innovative timber-based retrofit system for URM walls is introduced and analyzed in Part 2. The core of the research work is an extensive in-situ experimental campaign comprising small-scale sub-component testing and full-scale testing of the selected retrofit strategy.

***Chapter 8 – Use of timber for URM wall retrofit***

In Chapter 8, the research work presented in thesis Part 2 is introduced by means of a literature review regarding timber-based retrofit strategies for URM walls. The research presented in Giongo et al. (2017) is summarized since it represents the starting point of the research reported in Thesis Part 2.

***Chapter 9 – Experimental shear testing of timber-masonry connection systems***

In Chapter 9, an extensive in-situ experimental investigation on timber panel to masonry wall connections realized with screw anchor fasteners (dry connection system) and grouted steel dowels is presented. A series of shear tests under monotonic, cyclic and semi-cyclic loading conditions were performed on site in a historic URM building. The examined parameters were masonry type, timber panel (i.e. cross laminated timber vs. laminated veneer lumber, softwood vs. hardwood), load-to-grain direction, fastener geometry and steel grade. The outcomes of the campaign are then reported and discussed with focus on the strength and stiffness properties, on the dissipation capacity, and residual strength of the connections under cyclic loads.

***Chapter 10 – Onsite testing of masonry walls strengthened with timber panels***

In Chapter 10 an in-situ experimental campaign on full-scale brick masonry specimens is presented. URM piers obtained from a century-old building were subjected to in-plane semi-cyclic quasi-static loading in the as-built, repaired and retrofitted configurations. The application of the reinforcement on previously damaged piers led to a notable in-plane capacity increase while the initial stiffness of the repaired specimens was found to be consistent with that of the specimens tested as-built. When applied to undamaged masonry, the retrofit system allowed to reach an in-plane force 40% higher than the capacity of the unreinforced walls, with initial stiffness comparable with that of the repaired specimens. Both repaired and retrofitted specimens exhibited remarkable displacement capacity (drift levels > 2.0%) and energy dissipation capacities.

***Chapter 11 – Shear testing of retrofitted masonry wallets***

The effectiveness of the retrofit strategy analyzed in Part 2 is investigated in Chapter 11 where the results of experimental testing are reported. A total of 16 diagonal tension (shear) tests were undertaken on a series of purpose-realized masonry specimens. In order to provide a benchmark against which compare the timber-based retrofit, some specimens were retrofitted with a lime-based composite reinforced mortar (CRM) system.

---

## 1.2 REFERENCES

- Agbabian, M. S., Barnes, S. B. and Kariotis, J. C. (ABK) (1981). “Methodology for mitigation of seismic hazards in existing unreinforced masonry buildings. Diaphragm testing.” National Science Foundation. El Segundo, California.
- ASCE (American Society of Civil Engineers). (2017). “Seismic Evaluation and Retrofit of Existing Buildings” *ASCE 41-17*, Reston, Virginia.
- Augenti, N. and Parisi, F. (2010). “Learning from Construction Failures due to the 2009 L’Aquila, Italy, Earthquake”. *Journal of Performance of Constructed Facilities*, vol. 24, No. 6.
- Baldessari, C., Piazza, M. and Tomasi, R. (2009). “The refurbishment of timber floors: characterization of the in-plane behavior” *Proceedings, PROHITEC International Conference*, Taylor and Francis, Rome, Italy, 2009.
- Binda, L., Gambarotta, L., Lagomarsino, S., Modena, C. (1999) “A multilevel approach to the damage assessment and seismic improvement of masonry buildings in Italy”, *Seismic Damage to Masonry Buildings*, A. Bernardini Ed., Balkema, Rotterdam.
- Borri, A. (2011). “Manuale delle murature storiche”, ISBN: 9788849604030, ed. Dei, Rome, Italy – *in Italian*
- Brignola, A., Pampanin, S. and Podestà, S. (2012). “Experimental Evaluation of the In-Plane Stiffness of Timber Diaphragms”. *Earthquake Spectra*, vol. 28, n. 4, pp. 1687-1709.
- Dizhur, D., Ingham, J. M., Moon, L., Griffith, M. Schultz, A., Senaldi, I., Magenes, G., Dickie, J., Lissel, S., Centeno, J., Ventura, C., Leite, J. C., Lourenco, P. B. (2011). «Performance of masonry buildings and churches in the 22 February 2011 Christchurch earthquake». *Bull. N. Z. Soc. Earthquake Eng.* 44 (4): 279–296.
- Dizhur, D., Ingham, J. M., Biggs, D. and Schultz, A. (2016). “Performance of unreinforced masonry and infilled RC buildings during the 2015 Gorkha, Nepal earthquake sequence”. *Proceedings, 16th International Brick and Block Masonry Conference, IBMAC 2016*, pp 2399-2408.
- Giongo, I., Dizhur, D., Tomasi, R. and Ingham, J. M. (2015). “Field testing of flexible timber diaphragms in an existing vintage URM building”. *Journal of Structural Engineering*, vol. 141, 2015.
- Giongo, I., Schiro, G., Piazza, M. (2017) “On the use of timber-based panels for the seismic retrofit of masonry structures” *Proceedings of the 3rd International Conference on Protection of Historical Constructions (PROHITECH)*, Lisbon, Portugal, 2017.

Ingham, J. M. and Griffith, C. (2016). “Performance of unreinforced masonry buildings during the 2010 Darfield (Christchurch, NZ) earthquake”. *Australian Journal of Structural Engineering*, vol. 11, issue 3, pp. 207-224.

Keller, A. I., Parisi, M. A., Eleftheria, T., Mosoarca, M. (2019). “Influence of historic roof structures on the seismic behaviour of masonry structures”. *Proceedings of the Institution of Civil Engineers (ICE) – Journal of Structures and Buildings*, ISSN 0965-0911| E-ISSN 1751-7702.

NZSEE (New Zealand Society for Earthquake Engineering) (2017). “Assessment and improvement of the structural performance of buildings in earthquakes”. *NZSEE 2017*. Wellington, New Zealand.

Penna, A., Morandi, P., Rota, M., Manzini, C. F., da Porto, F. and Magenes, G. (2013). “Performance of masonry buildings during the Emilia 2012 earthquake”. *Bulletin of Earthquake Engineering*, vol. 12, pp. 2255–2273.

Peralta, D. F. , Bracci, J. M. and Hueste, M. B. (2003). “Seismic Performance of Rehabilitated Wood Diaphragms”. Texas AandM University, Department of Civil Engineering, 2003.

Rizzi E., Giongo I., Ingham J. M., Dizhur D. (2019). “Testing and modeling of retrofitted diaphragms loaded in-plane”, *ASCE Journal of Structural Engineering*, vol. 146(2) DOI: 10.1061/(ASCE)ST.1943-541X.0002473.

Schiro, G., Giongo, I., Ingham, J., Dizhur, D., (2018). «Lateral performance of as-built and retrofitted timber diaphragm fastener connections», *Journal of Materials in Civil Engineering*, vol. 30 (1), ISSN: 0899-1561, [https://doi.org/10.1061/\(ASCE\)MT.1943-5533.0002110](https://doi.org/10.1061/(ASCE)MT.1943-5533.0002110).

Tena-Colunga, A. and Abrams, D. P., (1996). “Seismic Behaviour of Structures with Flexible Diaphragms”, *Journal of Structural Engineering*, vol. 122, no. 4, pp. 439-445.

Raggett, J. D., Rojahn, C. (1991). “Dynamic Amplification of Ground Motions by Low-Rise, Stiff Shear Wall Buildings”, *SMIP91 Seminar on Seismological and Engineering Implications of Recent Strong-Motion Data*, pp. 16-1 - 16-11.

Wilson, A. W. (2012). “Seismic assessment of timber floor diaphragms in unreinforced masonry buildings”. Doctoral dissertation, The University of Auckland, Auckland, New Zealand

Wilson, A., Quenneville, P. J. H., Ingham, J. M. (2014). “In-plane orthotropic behavior of timber floor diaphragms in unreinforced masonry buildings”, *Journal of Structural Engineering* 2014;140(1):04013038

---

---

# **PART 1**



## **2 TIMBER DIAPHRAGMS - STATE OF THE ART**

### **2.1 LITERATURE REVIEW**

In this chapter a literature review concerning flexible diaphragms in URM buildings is presented. In the first part the focus is set on the effects induced by the in-plane diaphragm behavior on building response considering post-earthquake survey reports, experimental campaigns and numerical research works. Subsequent paragraphs most specifically focus on the in-plane assessment of timber floor diaphragms considering the most relevant previously reported experimental campaigns investigating timber diaphragms and the various modeling approaches proposed in literature. The last paragraphs deal with the seismic assessment procedures for timber diaphragms proposed by two International Standards.

#### **2.1.1 INFLUENCE OF FLEXIBLE DIAPHRAGMS ON BUILDING PERFORMANCE**

As outlined in the Introduction Chapter, several post-earthquake surveys have reported about the influence of flexible diaphragm behavior on the seismic response of URM buildings and such aspect has frequently been deemed as being the leading cause of building failure [Penna et al. (2013), Dizhur et al. (2016) and Dizhur et al. (2011)]. In this paragraph some experimental and numerical studies which identify flexible diaphragms as being capable of significantly affect building response are reported and briefly discussed.

Tena-Colunga and Abrams (1991) analyzed the response of three instrumented URM buildings with flexible floor diaphragms during the 1989 Loma Prieta Earthquake. The recorded data in terms of accelerations, displacements, torsional effects and natural periods were compared to the results of models developed considering alternative diaphragm stiffness scenarios illustrated in Figure 2.1. The results of the study highlighted that flexible diaphragms significantly amplified horizontal accelerations

and base shear amplitudes while torsional effects were found to be smaller compared to the case of rigid diaphragms.

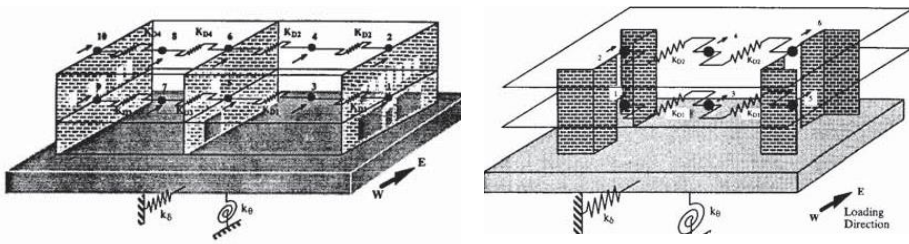


Figure 2.1: Building models adopted by Tena-Colunga and Abrams (1991). Reproduced from Tena-Colunga and Abrams (1991)

Similarly, Raggett and Rojahn (1991) analyzed the one story tilt-up reinforced concrete warehouse building featuring a timber roof diaphragm illustrated in Figure 2.2. Consistently with Tena-Colunga and Abrams (1991), the Authors reported that the flexible diaphragm introduced significant dynamic amplifications, even in the case of a low-rise building.

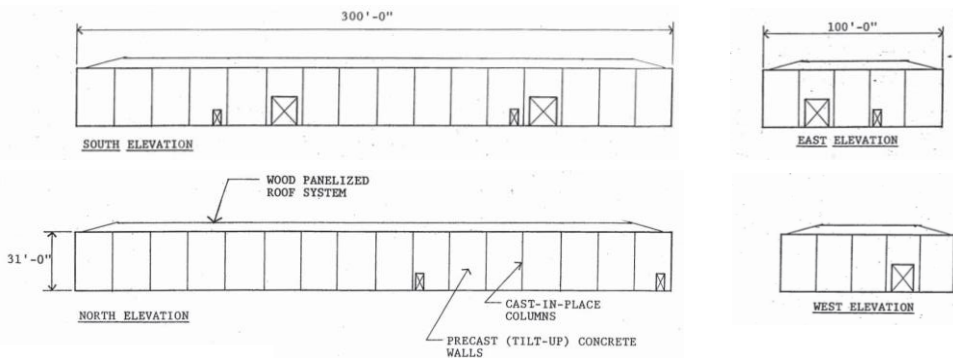


Figure 2.2: Warehouse building analyzed by Raggett and Rojahn (1991). Reproduced from Raggett and Rojahn (1991)

The influence of diaphragm in-plane behavior of URM building response was also experimentally observed in Tomazevic et al. (1993). Four  $\frac{1}{4}$  scale two story URM building specimens were purposely built featuring alternative diaphragm configurations and were dynamically tested (Figure 2.3). Results showed that the behavior of the specimens was strongly influenced by the in-plane stiffness of the floor diaphragms and by the quality of the diaphragm to wall connections. Both deformability and energy dissipation capacities were significantly improved when effective wall to diaphragm connections were provided and steel ties were inserted in the diaphragms.

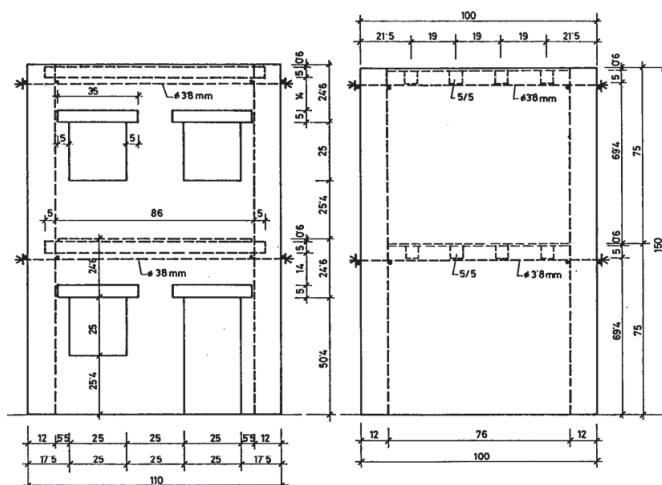


Figure 2.3: Reduced scale specimens tested by Tomazevic et al. (1993). Reproduced from Tomazevic et al. (1993)

Costley and Abrams (1995) realized two 1/3 scale URM building specimens with flexible floor diaphragms and tested them under a series of natural earthquake acceleration time history records. Among the results, flexible diaphragms were observed to amplify accelerations and displacements, especially prior to masonry cracking occurred. The effects of diaphragm in-plane deflections were also highlighted by the results of numerical models as illustrated in Figure 2.4.

Yi et al. (2006) dynamically tested a full scale two story URM building specimen with flexible diaphragms (Figure 2.5). Even if diaphragm behavior was not explicitly analyzed by the Authors, it was reported that floor structures were ineffective in providing coupling between masonry walls.

With the aim of investigating the vulnerability of the roof structures typical of the Dutch terraced houses comprising flexible timber roof diaphragms supported by URM gables, Tomassetti et al. (2019) shake-table tested three real scale building specimens. The research highlighted the importance of providing effective diaphragm to wall connections to ensure displacement compatibility, with the diaphragm accommodating the linear deflected shape induced by the gable rocking behavior. The Authors also provided a simplified SDOF model for predicting the dynamic behavior of the system accounting for both the rocking of the gable and the in-plane response of the diaphragm, implicitly stating the influence of the roof structure on the overall behavior.

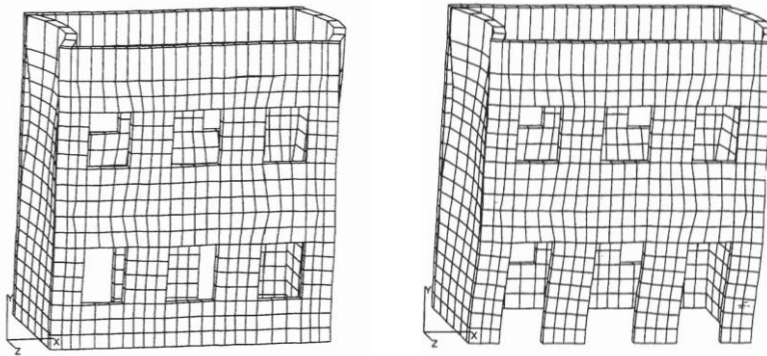


Figure 2.4: Modal shapes reported in Costley and Abrams (1995). Reproduced from Costley and Abrams (1995)

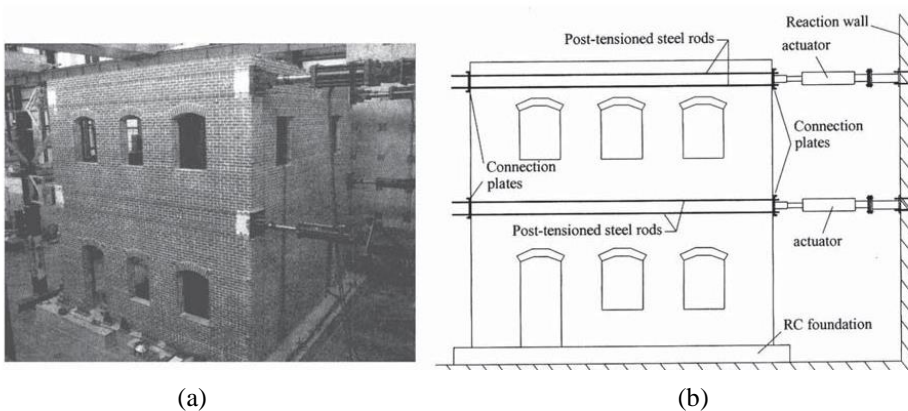


Figure 2.5: Experimental tests reported in Yi et al. (2006): a) Specimen prior to testing; b) Schematic of the test setup. Reproduced from Yi et al. (2006)

Giongo et al. (2011) modeled a two story URM building in which the in-plane behavior of floors was set based on the experimental results reported in Baldessari et al. (2009). From the pushover curves depicted in Figure 2.7 the Authors observed that each of the considered diaphragm retrofit solutions led to comparable strength, stiffness and displacement capacity increments compared to the as-built floors. The outcomes highlighted that retrofitting the diaphragms led to appreciable benefits on base shear capacity regardless of the implemented system. It must be considered that the increase in global stiffness, which in the case of timber-based retrofits doesn't imply significant mass increments, may reduce the natural periods of the building inducing higher spectral accelerations.

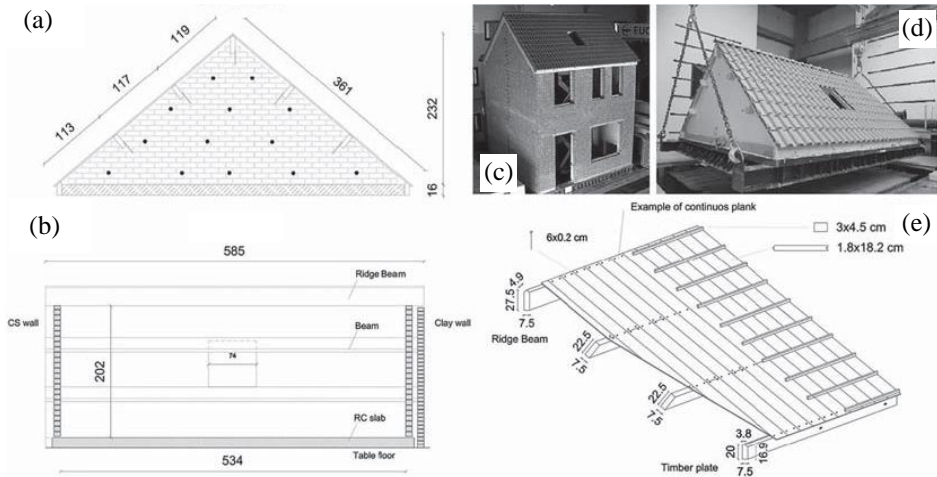


Figure 2.6: Experimental campaign reported in Tomassetti et al. (2019): a) Gable elevation; b) Roof and gable cross section; c) Building specimen; d) Gable and roof diaphragm specimen; e) Roof diaphragm details. Reproduced from Tomassetti et al. (2019)

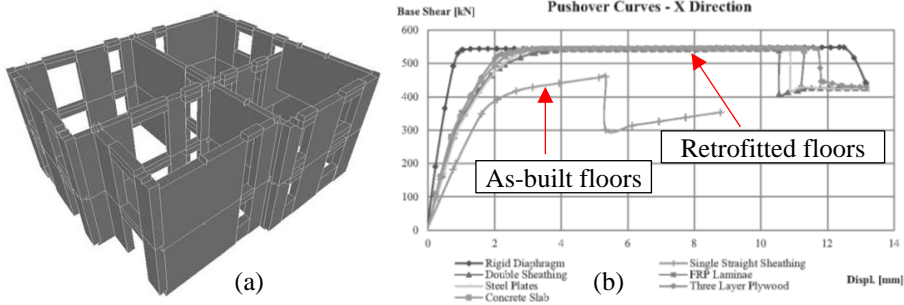


Figure 2.7: Numerical model reported in Giongo et al. (2011): a) 3D view of the model; b) Pushover curves. Reproduced from Giongo et al. (2011)

Kallioras et al. (2018) tested on a shake table a full scale URM building built according to construction details typical of the Northern European regions. The specimen, illustrated in Figure 2.8-a, featured clay brick masonry walls and flexible timber floor and roof diaphragms. The flexible floor diaphragm underwent significant shear deflections and prevented for global torsional effects as illustrated in the deformed shape plots of Figure 2.8-c. The Authors also reported that the large diaphragm in-plane flexibility led to negligible coupling between masonry walls which exhibited the tendency to displace almost independently and the flexible roof diaphragm was observed to dissipate a considerable amount of energy during the dynamic shaking.

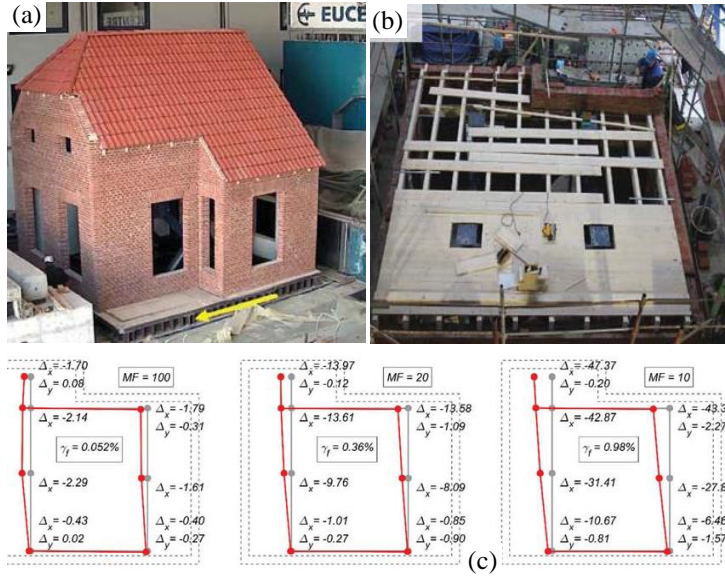


Figure 2.8: Experimental testing reported in Kallioras et al. (2018): a) Specimen prior to testing; b) Flexible floor diaphragm; c) Diaphragm in-plane deformed shape at increasing shaking intensities. Reproduced from Kallioras et al. (2018)

## 2.1.2 DIAPHRAGM IN-PLANE BEHAVIOR IDEALIZATION

Timber diaphragms are extremely simple structural components, especially in the case of single straight sheathed units. The assessment of the out-of-plane behavior of such structural elements is straightforward, being the floorboards simply supported by the joists which, in turn, are supported by perimeter walls and, in some cases, by intermediate supports. Therefore, diaphragm analysis under gravity loads can be done by decoupling the two principal directions. On the contrary, when subjected to in-plane loading, diaphragm response involves the typically nonlinear nail connection shear behavior and a certain number of internal constraints. Despite this, simplified diaphragm in-plane idealizations have been proposed in literature, with the shear beam analogy being the most commonly adopted by researchers and Standards [ASCE (2017), NZSEE (2017)]. According to such analogy the diaphragm is regarded as a deep beam which responds to in-plane loads deflecting in shear without any overall bending phenomena (Figure 2.9-a). Inertia loads are usually applied to diaphragms considering an uniform distribution (Figure 2.9-b), a concentrated load (Figure 2.9-c) or a parabolic distribution (Figure 2.9-d). Diaphragm shear deflection is calculated referring to the equivalent shear stiffness of the diaphragm  $G_d [N/m]$  which is the shear stiffness per unit width according to equation (2.1), where  $\gamma(x)$  is the shear deflection at the position  $x$ ,  $B$  is diaphragm width (Figure 2.9-a) and  $V(x)$  is the shear force on diaphragm at the position  $x$ .

$$\gamma(x) = \frac{V(x)}{B \cdot G_d} \quad (2.1)$$

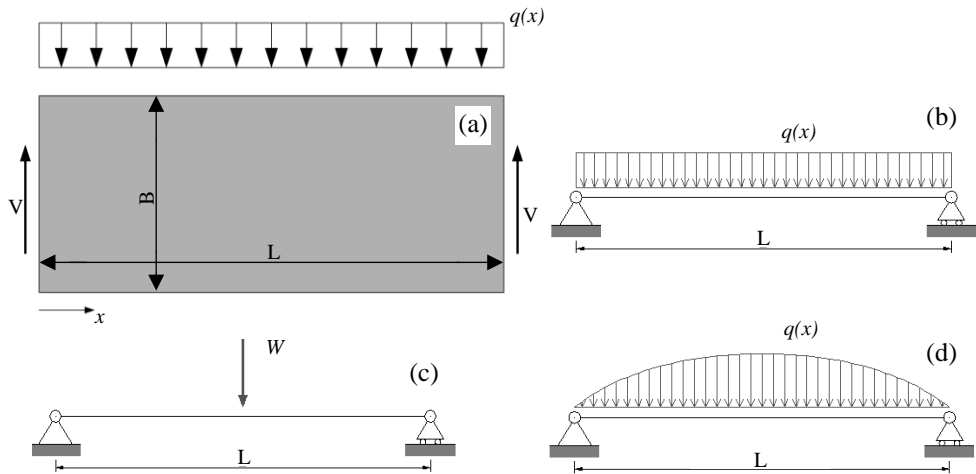


Figure 2.9: Diaphragm in-plane behavior idealization: a) Shear beam schematic; b) Uniform load distribution; c) Concentrated load at midspan; d) Parabolic load distribution

According to such assumptions the midspan displacement related to an inertial load resultant of amplitude  $W_d$  is given by equation (2.2), where  $\beta$  accounts for the selected load distribution and is equal to 0.25 for concentrated load at midspan (Figure 2.9-c), 0.125 for uniform load distribution (Figure 2.9-b) and  $5/32$  under parabolic load distribution (Figure 2.9-d).

$$\Delta_d = \beta \cdot \frac{W_d \cdot L}{B \cdot G_d} \quad (2.2)$$

### 2.1.3 EXPERIMENTAL TESTING OF DIAPHRAGMS

In-plane behavior of timber diaphragms was experimentally analyzed by the Agbabian, Barnes and Kariotis (ABK) Joint Venture and reported in the Topical Report 3 [ABK (1981)]. Fourteen  $18.3 \times 6.1 \text{ m}^2$  diaphragm specimens, representative of as many diaphragm construction types, were subjected to quasi-static and dynamic in-plane actions. The specimens also featured finishing layers that are representative for roofs and doesn't comply with floors. Moreover, some of the tested specimens have not particular relevance to timber diaphragms typically encountered in traditional URM buildings. In addition to single straight sheathed and single diagonal sheathed diaphragms, retrofit techniques including plywood panels and additional diagonal

sheathings were considered. Tested specimens exhibited a marked nonlinear behavior and actual diaphragm failure was never observed within the range of applied force magnitudes and dynamic shaking intensity levels. Despite this, both stiffness and expected strength of retrofitted units were significantly greater compared to the as built straight sheathed construction. It is worth noting that the roofing was observed to significantly affect diaphragm stiffness, therefore the extension of the attained results to floor diaphragms is not straightforward.

Peralta et al. (2003) tested three full scale straight sheathed diaphragm specimens considering both the as built and retrofitted configurations. Test sequences comprised reversed cyclic actions applied by means of the loading setup visible in Figure 2.10. As listed in Table 2.1 the sheathings representative of as-built scenario featured both straight-edged and tongue and groove (T&G) floorboard cross sections. Both parallel to joists and perpendicular to joists loading directions were considered. The specimens labeled as MAE-2 and MAE-3 were built according to the same specifications, but in the case of MAE-3 a  $0.8 \times 1.6 \text{ m}^2$  corner opening was present (see Figure 2.10-b).

*Table 2.1 Diaphragm specimens tested by Peralta et al. (2003)*

ID	L* [m]	B* [m]	Floorboards	Load direction **
MAE-1	7.32	3.66	T&G	Perpendicular
MAE-2	3.66	7.32	Straight edge	Parallel
MAE-3	3.66	7.32	Straight edge	Parallel

\* L is joist length, B is diaphragm dimension in perpendicular to joists direction

\*\* With respect to joist direction

Among the considered retrofit configurations the Authors considered blocked and unblocked plywood panel overlays, perimeter strapping and the addition of a steel frame. In the case of MAE-3 specimen the retrofit also included specific detailing in the opening area. The addition of a steel frame is not particularly meaningful for the work presented in this Thesis but, despite this, it provides an interesting comparison term. As illustrated in Figure 2.11 experimental results highlighted that the considered retrofit strategies are effective in significantly increase both diaphragm strength and stiffness. The steel truss was found to most effectively increase diaphragm in-plane stiffness and the influence of plywood blocking was appreciable.



Figure 2.10: Experimental tests from Peralta et al. (2003): a) Diaphragm MAE-1; b) Diaphragm MAE-3. Pictures taken from Peralta et al. (2003)

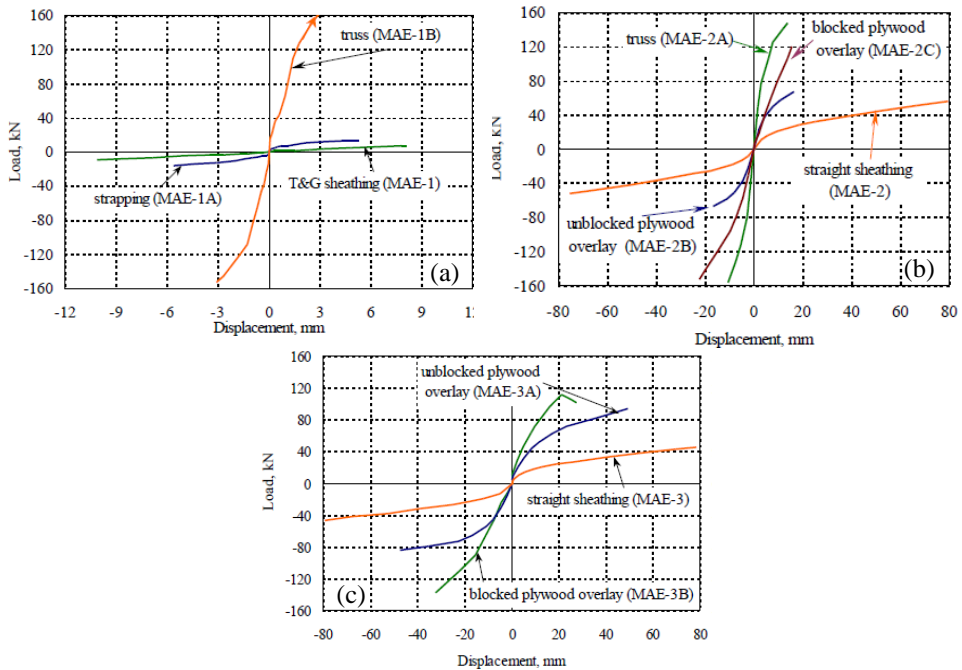


Figure 2.11: Experimental results from Peralta et al. (2003): a) Diaphragm MAE-1; b) Diaphragm MAE-2; c) Diaphragm MAE-3. Pictures taken from Peralta et al. (2003)

Further diaphragm testing was carried out by Brignola et al. (2012). Ten  $4 \times 4 \text{ m}^2$  floor specimens were subjected to reversed cyclic in-plane loading sequences with forces applied in parallel to joists direction only. Among the variables the Authors considered single straight sheathed specimens as representative of the as-built configuration (Figure 2.12-a) and straight sheathed specimens with an additional plywood layer (retrofitted, Figure 2.12-b). Three alternative boundary conditions were implemented. In

configuration CC1 side joists were fixed to the reaction frame, CC2 configuration consisted in the addition of an L-shaped steel chord screwed to the decking along diaphragm perimeter and CC3 configuration was similar to CC2 but it also accounted for diaphragm to wall connections. Specimens AB-5 and R-5 featured additional metal blocking strips stapled between floorboards (AB-5) or between plywood panels (R-5).

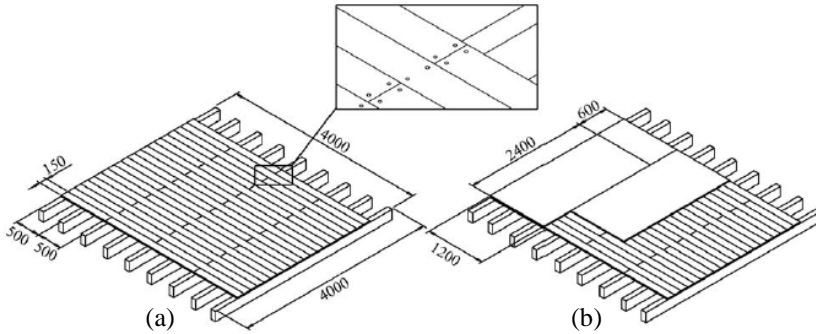


Figure 2.12: Diaphragms tested by Brignola et al. (2012): a) As-built; b) Retrofitted. Pictures taken from Brignola et al. (2012)

Table 2.2: Diaphragms tested in Brignola et al. (2012)

Diaphragm type	Boundary conditions		
	CC1	CC2	CC3
As-built	AB-1; AB-4	AB-2; AB-5	AB-3
Retrofitted	R-1; R-4	R-2; R-5	R-3

The plywood overlay was found to be an effective retrofit technique as it led to an average 300% increase of in-plane strength compared to the as-built configuration as illustrated in Figure 2.13-a. Deformed shapes illustrated in Figure 2.13-b, c suggest that the as-built diaphragm deformed according to an overall flexural behavior while the retrofitted underwent shear-like deflections. From the comparisons reported in Figure 2.14 the chord influence can be observed as being relevant (AB-1 vs. AB-2, R-1 vs. R-2).

The in-plane behavior of timber diaphragms was extensively investigated by Wilson (2012). The experimental program comprised testing of small-scale specimens (*racking assemblages* and *sub-components*) and full-scale diaphragms. The investigated parameters comprised inter-floorboard friction phenomena, straight edge vs. tongue and groove (T&G) floorboard type and floorboard interruptions. Both straight edged and T&G floorboards used for the specimens were consistent in terms of cross-section nominal dimensions and timber grade.

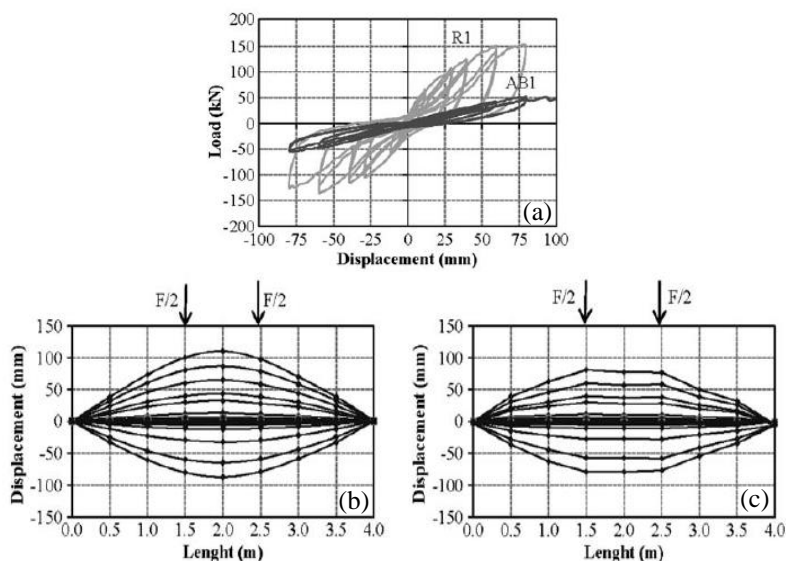


Figure 2.13: Experimental results obtained by Brignola et al. (2012) for the CCI boundary conditions: a) As-built (AB-1) vs. retrofitted (R-1) hysteresis loops; b) AB-1 diaphragm deflections for increasing loads; c) Retrofitted diaphragm deflections for increasing loads. Pictures taken from Brignola et al. (2012)

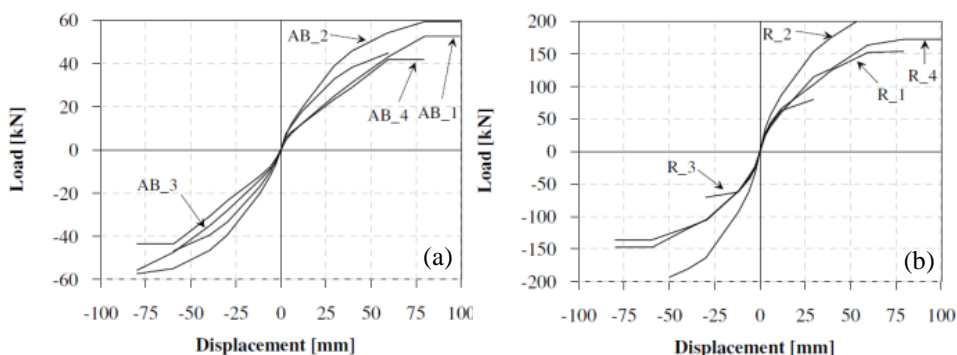


Figure 2.14: Experimental results obtained by Brignola et al. (2012): a) As-built specimens; b) Retrofitted specimens. Pictures taken from Brignola et al. (2012)

Diaphragm racks consisted of  $1.1 \times 1.1 \text{ m}^2$  assemblages, each built by connecting 1.1 m long joist elements to 5 floorboards as illustrated in Figure 2.15. A total of eight configurations were tested, obtained by varying the number of joists (2 and 3), the floorboard disposition (apart and together, see Figure 2.15) and floorboard type (straight edge and T&G). Specimens were subjected to cyclic shear tests according to the schematic provided in Figure 2.15-c.

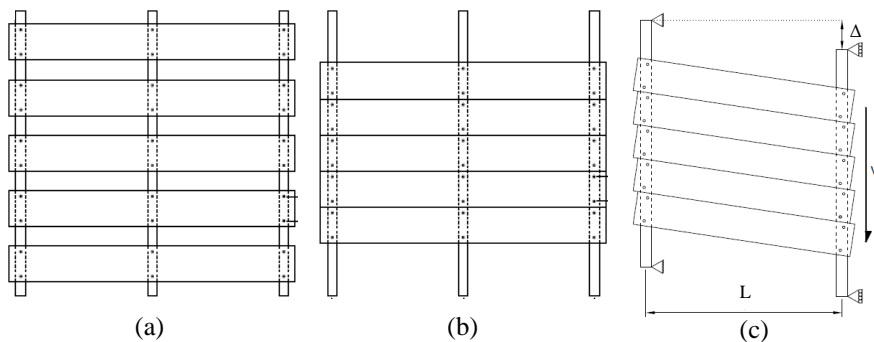


Figure 2.15: Diaphragm racks tested by Wilson (2012): a) Three joists, floorboards apart; b) Three joists, floorboards together; c) Schematic of the shear test. Pictures taken from Wilson (2012)

Comparing results obtained from the *floorboards together* and the *floorboards apart* configurations the Author observed that the specimen behavior was substantially identical up to a 6% drift level ( $drift = \Delta/L$ , see Figure 2.15-c). The *floorboards together* specimens exhibited a 10% higher force at a 10% drift level compared to the corresponding *floorboards apart* specimens. The same trend was observed for both straight edged and T&G floorboards and for 2 and 3 joists racks. From such results the influence of inter-floorboard friction was flagged as irrelevant when real case scenario diaphragm deflections are considered.

Sub-component testing was carried out on purposely built  $1.25 \times 2.45 \text{ m}^2$  specimens (new) and on two salvaged sub-components. New sub-components differed from each other in terms of floorboard type (straight edge and T&G) and floorboard disposition (continuous and staggered). The *continuous floorboards* configuration was obtained by using continuously spanning floorboard elements (Figure 2.16-a), while the *staggered floorboards* layout featured alternated floorboard interruptions at diaphragm midspan (Figure 2.16-b). Regarding straight edged floorboard configurations, sub-components with continuous floorboard arrangements exhibited strength and stiffness increments equal to 55% and 35% respectively compared to the sub-components with staggered floorboard layouts. Conversely, in the case of T&G floorboards, the differences between the behavior of the sub-components featuring the two alternative floorboard arrangements were found to be irrelevant. Such trend was attributed to the presence of defects in the continuous T&G floorboards that was postulated to be higher compared to the straight-edged floorboards. Results confirmed that the type of floorboards had irrelevant effects on both strength and stiffness of sub-components featuring staggered floorboard configuration, while in the case of continuously-spanning floorboards the

T&G sub-components exhibited approximately the 60% of both strength and stiffness compared to the sub-components featuring straight-edged floorboard type.

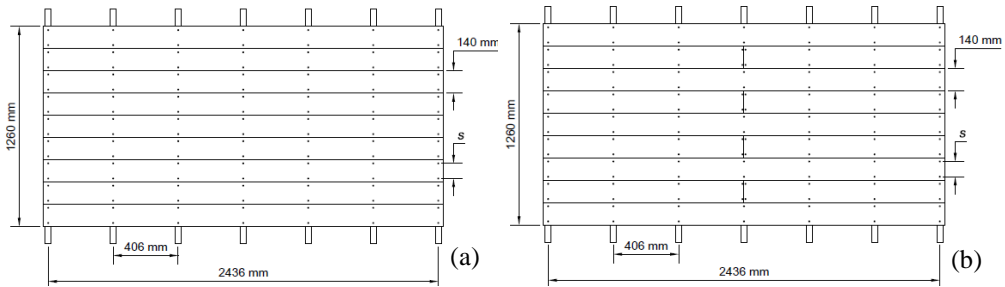


Figure 2.16: New sub-components tested by Wilson (2012): a) Continuous floorboard configuration; b) Staggered floorboard configuration. Pictures taken from Wilson (2012)

Two salvaged sub-components were extracted from floor sections of an historic New Zealand URM building constructed during the in 1890's. The floor specimens featured  $20 \times 135 \text{ mm}^2$  T&G floorboards arranged according to an irregularly staggered arrangement as illustrated in Figure 2.17. Plan dimensions of the Parnell-large specimen were  $2.15 \times 3.15 \text{ m}^2$  while the Parnell-small specimen measured  $1.90 \times 2.40 \text{ m}^2$ . Salvaged specimens exhibited specific stiffness 5 to 6 times greater compared to the new sub-components, while the observed specific shear strength was comparable to those of the new sub-components with continuous straight edged floorboards. The effect of such behavior was attributed to the presence of varnish and resin filling the gaps between adjacent T&G floorboards, causing the inter-floorboard friction to effectively restrain inter-floorboard slip.

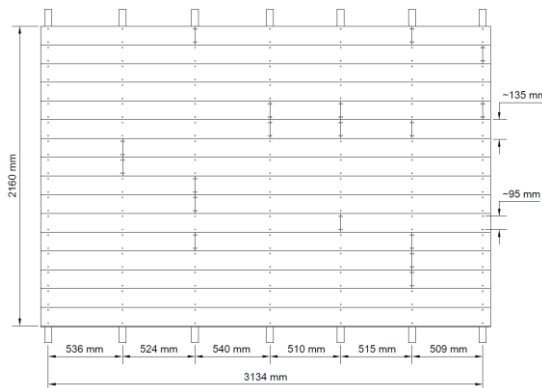
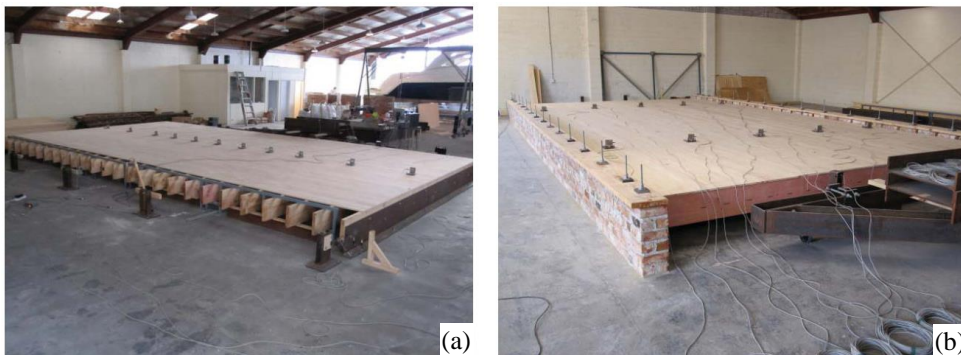


Figure 2.17 Salvaged specimen "Parnell-large" tested by Wilson (2012). Picture taken from Wilson (2012)

The experimental campaign was also extended to purposely built full-scale diaphragms. Diaphragm specimen dimensions were  $5.55 \times 10.4 \text{ m}^2$  with the joists spanning in the shorter direction. The influence of parameters such as diaphragm openings and joist continuity were considered. Diaphragms were tested in the straight sheathed configuration (representative of as-built condition) and with the addition of a layer of plywood panels nailed to the flooring underneath and connected to each other by means of light gauge steel staples (retrofitted configuration). For the purpose of providing realistic boundary conditions, in the case of perpendicular to joists loading the joists were pocketed into masonry wallets (see Figure 2.18).



*Figure 2.18: Full-scale specimens tested by Wilson (2012): a) Parallel-to-joists loading; b) Perpendicular-to-joists loading. Reproduced from Wilson (2012)*

Experimental results related to straight sheathed specimens showed that diaphragm specific shear stiffness in perpendicular to joists was approximately the 60% compared to the stiffness under parallel to joists loads. The retrofitted specimens exhibited an equivalent shear stiffness 28 and 14 times greater compared to the as-built in parallel and perpendicular to joists direction respectively, while diaphragm strength increments ranged between 2 to 5 times.

Diaphragm behavior was furtherly investigated by Baldessari et al (2009) by means of quasi-static cyclic tests on relatively small-scale diaphragm specimens measuring  $4 \times 5 \text{ m}^2$  loaded in parallel to the joist direction. Straight sheathed diaphragms were considered as representative for the as-built configuration and the effectiveness of several retrofits was investigated. Retrofit techniques comprised the addition of a layer of floorboards inclined at  $45^\circ$  with respect to joist direction, diagonal steel plates, a triple layer of plywood panels connected to the joists with steel dowels and adhesives and an additional RC slab (see Figure 2.19). Results illustrated in Figure 2.20 highlight that each of the considered retrofit strategies is significantly effective in increasing diaphragm in-plane stiffness, with the triple layer of plywood panels being the most

effective. The stiffness of the straight sheathed specimen was observed to be unaffected by the addition of a steel chord running along diaphragm perimeter.

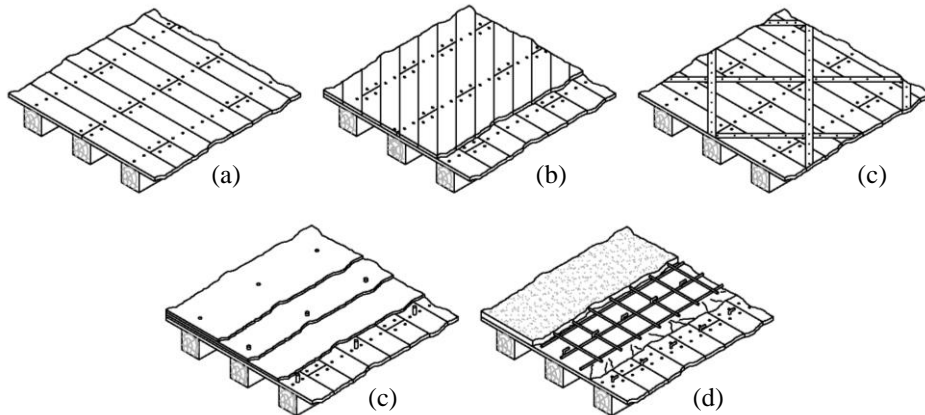


Figure 2.19: Diaphragm configurations tested in Baldessari et al. (2009): a) Straight sheathed diaphragm; b) Specimen retrofitted with diagonally-laid additional floorboard layer; c) Specimen retrofitted with diagonal steel plates; d) Specimen retrofitted with plywood panels and adhesives; e) Specimen retrofitted with additional RC slab. Picture taken from Baldessari et al. (2009).

Giongo et al. (2015) tested on-site two vintage diaphragm specimens located in an URM building in New Zealand constructed circa 1913. Tested specimens were cut from the same floor as visible in Figure 2.21 and were subjected to dynamic snap-back tests and reversed cyclic loading sequences in perpendicular to joists direction. Specimen A measured  $9.6 \times 5.6 \text{ m}^2$  while Specimen B measured  $9.6 \times 4.7 \text{ m}^2$  with the joists spanning in the 9.6 m long direction being overlapped and supported at midspan on a steel beam. Diaphragm decking consisted of T&G floorboards. Consistently with Wilson (2012) the Authors reported for higher stiffness values compared to those expected for newly built straight sheathed diaphragms.

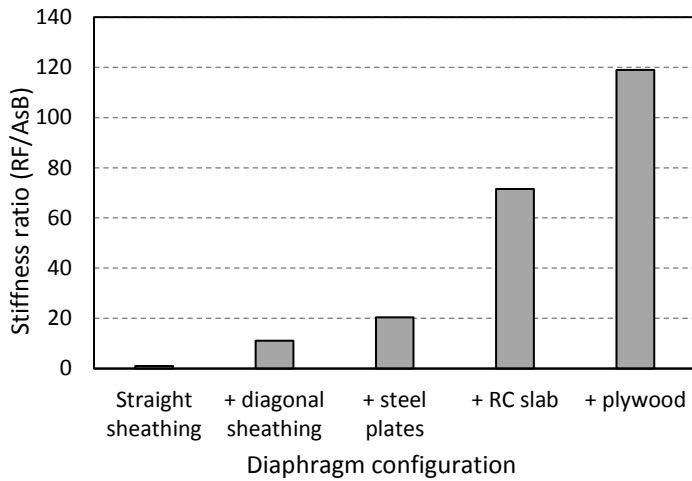


Figure 2.20: Results obtained by Baldessari et al. (2009), diaphragm stiffness comparisons



Figure 2.21: Specimen tested by Giongo et al. (2015): a) Floor sections; b) Floor view from below. Pictures taken from Giongo et al. (2015)

#### 2.1.4 MODELING OF DIAPHRAGMS

One of the earliest attempts to numerically simulate the in-plane behavior of timber diaphragms is the lumped parameter model proposed by Ewing et al. (1980) within the ABK joint venture project whose schematic is depicted in Figure 2.22. The diaphragm is divided into a certain number of segments with a mass placed at each segment interface which is assigned a DoF. Springs reproduce the nonlinear hysteretic diaphragm behavior while dampers are introduced to account for energy dissipation under dynamic excitation.

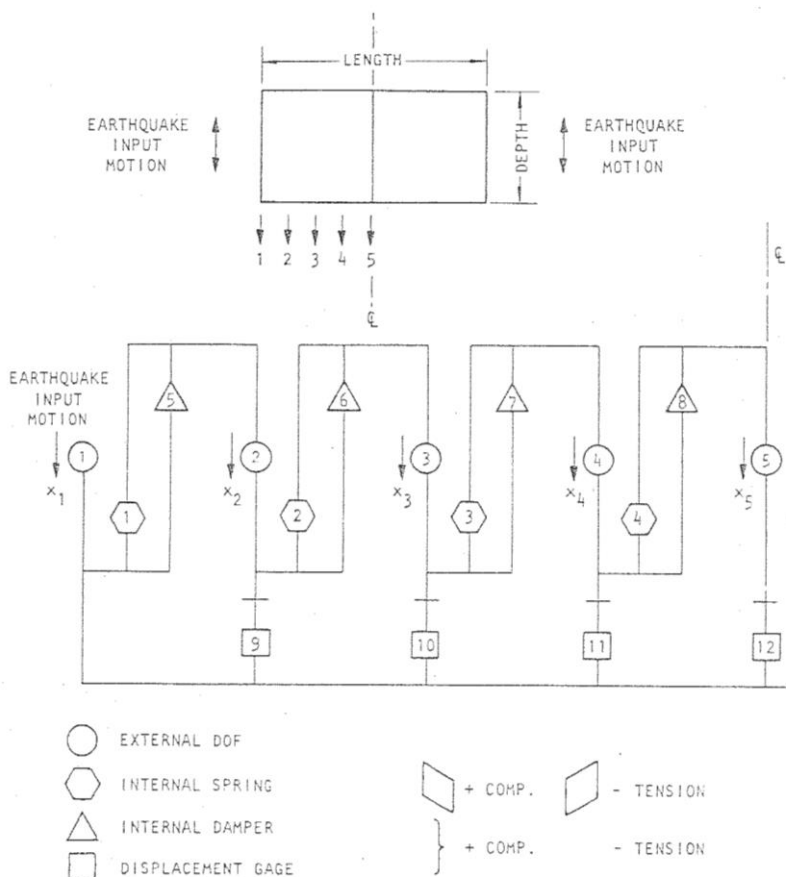


Figure 2.22: Schematic of the lumped parameter model, reproduced from ABK (1981)

Most recently, thanks to the remarkable increase in computer processing power which, in turn, led to the spread of powerful FEM software packages, numerical modeling of diaphragms have focused on micro-scale approaches based on the explicit modeling of each single diaphragm component (joists, floorboards, nails etc.).

Peralta et al. (2003) proposed a modeling strategy in which joists were modeled as linear-elastic 1D beam elements while floorboards and plywood panels were represented by linear elastic 2D elements. Nonlinear springs oriented along the principal axes and located at floorboard edges were used to reproduce nail connections (therefore nail spacing was increased). Inter-floorboard and inter-panel contact were not modeled and floorboard interruptions were disregarded as well as second order effects (linear geometry was considered). Nail behavior was defined according to the analytical formulation proposed by McLain (1975), while timber material was set as linear elastic. The modeling approach was validated considering the experimental tests undertaken by

the Authors and reported in section 2.1.3, providing the results illustrated in Figure 2.23. Numerical simulations were performed assigning the springs representative of nail connections alternative behaviors (upper bound and lower bound backbones). In the case of MAE-1 diaphragm the model failed to reproduce diaphragm response. The Authors also performed geometrically non-linear analyses (“Nonlinear” backbone) which was found to provide consistent results with the Galerkin formulation which accounts for second order effects related to nonlinear geometry. Even in this case the results were not found to be satisfactory. In the cases of MAE-2 and MAE-3 specimens the numerical backbones were in substantial good agreement with the experimental results, but a remarkable stiffness underestimation was observed for small displacement amplitudes.

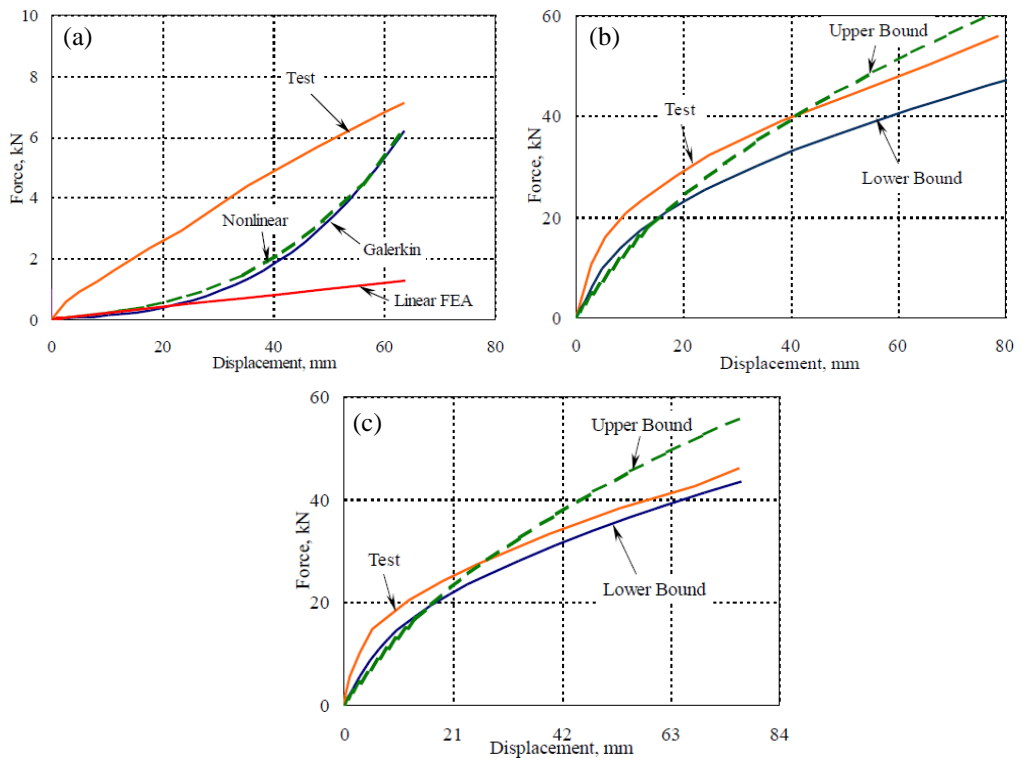


Figure 2.23: Model validation as reported in Peralta et al. (2003): a) MAE-1 diaphragm; b) MAE-2 diaphragm; c) MAE-3 diaphragm. Pictures taken from Peralta et al. (2003)

Brignola (2009) proposed a linear FE model aimed at reproducing diaphragm initial stiffness. Joists and chords were modeled as 1D beam elements, floorboards and panels were reproduced by means of 2D elements accounting for floorboard interruptions and nail connections were represented by means of elastic springs. The initial stiffness

evaluated by means of the model was compared with the experimental results obtained by the Authors and reported in section 2.1.3. Validation results are depicted in Figure 2.24, showing a good agreement between experimental and numerical stiffness values.

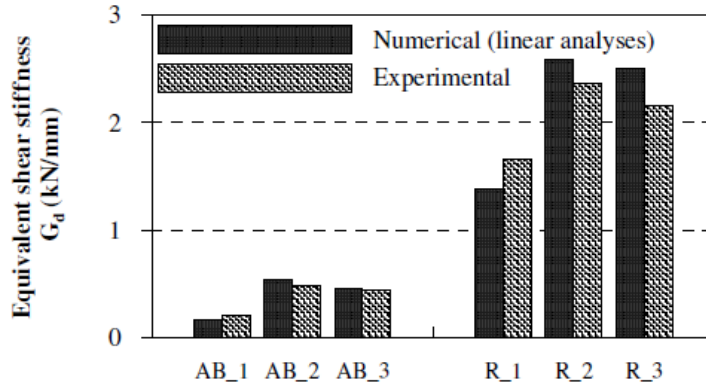


Figure 2.24: : Model validation as reported in Brignola (2009): Initial stiffness of diaphragms, numerical vs. experimental. Picture taken from Brignola (2009)

Wilson (2012) proposed a modeling strategy in which floorboards and joists were represented by 1D beams while nonlinear link elements were used to represent nail connections and placed at actual nail locations. Floorboard interruptions were modeled by means of bending releases at interruption locations and doubling the nonlinear links representing the nail couples. Rigid links were implemented to connect the nail elements to the floorboards (see Figure 2.25).

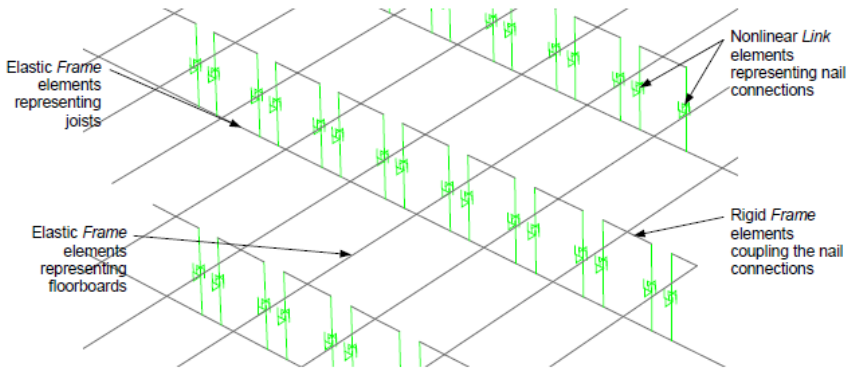


Figure 2.25: : Details of the model proposed by Wilson (2012). Picture taken from Wilson (2012)

Timber was assigned a linear elastic material type and inter-floorboard contact and friction phenomena were disregarded. The model was validated comparing its outputs with the experimental results attained by the Author in the experimental testing of the rack assemblages, the sub-components and the full-scale specimens reported in section 2.1.3. As illustrated in Figure 2.26, the model accurately reproduced the behavior of the full-scale specimens in both the parallel and the perpendicular to joists direction. In the case of the small scale “racking” tests the experimentally observed response was accurately reproduced up to a certain displacement amplitude, while the hardening experienced by the “*floorboards apart*” specimens was not replicated. The behavior of the sub-components was well replicated except for the floorboard failure experienced by the tested specimens. Conversely, the model was not capable of reproducing the response of the salvaged sub-components.

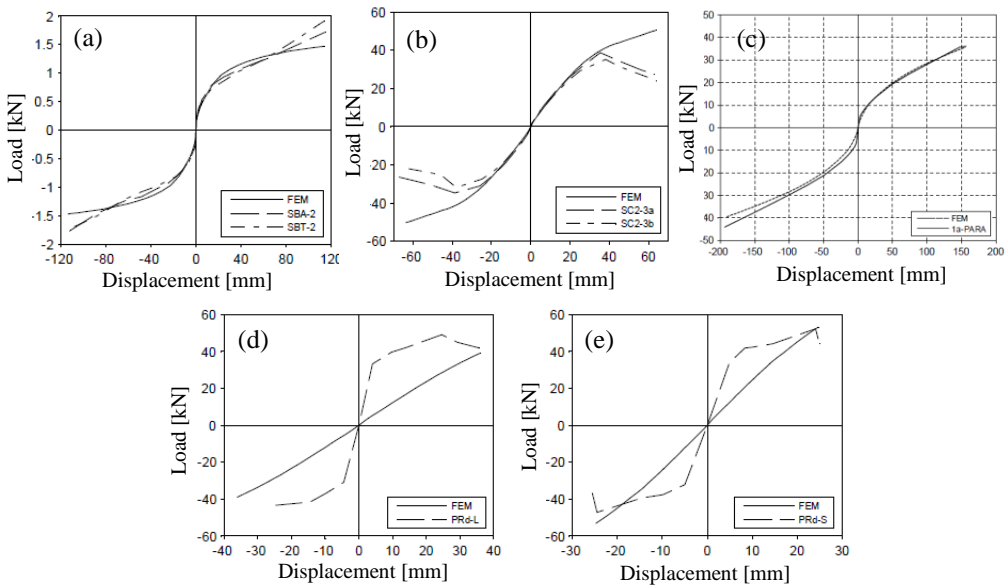


Figure 2.26: Model validation reported by Wilson (2012): a) Racking test with “floorboards together”; b) New sub-component; c) Full scale diaphragm; d) and e) Salvaged sub-components. Pictures taken from Wilson (2012)

## 2.1.5 GENERAL REMARKS

The literature review outlined in the previous sections testifies the importance of diaphragm behavior in assessing the response of URM buildings subjected to horizontal actions. The research efforts pertaining this subject provided a good understanding of diaphragm in-plane deflection mechanisms, but some aspects have not been deepened leaving place for some open gaps. Even among nominally consistent diaphragm types (e.g. straight sheathed, retrofitted with plywood panels etc.), the strength and stiffness

values reported by the Authors cited in the previous paragraphs often varied strongly from one to each other. This is not surprising since each of the experimental campaigns considered specimens built according to different construction details (such as timber species, timber element and connection geometries), specimens of different plan dimensions and aspect ratios that were subjected to different load distributions. Only in few cases the diaphragm behavior was investigated with respect to both parallel and perpendicular to joists direction and, if so, the specimens exhibited an appreciable tendency to orthotropic behavior. It should also be noted that most of the reported studies were undertaken considering diaphragm constructions typical of North America, Northern Europe and Oceania which feature slender joist cross sections ( $h/b > 5$ ), while typical traditional Mediterranean timber floors have squatter joists ( $h/b < 2$ ) and consistent joist spacings (400 – 600 mm). Such aspect will likely lead to macroscopic differences in diaphragm response, especially when loaded perpendicularly to the joists. Moreover, research reported in Wilson (2012) and in Giongo et al. (2015) have found that vintage diaphragms tested after several decades of service, whose performance is expected to be weak because of ageing, exhibited significantly greater stiffness and strength compared to the newly constructed specimens tested by other Authors. Wilson (2012) attributed the discrepancies to the presence of *“varnish or resin that was observed to cover the extracted diaphragm sections and to fill the T&G interfaces ..... to resist inter-floorboard slip during testing”* but such aspect seems to require further investigations.

The great variety of construction details makes it necessary to study the subject via numerical simulations based on reliable modeling approaches capable of accounting for the influence of the different construction details. Regarding this topic, several modeling strategies have been proposed by various Authors. In some cases, the models were capable of accurately replicate the experimentally observed diaphragm response, while in other cases the numerical approaches failed.

Peralta et al. (2003) found significant discrepancies between the numerical model outputs and experimental results regarding a diaphragm that was loaded in perpendicular to joists direction. Geometrical nonlinearities were cited among the possible leading causes, but their influence was not clarified. Wilson (2012) proposed a modeling strategy capable of accurately predicting the response of newly constructed diaphragms but significantly underestimating the stiffness of the vintage specimens.

Furthermore, the influence of floorboard interruptions and inter-floorboard phenomena were never completely accounted for in the models proposed in literature, despite their influence have been called into question to interpret the discrepancies between numerical outputs and the experimental results.

---

## 2.2 STANDARD FRAMEWORKS

In this section the most extensive seismic assessment procedures for timber diaphragms proposed by International Standards are reported and briefly discussed.

At present ASCE 41-17 “Seismic Evaluation and Retrofit of Existing Buildings” [ASCE (2017)] is the standard that addresses the flexible timber diaphragm issue most extensively. ASCE 41-17 is the updated version of the ASCE 41-07 “Seismic Rehabilitation of Existing Buildings” [ASCE (2006)] which is mainly based on FEMA 356 [FEMA (2000)]. FEMA 356 updates and converts FEMA 273 [FEMA (1997)] into mandatory language. Therefore, the “diaphragm assessment procedure” proposed by the ASCE 41 Standard is based on the procedure introduced in the ‘90s by FEMA 273. The procedures are mainly based on the experimental outcomes published by the Agbabian, Barnes and Kariotis joint venture as reported in the Topical Report TR03 [ABK (1981)] and briefly discussed in section 2.1.3. The influence of the experimental outcome from [ABK (1981)] is still noticeable even in the most recent standards. Timber diaphragm in plane assessment is also detailed in New Zealand NZSEE 2017 [NZSEE (2017)] which updates the NZSEE 2006 [NZSEE (2006)] Standard. Diaphragm assessment procedure in NZSEE 2006 [NZSEE (2006)] is based on ASCE and FEMA Standards. The experimental background for the changes introduced by NZSEE 2017 lays mainly in the research work recently carried out at the University of Auckland [see Giongo et al. (2014) for detailed reference].

### 2.2.1 AMERICAN STANDARD ASCE 41-17

#### 2.2.1.1 Seismic input

According to ASCE 41-17 [ASCE (2017)], the in-plane behavior of the diaphragms defines the distribution of seismic forces for unreinforced masonry (URM) buildings. In fact, for linear static procedures, the pseudo seismic force has to be calculated for each span of each diaphragm referring to a formula that accounts for diaphragm natural period. The Standard also gives directions for classifying the diaphragms which should be considered flexible if the maximum horizontal deformation is more than twice the average story drift. Calculations of diaphragm period  $T_d$  are based on the Rayleigh’s quotient for a fixed end flexural beam as per equation (2.3) where  $\Delta_d$  is the maximum deflection experienced by the diaphragm [m] when subjected to a lateral force equal to its tributary weight.

$$T_d = (3.07 \cdot \Delta_d)^{0.5} \quad (2.3)$$

The seismic action on the diaphragm is then calculated as a function of the period  $T_d$  according to equation (2.4), where  $V_d$  is the lateral force,  $C_1$  and  $C_2$  are modification factors depending on diaphragm natural period and  $C_m$  is a factor equal to 1.  $S_a$  is the response spectrum acceleration and  $W_d$  is the tributary seismic weight of the diaphragm which should include also the out-of-plane loaded walls contribution.

$$V_d = C_1 \cdot C_2 \cdot C_m \cdot S_a \cdot W_d \quad (2.4)$$

Such method of force distribution can be applied only if diaphragm deflections do not exceed 6 in. (approximately 150 mm). Since the in-plane loaded walls are considered to be rigid, seismic amplifications due to the diaphragm position with respect to the ground are not considered. To calculate  $\Delta_d$ , the default shear stiffness values ( $G_d$ ) given in Table 2.3 can be employed as the diaphragm shall be considered to remain elastic under the prescribed lateral forces. The value  $G_d$  is intended as the equivalent diaphragm stiffness as defined in paragraph 2.1.2, therefore  $\Delta_d$  can be obtained according to equation (2.5), where  $L$  is the diaphragm span (dimension orthogonal to the loading direction) and  $B$  is the diaphragm width.

$$\Delta_d = \beta \cdot \frac{W_d \cdot L}{G_d \cdot B} \quad (2.5)$$

As outlined in paragraph 2.1.2,  $\beta$  accounts for the adopted inertia load distribution and for the static scheme selected for the diaphragm ( $\beta = 0.25$  for a shear beam under point load;  $\beta = 0.125$  for a shear beam under uniformly distributed load;  $\beta = 5/32$  for a shear beam under parabolic load). For reference see paragraph 2.1.2.

Table 2.3: Default expected strength and stiffness values for wood diaphragms. Taken from ASCE (2017)

Diaphragm Type	Shear Stiffness ( $G_d$ )		Expected Strength ( $Q_{CE}$ )		
	[lb/in]	[KN/m]	[plf]	[KN/m]	
Single straight sheathing	2000	350	120	1.75	
Double straight sheathing	Chorded	15000	2627	600	8.76
	Unchorded	7000	1226	400	5.84
Single diagonal sheathing	Chorded	8000	1401	600	8.76
	Unchorded	4000	701	420	6.13
Straight sheathing over diagonal sheathing	Chorded	18000	3152	900	13.13
	Unchorded	9000	1576	625	9.12
Double diagonal sheathing	Chorded	18000	3152	900	13.13
	Unchorded	9000	1576	625	9.12
Panel overlay on sheathing Unblocked	Chorded	9000	1576	450	6.57
	Unchorded	5000	876	300	4.38
Panel overlay on sheathing Blocked	Chorded	18000	3152	-	-
	Unchorded	7000	1226	-	-

Within the framework of the ASCE 41-17 Standard equations to determine diaphragm midspan deflections at yield ( $\Delta_y$ ) are provided. For single straight sheathed diaphragms,

double straight sheathed diaphragms, single diagonal sheathed diaphragms, diagonal sheathing with straight sheathing or flooring above diaphragms and double diagonal sheathing diaphragms,  $\Delta_y$  is given by equation (2.6), where  $E$  is modulus of elasticity of diaphragm chords [lb/in<sup>2</sup>],  $A$  is the area of the diaphragm chords section [in<sup>2</sup>],  $\Sigma(\Delta_c X)$  accounts for chord slice slip values and  $v_y$  is the shear per unit length at yield [lb/in].

$$\Delta_y = \frac{5 \cdot v_y \cdot L^3}{8 \cdot EA \cdot B} + \frac{v_y \cdot L}{4 \cdot G_d} + \frac{\Sigma(\Delta_c X)}{2 \cdot B} \quad (2.6)$$

Some unit inconsistency can be reported since  $G_d$  is expressed in [lb/in], while the length quantities  $L$  and  $B$  are in [in] and [ft] respectively. Moreover, the calculation seems to be inconsistent since in the first term of the formula  $v_y$  is expressed in [lb/ft] and  $L$  is in [ft]. Equation (2.6) can be re-arranged obtaining equation (2.7), where  $\Delta_d$  [m],  $W_d$  [kN],  $G_d$  [kN/m],  $L$  [m],  $B$  [m],  $\Delta_c$  [m],  $X$  [m],  $A$  [mm<sup>2</sup>] and  $E$  [Gpa].

$$\Delta_d = \frac{5 \cdot v_y \cdot L^3}{192 \cdot EA \cdot B} + \frac{W_d \cdot L}{8 \cdot G_d \cdot B} + \frac{\Sigma(\Delta_c X)}{2 \cdot B} \quad (2.7)$$

According to the static schemes considered in paragraph 2.1.2, equation (2.6) is written re-arranging equation (2.5) and considering  $\beta=0.125$  (uniform distributed load). In the former version of ASCE 41 [ASCE (2006)], diaphragm displacement at yield  $\Delta_y$  was calculated according to equation (2.8), which corresponds to equation (2.5) written substituting  $\beta=0.25$  (concentrated load at midspan).

$$\Delta_y = \frac{v_y \cdot L}{2 \cdot G_d} \quad (2.8)$$

The three-term formula of equation (2.7) gives higher values of  $\Delta_d$  compared to equation (2.5) which generally leads to smaller lateral forces calculated according to equation (2.4). For timber diaphragms featuring wood-based structural panels (used as primary sheathing or in addition to straight sheathings beneath or above),  $\Delta_y$  should be calculated according to equation (2.9) where  $G$  is the actual shear modulus of the panels instead of the equivalent shear modulus adopted in previous equations. Parameter  $t$  is wood panel thickness,  $\alpha$  accounts for the nail pattern ( $\alpha = 0.188$  for constant nailing;  $\alpha = 0.376$  for variable nailing) and  $e_n$  is the yield slip of the nail connections.

$$\Delta_y = \frac{5 \cdot v_y \cdot L^3}{8 \cdot EA \cdot B} + \frac{v_y \cdot L}{4 \cdot G \cdot t} + \frac{\Sigma(\Delta_c X)}{2 \cdot B} + \alpha \cdot L \cdot e_n \quad (2.9)$$

Equation (2.9) arises from the girder analogy in which the sheathing acts as the web of an I beam and is subjected to shear actions while and the chords respond to the bending forces (representing the flanges of the I beam). As a consequence, each component should respond in series with each other with the behavior of the sheathing and the

behavior of the chords being uncoupled. Equivalent shear stiffness values  $G_d$  provided in Table 2.3 already account for the stiffening effect and deformability of chords since they are calculated from the experimentally-observed response of chorded diaphragms as reported in [ABK (1981)]. This is also reflected by the different stiffness values provided for chorded and un-chorded diaphragm configurations of the same typology. Hence, it appears that the first term of equation (2.6) accounts for a parameter whose effect is already included in the  $G_d$  value that appears in the second term of the equation.

### 2.2.1.2 Diaphragm verification

ASCE 41-17 also provides rules for checking the diaphragms under the actions defined according to the previous paragraph. Because in URM buildings diaphragms transfer the inertial load from out-of-plane loaded walls to the in-plane resisting elements, they are to be considered as primary elements. Component capacity must be determined distinguishing between deformation-controlled actions and force-controlled actions. The classification depends on the behavior of the component itself. Brittle components (type 3 curve in Figure 2.27-a) must be classified as force-controlled, while components that exhibit ductile behavior with plastic range almost double to the elastic range with non-significant strength losses (Type 1 and Type 2 curves in Figure 2.27-a) must be regarded as deformation-controlled.

Modeling parameters to be used for defining force-displacement relations for timber diaphragms are provided by the Standard and are reported in Table 2.4 (Figure 2.27-b).

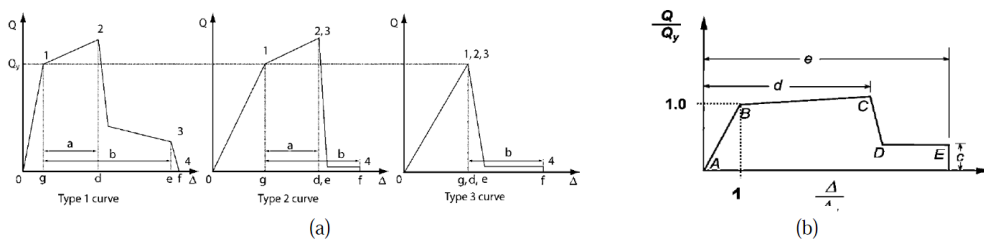


Figure 2.27: Component force vs deformation curves. Reproduced from ASCE (2017)

According to the provided parameters each timber diaphragm construction type addressed by the Standard must be regarded as deformation controlled ( $d$ -parameters in Table 2.4). The designation of  $m$ -factors (see Table 2.4) is a sufficient requirement for the classification of a component as deformation-controlled. The safety must be checked referring to equation (2.10) where  $k$  is the knowledge factor (which ranges from 0.75 to 1.00) and  $Q_{CE}$  is the mean value of the expected diaphragm strength which is provided by the Standard for each diaphragm type.

Table 2.4: Modeling parameters and acceptance criteria for linear and nonlinear procedures.  
Reproduced from ASCE (2017)

Diaphragms*	Chord	Linear Procedures		Nonlinear Procedures				
		m-factors Primary		Modelling Parameters			m-factors Primary	
		L/B	LS	L/B	d	e		Resid. s. c
Single straight sheathing	Yes	≤ 3	2	≤ 2	2.5	3.5	0.2	2.5
	No	≤ 3	1.5	≤ 2	2	3	0.3	2
Panel overlay on sheathing	Yes	≤ 3	2.5	≤ 3	3	4	0.3	3
		4	2	4	2.5	3.5	0.3	2.5
	No	≤ 2.5	2	≤ 2.5	2.5	3.5	0.4	2.5
		3.5	1.5	3.5	2	3	0.4	2

$$m \cdot k \cdot Q_{CE} \geq \frac{v_d}{2 \cdot B} \quad (2.10)$$

$Q_{CE}$  values are consistent with the experimental shear capacity observed by [ABK (1981)] and, as reported in paragraph 2.1.3 are related to timber diaphragms loaded parallel to the joists with an aspect ratio  $L/B = 3$ . The related bending capacity ( $M_{res}$ ) has therefore to be calculated according to equation (2.11) which ensures that the bending capacity required to resist the lateral seismic force is automatically guaranteed if equation (2.9) is satisfied, even when a parabolic inertial load distribution is adopted as prescribed by ASCE 41 (Figure 2.28).

$$M_{res} = m \cdot k \cdot Q_{CE} \cdot B \cdot \frac{L}{3} \quad (2.11)$$

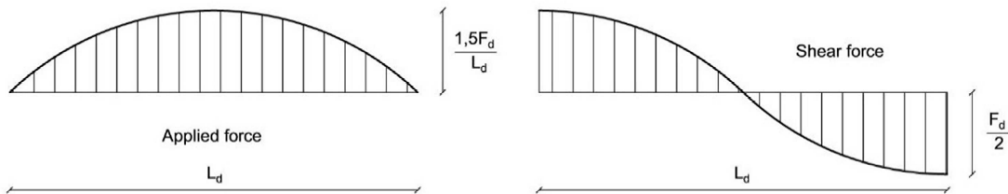


Figure 2.28: Plausible force distribution in a flexible diaphragm [ASCE (2017)]

It seems that diaphragms with the joists oriented parallel to the seismic action and supported on the out-of-plane walls should be regarded as force-controlled since the Standard reports that “If the diaphragm carries lateral loads from vertical-force-resisting elements above the diaphragm level, then  $M$  and  $V$  shall be considered force-controlled actions”. In such case, if the diaphragm is regarded as a force-controlled component, inequality (2.12) must be checked.

$$k \cdot Q_{CL} \geq Q_{UF} \rightarrow 0.85 \cdot k \cdot Q_{CE} \geq \frac{C_m \cdot S_a \cdot W_d}{2 \cdot B \cdot J} \quad (2.12)$$

In equation (2.12)  $Q_{CL}$  is the lower bound estimate of the component strength (the relation  $Q_{CL} = 0.85 \cdot Q_{CE}$  can be assumed),  $Q_{UF}$  is the force-controlled action and  $J$  is the force-delivery reduction factor ( $\geq 1$ ) taken as the small  $DCR$  of the components in the load path delivering force to the diaphragm. Approximately  $J$  is equal to 2.0 for high level of seismicity, 1.5 for moderate seismicity and 1.0 for low seismicity.

### 2.2.1.3 Non-linear procedures

When implementing nonlinear procedures, acceptance criteria consist in acceptable deformations that are defined for each selected performance level. Diaphragm backbone curves must be defined according to the parameters reported in Table 2.4. The standard procedure for calculating diaphragm backbones (illustrated in Figure 2.27-b) is based on the expected diaphragm strength  $Q_{CE}$  and the deformation limit. The yield capacity corresponding to the point B, is calculated dividing the expected strength  $Q_{CE}$  by 1.5, while deformation capacity is equal to the deformation limit multiplied by the knowledge factor. For force-controlled actions (diaphragm carrying lateral loads from vertical-force-resisting elements), diaphragms can be modeled as linear elastic components. If the case, strength check is required comparing the maximum analysis force to the diaphragm lower-bound strength multiplied by the knowledge factor ( $0.85 k Q_{CE}$ ).

## 2.2.2 NEW ZEALAND STANDARD NZSEE 2017

### 2.2.2.1 Seismic input and diaphragm demand

The general building idealization is consistent with that of ASCE 41-17, therefore the in-plane loaded walls are regarded as rigidly respond to seismic actions with the dynamic behavior of the flexible diaphragms governing the building response in terms of equivalent actions and deflections. Therefore, amplification factors due to the diaphragm location are not considered. The diaphragm period is calculated applying the Rayleigh's quotient to a shear beam subjected to parabolic load distribution according to equation (2.13) as proposed by Wilson (2012), being  $G'_{d,eff}$  is the effective shear stiffness of diaphragm.

$$T_d = 0.7 \cdot \left( \frac{W_d \cdot L}{G'_{d,eff} \cdot B} \right)^{0.5} \quad (2.13)$$

Experimental support to the approach adopted in equation (2.13) can also be found in Giongo et al. (2013) and in Giongo et al. (2015), where dynamic snap-back testing was performed on full-scale vintage diaphragms. The effective shear stiffness  $G'_{d,eff}$  is

evaluated according to equation (2.14), being  $A_{gross}$  the gross diaphragm plan area (also including penetrations, if any),  $A_{net}$  is the diaphragm net area (background on the effects of penetrations is reported in Wilson (2012), the formula is applicable for penetrations smaller than the 10% of  $A_{gross}$ ). Parameter  $\alpha_w$  accounts for the out-of-plane stiffness of face-loaded walls.

$$G'_{d,eff} = \alpha_w \cdot \frac{A_{net}}{A_{gross}} \cdot G_d \quad (2.14)$$

Consistently with the American Standard, also the New Zealand Standard provides reference values for diaphragm shear stiffness, which are reported in Table 2.5. In contrast with the ASCE 41, diaphragm orthotropic behavior is accounted for based on the research outcomes reported in Wilson (2012). Namely, floors loaded parallel to the joists should be considered stiffer than the floors loaded orthogonal to the joists. Data in Table 2.5 refer to single straight sheathed diaphragms which are the most representative of New Zealand existing timber diaphragms. For different floor typologies (including alternative sheathing types and also retrofits), the stiffness related to straight sheathed units can be multiplied by amplification factors that are calculated according to the values proposed by the American Standard and related to the experimental campaign reported in ABK (1981).

*Table 2.5: Shear stiffness values [kN/m] for straight sheathed vintage timber floor diaphragms. Reproduced from NZSEE (2017)*

Direction of loading	Joist continuity	Condition rating	Shear stiffness (G <sub>d</sub> )*
Parallel to joists	Continuous or discontinuous joists	Good	350
		Fair	285
		Poor	225
Perpendicular to joists**	Continuous joist, or discontinuous joist with reliable mechanical anchorage	Good	265
		Fair	215
		Poor	170
	Discontinuous joist without reliable mechanical anchorage	Good	210
		Fair	170
		Poor	135

\* Values may be amplified by 20% when the diaphragm has been railed using modern nails and nail guns

\*\* Values should be interpolated when there is mixed continuity of joists or to account for continuous sheathing at joist splice

The components must be classified according to three condition classes: good, fair and poor. Each class is assigned a condition assessment factor to be used for determining diaphragm mechanical properties. Diaphragm mid-span displacement demand is determined according to equation (2.15) assuming an ideal scheme of a shear beam under parabolic load distribution (consistently with ASCE 41-17) also accounting for the shear factor for rectangular sections equal to 6/5. In equation (2.15)  $C(T_d)$  is the horizontal design action coefficient for the diaphragm as a function of diaphragm period  $T_d$  evaluated by means of equation (2.13).

$$\Delta_d = \frac{3 \cdot C(T_d) \cdot W_d \cdot L}{G'_{d,eff} \cdot B} \quad (2.15)$$

### 2.2.2.2 Diaphragm verification

Diaphragm in-plane displacement demand given by equation (2.15) must be checked against the diaphragm deformation capacity. Diaphragm capacity must be defined according to three different acceptance criteria [Giongo et al. (2014)]. The first criterion limits diaphragm deflection based the maximum allowable slip of most stressed nailed connections that are located at diaphragm ends. Such check is reflected by equation (2.16), where  $e_n$  is the maximum allowable slip of the nail connection,  $s$  is the nail couple spacing and  $\varphi$  is a coefficient that accounts for the relation between the midspan displacement and the rotation of the most stressed nail couple and depends on the assumed deformed shape.

$$\Delta_d \leq \varphi \cdot \frac{L \cdot e_n}{2 \cdot s} \quad (2.16)$$

The deflection limit values suggested by the Standard implements the average geometrical and mechanical properties of board-to-joist connections in New Zealand vintage diaphragms. By assuming a permissible nail slip of 6 mm, a nail spacing of 100 mm, equation (2.16) becomes equation (2.17).

$$\left\{ \begin{array}{l} \text{Parallel to joists} \rightarrow \Delta_d \leq \frac{L}{33} ; \\ \text{Perpendicular to joists} \rightarrow \Delta_d \leq \frac{L}{53} ; \end{array} \right. \quad (2.17)$$

The second criterion accounts for the stability of the out of plane loaded walls. The critical diaphragm in-plane displacement that can induce the out-of-plane collapse of the tributary walls can be defined according to experimental results reported in Griffith et al. (2007) and is equal to 50% of the wall thickness. Therefore, the second criterion can be written according to equation (2.18) in which  $t_w$  is the thickness of the out-of-plane wall connected to the diaphragm being checked.

$$\Delta_d \leq 0.5 \cdot t_w \quad (2.18)$$

The third criterion is taken from NZS 1170.5 [NZS (2004)] and reflects the 2.5% limit for inter-story drift. If the deformation of the in-plane loaded walls is referred to (consistently with the building idealization adopted to define seismic force demand) and rigid foundations are assumed, the third criterion is explicated by equation (2.19).

$$\Delta_d \leq 0.025H_1 + \Delta_{d,level\ below} \quad (2.19)$$

It is worth noting that the diaphragms located on levels adjacent to that of the diaphragm being assessed are assumed to remain undeformed, therefore no out-of-phase swaying issues are addressed by the Standard. The actual displacement capacity of the diaphragm should be taken as the minimum among the three values provided by the acceptance criteria.

In addition to displacement capacity, also diaphragm strength capacity shall be assessed. When experimental results are not available, the values reported in Table 2.6, referred to expected yield capacity of diaphragms, can be considered.

$$Strength\ value \geq \frac{C(T_d) \cdot W_d}{2 \cdot B} \quad (2.20)$$

As an alternative, Appendix 11B of [NZSEE (2006)] provides a procedure to estimate diaphragm in-plane strength values. Oliver (2010) evidenced that such procedure leads to significantly smaller strength values compared to the default values reported in Table 2.6.

*Table 2.6: Strength values for existing materials. Taken from NZSEE (2017)*

Materials	Strength values [KN/m]	$\Phi^*$
Roofs with straight sheathing and roofing applied directly to the sheathing	6	
Roofs with diagonal sheathing and roofing applied directly to the sheathing	15	
Floors with straight tongue and groove sheathing	6	0.7
Floors and roofs with sheathing and existing plaster railed to the joists or rafters	Add 2 KN/m to the values for timber framed walls	

\*  $\Phi$  is the strength reduction factor

### 2.2.3 FURTHER REMARKS ON DEFAULT STIFFNESS AND STRENGTH VALUES

As already mentioned, the  $G_s$  values provided by ASCE Standard (Table 2.3) derive from experimental evidence. In particular they refer to the equivalent secant shear-stiffness at yield which is based on estimated value (which for straight sheathed diaphragms corresponds to approximately 15 mm) obtained from quasi-static cyclic tests carried out on specimens which had been previously subjected to testing. Stiffness values given in Table 2.5 are also experimentally derived but relate to equivalent secant shear-stiffness corresponding to a midspan displacement of 100 mm, due to the critical condition of out-of-plane loaded URM walls and also maximum admissible inter-story drift. Despite the default shear strength value for straight sheathed diaphragms from NZSEE (yield strength = 6 KN/m, Table 2.6) is significantly higher than that suggested by ASCE (peak strength = 1.75 KN/m, Table 2.3), it appears to be consistent with the

experimental data available for vintage timber diaphragms in New Zealand (Giongo et al (2015) observed no damage up to a shear load of approximately 6 KN/m).

---

## 2.3 REFERENCES

- Agbabian, M. S., Barnes, S. B. and Kariotis, J. C. (ABK) (1981). "Methodology for mitigation of seismic hazards in existing unreinforced masonry buildings. Diaphragm testing." National Science Foundation. El Segundo, California.
- ASCE (American Society of Civil Engineers). (2017). "Seismic Evaluation and Retrofit of Existing Buildings" *ASCE 41-17*, Reston, Virginia.
- ASCE (American Society of Civil Engineers). (2006). "Seismic Rehabilitation of Existing Buildings" *ASCE 41-06*, Reston, Virginia.
- ATC (Applied Technology Council). (1981). "Guidelines for the design of horizontal wood diaphragms" Berkeley, California.
- Baldessari, C., Piazza, M. and Tomasi, R. (2009). "The refurbishment of timber floors: characterization of the in-plane behavior" Proceedings, PROHITEC International Conference, Taylor and Francis, Rome, Italy, 2009.
- Brignola, A (2009). "Evaluation of the in-plane stiffness of timber floors for the performance-based retrofit of URM buildings". Doctoral dissertation, The University of Genoa, Genova, Italy.
- Brignola, A., Pampanin, S. and Podestà, S. (2012). "Experimental Evaluation of the In-Plane Stiffness of Timber Diaphragms". *Earthquake Spectra*, vol. 28, n. 4, pp. 1687-1709.
- Costley, A. C., and Abrams, D. P. (1995). "Dynamic response of unreinforced masonry buildings with flexible diaphragms." UILU-ENG-95-2009, Illinois at Urbana- Champaign, Urbana.
- Derakhshan H., Griffith M. C., Ingham J. M. (2013), "Out-of-plane behavior of one-way spanning URM walls", *ASCE Journal of Engineering Mechanics*, pp. 409-417.
- Dizhur, D., Ingham, J. M., Moon, L., Griffith, M. Schultz, A., Senaldi, I., Magenes, G., Dickie, J., Lissel, S., Centeno, J., Ventura, C., Leite, J. C., Lourenco, P. B. (2011). «Performance of masonry buildings and churches in the 22 February 2011 Christchurch earthquake». *Bull. N. Z. Soc. Earthquake Eng.* 44 (4): 279–296.
- Dizhur, D., Ingham, J. M., Biggs, D. and Schultz, A. (2016). "Performance of unreinforced masonry and infilled RC buildings during the 2015 Gorkha, Nepal earthquake sequence". Proceedings, 16th International Brick and Block Masonry Conference, IBMAC 2016, pp 2399-2408.
- Ewing, R. D., Healey, T. J., and Agbabian, M. S. (1980). "Seismic analysis of wood diaphragms in masonry buildings." Workshop on Design of Horizontal Wood Diaphragms: A TC-7-1, Applied Technology Council, Redwood City, California, 253-276.
- FEMA (Federal Emergency Management Agency). (2000). "Prestandard and Commentary for the Seismic Rehabilitation of Buildings" *FEMA 356*, Reston, Virginia.

FEMA (Federal Emergency Management Agency). (1997). “*NEHRP Guidelines for the Seismic Rehabilitation of Buildings*” FEMA 273, Reston, Virginia.

Giongo, I., Piazza, M., and Tomasi, R. (2011). "Pushover analysis of traditional masonry buildings: influence of refurbished timber-floor stiffness." International conference on structural health assessment of timber structures, Lisbon, Portugal, 16-17 June.

Giongo, I., Dizhur, D., Tomasi, R. and Ingham, J. M. (2013). “In-plane assessment of existing timber diaphragms in URM buildings via quasi-static and dynamic in-situ tests”. Advanced Materials research, SHATIS 2013, vol. 778, pp. 495-502.

Giongo, I., Wilson, A., Dizhur, D., Derakhshan H., Tomasi R., Griffith M. C., Quenneville P., Ingham J. (2014), “Detailed seismic assessment and improvement procedure for vintage flexible timber diaphragms”, NZSEE Bulletin, vol.47, pp. 97-118.

Giongo, I., Dizhur, D., Tomasi, R. and Ingham, J. M. (2015). “Field testing of flexible timber diaphragms in an existing vintage URM building”. Journal of Structural Engineering, vol. 141, 2015.

Griffith M. C., Vaculik J., Lam N. T. K., Wilson J., Lumantarna E. (2007) “Cyclic testing of unreinforced masonry walls in two-way bending”, Earthquake Eng. Struc., pp. 801-821.  
NZS (Standards New Zealand), (2004) “Structural design actions, Part 5: Earthquake actions” – NZS 1170.5, Wellington, New Zealand

Kallioras, S., Guerrini, G., Tomassetti, U., Marchesi, B., Penna, A., Graziotti, F. and Magenes, G. (2018). “Experimental seismic performance of a full-scale unreinforced clay-masonry building with flexible timber diaphragms”, Engineering Structures, 161 (2018), pp. 231-249

NZSEE (New Zealand Society for Earthquake Engineering) (2006). “Assessment and improvement of the structural performance of buildings in earthquakes”. *NZSEE 2017*. Wellington, New Zealand.

NZSEE (New Zealand Society for Earthquake Engineering) (2017). “Assessment and improvement of the structural performance of buildings in earthquakes”. *NZSEE 2017*. Wellington, New Zealand.

Oliver S. J. (2010) “A design methodology for the assessment and retrofit of flexible diaphragms in unreinforced masonry buildings”, SESOC Journal, pp. 19-49.

Penna, A., Morandi, P., Rota, M., Manzini, C. F., da Porto, F. and Magenes, G. (2013). “Performance of masonry buildings during the Emilia 2012 earthquake”. Bulletin of Earthquake Engineering, vol. 12, pp. 2255–2273.

Peralta, D. F. , Bracci, J. M. and Hueste, M. B. (2003). “Seismic Performance of Rehabilitated Wood Diaphragms”. Texas AandM University, Department of Civil Engineering, 2003.

---

Raggett, J. D., Rojahn, C. (1991). "Dynamic Amplification of Ground Motions by Low-Rise, Stiff Shear Wall Buildings", SMIP91 Seminar on Seismological and Engineering Implications of Recent Strong-Motion Data, pp. 16-1 - 16-11.

Tena-Colunga, A. and Abrams, D. P., (1996). "Seismic Behaviour of Structures with Flexible Diaphragms", *Journal of Structural Engineering*, vol. 122, no. 4, pp. 439-445.

Tomassetti, U., Correia, A. A., Graziotti, F., Penna, A. (2019). "Seismic vulnerability of roof systems combining URM gable walls and timber diaphragms". *Earthquake Engineering and Structural Dynamics* Vol. 48 Issue 11 pp. 1297-1318

Tomazevic, M., Lutman, M., and Weiss, P. (1993). "The seismic resistance of historical urban buildings and the interventions in their floor systems: an experimental study." *The Masonry Society Journal*, 12(1), 77-86.

Wilson, A. W. (2012). "Seismic assessment of timber floor diaphragms in unreinforced masonry buildings". Doctoral dissertation, The University of Auckland, Auckland, New Zealand.

Wilson, A., Quenneville, P. J. H., Ingham, J. M. (2014). "In-plane orthotropic behavior of timber floor diaphragms in unreinforced masonry buildings", *Journal of Structural Engineering* 2014;140(1):04013038.

Yi, T., Moon, F. L., Leon, R. T., and Kahn, L. F. (2006). "Lateral load tests on a two-story unreinforced masonry building." *Journal of Structural Engineering*, 132(5), 643- 652.

# **3 AS-BUILT STRAIGHT SHEATHED TIMBER DIAPHRAGMS**

## **3.1 INTRODUCTION**

The aim of the work presented Chapter 3 was to use numerical modeling in order to investigate the aspects that potentially contribute to the difference in experimental behavior reported in the literature [Peralta et al. (2003), Wilson (2012), Brignola et al. (2012), Giongo et al. (2015)] and determine the extent to which their influence should be considered when developing general codified provisions for assessment of existing timber diaphragms. Focus is given to the diaphragm aspect ratio and the scale factor (i.e. diaphragm size), and to the response orthotropy associated with the loading directions parallel and perpendicular to the joists. In addition, the effects of board-to-board contact and friction effects are investigated.

## **3.2 FINITE ELEMENT MODEL DEFINITION**

A series of numerical analyses of timber floor diaphragms were conducted using two finite element software packages: TNO DIANA [Manie and Kikstra (2014)] and SAP2000 [CSI (2014)]. TNO DIANA (hereafter referred to as Modeling approach 1 (M1)) was used to analyze the effects of floorboard friction. TNO DIANA enables a refined modeling of friction effects by using interface elements. The results obtained from refined M1 models were used to calibrate a simplified modeling approach using SAP2000 (hereafter referred to as Modeling approach 2, M2). SAP2000 is a well-known and widely used tool in the engineering industry and hence users could potentially benefit from the application of simplified modeling strategies for timber diaphragms. In addition, because M2 is based on 1-dimensional elements, it is compatible with the

---

adoption of the 1-dimensional hysteresis rules commonly used for simulating energy dissipation in nonlinear dynamic analyses.

### 3.2.1 MODELING APPROACH 1 (M1)

In the first modeling approach the TNO DIANA software package was used to model the timber joists of diaphragms as linear-elastic frame elements, while floorboards were reproduced by linear-elastic curved shell elements. A realistic floorboard layout (made of staggered and continuous boards) was simulated by generating separate mesh subsets for each of the boards. Inter-floorboard contact and friction interaction effects were modeled using line interface elements located at the floorboard free edges. In order to represent the contact between the floorboards, a ‘no tension’ attribute was assigned to the otherwise rigid compression interface. A ‘*Coulomb Friction*’ shear model [Manie and Kikstra (2014)] was adopted to simulate friction at the floorboard edges. Interface shear resistance ( $t_s$ ) versus normal compression force ( $t_n$ ) on the floorboard edges was defined by means of cohesive resistance ( $c$ ), dilatancy ( $\psi$ ), friction angle ( $\phi$ ) and normal tensile strength ( $f_t$ ). A tension cut-off ( $f_t = 0$ ) and a dilatancy angle equal to zero were selected, as negligible tensile strength and dilatancy are expected to occur at the floorboard interface (see Figure 3.1 for comparative examples). Orthotropic material properties were adopted for all timber elements as suggested by NZS 3603:1993 [NZS (1993), EN338:2009 [CEN (2009)]] and where available, experimentally attained properties were adopted from literature.

The possible bending failure of the floorboards (observed in experimental testing, [Wilson (2012), Brignola et al. (2012)]) was modeled using linear interface elements that extended perpendicular to the longitudinal axis of the floorboards and were inserted where the highest bending stresses were expected. Such rigidly responding interface elements exhibit a linear softening behavior once the tension stress parallel to the grain (perpendicular to the interface elements) exceeds the timber tensile strength.

Nailed connections were modeled by using point interface elements and were positioned at the locations of the nails as in the experimental specimens. The force-displacement response of the nail connections was defined by considering the principal directions parallel and orthogonal to the floorboards to be uncoupled. The influence of such uncoupled response is further investigated herein. The force-displacement reference curve matched the experimental results described in Schiro et al. (2018).

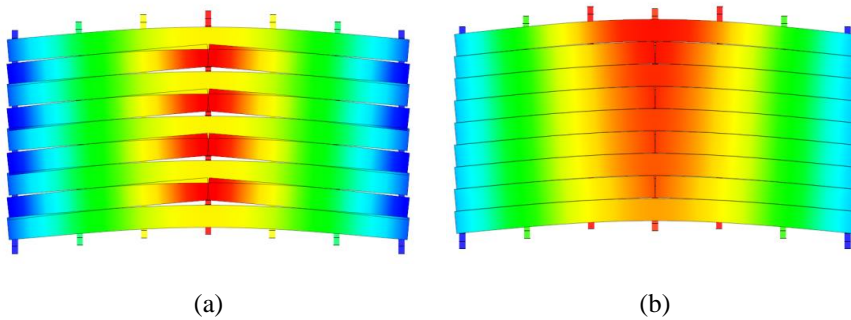


Figure 3.1 – Visual plan view representation of diaphragm deformed shape for the M1 approach: a) without contact interface; b) with contact interface

### 3.2.2 MODELING APPROACH 2 (M2)

SAP2000 finite element software was used to implement an alternative and simplified approach for modeling the timber diaphragms. The following consolidated assumptions that are commonly referred to in literature [Wilson (2012), Brignola et al. (2012), Peralta et al. (2003)] were initially adopted. Firstly, the timber floorboards and joist elements were modeled as linear-elastic frame elements. As a result, the nonlinear behavior of the diaphragms was concentrated at the location of nailed connections, which were modeled as link elements connected to the timber frame elements through rigid links. Secondly, contact between the timber elements was not modeled and consequently overlapping of floorboards during diaphragm deformation was allowed to occur (material penetration). Longitudinal floorboard discontinuities along the diaphragm length were modeled as a discontinuity in the frame element. Because each degree of freedom (DoF) of the multi-linear element behaves independently, a nonlinear force-displacement curve derived from experimental data was assigned to the translational  $U2$  and  $U3$  DoFs (see Figure 3.2-b). The  $U1$ ,  $R2$  and  $R3$  DoFs were fully restrained (such as no flexural or axial nail deformation allowed) while the  $R1$  (torsional) DoF was unrestrained (Figure 3.2-b). Pinned supports were inserted along the outermost joists where global beam-like rotation was restrained, while only vertical constraint parallel to gravity direction was provided to all other joists. For comparison purposes, additional analyses were also performed without restraining in-plane rotation of the outermost joist, without significant differences in results being observed. Axially rigid rods were introduced to simulate timber blocking elements and to ensure a more realistic inertial load transfer over the diaphragm depth in case of loading perpendicular to the joists. Vertical out-of-plane support was provided to the outermost joist, whose ends were axially restrained to reproduce the effect of inter-floorboard contact.

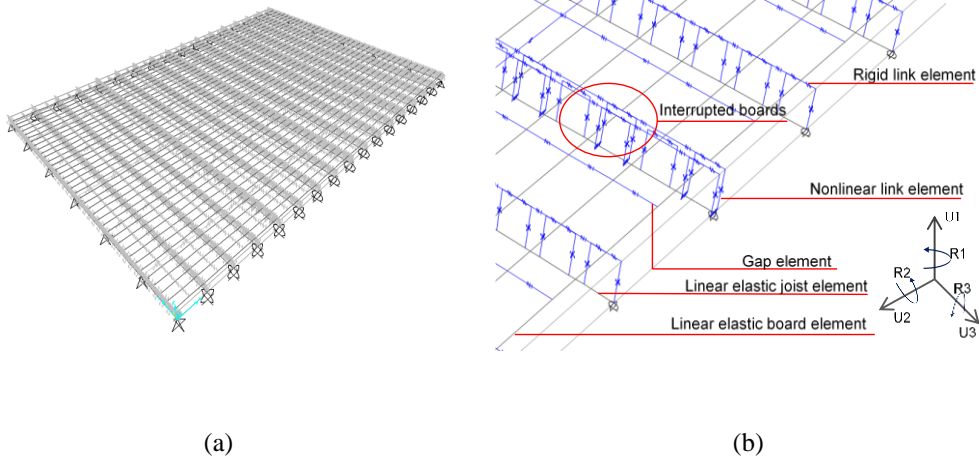


Figure 3.2 - Numerical model details for M2 modeling approach: a) global view of the M2 model; b) model close-up

### 3.3 VALIDATION OF THE MODELING APPROACHES

Previous experimental testing [Wilson (2012), Brignola et al. (2012), Peralta et al. (2003), Giongo et al. (2015) and Baldessari et al. (2009)] of newly constructed and vintage timber diaphragms of different sizes, which were loaded parallel and perpendicular to the joist orientation, were considered for validation of the M1 and M2 modeling approaches. A summary of the considered experimental tests is provided in Table 3.1 where  $L$  is the diaphragm dimension parallel to the joist orientation and  $B$  is the diaphragm dimension perpendicular to the joist orientation. Diaphragm IDs in Table 3.1 are reported as per the original naming conventions used by Authors. When available, direct experimental data for material properties and connection behavior were adopted.

#### 3.3.1 M1 VALIDATION PROCESS

Analyses were undertaken on differently sized diaphragm specimens (provided in Table 3.1) to investigate the influence of interface contact and interface friction considering loading directions parallel and perpendicular to the joists.

##### 3.3.1.1 Influence of interface contact

Using the M1 approach it was shown that the loading direction and the diaphragm size influenced interface contact forces and hence the global behavior of the modeled diaphragms. In Figure 3.3 the backbone force-displacement curves for cases with and without the interface contact are compared. In the case of loading parallel to joists, the

response of small and medium sized diaphragms (Figure 3.3-b, c) appeared to be affected by inter-floorboard contact at all displacement levels, while the effect was found to be less significant on wider diaphragms (Figure 3.3-a).

Table 3.1 - Experimental tests considered in the validation process

Reference	Diaphragm ID	L [m]	B [m]	Load direction	Condition
Wilson et al. (2014)	1a-PARA	5.55	10.40	Parallel	New
Wilson et al. (2014)	1a-PERP	5.55	10.40	Perpendicular	
Wilson (2012)	SC*	1.25	2.45	Parallel	
Brignola et al. (2012)	AB - 1	4.00	4.00	Parallel	
Baldessari et al. (2009)	5 x 4	4.00	5.00	Parallel	
Peralta et al. (2002)	MAE-2	3.65	7.30	Parallel	
Giongo et al. (2015)	Specimen A	9.60	5.60	Perpendicular	Vintage
Giongo et al. (2015)	Specimen B	9.60	4.70	Perpendicular	
Wilson et al. (2014)	Parnell-Large	2.15	3.15	Parallel	
-	D2-PARA**	6.00	6.00	Parallel	Parametric analysis
-	D2-PERP**	6.00	6.00	Perpendicular	

\* - SC diaphragm testing comprised two identical specimens

\*\* - Virtual diaphragm used for the parametric analysis, presented in subsequent sections (diaphragm D2), was included to provide supplementary data for comparison.

In the case of loading perpendicular to joists, the influence of inter-floorboard contact was noticeable only at large displacements (greater than 1.25% drift) when geometrical nonlinearity was included in the analysis (Figure 3.3-d, e, f).

Table 3.2 and Table 3.3 provide a comparison of results for cases with and without interface contact in terms of force variation at different diaphragm drift levels. Drift ( $dr$ ) values were calculated according to equation (3.1) where mid-span displacement  $\delta$  is related to the diaphragm dimension perpendicular to the loading direction ( $L_{perp}$ ). The above-mentioned force variation was evaluated via equation (3.2) where  $F_{contact}$  and  $F_{w/o\ contact}$  are the force values provided by the numerical model when interface contact is considered or neglected, respectively. It is evident that under certain circumstances the omission of interface contact from the numerical models led to a noticeable underestimation of the diaphragm stiffness.

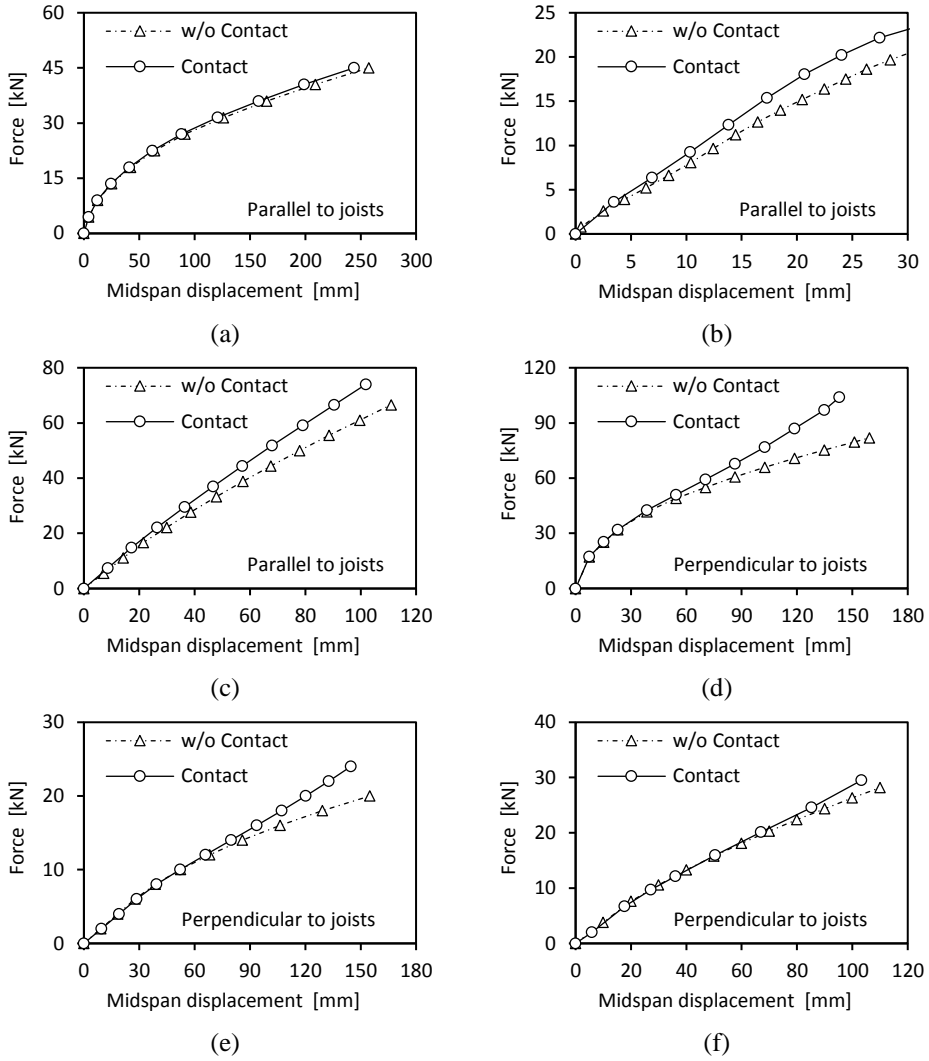


Figure 3.3 - Backbone comparisons showing the influence of interface contact: a) 1a-PARA; b) SC; c) D2-PARA; d) 1a-PERP; e) Specimen B; f) D2-PERP

$$dr [\%] = 2 \frac{\delta}{L_{perp}} \quad (3.1)$$

$$Variation [\%] = 100 \frac{F_{contact} - F_{w/o\ contact}}{F_{contact}} \quad (3.2)$$

Table 3.2 - Influence of inter-floorboard contact - parallel to joist loading direction

Diaphragm ID	L [m]	B [m]	Variation [%]	
			drift=0.25%	drift=3%
SC	1.25	2.45	20.2	20.5
D2	6.00	6.00	9.5	15.3
1a-PARA	5.50	10.40	1.0	2.3

Table 3.3 - Influence of inter-floorboard contact - perpendicular to joist loading direction

Diaphragm ID	L [m]	B [m]	Variation [%]	
			drift=0.25%	drift=3%
D2	6.00	6.00	0.4	5.8
Specimen B	9.60	4.70	3.7	20.0
1a-PERP	5.50	10.40	0.3	9.8

The influence of inter-floorboard contact at large displacements appears evident; for example, a 20% force increase was required to displace the Specimen B diaphragm to 3.0% drift level (perpendicular to the joist loading direction) compared to only a 3.7% force increase required to displace the same diaphragm to 0.25% drift. Figure 3.4 depicts the flexural in-plane deformation of a joist at large displacement.

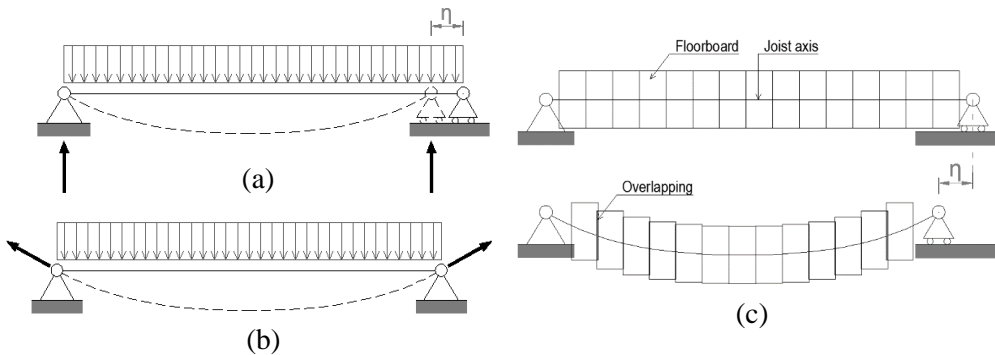


Figure 3.4 - In-plane joist and floor-board behavior at large displacements when loaded perpendicular to the joists: a) isostatic boundary conditions; b) pinned end restraint; c) internal constraints related to the presence of the floorboards at large displacements

For the case of isostatic boundary conditions (Figure 3.4-a), the beam supports are drawn closer to each other by a displacement ( $\eta$ ) with increasing applied load. Pinned restraints (Figure 3.4-b) induce a rope effect that stiffens the flexural in-plane response and is generally not representative of the real condition, as wall-to-diaphragm connections are typically simply supported on side URM walls or pocketed into the

URM walls without mechanical connection. For cases where  $\eta$  is not restrained at the boundaries, the presence of floorboards that are nailed to the joist generates an internal constraint on the relative movement of the joist free ends and bending of the joist (Figure 3.4-c).

### 3.3.1.2 Influence of interface friction

As shown in Figure 3.5, the M1 approach permits the experimental behavior of newly constructed diaphragm specimens to be reproduced without requiring the *Coulomb Friction* shear model to be included. The two branches (corresponding to negative and positive loading/deformation directions) of the force vs mid-span displacement backbone experimental curve are reported in Figure 3.5 within the same quadrant (positive load and positive deformation) to allow comparison against predicted response.

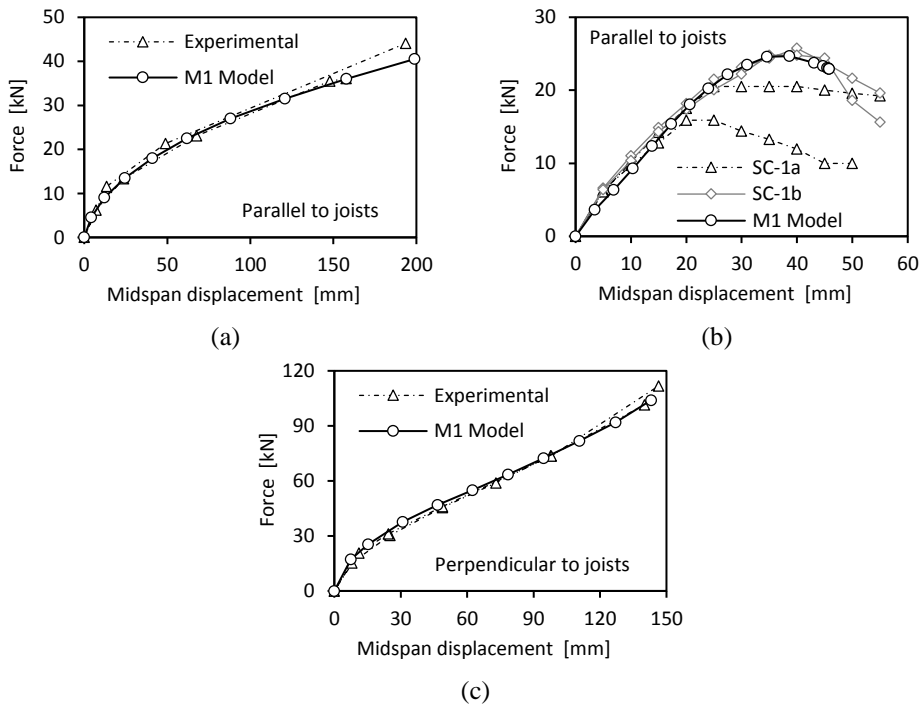


Figure 3.5 - M1 – FE model (interface contact without Coulomb Friction) vs experimental results for newly constructed diaphragm specimens: a) 1a-PARA; b) SC; c) 1a-PERP

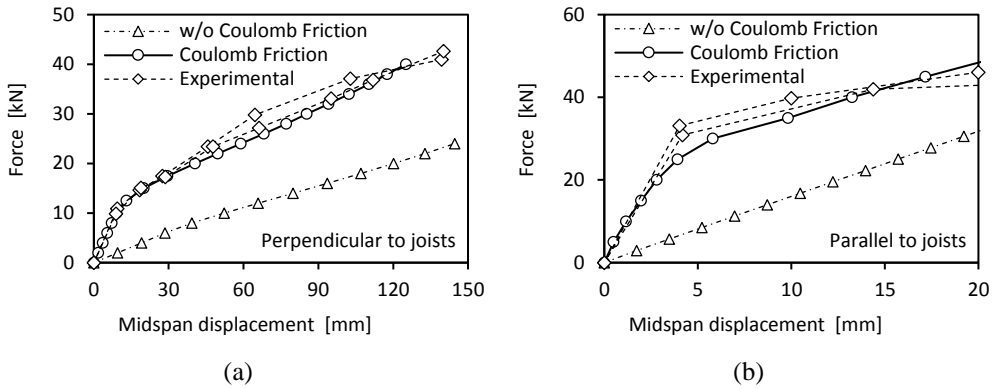


Figure 3.6 - M1 – FE model with and w/o friction: result comparison: a) Specimen B; b) Parnell large, premature test setup failure reported by Wilson et al (2011) at 20 mm midspan displacement

When the M1 approach was used to simulate the response of vintage diaphragms, a significant stiffness underestimation was observed (see Figure 3.6). Comparison between experimental and numerical stiffness values is summarized in Table 3.4 (note that *Specimen B* and *Parnell large* featured tongue and groove floorboards). This stiffness underestimation was attributed to the presence of shear forces between the floorboard interface surfaces. Similarly, Peralta et al (2003) observed remarkable stiffness underestimation when modeling a T&G diaphragm specimen (MAE-1) loaded orthogonal to the joist direction, where mechanical contact and friction were not included in the used ABAQUS model.

Table 3.4 - Direct stiffness\* comparison, M1 – FE model (interface contact without Coulomb Friction) vs. experimental results

Diaphragm ID	Experimental [kN/m]	FEM [kN/m]	$K_{exp}/K_{FEM}$
Specimen B	956	210	4.6
Parnell large	8245	1645	5.0

\* Secant stiffness at drift = 0.25%

Figure 3.6 shows that the introduction of the *Coulomb Friction* model into M1 resulted in numerically predicted behavior that accurately matched the experimental response of vintage diaphragms. For *Specimen B* a friction coefficient of 0.05 and a cohesion of 0.04 MPa were selected, and for the *Parnell large* specimen a friction coefficient of 0.05 and a cohesion of 0.25 MPa were selected. The nail connection behavior was set in accordance with experimental results reported in Schiro et al. (2018) on floorboard-

---

to-joist connections that were extracted from the same floor sections as the specimens. The cohesion parameter for the *Parnell large* specimen included the effect of possible ‘shear locking’ caused by the geometrical shape of the T&G cuts combined with possible effects due to dirt and dust filling the gaps. Wilson (2012) has reported the presence of *varnish/resin filling the T&G interfaces and allegedly increasing the shear bond strength*). Brignola et al. (2012) affirm that neglecting board interlocking and friction at the board edges is excessively conservative. In the case of diaphragms with floorboards that have not ‘shrunk apart’, NZSEE (2017) permits the diaphragm shear capacity to be increased to account for friction between board edges, with the strength contribution from T&G edges being three times higher when compared to straight edged floorboards. Conversely, tests on newly constructed small sized specimens from Wilson (2012) suggest that the effects of inter-floorboard friction is generally negligible (except for large displacement amplitudes) and that the diaphragm response is not influenced by the floorboard type (straight edge or T&G) (see Figure 3.5). A limited number of experimental tests on vintage floors are available, making it difficult to determine the contributions of shear forces at the floorboard interface (swelling and shrinkage related to moisture content variation might have a detrimental effect) and which phenomenon contributes the most to the interface bond.

### 3.3.2 M2 VALIDATION PROCESS

Several experimental results from different campaigns considering new and vintage diaphragms loaded in both principal directions [Wilson et al. (2012), Brignola et al. (2012), Peralta et al. (2003), Giongo et al. (2015), Baldessari et al. (2009)] were used in the subsequent sections as part of a validation process for the M2 modeling approach. As was established in the M1 approach, the influence of interface contact was substantial and hence it was reproduced in the M2 approach.

#### 3.3.2.1 Newly constructed diaphragms with board-to-board contact

For newly constructed diaphragms loaded parallel to the joists, contact forces were accounted for by positioning *nonlinear gap links* (no-tension compression only behavior) between the floorboard elements. Comparisons with experimental results are summarized in Figure 3.7, where it is shown that the M2 models accurately predicted the response of the experimentally tested specimens. By assigning nonlinear hinge properties to floorboard elements that were activated when the bending capacity of the floorboard was reached, diaphragm resistance and ultimate displacement were accurately predicted even for cases where floorboard rupture was observed [Wilson (2012), Brignola et al. (2012)] (see Figure 3.7-d, e).

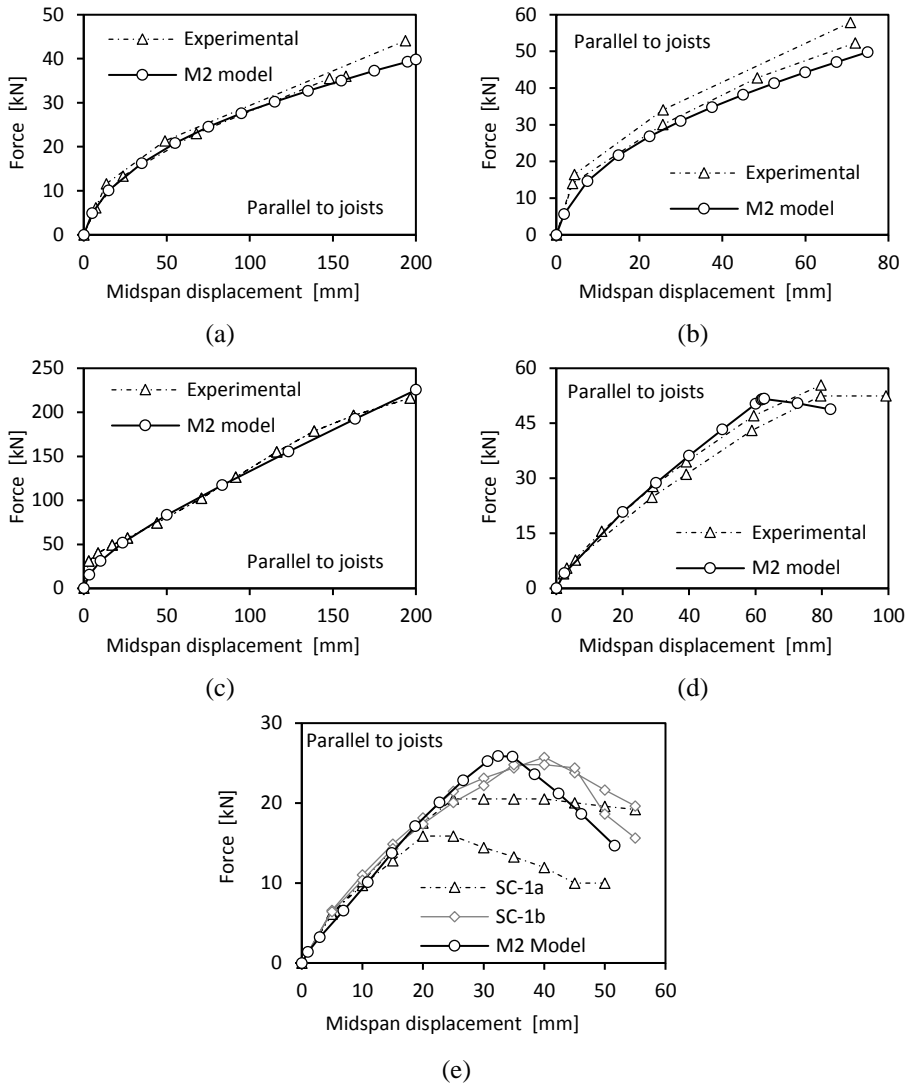


Figure 3.7 - M2 model validation, newly-constructed diaphragms loaded parallel to joist: a) 1a-PARA; b) MAE-2; c) 5x4; d) AB-1; e) SC

For diaphragms that were loaded perpendicular to joists, geometrical nonlinearity was required to capture the effect of interface contact (as was evident in the M1 approach). At large displacements the gap links that reproduce board-to-board contact rotate rigidly as the end nodes of the board move due to joist deformation ( $\Delta x$ , see Figure 3.8). As a result, the relative distance between adjacent floorboard elements decreases ( $\Delta y$ ) without engaging the axial stiffness of the gap links. Hence, the use of gap links cannot adequately simulate board-to-board interface contact and therefore it was not possible

to adopt the same M2 modeling approach that was used for diaphragms loaded parallel to joist.

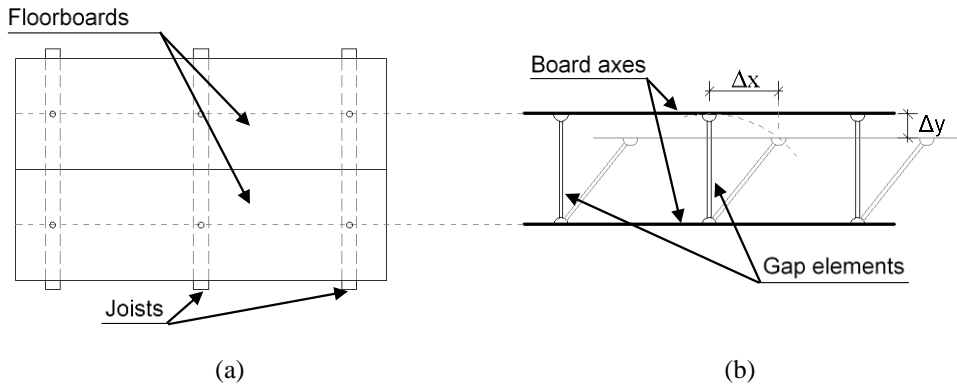


Figure 3.8 – Schematic showing gap link behavior for large-displacement analyses of diaphragms loaded perpendicular to joists: a) Plan view; b) Model schematic

In order to account for the board-to-board interface contact, a simplified method was derived based on the following assumptions: inextensible joists, rigid nail-connections, and pre-defined deformed shape of joists. The interaction between the joists and the floorboards was modeled by introducing an elastic spring at each joist end as schematized in Figure 3.9.

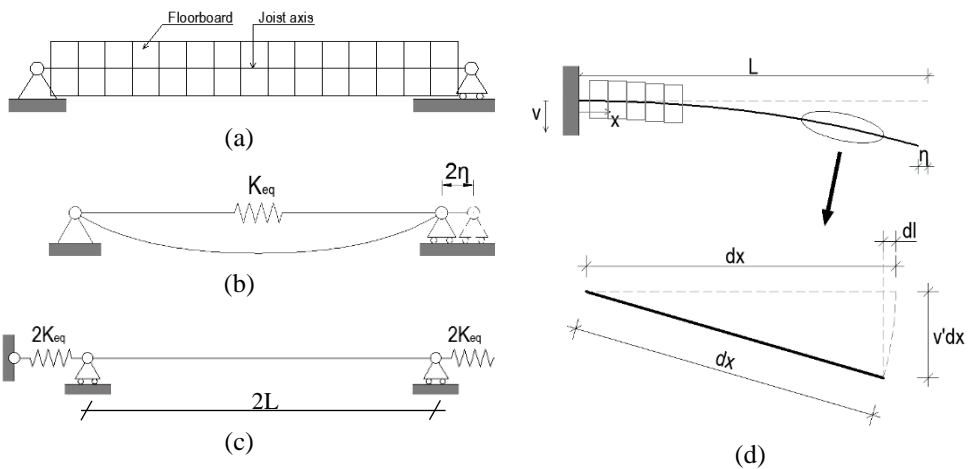


Figure 3.9 - Simplified modeling of board-to-board interface contact: a) floorboards over joist; b) equivalent compressive stiffness of flooring; c) elastic restraints used in the models; d) half-joist deformed shape at large-displacement

Equivalent compressive stiffness of flooring ( $K_{eq}$ ) was evaluated by assuming that the response of half of the joist span is equivalent to a cantilever (see Figure 3.9-d). Once the deformed shape of the joist  $v(x)$  was established (shear beams type response was assumed), the compression force  $F_b(x)$  acting on the floorboards with tributary length equal to the joist spacing was evaluated according to equation (3.3).  $F_b(x)$  was then checked against the total capacity of nail joints ( $R_n$ ) located between the joist free-end and a location ( $x$ ) where  $F_b(x)$  was calculated ( $R_n = \sum R_i$ ,  $R_i$  = nail capacity).

$$F_b(x) = \varepsilon(x)E_{90}A_b \cong \{1 - \cos [\arctan(v'(x))]\}E_{90}A_b \quad (3.3)$$

here:

- $E_{90}$  is the elastic modulus of floorboards in the direction perpendicular to the grain
- $A_b$  is the area equivalent to the board thickness multiplied by the joist spacing
- $v'(x)$  is the first derivative of  $v(x)$ .

Once  $F_b(x)$  was determined, the equivalent compressive stiffness  $K_{eq}$  was obtained from application of the energy conservation principle by equating the spring deformation energy to the elastic energy absorbed by the compressed floorboards (equation (3.4)).

$$K_{eq}\eta^2 = \frac{1}{2}E_{90}A_b \int_0^L \varepsilon(x)^2 dx \quad (3.4)$$

The aforementioned method for incorporating the interface contact was validated with reference to the *1a-PERP* specimen), see Figure 3.10-a. Due to the paucity of experimental results available in literature on diaphragms loaded perpendicular to joist, further reference was made to the M1 models developed for diaphragm *D2* and for *Specimen B* (a free-slip condition was set for the floorboard interfaces by disabling the *Coulomb Friction* shear model). All of the validated scenarios highlighted good correlation between available experimental data, the M1 approach, and the M2 approach. Based on the attained results, ‘hardening’ observed by Wilson (2012) for the *1a-PERP* test appears to be related to the combined effect of contact forces and geometrical nonlinearities and not only to the interaction between joist ends and masonry pockets as suggested by Wilson (2012).

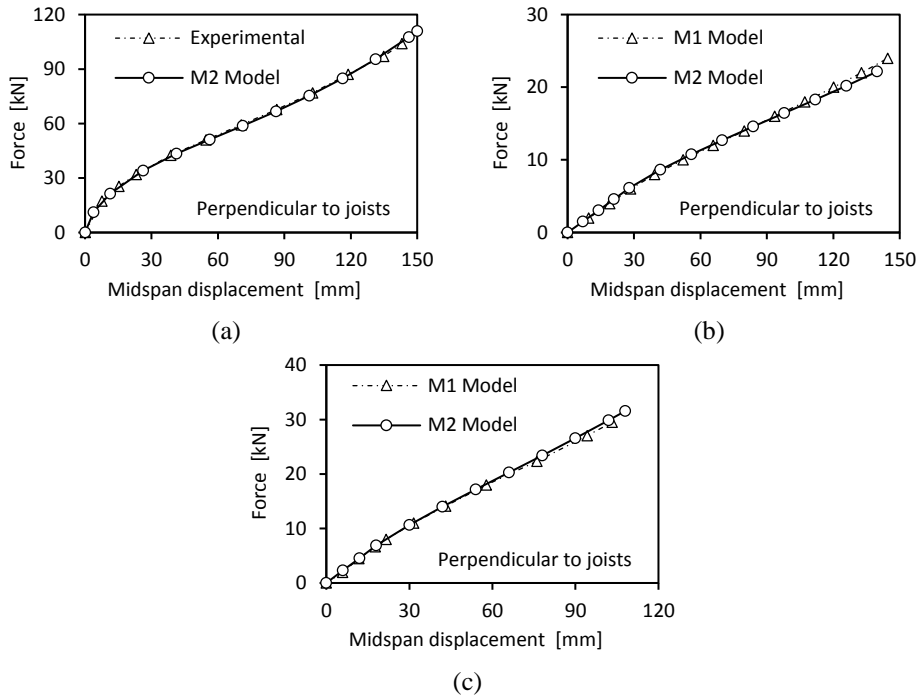


Figure 3.10 - M2 model validation of new diaphragms loaded in the direction perpendicular to joists: a) 1a-PERP; b) Specimen B w/o friction effects; c) D2-PERP

### 3.3.2.2 Vintage diaphragms with board-to-board contact

As outlined in the previous sections, the response of vintage diaphragms can be significantly influenced by the presence of inter-floorboard friction. The M2 model validation procedure for vintage diaphragms was instituted by reproducing experimental tests performed on vintage diaphragm specimens. For analyses where loading was applied parallel to joists, friction was modeled by positioning *nonlinear friction isolator links* between adjacent floorboard elements. The inter-floorboard cohesion was simulated by introducing additional *plastic links* that acted in parallel with the *friction isolator links*.

For analyses in the direction loaded perpendicular to the joists, the effect of board-to-board interaction was simulated by connecting adjacent floorboards with special equivalent links placed at regular spacing (corresponding to the joist spacing) over the floorboard length. The behavior of such links is shown in Figure 3.11-c and was defined by assuming that the joists were inextensible and that nail connections were rigid. Under these hypotheses, the rigid rotation  $\theta$  of the joists generates a compression force  $F_l$  (force resultant over the link tributary area,  $A_b$ ) that pushes the floorboards against each other (Figure 3.11-a, b), see equation (3.6). In cases where friction was present at the

board-to-board interface, the corresponding friction force  $F_2$  was obtained by multiplying  $F_1$  by the friction coefficient  $\mu$  (equation (3.7)). The link behavior can then be described by equation (3.8), where  $C$  corresponds to the cohesion value multiplied by the link tributary area,  $A_b$ .

$$\epsilon_1(u_2) = \frac{u_1}{a} \cong 1 - \cos \left[ \arcsin \left( \frac{u_2}{a} \right) \right] \quad (3.5)$$

$$F_1(u_2) = f_1(u_2)A_b = E_{90}A_b\epsilon_1(u_2) \quad (3.6)$$

$$F_2(u_2) = \mu F_1(u_2) \quad (3.7)$$

$$F_{link}(u_2) = \mu F_1(u_2) + C \quad (3.8)$$

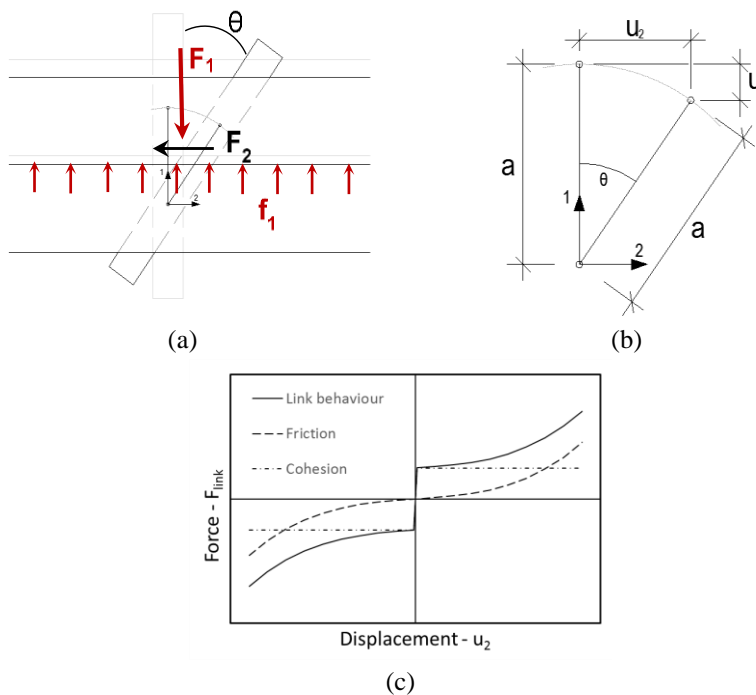


Figure 3.11 - M2 approach for modeling of board-to-board interaction for vintage diaphragms loaded perpendicular to joist: a) compression force induced by board-to-board contact due to joist rotation (plan view); b) vector diagram; c) link constitutive behavior

The salvaged *Parnell-Large* floor from Wilson (2012) was tested in the direction parallel to joist while the diaphragm specimen tests reported in Giongo et al. (2015) were loaded perpendicular to the joist direction. The friction parameters used for the equivalent link were assumed to be nominally identical for all diaphragm specimens tested in Giongo et al. (2015) as the specimens were portions of the same vintage floor diaphragm. A higher cohesion coefficient was adopted for *Parnell-Large* to recreate the

effect of varnish adhesion reported in Wilson (2012). As for M1, nail connection behavior was set in accordance with experimental results obtained by the authors [Schiro et al. (2018), Wilson (2012)]. Comparison between the M2 model and the experimental results is provided in Figure 3.12.

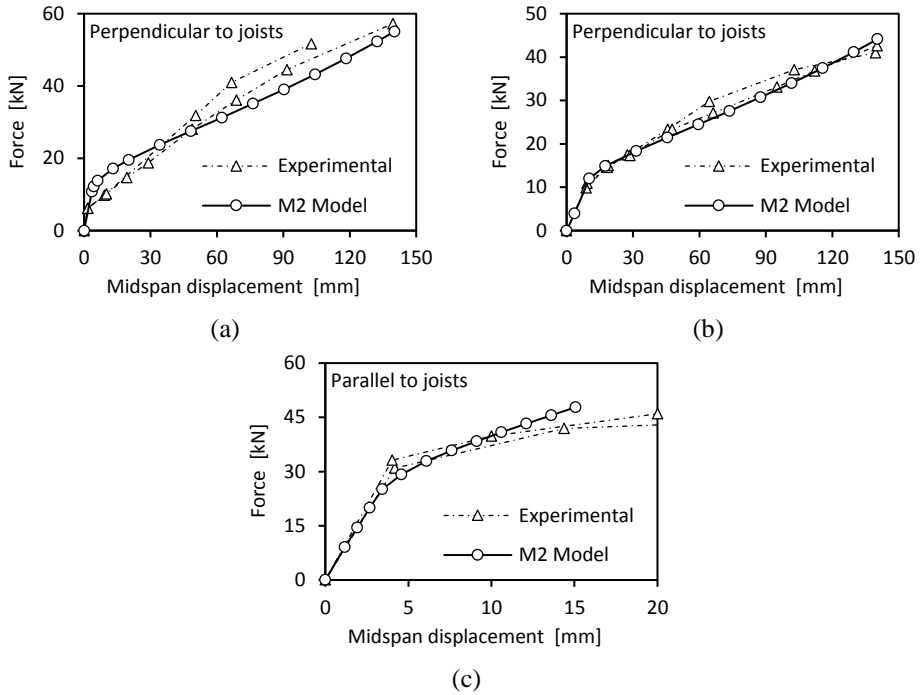


Figure 3.12 - Model validation via comparisons for vintage components: a) Specimen A; b) Specimen B; c) Parnell-Large

### 3.3.2.3 Influence of uncoupled nail response

The individual nails in floorboard-to-joist connections of newly constructed and vintage diaphragms were modeled by using a *link element* with behavior that reproduced two nonlinear springs oriented along the reference axes ( $x$  and  $y$ , with  $z$  axis corresponding to the diaphragm out-of-plane direction). The nonlinear spring behavior was considered as uncoupled with springs acting independently. The load and stiffness response of small-diameter dowels (such as nails or screws) in timber connections is commonly considered to be independent of the loading direction [Smith and Whale (1987)]. For example, a straight deformation-trajectory of a fastener results in displacement  $d$  and restoring force  $F_R$  (force acting parallel to the displacement but oriented in the opposite direction) being independent from the  $\alpha$  angle (such as ‘*isotropic*’ fastener-response, see Figure 3.13-a). Under such an assumption,  $F(d)$ , the curve representative of the connection behavior (e.g. backbone curve from experimental testing) and the restoring

force  $F_R(u_x, u_y)$  is evaluated using equation (3.9). Conversely, if the fastener behavior along the principal directions is constituted by independent uncoupled nonlinear  $F(d)$  response, then the restoring force (that is not aligned with the displacement vector) can be determined using equation (3.10). Such uncoupled nonlinear response results in overestimation of the connection stiffness and maximum capacity, with the overestimation being null when  $\alpha = 0^\circ$  or  $\alpha = 90^\circ$  while maximum when  $\alpha = 45^\circ$  (overestimation factor of 1.4). In Figure 3.13-b, the restoring force overestimation associated with the uncoupled approach is shown for  $\alpha$  ranging between  $0^\circ$  and  $90^\circ$ .

$$F_R(u_x, u_y) = F(d) = F\left(\sqrt{u_x^2 + u_y^2}\right), \begin{cases} u_x = d \cos(\alpha) \\ u_y = d \sin(\alpha) \end{cases} \quad (3.9)$$

$$F_R(u_x, u_y) = \sqrt{F(u_x)^2 + F(u_y)^2} \quad (3.10)$$

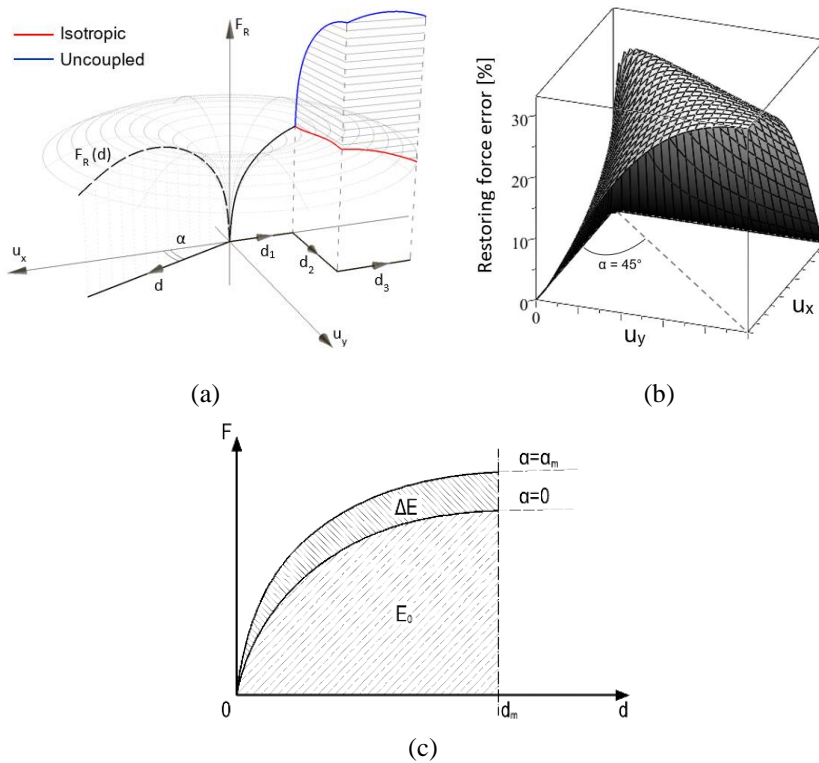


Figure 3.13 - Modeling of nail fasteners: strategies and issues: a) 'Isotropic' fastener-response; b) Overestimation of the restoring force; c) Mean energy increase due to uncoupled nail-response (per single fastener connection)

For diaphragm models that consist of thousands of structural elements having nonlinear behavior, the deformation-trajectory of sub-components (such as the nails) even under monotonic loading of the diaphragms might not correspond to a single straight line. For example, if the nail deformation path was characterized by direction changes such as shown in Figure 3.13-a, then the isotropic model might be unsuitable for representing the experimental response. If local failure of the wood fibers was observed at the end of step  $d_1$ , then the fastener will be pushing against unstressed/undamaged material once the loading direction changes ( $d_2$ ). Recognizing such considerations, the uncoupled approach would appear preferable in order to simulate the connection behavior when multi-directional deformation is expected. Aspects such as fastener yielding and fatigue might limit the possibility of considering the response in one direction as unaffected by previous deformation in a different direction.

In cases where displacement sub-steps are not parallel to principal directions, nail-link response would be affected by stiffness/strength overestimation as described in the case of single-step straight line deformation. Deformation analysis of numerical models adopted in the validation phase showed that for nails that deformed mostly along *quasi-straight* lines, this behavior reduces the impact of possible uncertainties associated with the behavior of connections subjected to multi-direction deformation paths.

In order to estimate the error arising from the use of an uncoupled nail behavior in lieu of an isotropic behavior, deformation energy associated with the two approaches was calculated and compared. Mean values for the connection-slip ( $d_m$ ) and the trajectory deformation ( $\alpha_m$ ) were evaluated (with reference to the last steps of the analyses) by means of equations (3.11), (3.12) and (3.13).

$$d_j = \sqrt{u_{x,j}^2 + u_{y,j}^2} \quad (3.11)$$

$$d_m = \frac{\sum_j d_j}{n_{nails}} \quad (3.12)$$

$$\alpha_m = \frac{\sum_j \Delta\alpha_j d_j}{\sum_j d_j} \quad (3.13)$$

where:

- $n_{nails}$  is the number of fasteners
- $\Delta\alpha_j$  is the smallest angle between the deformation direction of the j-th connection and the principal directions
- $u_{x,j}$ ,  $u_{y,j}$  are the deformations of the connection j along the principal directions, x and y respectively.

Mean energy increase  $\Delta E$  per single fastener connection due to uncoupled nail-response was obtained as reported in Figure 3.13-c. Total energy variation was then evaluated by multiplying the mean energy increase by the total number of fasteners present in any given investigated diaphragm. In order to estimate the % error, the total energy variation was compared to the total strain energy absorbed by the diaphragm, which corresponded to the work done by external forces. The results summarized in Table 3.5 show relatively insignificant overestimation ( $< 7.0\%$ ) which reduced as the diaphragm size increased (smaller  $d_m$  values). Consequently, the modeling assumption of uncoupled nail response appears to be adequate and was adopted in the M1 and M2 validation process and the subsequently reported parametric study.

*Table 3.5: Energy overestimation errors derived when assuming fasteners with ‘uncoupled’ response*

Specimen	$n_{\text{nails}}$	$\alpha_m$ [deg]	$d_m$ [mm]	Overestimation error [%]
ABK E	3320	2.45	0.27	0.1
1a-PARA	2378	2.45	1.81	1.1
1a-PERP	2378	1.19	2.49	0.2
Specimen B	1810	8.07	1.47	3.1
Specimen A	2292	4.87	1.47	1.5
AB-1	420	20.45	3.15	3.8
SC	134	13.15	5.30	5.6
5 x 4	880	31.55	5.75	6.6

### 3.4 PARAMETRIC ANALYSES

In order to investigate a range of floor diaphragm geometries, a series of parametric analyses were performed using the M2 approach. As aforementioned, the influence of friction was found to be limited to the cases of vintage diaphragms with T&G floorboards. Hence friction was not considered in the parametric study due to uncertainties associated with an appropriate magnitude in order to provide lower-bound results. Unless stated otherwise, all other aspects were modeled as previously described for the M2 modeling approach. The study was focused on the potential floor diaphragm geometries that could be encountered in real buildings, and are listed in Table 3.6 where  $L$  is the joist span and  $B$  is the dimension perpendicular to the joists. Aspect ratio was defined as  $AR = L/B$ . The influence of diaphragm aspect ratio  $AR$ , diaphragm size and loading direction were investigated. For analyses perpendicular to the joists, nonlinear

hinges with coupled *axial-force/moment* behavior were assigned to the joists and a linear yield surface was selected (equation (3.14)).

$$\frac{N_d}{N_R} + \frac{M_d}{M_R} = 1 \quad (3.14)$$

Table 3.6: Diaphragm geometric details used in the parametric study

Diaphragm	L [m]	B [m]	AR
D1	5.65	8.00	0.7
D2	6.00	6.00	1.0
D3	6.00	12.00	0.5
D4	10.00	20.00	0.5
D5	10.80	10.50	1.0
D6	9.60	14.00	0.7

Table 3.7 provides geometrical and material properties that were common to all diaphragms modeled in the parametric study.

Table 3.7: Parametric study - common properties

Item	Value
Floorboard section	150 x 20 mm
Joist section	50 x 300 mm
Timber grade (floorboards and joists)	C 24 <sup>1</sup>
Joist spacing	500 mm
Nail couple spacing <sup>2</sup>	100 mm
Maximum floorboard length	4000 mm

<sup>1</sup> material properties are reported in EN 338:2009 [CEN (2009)]

<sup>2</sup> nail properties as per vintage nail connections in Schiro et al. (2018)

Diaphragm responses were evaluated considering a parabolic load profiles and using nonlinear static (pushover) analyses as suggested by ASCE 41-17 [ASCE (2017)]. For analyses where load was applied parallel to the joists, forces were applied directly to joist ends. In analysis cases where load was applied perpendicular to the joists (Figure 3.14-b) the loads were applied directly to the outermost joist. Large displacement analyses were then performed, with results presented in subsequent sections.

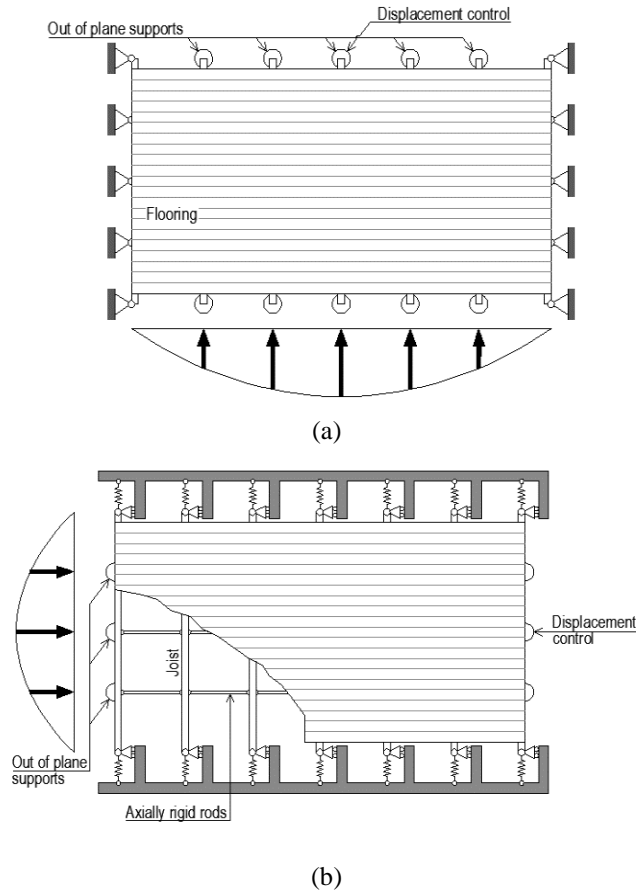


Figure 3.14: Diaphragm loading schemes: a) parallel-to-joists; b) perpendicular-to-joists

### 3.4.1 ANALYSIS RESULTS

Analyses were performed by loading the diaphragms to a 10% drift parallel and perpendicular to joist directions. Some of the diaphragms that were loaded parallel to the joists exhibited bending failure of the floorboards prior to reaching 10% drift. The stress levels of other diaphragm components were carefully monitored in order to verify that strength properties other than flexural capacity were not exceeded during the analysis. From the data summarized in Table 3.8, it appears that the drift at failure ( $dr_{max}$ ) is proportional to the diaphragm span with decreasing maximum unit shear capacity ( $v_{max}$ ) as the diaphragm span increased.

Table 3.8: Diaphragm force and deformation capacities in the loading direction parallel to the joists ( $v_{\max} = F_{\max}/L$ )

Diaphragm	$\alpha$	L [m]	B [m]	$dr_{\max}$ [%]	$F_{\max}$ [kN]	$v_{\max}$ [kN/m]
D1	0.7	5.65	8.00	4.00	44.00	3.89
D2	1.0	6.00	6.00	3.70	66.35	5.53
D3	0.5	6.00	12.00	6.30	42.73	3.56
D4	0.5	10.00	20.00	10.00	55.00	2.75
D5	1.0	10.80	10.50	5.60	82.00	3.80
D6	0.7	9.60	14.00	7.00	63.41	3.30

Analysis results were compared in terms of equivalent shear stiffness  $G_d$  obtained by assuming a static scheme of a shear beam subjected to a parabolic load distribution. Two drift amplitude levels were considered: (1) representative of the initial stiffness which was equal to 0.25% drift, (2) drift amplitude equal to 3.5% drift, which corresponded to the maximum deformation level that was reached by all diaphragms without failure. In the subsequent discussion,  $G_{d,0}$  denotes the equivalent shear stiffness for analyses where the diaphragm was loaded parallel to the joists and  $G_{d,90}$  refers to analyses where the diaphragm was loaded perpendicular to the joists. From the graphs reported in Figure 3.15 and Figure 3.16 it is evident that variations in diaphragm size (scale factor) and diaphragm aspect ratio had a significant influence on the equivalent stiffness values (variation range of 250%). The  $G_{d,90}/G_{d,0}$  ratio was also significantly influenced by the aforementioned parameters, indicating that the orthotropy in the in-plane diaphragm response is strongly related to the floor geometry.

Aspect ratio had a negligible influence for diaphragms that were loaded perpendicular to the joist. For any given scale factor (represented by the joist span  $L$ ), a reduction in the aspect ratio corresponds to an increase in the number of joists in a diaphragm. Hence, each individual joist contributes approximately similar to the global  $G_{d,90}$  in-plane stiffness of a diaphragm and consequently the global stiffness is expected to be proportional to the number of joists present in a diaphragm.  $G_{d,90}$  was determined by dividing the global stiffness by the diaphragm width (proportional to the number of joists), such that  $G_{d,90}$  was not significantly affected by variations in the diaphragm aspect ratio.

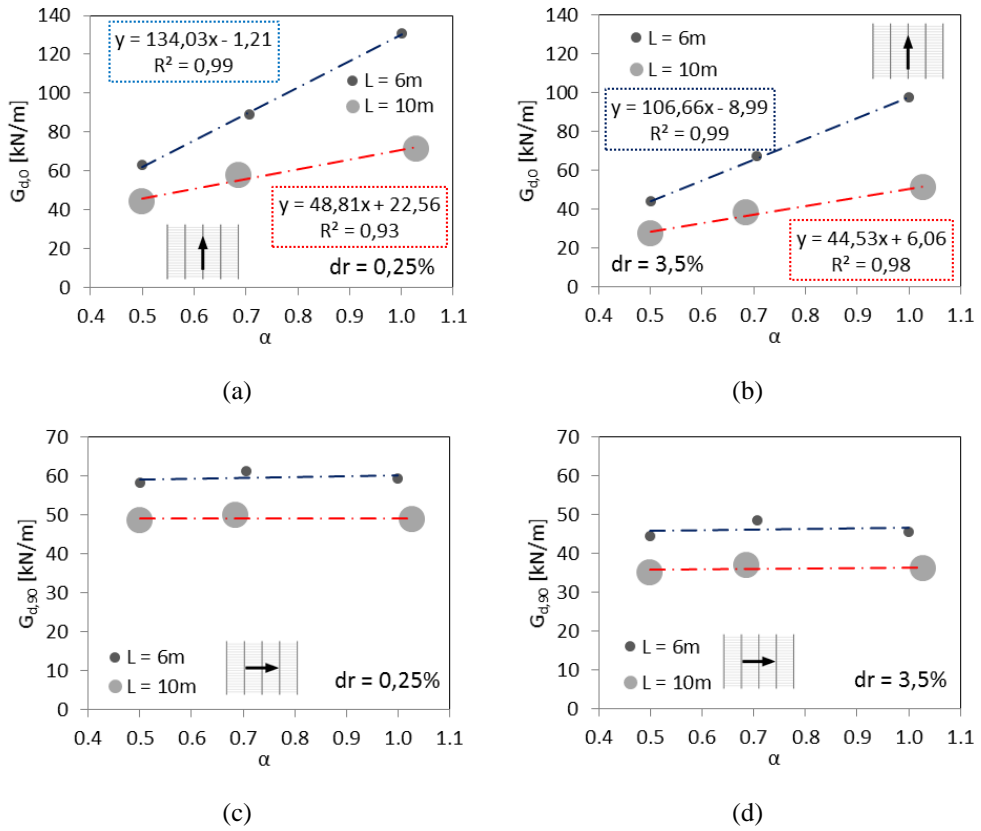


Figure 3.15: Equivalent stiffness variation trends: a) loading direction parallel to joists, 0.25% drift level; b) loading direction parallel to joists, 3.5% drift level; c) loading direction perpendicular to joists, 0.25% drift level; d) loading direction perpendicular to joists, 3.5% drift level

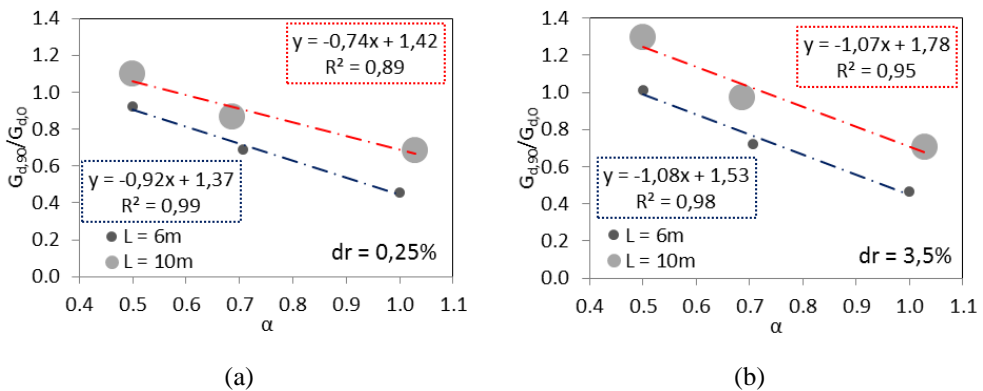


Figure 3.16: Diaphragm orthotropy: a)  $G_{d,90}/G_{d,0}$  ratio for 0.25% drift level; b)  $G_{d,90}/G_{d,0}$  ratio for 3.5% drift level

Table 3.9: Stiffness values and orthotropy ratios,  $dr=0.25\%$

Diaphragm	$G_{d,0}$ [kN/m]	$G_{d,90}$ [kN/m]	$G_{d,90}/G_{d,0}$
D1	88.96	61.19	0.69
D2	130.99	59.49	0.45
D3	63.20	58.20	0.92
D4	71.12	57.45	0.81
D5	44.31	48.65	1.10
D6	71.33	48.83	0.68

Table 3.10: Stiffness values and orthotropy ratios,  $dr=3.5\%$

Diaphragm	$G_{d,0}$ [kN/m]	$G_{d,90}$ [kN/m]	$G_{d,90}/G_{d,0}$
D1	67.06	48.51	0.72
D2	97.37	45.68	0.47
D3	43.91	44.55	1.01
D4	51.02	56.84	1.11
D5	27.21	35.23	1.29
D6	51.26	36.15	0.71

### 3.4.2 REMARKS ON TRADITIONAL TIMBER FLOORS FOUND IN MEDITERRANEAN COUNTRIES

Except for the test campaign reported in Baldessari et al. (2009), all of the experimental data and analysis results presented herein refer to floor diaphragms with slender joist cross-sections ( $SL$ ) that are typically encountered in North America, Northern Europe and Oceania. Such slender joists are typically characterized by *height to width* ratios that range between 4.0 and 6.0. By contrast, traditional timber diaphragms that are commonly encountered in the Mediterranean countries present squatter joist cross-sections ( $SQ$ ) with a typical *height to width* ratio of 1.3 - 1.5. Joist spacing is consistent among the  $SL$  and  $SQ$  type joists and ranges between 450 mm and 600 mm. To evaluate the influence of joist aspect ratio on the diaphragm in-plane response, analyses with  $SQ$  joists were performed by assuming the joist section of 200 mm deep and 150 mm wide. Predictably, diaphragm response in the direction perpendicular to the joists was observed to be considerably affected by the joist type, while no dependency was noted for parallel to joists analyses (see Table 3.11).

Table 3.11: Diaphragm stiffness ratios ( $SQ/SL$ ) in the direction perpendicular to the joists

drift [%]	D1	D2	D3	D4	D5	D6
0.25	7.0	6.5	6.4	3.5	3.1	3.6
3.5	8.6	8.1	8.0	4.5	3.9	4.5

Joist contribution to the diaphragm in-plane stiffness (when loaded perpendicular to the joists) can be determined using equation (3.14), where an equivalent shear stiffness value  $G_{d,bend}$  is determined by considering the sole bending stiffness of the joists under parabolic loading:

$$G_{d,bend} = n_j \cdot 9.84 \cdot \frac{E \cdot J_2}{B \cdot L^2} \quad (3.14)$$

Where:

- $G_{d,bend}$  is the diaphragm equivalent shear stiffness when the sole bending deformation of the joists is accounted for.
- $n_j$  is the number of joists.
- $EJ_2$  is the joist moment of inertia with respect to the weak axis.

In order to isolate the contribution of the flooring to the global stiffness, equivalent shear stiffness values obtained by means of equation (3.14) were compared with the values derived from the numerical analyses. As summarized in Table 3.12, the majority of the in-plane diaphragm stiffness with *SQ* type joists is attributable to the bending stiffness of the joists. From the results reported in Table 3.12 it is evident that the flooring contribution becomes greater with increasing joist length.

*Table 3.12: In-plane stiffness contribution of the flooring, diaphragms with SQ joist vs SL joist,  $d_r = 0.25\%$*

		D1	D2	D3	D4	D5	D6
$n_j$		17	13	25	41	22	29
SQ joists [kN/m]	$\Delta_{Gd}$	25.73	18.73	18.88	47.20	44.35	43.33
	<b>Influence</b>	<b>6%</b>	<b>5%</b>	<b>5%</b>	<b>27%</b>	<b>29%</b>	<b>24%</b>
SL joists [kN/m]	$\Delta_{Gd}$	38.69	39.14	38.63	41.72	42.75	42.42
	<b>Influence</b>	<b>63%</b>	<b>66%</b>	<b>66%</b>	<b>86%</b>	<b>88%</b>	<b>85%</b>

### 3.5 RESULTS FITTING RELATIONS

Based on the numerical results explained in the previous paragraphs a simplified formulation for predicting diaphragm in-plane stiffness was derived. Such formulation consists in the data fitting of the reported numerical results therefore its extension to different diaphragm construction details may not be appropriate.

Diaphragm stiffness in parallel to joist direction  $G_{d,0}$  can be evaluated by means of equation (3.15), where  $\alpha=L/B$  is diaphragm aspect ratio.

$$G_{d,0} = A \cdot \alpha + B \quad (3.15)$$

Parameters  $A$  [ $kN/m$ ] and  $B$  [ $kN/m$ ] account for joist length  $L$  [ $m$ ] and are defined via equations (3.16) and (3.17).

$$A = A_1 \cdot L + A_2 \quad (3.16)$$

$$B = B_1 \cdot L + B_2 \quad (3.17)$$

Values to be assigned to correlation factors  $A_1$ ,  $A_2$ ,  $B_1$ ,  $B_2$  are listed in Table 3.13.

Table 3.13: Correlation factors

Parameter	Value	Unit
A1	-35.18	kN/m <sup>2</sup>
A2	385.23	kN/m
B1	8.36	kN/m <sup>2</sup>
B2	-67.21	kN/m

Diaphragm stiffness in perpendicular to joists direction can be calculated according to equation (3.18), where  $G_{d,0}$  is given by equation (3.15).

$$G_{d,90} = \mu \cdot G_{d,0} + k_j \quad (3.18)$$

Parameter  $\mu$  accounts for diaphragm orthotropy and should be evaluated as a function of diaphragm aspect ratio  $\alpha$  according to equation (3.19). Parameter  $k_j$  accounts for in-plane bending stiffness of the joists and can be calculated according to equation (3.20) where  $EJ$  is in-plane bending stiffness of joists and  $n_j$  is the number of joists.

$$\mu(\alpha) = 1.35 - 0.7 \cdot \alpha \quad (3.19)$$

$$k_j = 9.84 \cdot n_j \cdot \frac{EJ}{B \cdot L^2} \quad (3.20)$$

## 3.6 CONCLUSIONS

Two modeling approaches with different levels of refinement were employed to numerically investigate the influence of different parameters on the response of straight sheathed timber diaphragms when subjected to in-plane loading. The approaches were selected in order to isolate the influence of certain parameters (i.e. diaphragm aspect ratio, scale factor, diaphragm size, board-to-board contact and friction) that are generally overlooked by numerical research studies currently available in literature. These parameters were specifically investigated because it was postulated that they explained the notable differences that are encountered when comparing the findings from experimental studies. To address this knowledge gap, a wide range of experimental

data on straight sheathed timber floor diaphragms was selected for validation of the modeling strategies. From the results of the numerical study reported herein, the following remarks are highlighted:

- The M2 approach permitted the contact and friction phenomena to be simulated with sufficient accuracy (comparable to the refined M1 approach) and computational efficiency. This finding appears markedly favorable for the adoption of the M2 approach for nonlinear dynamic analyses;
- The influence of the board-to-board contact phenomena appeared to be notable in both loading directions (both parallel and perpendicular to the joist orientation), with a stiffness variation of up to approximately 20% being observed;
- Effects of friction were found to influence timber floor diaphragm response in both loading directions (both parallel and perpendicular to the joist orientation). However, the presence of friction appeared to be limited to the case of diaphragms sheathed with tongue and groove floorboards. Additionally, friction seems to contribute to a stiffer response for vintage timber floor diaphragms when compared to that of newly constructed laboratory diaphragms.
- The in-plane stiffness ( $G_d$ ) of timber floor diaphragms appears to be related to the diaphragm size (scale factor), with the  $G_d$  values for small size diaphragms being larger than that observed for greater floor sizes.
- Aspect ratio  $AR$  was found to significantly influence diaphragm orthotropy. The difference in response observed for the loading directions parallel and perpendicular to the joist orientation was more pronounced when  $AR$  was close to unity.

**NOTE:** Research outcomes presented in this Chapter have been published in:

Giongo I., Rizzi E., Ingham J. M., Dizhur D. (2018) “Numerical modeling strategies for the in-plane behavior of straight sheathed timber diaphragms”, *ASCE Journal of Structural Engineering*, vol. 144(10), ISSN: 0733-9445, doi:10.1061/(ASCE)ST.1943-541X.0002148.

---

## 3.7 REFERENCES

- Agbabian, M. S., Barnes, S. B. and Kariotis, J. C. (ABK) (1981). "Methodology for mitigation of seismic hazards in existing unreinforced masonry buildings. Diaphragm testing." National Science Foundation. El Segundo, California.
- ASCE (American Society of Civil Engineers). (2013). "Seismic Evaluation and Retrofit of Existing Buildings" *ASCE 41-13*, Reston, Virginia.
- Augenti, N. and Parisi, F. (2010). "Learning from Construction Failures due to the 2009 L'Aquila, Italy, Earthquake". *Journal of Performance of Constructed Facilities*, vol. 24, No. 6.
- Baldessari, C., Piazza, M. and Tomasi, R. (2009). "The refurbishment of timber floors: characterization of the in-plane behavior" *Proceedings, PROHITEC International Conference*, Taylor and Francis, Rome, Italy, 2009.
- Brignola, A., Pampanin, S. and Podestà, S. (2012). "Experimental Evaluation of the In-Plane Stiffness of Timber Diaphragms". *Earthquake Spectra*, vol. 28, n. 4, pp. 1687-1709.
- CEN (European Committee for Standardization) (2009). "Structural timber - Strength classes". *EN 338*. Brussels, Belgium.
- CSI (Computers and Structures Inc.). (2014). "CSI Analysis Reference Manual, SAP2000 v17". Berkeley, California.
- Derakhshan, H., Griffith, M. C. and Ingham, J. M. (2016). "Out-of-plane seismic response of vertically spanning URM walls connected to flexible diaphragms". *Earthquake Engineering and Structural Dynamics*, vol. 45, Issue 4, 10 April 2016, pp. 563-580.
- Dizhur, D., Ingham, J. M., Biggs, D. and Schultz, A. (2016). "Performance of unreinforced masonry and infilled RC buildings during the 2015 Gorkha, Nepal earthquake sequence". *Proceedings, 16th International Brick and Block Masonry Conference, IBMAC 2016*, pp 2399-2408.
- Giongo, I., Dizhur, D., Tomasi, R. and Ingham, J. M. (2015). "Field testing of flexible timber diaphragms in an existing vintage URM building". *Journal of Structural Engineering*, vol. 141, 2015.
- Ingham, J. M. and Griffith, C. (2016). "Performance of unreinforced masonry buildings during the 2010 Darfield (Christchurch, NZ) earthquake". *Australian Journal of Structural Engineering*, vol. 11, issue 3, pp. 207-224.
- Manie, J., and Kikstra, W. P., eds. (2014). *DIANA—Finite element analysis. User's manual release 9.5*. Delft, Netherlands: TNO DIANA BV.
- Nakamura, Y., Derakhshan, H., Magenes, G. and Griffith, C. (2016). "Influence of Diaphragm Flexibility on Seismic Response of Unreinforced Masonry Buildings". *Journal of earthquake Engineering*, DOI: 10.1080/13632469.2016.1190799.

- NZS (Standards New Zealand) (1993). “Timber Structures Standard”. *NZS 3603:1993*. Wellington, New Zealand.
- NZSEE (New Zealand Society for Earthquake Engineering) (2006). “Assessment and improvement of the structural performance of buildings in earthquakes”. *NZSEE 2006*. Wellington, New Zealand.
- NZSEE (New Zealand Society for Earthquake Engineering) (2017). “Assessment and improvement of the structural performance of buildings in earthquakes”. *NZSEE 2017*. Wellington, New Zealand.
- Penna, A., Morandi, P., Rota, M., Manzini, C. F., da Porto, F. and Magenes, G. (2013). “Performance of masonry buildings during the Emilia 2012 earthquake”. *Bulletin of Earthquake Engineering*, vol. 12, pp. 2255–2273.
- Peralta, D. F. , Bracci, J. M. and Hueste, M. B. (2003). “Seismic Performance of Rehabilitated Wood Diaphragms”. Texas AandM University, Department of Civil Engineering, 2003.
- Prajapati, S., AlShawa, O. and Sorrentino, L. (2015). “Out-of-plane behavior of single-body unreinforced-masonry wall restrained by a flexible diaphragm”, *COMPdyn 2015 – 5th ECCOMAS Thematic Conference on Computational Methods in Structural Dynamics and Earthquake Engineering*, pp. 3127-3138.
- Raggett, J. D., Rojahn, C. (1991). “Dynamic Amplification of Ground Motions by Low-Rise, Stiff Shear Wall Buildings”, *SMIP91 Seminar on Seismological and Engineering Implications of Recent Strong-Motion Data*, pp. 16-1 - 16-11.
- Schiro, G, Giongo, I., Ingham, J. M. and Dizhur, D. (2018). “Lateral performance of as-built and retrofitted timber diaphragm fastener connections”. *Journal of Materials in Civil Engineering*, *in press*.
- Smith, I. and Whale, L. R. J. (1987). “Characteristic properties of nailed and bolted joints under short term lateral load, part 1. Research philosophy and test program”. *Journal of Wood Science*, vol.11, n. 2, pp. 53-59.
- Tena-Colunga, A. and Abrams, D. P. (1996). “Seismic Behavior of Structures with Flexible Diaphragms”, *Journal of Structural Engineering*, vol. 122, no. 4, pp. 439-445.
- Wilson, A. W. (2012). “Seismic assessment of timber floor diaphragms in unreinforced masonry buildings”. *Doctoral dissertation, The University of Auckland, Auckland, New Zealand*.
- Wilson, A., Quenneville, P. J. H., Ingham, J. M. (2014). “In-plane orthotropic behavior of timber floor diaphragms in unreinforced masonry buildings”, *Journal of Structural Engineering* 2014;140(1):04013038.

---

# 4 TIMBER DIAPHRAGMS RETROFITTED WITH PLYWOOD SHEATHING OVERLAY

## 4.1 INTRODUCTION

In sections 4.2 and 4.3 a previously reported in-situ experimental campaign investigating the in-plane behavior of retrofitted timber floor diaphragms that was undertaken on full scale specimens located in an URM building constructed circa 1913 is summarized. The experimental testing campaign comprised timber floor diaphragms tested with retrofit strategies that were characterized by being economical and simple to implement. The retrofit strategies included re-nailing of board-to-joist connections, use of fire-rated ceiling, use of steel chords and the application of plywood sheet overlay. In the second part of the Chapter an extensive numerical study based on the retrofit schemes considered in the aforementioned experimental campaign is presented. Alternative modeling strategies, validated against the summarized experimental results, are presented. Subsequently a detailed parametric study on retrofitted timber floor diaphragms was undertaken.

## 4.2 EXPERIMENTAL CAMPAIGN

### 4.2.1 GENERAL DESCRIPTION

An *in-situ* experimental campaign investigating the in-plane behavior of retrofitted timber floor diaphragms was undertaken on full scale specimens located in a two-story clay brick URM building constructed circa 1913 in Whanganui, New Zealand. The original timber floor diaphragm of  $9.6 \times 17 \text{ m}^2$  was cut to form two individual test specimens. The timber floor diaphragm consisted of New Zealand native Rimu timber

---

joists measuring  $300 \times 50 \text{ mm}^2$ , with a layer of orthogonally positioned  $130 \times 22 \text{ mm}^2$  tongue and groove New Zealand native Matai timber floorboards. The timber joists extended parallel to the 9.6 m direction with approximate spacing of 450 mm. The joists consisted of two planks which overlapped by approximately 400 mm and were supported mid-span on a timber beam which, in turn, was supported by cast iron columns. The mid-span overlapping portion of the joist was not interconnected. In the direction orthogonal to the joists, cross bracing timber elements with a spacing of approximately 1.5 m were present between the joists. The two individual test specimens measured  $9.6 \times 5.6 \text{ m}^2$  (Specimen A) and  $9.6 \times 4.7 \text{ m}^2$  (Specimen B) and were isolated from the mid-span support timber beam by cutting the nails that fixed the joists to the support beam. Two low-friction, well-greased polystone plates (3 mm thick) were inserted between each joist and the mid-span support timber beam. Wall-to-diaphragm connections were installed using adhesive anchorage (as recommended by FEMA 547, FEMA (2006)) consisting of  $\text{Ø } 16 \text{ mm}$  threaded mild-steel rods bonded to masonry along the diaphragm specimen edges at spacing ranging between 1.5 m and 2.0 m.

#### **4.2.2 TEST SETUP**

The lateral force was applied to the diaphragm test specimens using a loading test setup consisting of wire ropes and pulleys as previously reported in detail by Giongo et al. (2015). Using the specifically designed loading system, the total force introduced by the hydraulic actuator was distributed to four loading points as shown in Figure 4.1. Such loading system permitted to approximate the distribution of inertia forces suggested by ASCE 41-17 [ASCE, (2017)]. The use of two nominally identical loading test setups that were connected to either sides of the test diaphragms allowed for reversed cyclic loading to be undertaken. The adopted loading protocol for diaphragm tests was consistent with that suggested by EN 12512 [CEN, (2003)], with cycles of increasing amplitudes up to a maximum of 150 mm mid-span displacement. In some instances it was not possible to reach the target mid-span displacement of 150 mm, despite the use of two 200 mm stroke hydraulic actuators in sequence and turnbuckles at reaction points. This inability to reach maximum required mid-span displacement was attributed to wire rope flexibility and minimal slippage of the rope grips at high tensile forces.

The experimental testing campaign was divided into two stages: (1) timber floor diaphragms tested in as-built condition (i.e. diaphragm specimens comprised of original timber floorboards nailed perpendicularly to the original timber joists); (2) timber floor diaphragms tested with retrofit strategies that were characterized by being economical and simple to implement. Additionally, the in-plane diaphragm behavior was investigated due to the installation of fire-rated ceiling that is commonly used to comply with building fire requirements. The first stage results are reported by Giongo et al.

(2015) and the second stage results are reported herein. It was not possible to isolate more than two floor specimens for testing due to other portions of the floor being severely deteriorated. Each isolated diaphragm specimen was inevitably subjected to multiple cycle tests in order to investigate different diaphragm conditions.

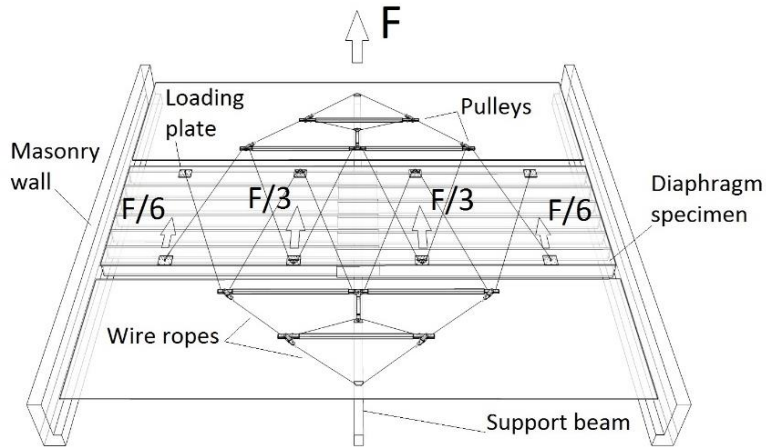


Figure 4.1: Schematic of the test setup and the loading arrangement

Therefore, to ensure that strength loss and stiffness degradation did not negatively impact on the evaluation of the retrofit effectiveness, test comparisons included reference to the ‘last test-cycle’, as well as backbone envelope curves preceding the application of interventions.

### 4.2.3 DIAPHRAGM IMPROVEMENT TECHNIQUES

#### 4.2.3.1 Re-nailing of board-to-joist connections

It is well-known that the in-plane response of single straight sheathed diaphragms is mainly governed by the strength/stiffness of the nail couples that connect the floorboards to the joists. Consequently, strengthening and/or stiffening of individual board-to-joist connections would result in improved in-plane behavior of the diaphragm. In order to investigate the validity of the aforementioned statement, Specimen A was retrofitted by installing two new 2.85 mm × 75 mm nails spaced at approximately 100 mm into each board-to-joist intersection (see Figure 4.2-a, b, c).

#### 4.2.3.2 Fire-rated ceiling

Subsequently to testing of Specimen A with re-nailed board-to-joist connections, fire-rated sheets were installed on the underside of the diaphragm specimen. The fire-rated lining system consisted of a layer of 13 mm gypsum sheets arranged perpendicularly to

---

the joist direction (Figure 4.2-d, e) and directly fixed to the timber joists. Sheet fixing was provided accordingly to product specifications [CBI (2012)] by using 40 mm long gauge 6 screws, as shown in Figure 4.2-b.

#### **4.2.3.3 Steel chords**

Following test completion of Specimen A with the fire-rated ceiling, all gypsum sheets were removed and a single cycle test was performed to establish a benchmark condition. Subsequently,  $50 \times 50 \times 5$  mm L-shaped steel angles were fixed to the diaphragm edges perpendicular to the loading direction by using  $M8 \times 90$  mm coach screws spaced at 100 mm as shown in Figure 4.3. Due to large diaphragm span, the steel chords were interrupted at approximately 2.0 m from the diaphragm ends, with chord continuity provided by using steel gussets fixed to the profile extremities using four M16 bolts (see Figure 4.3-b). The use of steel chords fixed continuously to the diaphragm perimeter and to the masonry walls can be adopted as an effective retrofit strategy that ensures adequate wall-to-diaphragm connections [Doglioni (2000)]. The addition of steel chords also provides a ‘tying effect’ that confines masonry and permits effective engagement of spandrel rocking capacity when perforated walls are loaded in-plane [Beyer & Dazio (2012), Rinaldin et al. (2017)]. Hsiao & Tezcan (2012) have emphasised the importance of steel chord contribution in determining diaphragm flexural behavior (especially in the loading direction parallel to the joist orientation) in accordance with the girder analogy [ATC, (1981)], where a diaphragm chord represents a flange of a girder and is responsible for resisting bending forces, while shear forces are absorbed by sheathing that represent a web of a girder. Similarly, ASCE 41-17 [ASCE (2017)] states: “*The presence of chords at the perimeter of a diaphragm significantly reduces the diaphragm deflection caused by bending and increases the stiffness of the diaphragm over that of an unchorded diaphragm*”. While the same standard recognizes that: “*However, the increase in stiffness caused by chords in a single straight-sheathed diaphragm is minimal because of the flexible nature of these diaphragms*”.

#### **4.2.3.4 Plywood sheet overlay**

Specimen B was retrofitted by applying a layer of 9 mm-thick plywood sheets over the existing flooring. The plywood sheets were arranged as shown in Figure 4.4-a and fixed using 40 mm-long gauge 6 screws, as reported in Figure 4.4-b. At the specimen perimeter, 60 mm long gauge 8 screws were used to connect the plywood overlay to the timber joists. The sheet arrangement was selected in order to favor a homogeneous diaphragm response in parallel/perpendicular to the joists loading directions due to the improved in-plane interlocking of the plywood sheets.

The maximum achieved deformation of the retrofitted Specimen B corresponded to a mid-span displacement of approximately 25 mm due to load limitations by the test setup

(for safety reasons the total force was limited to 120 kN). Therefore, to capture the diaphragm behavior at larger displacements and to identify a lower bound capacity suitable for design, retrofitted Specimen B was cut into a smaller specimen (referred to as Specimen C) with a depth of 2.8 m. The cut line extended parallel to the joist direction and was positioned in order to minimize sheet interlocking determining the effectiveness of the retrofit solution in a worst-case scenario.

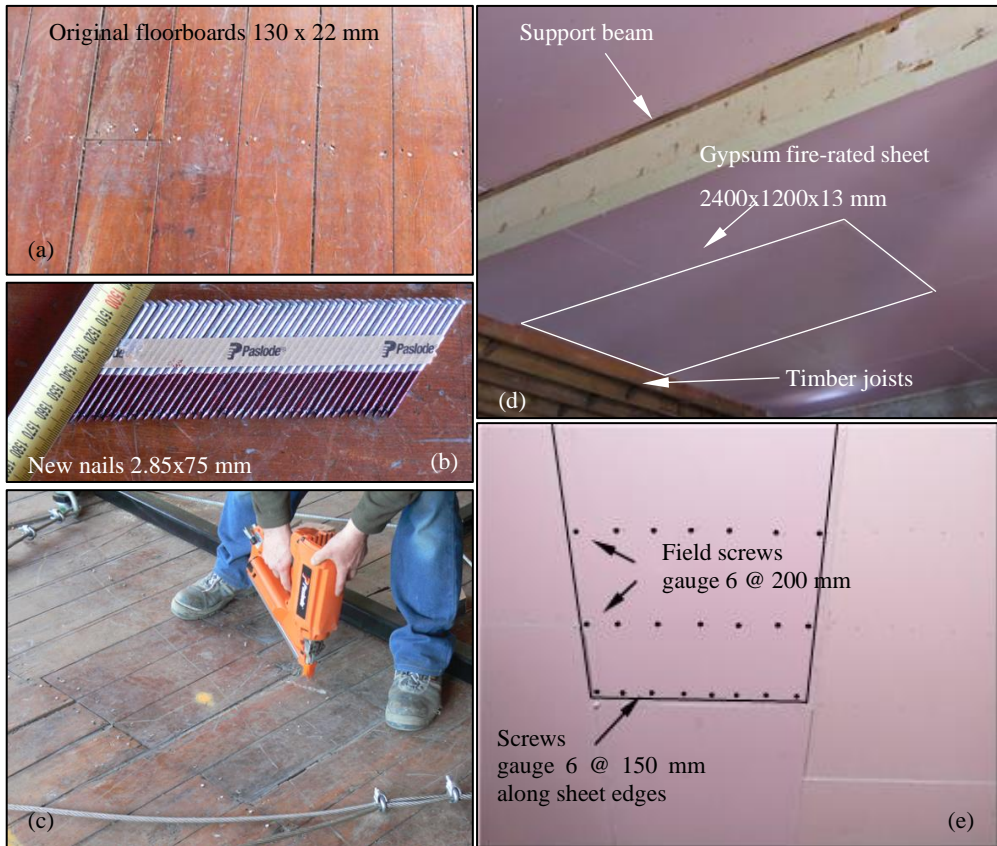


Figure 4.2: Board-to-joist re-nailing of Specimen A

## 4.3 TEST RESULTS

### 4.3.1 RE-NAILING OF BOARD-TO-JOIST CONNECTIONS

Figure 4.5-b provides the experimental total force vs mid-span displacement obtained from testing Specimen A following the re-nailing of every floorboard-to-joist node. In-plane behavior of Specimen A in the as-built configuration [Giongo et al. (2015)] is provided in Figure 4.5-a for reference. As observed for the as-built diaphragm, no signs

of softening or noticeable stiffness reduction were registered in the re-nailed Specimen A up to the maximum mid-span displacement of the tested diaphragm that was allowed by the test setup.



Figure 4.3: Re-nailed diaphragm with a steel chord running along the diaphragm perimeter

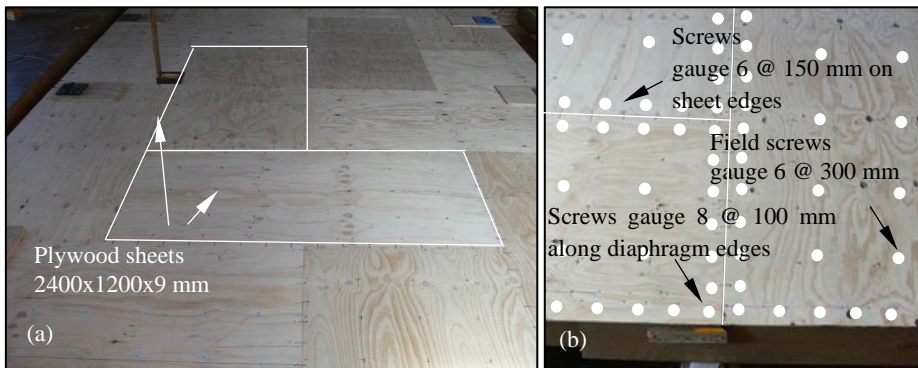


Figure 4.4: Diaphragm retrofitted using a layer of 9 mm thick plywood sheets

Limited strength loss ( $< 5\%$ ) was measured for repeated cycles of same mid-span displacement amplitudes. The overall response variation induced by node re-nailing is visible in Figure 4.5-c where diaphragm behavior before and after improvement is directly compared in terms of backbone envelopes.

From Figure 4.5-d, a non-negligible increase in the diaphragm stiffness can be noted for all deformation levels ( $> 30\%$ ). Secant values of the equivalent shear stiffness ( $G_d$ ) determined by assuming a shear beam schematization, as per ASCE (2017) and NZSEE (2017), are given in Table 4.1 for 0.5% and 2.1% drift levels (drift = mid-span displacement / half-span length).

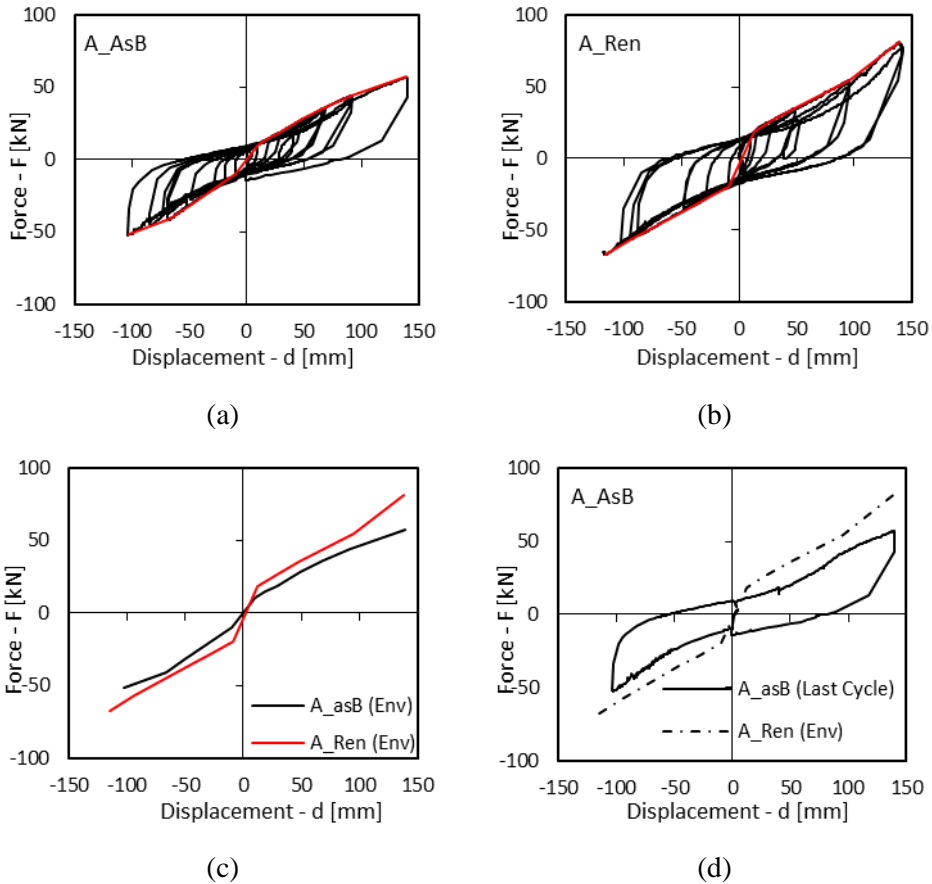


Figure 4.5: Experimental results from testing of Specimen A in 'as-built' and renailed conditions: a) as-built condition (A\_AsB) | Cyclic testing [Giongo et al. (2014)]; b) re-nailed specimen (A\_Ren) | Cyclic testing; c) envelope curve (Env) comparison; d) comparison between the last cycle of the test in the 'as-built' condition and the envelope curve from testing in the re-nailed conditions

### 4.3.2 FIRE-RATED CEILING

The attained experimental total force vs mid-span displacement of the testing Specimen A with fire-rated ceiling is reported in Figure 4.6. The specimen exhibited a substantial stiffness decrease at approximately 45 mm of mid-span displacement that corresponded to a capacity plateau characterised by an unit shear strength ( $0.5 \times \text{total force} / \text{specimen width}$ ) of approximately 6.8 kN/m. Noticeable strength reduction (up to 20%) was observed for subsequent cycles performed at the same displacement amplitude. At a mid-span displacement larger than 100 mm, detachment of the gypsum sheets close to the diaphragm lateral edges was observed, as the maximum displacement capacity

[Schiro et al. (2018)] of the screws connecting the gypsum sheets to the joists was exceeded (see Figure 4.7-b). Degradation of performance of the original diaphragm as a result of the test cycles was not observed, as can be noted by comparing the last cycle plot from testing Specimen A prior to application of the fire-rated ceiling and the benchmark cycle performed following the removal of the remaining gypsum sheets, as reported in Figure 4.6-c.

### 4.3.3 STEEL CHORDS

The effect of the steel chords over the diaphragm response is shown in Figure 4.6-c, where the experimental curve obtained from the chorded specimen is provided. By comparing the envelope curve from the test with the steel chords to the benchmark cycle performed before the chord application, no appreciable improvement can be noted.

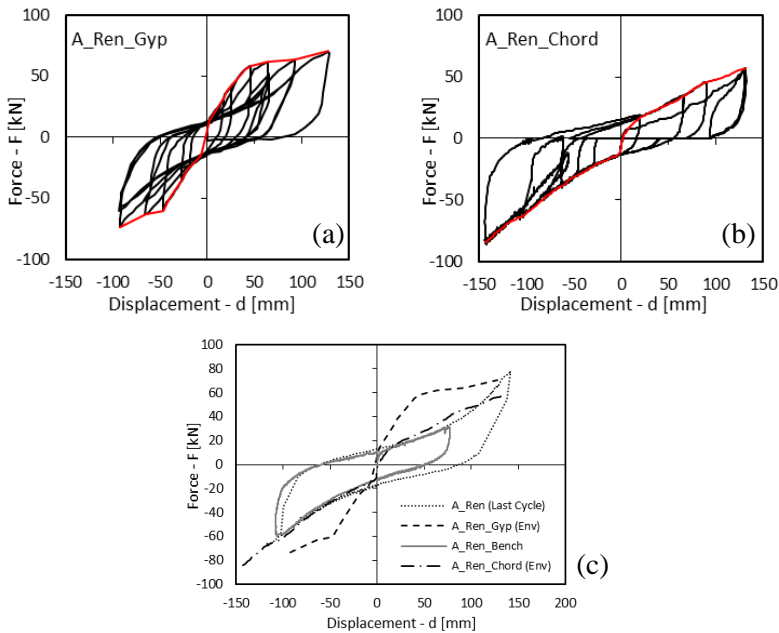


Figure 4.6: Experimental results from testing re-nailed Specimen A after installation of the fire-rated sheets and the steel chords: a) renailed specimen sheathed with a gypsum panel underlay (A\_Ren\_Gyp) / Cyclic testing; b) Renailed, chorded specimen (A\_Ren\_Chord) / Cyclic testing; c) Curve comparison

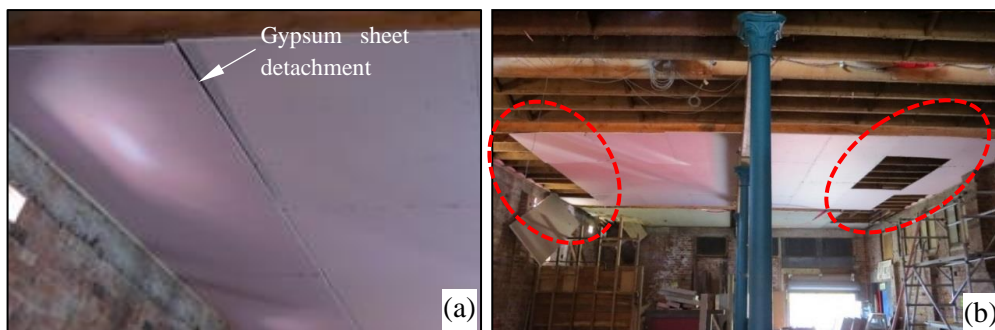


Figure 4.7: Specimen A with fire-rated ceiling showing damage progression: a) Mid-span displacement = 70 mm (third cycle); b) Mid-span displacement = 130 mm (first cycle). Showing location of collapsed gypsum sheets

This appears to be consistent with the aforementioned statement from ASCE 41-17 [ASCE (2017)] and also with the following remark from [ATC (1981)]: “*Straight-sheathed and unblocked plywood diaphragms resist lateral forces in a completely different manner from those of either the girder or truss analogy*”. Particularly, single straight sheathed diaphragms appear to exhibit overall negligible flexural behavior. It is worth noting that the joists were interrupted at the mid-span timber beam support with no direct mechanical connection between the two overlapping joist portions. In case of the timber joists being continuous over the full diaphragm span, the possible influence of the steel chords might have been shadowed by the capacity of individual timber joists acting as chords.

#### 4.3.4 PLYWOOD SHEET OVERLAY

The lateral performance of Specimen B that was retrofitted using plywood overlay is reported in Figure 4.8-b. Strength loss was not observed between cycles to the same deformation levels, illustrating the ability of the plywood overlaid diaphragm to resist multi-cyclic loading. Similar multi-cyclic loading consideration can be seen in the test undertaken on Specimen B in the as-built condition, see Figure 4.8-a. The stiffness increase as a result of the plywood overlay was almost tenfold at small mid-span deformation levels (compare the  $G_d$  values at 0.5% drift as shown in Table 4.1 for B\_Plyw or C\_Plyw, with the value at 0.5% drift for the last cycle of B\_AsB) and exceeded 600% at deformation levels compatible with onset of out-of-plane failure of face-loaded masonry walls as described in NZSEE (2017) (compare the  $G_d$  value at 2.1% drift as shown in Table 4.1, for C\_Plyw with the value at 2.1% drift for the last cycle of B\_AsB).

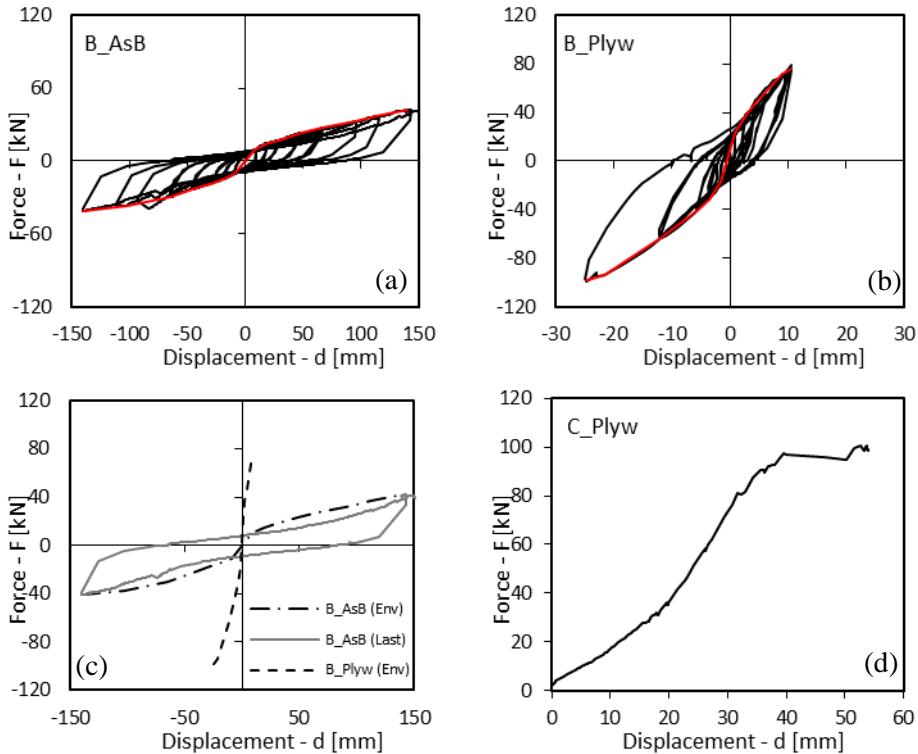


Figure 4.8: Experimental backbones of Specimen B and Specimen C: a) specimen B in the as-built condition (B\_AsB) | Cyclic testing (Giongo et al. 2014); b) specimen B with the plywood sheet overlay (B\_Plyw) | Cyclic testing; c) Specimen B with the plywood sheet overlay (B\_Plyw) | Cyclic testing; d) Specimen C (C\_Plyw) | Monotonic testing

Table 4.1: Equivalent shear stiffness values –  $G_d$  [kN/m]

Mid-span Displ. [mm]	Drift [%]	A_AsB		A_Ren		A_Ren_Gyps	A_Ren_Chord	B_AsB		B_Plyw	C_Plyw
		ENV	LC	ENV	LC	ENV	ENV	ENV	LC	ENV	ENV
25	0.5	154	137	199	173	315	172	169	99	961	986
100	2.1	104	102	136	110	145	116	91	61	-	411

ENV - stiffness value determined by referring to the backbone envelope curve

LC - stiffness value determined by referring to the 'last-cycle'

A\_AsB - Specimen A diaphragm in as-built condition

A\_Ren - Specimen A diaphragm in re-nailed condition

A\_Ren\_Gyps - Specimen A diaphragm in re-nailed and fire-rated ceiling condition

A\_Ren\_Chord - Specimen A diaphragm in re-nailed with steel chords

B\_AsB - Specimen B diaphragm in as-built condition

B\_Plyw - Specimen B diaphragm with 9 mm plywood overlay

C\_Plyw - Specimen C diaphragm with 9 mm plywood overlay

A lower bound capacity for the plywood overlay retrofit was determined by referring to the monotonic test conducted on Specimen C (see Figure 4.8-d). Specimen C resisted a total lateral force of approximately 98 kN, that corresponded to a unit shear strength of 17.5 kN/m. At the maximum loading, buckling of the plywood sheets on the compression side (Figure 4.9-b) and separation of the sheets on the tension side (see Figure 4.9-a) was observed. Such phenomena evidenced a beam-like flexural behavior that was not observed for Specimens A and B and that was attributed to the increased aspect ratio (*diaphragm dimension parallel to the joists / diaphragm dimension perpendicular to the joists*) of Specimen C.

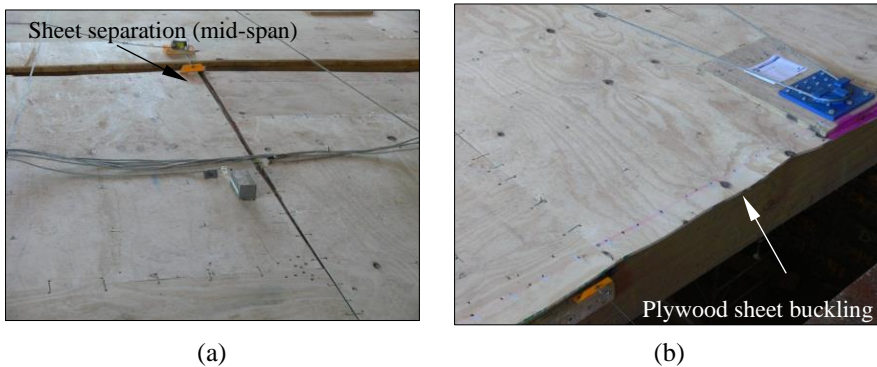


Figure 4.9: Deformation of Specimen C at the end of testing: a) tension side, showing separation gap between plywood sheets: b) Compression side showing buckling of sheets

## 4.4 FINITE ELEMENT MODELING

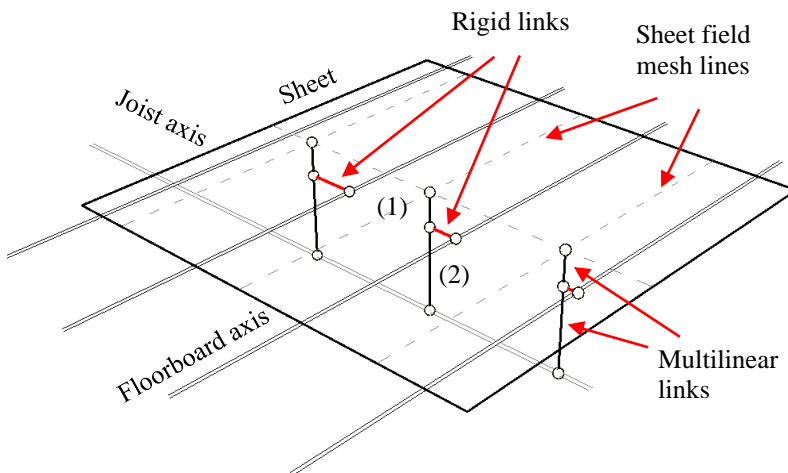
### 4.4.1 FE MODELING DETAILS

The numerical models adopted for a parametric study on retrofitted timber floor diaphragms reported herein, were implemented using a finite element software SAP2000 [CSI (2014)]. Diaphragm components representative of the as-built condition (i.e. timber framing and single straight sheathing) were modeled consistently with the M2 modeling approach presented in Chapter 3.

Diaphragm specimens with re-nailed floorboard-to-joist connections (i.e. insertion of new nails), had no additional elements introduced into the model. The new nails were simulated by modifying the original nails behavior curve of the *multilinear link elements*, in accordance with the experimental results reported in Schiro et al. (2018). Diaphragm steel chords were modeled using linear elastic frame elements with geometry and material properties simulating the actual steel chords profiles used. Strength and post-elastic behavior of the steel chords was simulated by introducing *non-linear hinges* with the yield stress and ultimate deformation elected according to the

chord material properties. Connection between chord elements and diaphragm framing members (i.e. joists and blocking elements) was modeled by using *multi-linear links* placed at the fastener locations.

The addition of plywood sheet overlays was modeled using two-dimensional *shell* elements characterized by orthotropic material properties. Sheet-to-sheet contact interface phenomena were reproduced by inserting non-linear *gap link-elements* between adjacent sheets (described in detail in Chapter 3 for inter-floorboard contact). Plywood-to-solid wood connections with nails or screws were simulated using *multilinear link-elements*, where non-linear backbone curves were assigned to the link elements along the principal shear directions (Degrees of Freedom – DoFs -  $U2$  and  $U3$ ). DoFs  $U1$ ,  $R2$  and  $R3$  were fully restrained (no flexural or axial deformation was allowed) while  $R1$  (torsional DoF) was unrestrained. Fasteners crossing multiple shear planes (e.g. nails that are driven through the floorboards in order to connect the plywood sheets to the underlying joists) were modeled by introducing one *multilinear link* per shear plane (Figure 4.10). *Rigid links* connecting each *multilinear link* to the closest floorboard element were also added in order to account for the stiffening contribution to the in-plane response of the original flooring of the fastener fixing the sheets to the joists (see Figure 4.10).



(1) sheet-to-floorboard shear plane, (2) Floorboard-to-joist shear plane

Figure 4.10: Modeling details for straight sheathed diaphragms retrofitted using plywood sheet overlay

#### 4.4.2 FE MODEL VALIDATION

The finite element modeling approach was validated on several experimental tests undertaken on rehabilitated timber floors that were previously reported by various authors [Peralta et al. (2003), Baldessari et al. (2009), Brignola et al. (2012), Wilson et al. (2014)]. The test diaphragms that were included in the validation process are listed in Table 4.2, where  $L$  is the specimen dimension parallel to the joists and  $B$  is the dimension in the direction perpendicular to the joists.

Table 4.2: Experimental tests and refined models considered as reference for validation

Diaphragm ID	Authors	L [m]	B [m]	Load direction*	Retrofit type
1b-PARA	Wilson et al. (2014)	5.55	10.40	Parallel	Plywood
1b-PERP	Wilson et al. (2014)	5.55	10.40	Perpendicular	Plywood
Specimen A	-	9.60	5.60	Perpendicular	Re-nailing
Specimen B	-	9.60	4.70	Perpendicular	Plywood
AB-2	Brignola et al. (2012)	4.00	4.00	Parallel	Steel chord
R-1	Brignola et al. (2012)	3.00	4.00	Parallel	Plywood
MAE-2B	Peralta et al. (2003)	3.65	7.30	Parallel	Plywood
Diaphragm H	ABK (1981)	6.10	18.30	Parallel	Plywood
6x6 P1 PARA**	---	6.00	6.00	Parallel	Plywood
6x6 P1 PERP**	---	6.00	6.00	Perpendicular	Plywood

\*With reference to the joist axis.

\*\*Diaphragm used in the parametric study, validated on the results from the refined model.

Where available, experimental data was used to define material properties of the diaphragm components and fastener load-slip behavior. Where experimental data was unavailable, parameters were determined by referring to the mean values recommended by widely recognized standards (e.g. for wood materials, EN338/NZS3603) and/or product specifications [e.g. CBI (2012)]. In the cases where the experimental response of connections was not available, fastener load-slip behavior was predicted by using a formulation proposed by McLain (1975) and modified by Pellicane et al. (1991). Further validation of the models in the parametric study was undertaken using more refined modeling approach based on the TNO DIANA software package [Manie and Kikstra (2014)] and the M1 modeling approach presented in Chapter 3 (see Figure 4.11). The plywood sheets were modeled using orthotropic *quadratic curved shell* elements. Contact between sheets was simulated using non-linear *interface elements* to which no-tension (compression only) behavior was assigned. As visible in Figure 4.12, Figure

4.13 and Figure 4.14, the results obtained from the FE models show an overall agreement with the experimental data and the results from the M1-modeling approach.

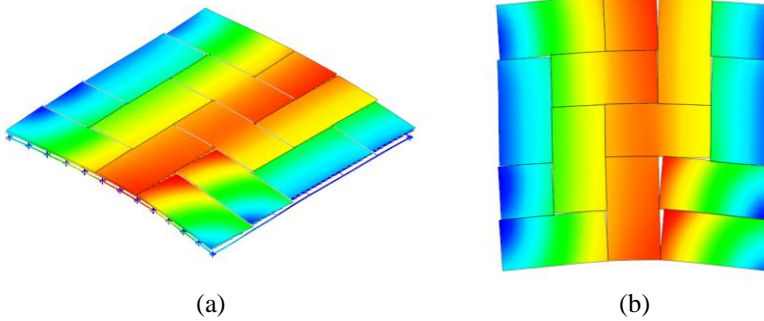


Figure 4.11: Refined M1-model | deformation of diaphragm retrofitted with a plywood overlay: a) Perspective view; b) Top view

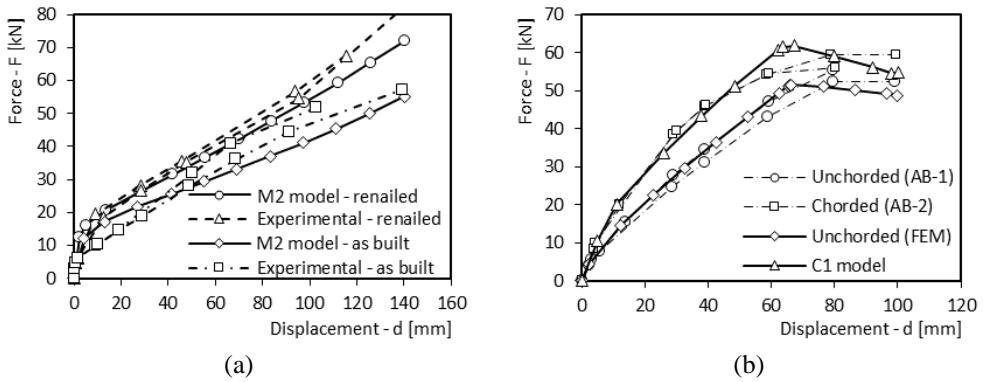


Figure 4.12: Model validation | FE modeling results vs experimental results of 90etrofitted diaphragms: a) Specimen A as-built and retrofitted; b) Specimens AB-1 and AB-2

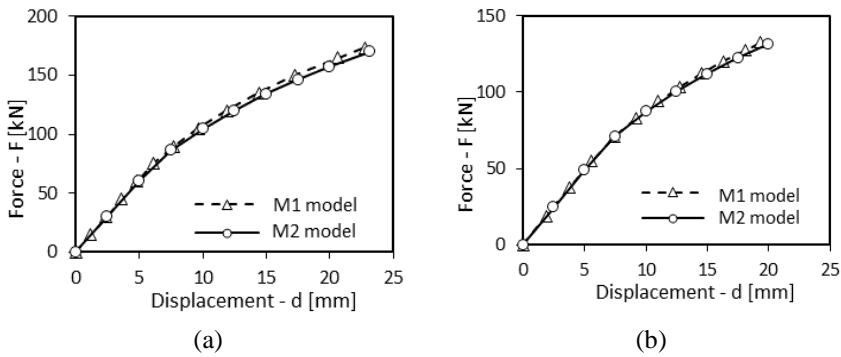


Figure 4.13: Result comparison M2 model vs M1 model: a) 6x6 P1 – PARA; b) 6x6 P1- PERP

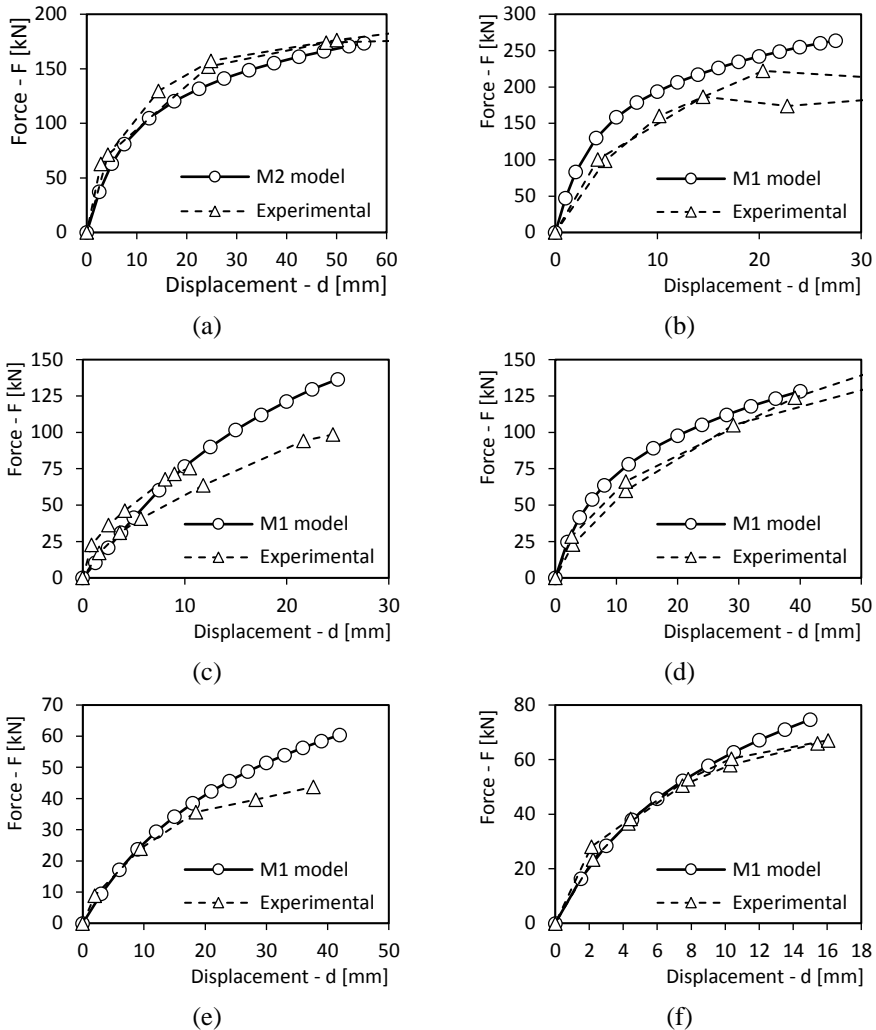


Figure 4.14: Model validation | FE modeling results vs experimental results of 91retrofitted diaphragms: a) 1b-PARA; b) 1b-PERP; c) Specimen B; d) Specimen R-1; e) Diaphragm H; f) MAE-2B

#### 4.4.3 CHORD INFLUENCE

Limited experimental data is available in literature that permits to evaluate the influence of additional chords on the in-plane response of straight sheathed diaphragms. Brignola et al. (2012), and Baldessari et al. (2009) have presented results on straight sheathed floors (loaded in the direction parallel to the joists) where chords were flat steel plates (Brignola et al. (2012) used steel angles instead of steel plates on the specimen edges parallel to the joist direction) were screwed to the diaphragm perimeter. As visible from

the equivalent stiffness ratios reported in Table 4.3, the diaphragms tested by Brignola et al. (2012) (specimen size:  $3 \times 4 \text{ m}^2$ ,  $L \times B$ ) exhibited a notable stiffness increase ( $\geq 20\%$ ) at both small and large deformation levels. Conversely, Baldessari et al. 2008 (specimen size:  $4 \times 5 \text{ m}^2$ ,  $L \times B$ ) registered a negligible variation in the diaphragm response due to the chord presence (stiffness variation  $< 10\%$ ), consistently with the experimental test campaign described herein. The chord stiffening registered by Brignola et al. (2012), appears to be associated with the size of the steel profile cross-section in relation to the diaphragm specimen size.

Two FE models were created (C1 and C2) to simulate the AB-2 diaphragm specimen from Brignola et al. (2012). The C1-model was validated using the experimental data with reference to chorded and unchorded diaphragm configurations (see Figure 4.12). Material properties for the timber elements were selected from NZS 3603 [NZS (1993)] in accordance with wood species and strength class details provided by Brignola et al. (2012). In order to simulate floorboard cracking when the section flexural capacity is exceeded, flexural plastic hinges were introduced at the location of floorboards maximum bending moment. C2-model was assumed to have zero bending stiffness and the same chord axial stiffness and strength properties as that of C1-model.

Table 4.3: Influence of chords on diaphragm stiffness based on previous experimental evidence

drift [%]	$G_{d,\text{chorded}}/G_{d,\text{unchorded}}$	
	Brignola et al. (2012)	Baldessari et al. (2009)
0.25	1.45	1.09
3.00	1.20	-

Pushover curves obtained from the numerical analyses for C1 and C2-models are compared in Figure 4.15-b. Where the chord bending stiffness is neglected (*C2-model*), the pushover curve closely matches that of the unchorded diaphragm. This result demonstrates that steel chords applied to straight sheathed diaphragms tend to exhibit beam element type behavior instead of responding as ‘tie’ elements (i.e. flanges in a girder). Consequently, the chord contribution to the in-plane diaphragm stiffness depends solely on the chord moment of inertia. To evaluate the effect of joist boundary conditions on the chorded diaphragm behavior, further analyses were undertaken allowing the in-plane rotation of the joists (in contrast to the Brignola et al. (2012) experimental test where joist rotation was restrained) and considering geometric non-linearity. The attained results were consistent with the outcomes presented in Figure 4.15.

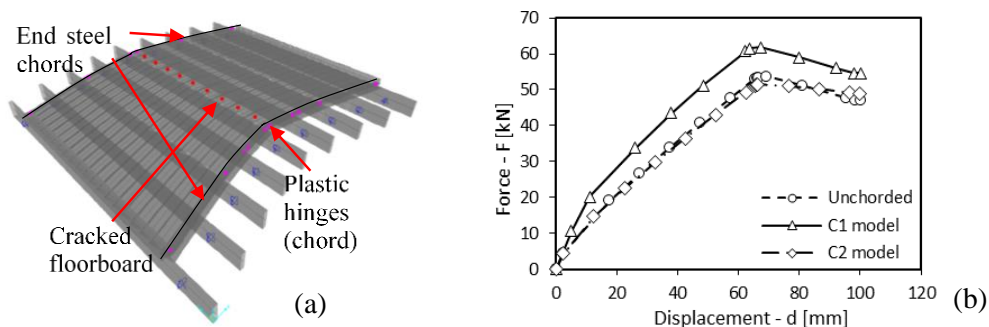


Figure 4.15: Chord influence: numerical results from C1 and C2 models: a) C1-model deformation, last analysis-step; b) Pushover curves

## 4.5 PARAMETRIC STUDY ON DIAPHRAGMS WITH PLYWOOD OVERLAYS

A series of parametric analyses were performed on the diaphragm geometries listed in Table 4.4, where  $L$  and  $B$  are the dimensions respectively parallel and perpendicular to joists directions. In the case of joists with a 10 m span length, the presence of an intermediate support in the out-of-plane direction was assumed. The contribution of the intermediate support to diaphragm in-plane behavior was neglected. Aspect ratio was defined as  $AR = L/B$ . The influence of (1) sheet disposition, (2) sheet thickness and (3) plywood-to-timber connections (in terms of spacing and fastener type) were investigated. Construction details from Specimen B retrofitted with the plywood overlay were replicated in the models. Blocking elements at the diaphragm edges perpendicular to the joist direction were modeled using truss elements (Figure 4.16-a). Plywood sheets were assumed to be nailed to the floorboards only, with the exception of the connections at the diaphragm perimeter. Plywood nail spacing was approximately 150 mm along the sheet edges while 300 mm grid pattern on the rest of the sheet. Along the diaphragm perimeter, sheet edges were assumed to be fixed to the joists or the blocking elements by means of gauge 8 screws (such as penetrating through intermediate floorboard layer) spaced 150 mm centers. Nails intersected one shear plane (sheet-to-floorboard) while screws along the diaphragm perimeter intersected 2 planes (i.e. sheet-to-floorboard and floorboard-to-joist). Load-slip behavior of perimeter screws and existing floorboard-to-joist fasteners were selected in accordance with the experimental results presented by Schiro et al. (2018).

*Table 4.4: Parametric analyses – diaphragm geometries*

Diaphragm ID	L [m]	B [m]	AR
6×8	5.65	8.00	0.7
6×6	6.00	6.00	1.0
6×12	6.00	12.00	0.5
10×20	10.00	20.00	0.5
10×10	10.80	10.50	1.0
10×14	9.60	14.00	0.7

Common diaphragm properties adopted in the parametric study are listed in Table 4.5. The in-plane diaphragm response was evaluated using monotonic non-linear static (pushover) analyses. Forces were applied to the diaphragms according to a parabolic load profile as suggested by ASCE 41-17 [ASCE (2017)] in order to reproduce the inertia force distribution. Loads and external restraints were applied at the joist level. For parallel to the joists analyses, point forces were applied to the joist ends and pinned supports were provided along the outermost joists. For perpendicular to the joists analyses, loads were applied to the outermost joists (joist out-of-plane DoF was restrained) and pinned supports were provided at all joist ends. Because the parametric analyses reached relatively small displacement amplitudes, contact between floorboards was not considered in perpendicular-to-joists simulations (see Chapter 3) and geometrically linear analyses were performed. The effect of geometric nonlinearities and variations in the boundary conditions (i.e. allowing rotation of the diaphragm edges parallel to the loading direction in order to capture possible diaphragm flexural behavior) were also investigated by performing additional analyses which resulted in negligible differences in the force versus mid-span displacement response.

*Table 4.5: Parametric analyses - common properties*

Feature	Value
Floorboard section	150 × 20 mm <sup>2</sup>
Joist section	50 × 300 mm <sup>2</sup>
Timber grade	C 24 <sup>(1)</sup>
Joist spacing	500 mm
Nail couple spacing (floorboard to joist)	100 mm
Maximum floorboard length	4000 mm
Sheet size	1200 × 2400 mm <sup>2</sup>
Plywood grade	F8 <sup>(2)</sup>

<sup>1</sup> EN 338:2009

<sup>2</sup> Standard AS/NZS 2269

Parametric study results were compared in terms of equivalent shear stiffness  $G_d$  defined via equation (4.1), by considering the deformation of a shear beam subject to a parabolic load profile.

$$G_d = \frac{5 W_d L}{32 B \Delta_d} \quad (4.1)$$

$W_d$  is total in-plane load applied to the diaphragm,  $L$  is diaphragm span with respect to applied loads,  $B$  is the dimension of the diaphragm in the parallel to loads direction and  $\Delta_d$  is mid-span displacement.

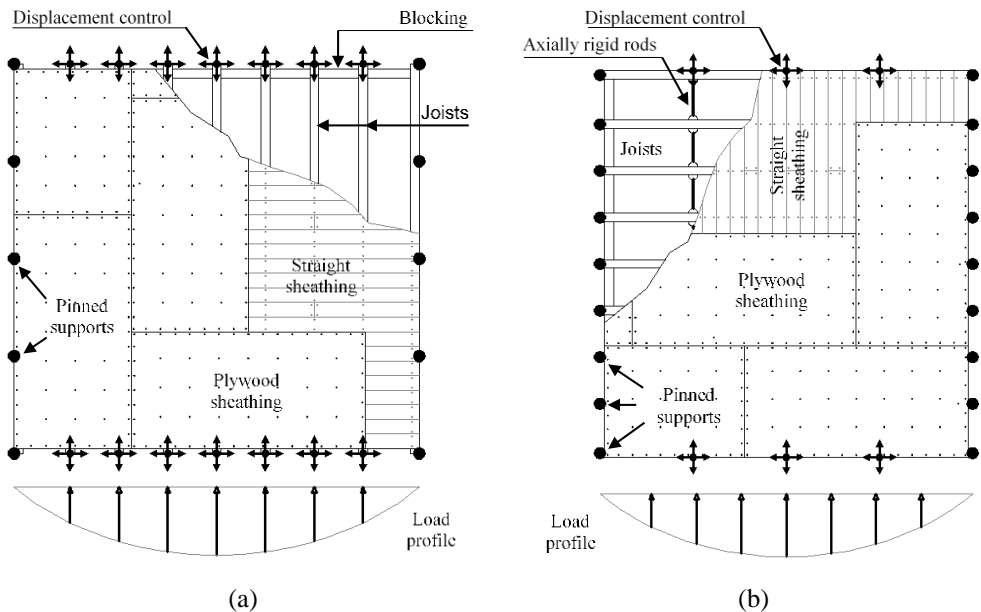


Figure 4.16: Load schemes and boundary conditions for modeled diaphragms that were retrofitted using plywood sheets.

The experimental curves adopted in the validation phase for the plywood-to-solidwood connection modeling were replaced by behavior obtained from analytical formulations available in literature [McLain (1975) and Pellicane et al. (1991)]. The adaptation of such formulations allowed to investigate the effects on in-plane diaphragm response produced by a variation in parameters that directly affect the behavior of the plywood-to-solidwood connections (e.g. plywood thickness, fastener size and fastener spacing).

The formulation proposed by McLain (1975) and later modified by Pellicane et al. (1991) is strongly affected by the *a-priori* initial stiffness evaluation (i.e. one point of

the load-slip curve needs to be known in advance or evaluated using simplified techniques proposed by Wilkinson (1971)). Alternatively, ASCE 41-17 (ASCE 2017) provides a multi-linear force-deformation curve (Figure 4.17) based on the connection yield strength and yield displacement. The yield strength can be evaluated according to AWC-NDS 2012 (AWC 2012), while the yield displacement can be taken as  $0.03 \text{ in} = 0.76 \text{ mm}$  for nailed connections and  $0.04 \text{ in} = 1.02 \text{ mm}$  for screw connections or determined as  $180 \times (\text{fastener diameter})^{1.5} \text{ [kip/in]}$ .

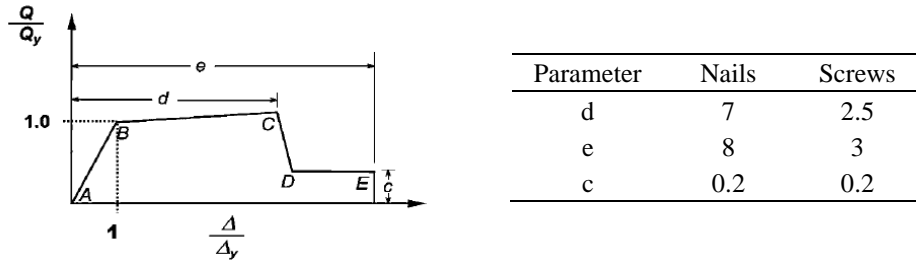


Figure 4.17: Generalized force-deformation behavior for displacement-controlled components (reproduced from ASCE 2013)

The adequacy of the multi-linear force-deformation curves was evaluated by comparing it to the experimental backbone curves provided by Wilson (2012) for newly constructed connections (see Figure 4.18). In Figure 4.18 curves labelled as “ASCE  $\Delta_y$ ” were obtained using the constant yield displacement of 0.76 mm, while curves labelled as “ASCE  $k_y$ ” were derived by evaluating initial stiffness on the connector base shank diameter.

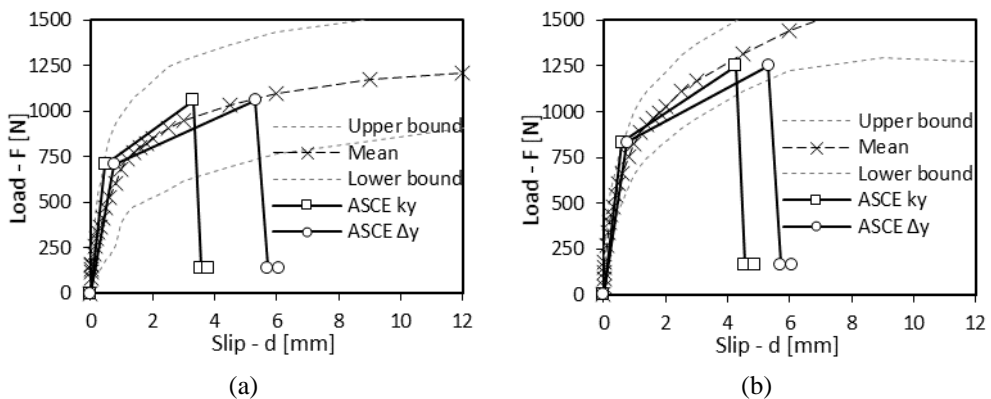


Figure 4.18: Analytical predictions based on standard provisions vs. experimental data on nailed connections: a) Wilson (2012) | “New – USA” specimens; b) Wilson (2012) | “New – NZ” specimens

While initial and post-yield stiffness was well predicted by the analytical formulations, the ultimate displacement and consequently the ductility level appeared to be considerably underestimated. It is noted that the displacement capacity attained by Wilson (2012) might have been positively influenced by the test setup adopted by the authors, as also evidenced by Schiro et al. (2018).

The analysis results that will be presented in the next three paragraphs were obtained under the assumption that the plywood-to-solid wood connections were constituted by nailed connections with a force-displacement behavior consistent with the “ASCE  $k_y$ ” approach.

#### 4.5.1 INFLUENCE OF PLYWOOD SHEET LAYOUT

The influence of the plywood sheet arrangement on the response of floor diaphragms was investigated in accordance with the layouts reported in Figure 4.19. In *P2* and *P3* layouts, the sheets were oriented parallel to each other, forming continuous slip joints between adjacent sheet rows (see Figure 4.19-b and c). Conversely, the *P1* layout follows a herringbone pattern that creates physical *interlocking* between the plywood sheets (see Figure 4.19-a). All plywood sheathing considered for the analyses was 9 mm thick.

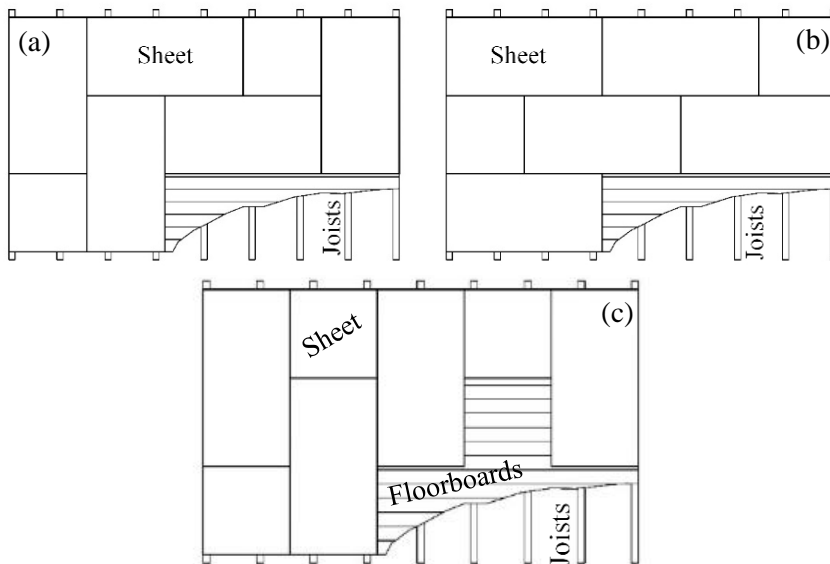


Figure 4.19: Plywood sheet layouts: a) *P1* layout; b) *P2* layout; c) *P3* layout

Diaphragm equivalent stiffness values were compared by referring to two drift ( $dr$ ) levels:  $dr_1 = 0.165\%$  and  $dr_2 = 0.500\%$ . Drift level  $dr_1$  was compatible with the yield

displacement values reported in ABK (1981), while  $dr_2$  was considered as the largest deformation level reached by all numerical analyses. For some configurations, due to model numerical convergence issues (caused by a large number of fasteners approaching maximum deformation capacity), the analysis stopped at deformation levels not representative of the actual ultimate diaphragm conditions. Up to 0.50% drift level, maximum stresses in timber elements and plywood sheets were observed to be well below the material strength limits. Due to the selected fastener spacing and the use of screws or threaded nails being adopted in the analyses herein, in-plane plywood sheet buckling was effectively inhibited.

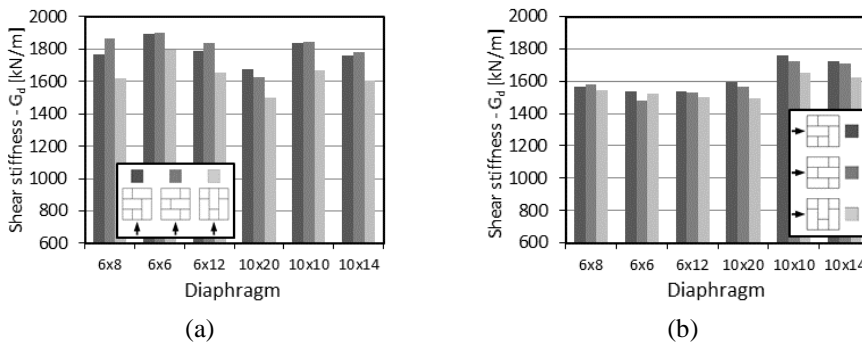


Figure 4.20: Stiffness comparisons for different plywood sheet dispositions,  $dr=0.165\%$ : a) Loading parallel to joists; b) Loading perpendicular to joists

At small displacements ( $dr = 0.165\%$ ), both  $P1$  and  $P2$  layouts appeared to be stiffer than  $P3$ , with such trend being more pronounced in the loading direction parallel to the joists (Figure 4.20). As visible from Figure 4.21, at a 0.5% drift level, the solution with the sheets oriented parallel to the loading direction (i.e.  $P3$  for loading parallel to the joists and  $P2$  for loading perpendicular to the joists) exhibited the smallest stiffness value for all of diaphragm geometries. These observations are attributed to predominance of the shear type diaphragm response. In most cases,  $P1$  sheet disposition showed the highest stiffness values for both loading directions, resulting in the most effective solution when both diaphragm loading directions are considered.

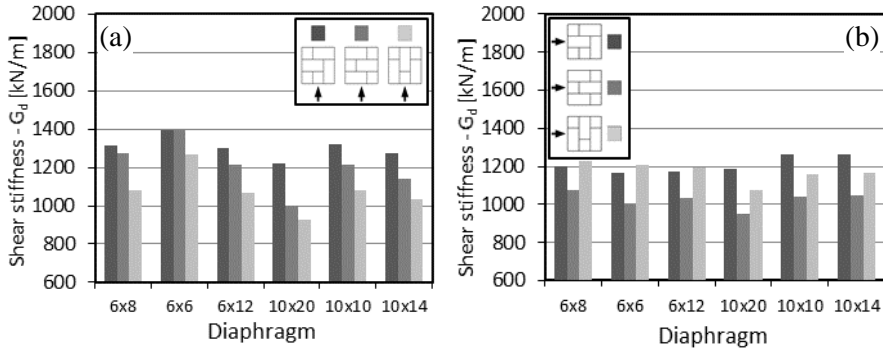


Figure 4.21: Diaphragm stiffness comparisons for different plywood sheet dispositions,  $dr=0.50\%$ : a) Loading parallel to joists; b) Loading perpendicular to joists

#### 4.5.2 SHEET-TO-SHEET CONTACT INFLUENCE

In order to establish the influence of inter-panel contact, gap links between plywood elements were removed allowing for the sheets to overlap. The sheet-to-sheet contact influence is reported in Figure 4.22 in terms of percentage stiffness variation with respect to the condition where the sheet-to-sheet contact is neglected.

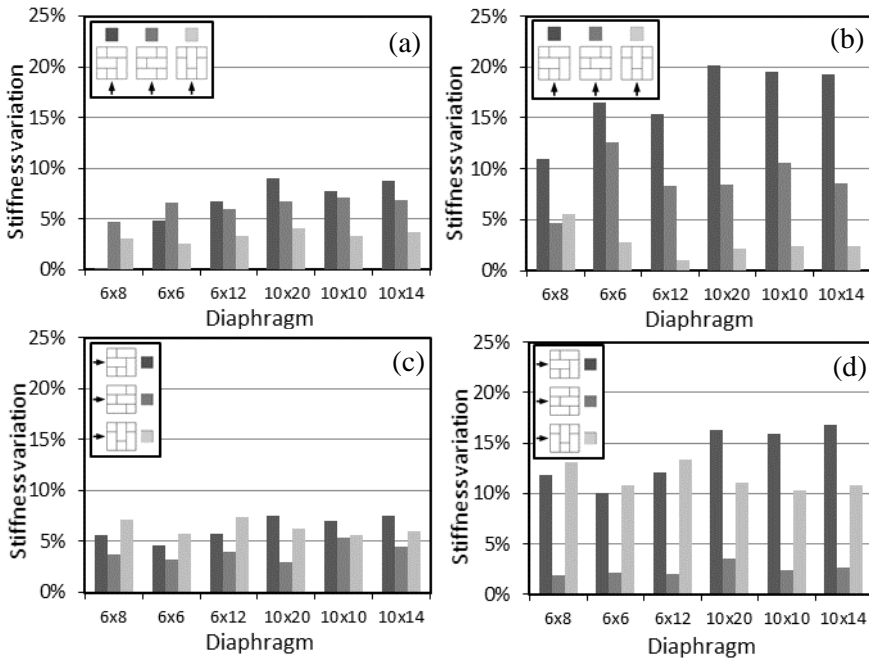


Figure 4.22: Sheet-to-sheet contact stiffening effect: a) Loading parallel to the joists,  $dr=0.165\%$ ; b) Loading parallel to the joists,  $dr=0.50\%$ ; c) Loading perpendicular to the joists,  $dr=0.165\%$ ; Loading perpendicular to the joists,  $dr=0.50\%$

As expected, the results showed the contact stiffening effect being more pronounced for the *PI* layout at relatively large deformations. These results are consistent with the trend previously observed for the sheet disposition having a greater influence at  $d_r = 0.5\%$ .

### 4.5.3 PLYWOOD SHEET THICKNESS INFLUENCE

The influence of the plywood sheet thickness on the diaphragm response was investigated by considering the representative thickness values reported in Table 4.6. The effect of a varied sheet thickness on the plywood-to-solid wood connection response was accounted for by modifying the connection curve according to the aforementioned analytical formulations. All diaphragm layouts reported in Table 4.4 were analyzed with varying plywood thickness for each sheet disposition in both loading directions.

*Table 4.6: Plywood sheet thickness range*

Lower bound [mm]	Mean value [mm]	Upper bound [mm]
9	15	21

Within the selected plywood thickness range, the relation between the plywood thickness and the diaphragm equivalent shear stiffness was observed to be approximately linear with a coefficient of determination  $R^2$  being greater than 0.97, (see Figure 4.23, where the diaphragm stiffness  $G_d$  is normalized to the reference stiffness value corresponding to a plywood thickness of 15 mm ( $G_{d,15}$ )).

Table 4.7 and Table 4.8 show the diaphragm stiffness variation per millimeter of plywood thickness increase (also see Figure 4.23). With increasing displacements, the deformation tends to concentrate in the connections and the plywood sheet stiffness (and consequently thickness) becomes less relevant. This deformation concentration is partially influenced by the lateral loading being applied at the diaphragm joists. Based on the attained results, an average of 2% per millimeter of plywood thickness could be adopted as reference value up to a drift level of 0.5% for sheets ranging in thickness between 9 mm and 21 mm.

*Table 4.7: Diaphragm stiffness variation due to a 1 mm plywood thickness increment,  $dr = 0.165\%$*

Lower bound [mm <sup>-1</sup> ]	Mean value [mm <sup>-1</sup> ]	Upper bound [mm <sup>-1</sup> ]
2.1%	2.5%	3.0%

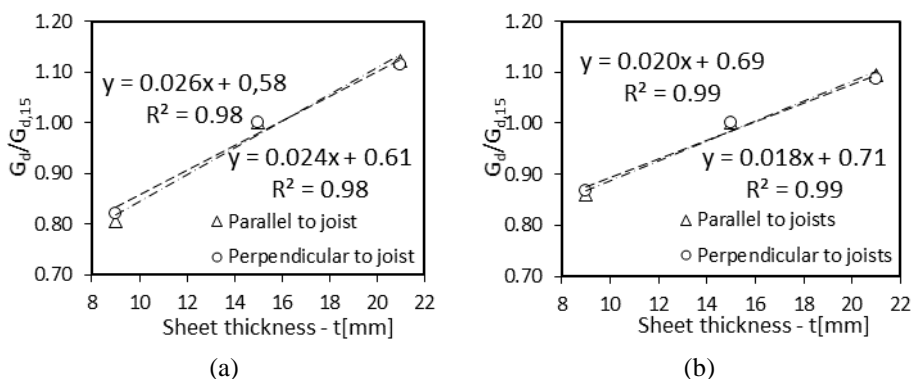


Figure 4.23: Typical results showing the influence of the plywood thickness over the diaphragm stiffness: a) Diaphragm 6x8 P1 |  $dr = 0.165\%$ ; b) Diaphragm 6x8 P1 |  $dr = 0.5\%$

Table 4.8: Diaphragm stiffness variation due to a 1 mm plywood thickness increment,  $dr = 0.50\%$

Lower bound [mm <sup>-1</sup> ]	Mean value [mm <sup>-1</sup> ]	Upper bound [mm <sup>-1</sup> ]
1.4%	1.8%	2.4%

#### 4.5.4 PLYWOOD-TO-SOLIDWOOD CONNECTION INFLUENCE

The influence of plywood-to-solid wood fastener spacing and type on the diaphragm response was investigated. The subsequent analysis results are reported in terms of equivalent stiffness ratios  $G_d/G_{d,ref}$  where  $G_{d,ref}$  is the reference stiffness value corresponding to a *E150\_F300* fixing pattern that is characterized by fasteners spaced at 150 mm at the sheet edges (*E150*) and field fasteners fixed at  $300 \times 300$  mm grid (*F300*). The numerical simulations were performed considering a 9 mm thick plywood sheathing. The  $G_d/G_{d,ref}$  ratios trends resulting from changes in the fastener fixing pattern were found to be sensitive to the diaphragm geometry, the sheet disposition and the loading direction. Representative values obtained from two fixing patterns are summarised in Table 4.9, where # is the ratio between the reference edge spacing (i.e. *E150*) and the edge spacing of the fixing pattern being evaluated. The relation between the edge spacing  $E$  and the field grid  $F$  was assumed as constant and equal to  $E/F = 0.5$ . The influence of fastener type was evaluated by adopting the experimentally-derived backbone curves for screwed plywood-to-solidwood connections provided by Schiro et al. (2018). Such curves were assigned to the fasteners in the “*field regions*” and at the sheet edges, while properties of the fasteners at the diaphragm perimeter were not modified. Consistently with the specimens tested by Schiro et al. (2018), a 9 mm thick

plywood sheathing was considered with a reference *E150\_F300* fixing pattern being adopted. Results in terms of  $G_{d,screws}/G_{d,nails}$  stiffness ratios ranged between 1.19 and 1.33 with a mean value equal to 1.25. No clear correlation trends linking the values of such increase range to either the scale factor or the aspect ratio or the loading direction or the sheet disposition were observed.

Table 4.9: Influence of the fixing pattern: representative values of stiffness ratios  $G_d/G_{d,ref}$

Pattern	#	dr = 0.165%			dr = 0.50%		
		Lower	Mean	Upper	Lower	Mean	Upper
E100_F200	1.50	1.14	1.18	1.26	1.24	1.29	1.39
E200_F400	0.75	0.75	0.84	0.92	0.63	0.77	0.90

#### 4.5.5 OBSERVATIONS ON DIAPHRAGM LATERAL CAPACITY

Figure 4.24 gives the capacity curves obtained for the diaphragm geometries reported in Table 4.4. In order to provide an insight on the “lower bound” capacity of the diaphragms retrofitted with plywood overlays, a plywood thickness of 9 mm was assumed. Nonlinear hinges were assigned to the floorboards and joists as described in Chapter 3, while a Rankine failure surface (with perfect plasticity condition) was employed to capture the plywood sheet post-elastic response. To facilitate the comparison, the diaphragm responses are reported in terms of unit shear  $v$  ( $v$  is  $0.5 \times$  total load on the diaphragm / diaphragm dimension parallel to the loading direction) versus drift  $dr$ .

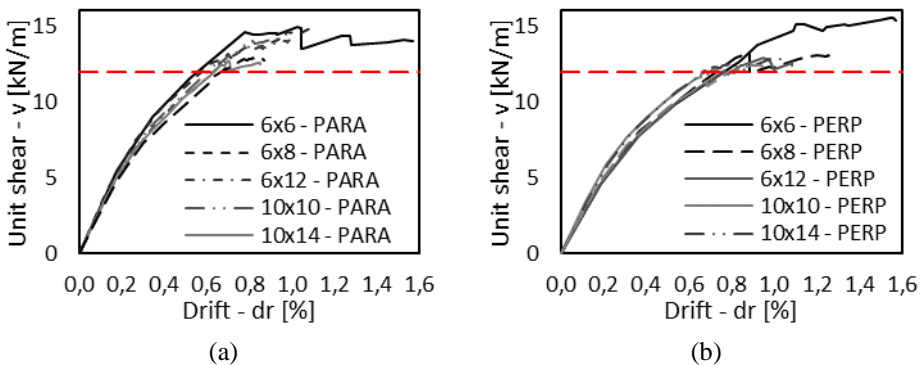


Figure 4.24: Capacity curves for diaphragms with 9 mm thick plywood sheets arranged consistently with the P1 configuration: a) Loading parallel to the joists; b) Loading perpendicular to the joists

As visible from the graphs, all diaphragm geometries exhibited a unit shear strength  $\geq 12$  kN/m, consistent with the experimental evidence reported herein. Up to the maximum force level reached by the analyses, no hinge activation was observed in the floorboards and joists, with the sheet strain level being well within the elastic range, with few limited exceptions at the sheet corners.

#### 4.5.6 OBSERVATIONS ON TRADITIONAL WOODEN FLOORS TYPICAL OF MEDITERRANEAN COUNTRIES

Analysis results presented in the previous paragraphs refer to slender joist (*SL*) diaphragm constructions, typical of North America, Northern Europe and Oceania. In Mediterranean countries, traditional timber floors typically have squatter joist cross-sections (*SQ*) but consistent joist spacing (ranging between 400 to 600 mm). As outlined in Chapter 3, the in-plane response of as-built diaphragms in the direction perpendicular to the joists is strongly affected by the joist flexural rigidity. This results in diaphragms with *SQ* joists being significantly stiffer than diaphragms with *SL* joists. To investigate the influence of such aspect on floors strengthened with a plywood overlay, further analyses were carried out on the diaphragm geometries listed in Table 4.4 by considering 9-mm plywood sheets arranged according to the *PI* scheme and the *E150\_F300* fixing pattern. The joist cross-sections described in in Table 4.10 were selected as representative of *SL* joists ( $50 \times 300$  mm<sup>2</sup>) and *SQ* joists ( $150 \times 200$  mm<sup>2</sup>). The *SQ* section was defined so that the moment of inertia with respect to the strong axis  $J_1$  was consistent with that of *SL* joists.

*Table 4.10: Representative SL and SQ joist cross-sections*

Joist type	b [mm]	h [mm]	h/b [-]	$J_1$ (strong axis) x10 <sup>6</sup> [mm <sup>4</sup> ]	$J_2$ (weak axis) x10 <sup>6</sup> [mm <sup>4</sup> ]
SL	50	300	6	100	3.125
SQ	150	200	1.33	112.5	56.25

Analysis outcome is summarized in Table 4.11, where  $G_{d,SQ}$  and  $G_{d,SL}$  are the equivalent shear stiffness values referred to *SQ* and *SL* configurations respectively and  $\Delta G_d$  is equivalent shear stiffness increase associated to *SQ* joist diaphragms. Joist type influence was observed to be more relevant for short-length joists ( $\approx +26\%$  stiffness from *SL* to *SQ*) and less pronounced for long-span diaphragms ( $\approx +10\%$  stiffness from *SL* to *SQ*). Such trend can be explained by comparing the results with the shear stiffness predictions (in the direction perpendicular to the joists) obtained by considering the sole contribution of the joist bending stiffness.  $\Delta G_{d,BEND}$  values give the diaphragm stiffness increase associated to *SQ* construction type as obtained by determining the diaphragm

in-plane stiffness based on the sole contribution of the joist bending stiffness. As noticeable from Table 4.11, for all diaphragms the stiffness increase observed for *SQ* diaphragms is largely due to the higher bending stiffness of the *SQ* joists.

Table 4.11: Equivalent shear stiffness comparison, *SQ* vs. *SL* joists,  $dr=0.165\%$

Diaph. ID	$G_{d,SQ}$ [kN/m]	$G_{d,SL}$ [kN/m]	$\Delta G_d$ [kN/m]	$G_{d,SQ}/G_{d,SL}$	$\Delta G_{d,BEND}$ [kN/m]	Err.*
6x8	1994.4	1566.3	428.1	1.27	382.8	11%
6x6	1936.0	1540.5	395.5	1.26	346.1	12%
6x12	1916.4	1536.5	380.0	1.25	332.8	12%
10x20	1790.5	1598.0	192.5	1.12	117.9	39%
10x10	1911.1	1762.1	149.0	1.08	98.6	34%
10x14	1894.3	1721.2	173.0	1.10	129.2	25%

\*  $Err. = (\Delta G_d - \Delta G_{d,BEND}) / \Delta G_d$

## 4.6 ANALYSIS OF DIAPHRAGMS WITH RE-NAILED FLOORBOARD-TO-JOIST CONNECTIONS

The effect of rehabilitated floorboard-to-joist connections was evaluated by analyzing the diaphragms listed in Table 4.4 in both loading directions and making comparisons with the as-built condition. The experimental behavior of rehabilitated connections (i.e. floorboard-to-joist joints comprising 2 original nails and 2 new nails) derived from Schiro et al. (2018) was assigned to nonlinear links reproducing the floorboard-to-joist connections. Diaphragm responses were compared in terms of equivalent shear stiffness at two drift levels ( $dr = 0.25\%$  and  $dr = 3.5\%$ ). From the attained results (see Table 4.12) it was concluded that for small displacements, re-nailing had negligible effects on the global diaphragm response. At larger diaphragm displacements, the effect was observed to be more pronounced, with an average stiffness increase of 14% in the direction parallel to the joists and 18% in the direction perpendicular to the joists. Such trend partially reflects the differences between the as-built and retrofitted connections observed by Schiro et al. (2018), where at small displacements the stiffness of the retrofitted connection was dominated by the stiffness of the original (larger in size) nails.

An upper-bound scenario for re-nailed diaphragms was defined by assuming that the behavior of the strengthened connection is given by the response of the original floorboard-to-joist connection from Schiro et al. (2018) working in parallel with the response of a new floorboard-to-joist connection formed by a couple of nails such as

that reported by Wilson (2012). From the results summarized in Table 4.13, re-nailing was found to be significantly more effective with a stiffness increase > 60% at large deformation levels.

*Table 4.12: Effectiveness of the “renailing technique” |  $G_{d,RA} = G_{d,Renailed}/G_{d,as-built} =$  equivalent stiffness of renailed diaphragms over the equivalent stiffness of as-built diaphragms*

	dr = 0.25%		dr = 3.5%	
	$G_{d,0,R/A}$	$G_{d,90,R/A}$	$G_{d,0,R/A}$	$G_{d,90,R/A}$
6x8	1.00	1.00	1.10	1.13
6x6	1.01	1.00	1.04	1.15
6x12	1.00	1.00	1.16	1.15
10x20	1.00	1.03	1.24	1.26
10x10	1.00	1.00	1.14	1.19
10x14	1.00	1.00	1.18	1.19
Average	1.00	1.01	1.14	1.18

*Table 4.13: Upper bound scenario for renailed diaphragms |  $G_{d,RN}/G_{d,AS-B}$*

	dr = 0.25%		dr = 3.5%	
	$G_{d,0}$	$G_{d,90}$	$G_{d,0}$	$G_{d,90}$
6x8	1.77	2.10	1.48	1.61
6x6	1.57	2.15	1.28	1.66
6x12	2.09	2.16	1.70	1.66
10x20	2.41	2.57	1.99	1.96
10x10	2.00	2.49	1.60	1.87
10x14	2.20	2.44	1.80	1.85
Average	2.01	2.32	1.64	1.77

As expected, the effectiveness of re-nailing appeared to be strongly related to the behavior of the additional fasteners. For timber elements that are in poor condition, such intervention will likely be ineffective, particularly at small deformation levels.

## 4.7 SIMPLIFIED ANALYTICAL MODEL

Numerical results reported in previous paragraphs were implemented to calibrate a simplified procedure for predicting diaphragm in-plane stiffness.

Diaphragm stiffness in parallel-to-joists direction  $G_{d,0}$  [kN/m] can be evaluated according to equation (4.2).

$$G_{d,0} = 2000 \cdot \alpha_{th} \cdot \alpha_{sp} \quad (4.2)$$

Parameters  $\alpha_{th}$  and  $\alpha_{sp}$  account for panel thickness and connector spacing respectively and should be calculated according to equation (4.3) and equation (4.4), where:

- $t$  is panel thickness, in mm;
- $spr$  depends on edge connector spacing  $s$  [mm] and is equal to  $spr=s/150$ .

$$\alpha_{th} = 1 + 0.03 \cdot (t - 15) \quad (4.3)$$

$$\alpha_{sp} = 1.5 - 0.5 \cdot spr \quad (4.4)$$

Diaphragm stiffness in perpendicular-to-joists direction can be evaluated according to equation (4.5) where  $G_{d,0}$  is diaphragm stiffness in parallel-to-joists direction given by equation (4.2) and  $k_j$  accounts for in-plane bending stiffness of the joists and should be calculated according to equation (4.6), where  $EJ$  is joist in-plane bending stiffness and  $n_j$  is the number of joists.

$$G_{d,90} = G_{d,0} + k_j \quad (4.5)$$

$$k_j = 9.84 \cdot n_j \cdot \frac{EJ}{B \cdot L^2} \quad (4.6)$$

## 4.8 FINAL REMARKS

An in-situ experimental campaign investigating the in-plane behavior of retrofitted timber floor diaphragms undertaken on full scale specimens located in a two-storey URM building constructed circa 1913 is summarized. The diaphragm retrofit strategies included re-nailing of board-to-joist connections, use of fire-rated ceiling, use of steel chords and the application of plywood sheet overlay. The subsequent phase of the study included numerical modeling of the adopted retrofit schemes and their validation against the attained experimental results.

The re-nailed Specimen A did not show signs of softening or noticeable stiffness reduction up to the maximum mid-span displacement of the tested diaphragm. A non-negligible increase in the diaphragm stiffness if compared to as-built diaphragms was noted for all deformation levels (> 30%).

The diaphragm specimen with fire-rated ceiling exhibited a substantial stiffness decrease at approximately 45 mm of mid-span displacement that corresponded to a capacity plateau. At a mid-span displacement larger than 100 mm, detachment of the

gypsum sheets close to the diaphragm lateral edges was observed. When comparing the envelope curve from the test with the steel chords to the benchmark cycle performed before the chord application, no appreciable improvement can be noted. As expected, the single straight sheathed diaphragms appeared to exhibit overall negligible flexural behavior.

The diaphragm specimen retrofitted using plywood exhibited no strength losses between cycles to the same deformation levels, illustrating the ability of the plywood overlaid diaphragm to resist multi-cyclic loading. The stiffness increase as a result of the plywood overlay was almost tenfold at small mid-span deformation levels.

Subsequently, numerical models were implemented and successfully validated using experimental data for sheet overlaid and chord retrofitted timber floor diaphragms using monotonic non-linear static (pushover) analyses in finite element software SAP2000. Sheet disposition layouts forming parallel-to-loading continuous slip joints were observed to be incapable to draw from the stiffening effect related to sheet-to-sheet contact forces. Conversely, the herringbone pattern resulting in physical interlocking between sheathing elements was found to be the most effective, especially if diaphragm response in both the in-plane loading directions is considered. Contact forces between adjacent sheets were found to produce, in general, non-negligible effects on overall diaphragm behavior, especially for greater displacement amplitudes and for the herringbone sheathing layout. Within commercial plywood sheet thickness ranging from 9 to 21 mm the in-plane stiffness ratio vs. panel thickness relations were found to be, to a good approximation, linear and consistent among the selected specimens. An average 2% stiffness increment per millimeter in sheet thickness was observed. The influence of plywood-to-solid wood connection on diaphragm behavior (in terms of both connector type and connector spacing) was found to be greater for greater displacements and to produce stiffness increments that are smaller than the increment in the number of connectors. Analyses were extended to Mediterranean-style squat-joint diaphragm construction. Consistently with results obtained in Chapter 3, the higher in-plane stiffness of squatter joist elements led to a diaphragm in-plane shear stiffness increment for loads applied in perpendicular-to-joists direction, while no significant differences were observed for the other loading direction. For the selected joist geometries, squat joist construction over slender joist construction stiffness ratios ranged between 10% to 30%, depending essentially on joist length.

From experimental data in literature, including the results of the experimental campaign reported herein, chord contribution on diaphragm in-plane behavior is not clear. Numerical analyses on chorded diaphragms provided results that are consistent with those obtained in the experimental campaign presented in this Chapter. Chord elements

---

were observed to exhibit a beam behavior instead of acting as tie-beams. Anyway, the use of steel chords can be an effective strategy for the improvement of diaphragm-to-wall connections and to provide a confinement effect in the masonry, improving the spandrel rocking capacity. Numerical analyses showed that re-nailing of floorboard-to-joist connections can be effective in increasing diaphragm in-plane stiffness. In the ideal case scenario re-nailed units exhibited twice the in-plane stiffness compared to the as-built configuration. On the other hand, the effectiveness of such intervention is strictly related to the conservation state of timber elements, and in the case of poor element conditions it can result in no significant improvements, therefore the adoption of such technique must be carefully evaluated.

**NOTE:** Research outcomes presented in this Chapter have been published in:

Rizzi E., Giongo I., Ingham J. M., Dizhur D. (2019). “Testing and modeling of retrofitted diaphragms loaded in-plane”, *ASCE Journal of Structural Engineering*, vol. 146(2) DOI: 10.1061/(ASCE)ST.1943-541X.0002473.

## 4.9 REFERENCES

- Agbabian, M. S., Barnes, S. B. and Kariotis, J. C. (ABK) (1981). “Methodology for mitigation of seismic hazards in existing unreinforced masonry buildings. Diaphragm testing.” National Science Foundation. El Segundo, California.
- ASCE (American Society of Civil Engineers). (2017). “Seismic Evaluation and Retrofit of Existing Buildings” *ASCE 41-17*, Reston, Virginia.
- AS/NZS (Australian/New Zealand Standard). (2008). «Structural Plywood», AS/NZS 2269:2008.
- Applied Technology Council (ATC). (1981). «Guidelines for the design of horizontal wood diaphragms». Berkeley, California
- Baldessari, C., Piazza, M. and Tomasi, R. (2009). “The refurbishment of timber floors: characterization of the in-plane behavior” Proceedings, PROHITEC International Conference, Taylor and Francis, Rome, Italy, 2009.
- Beyer K, Dazio A., (2012). «Quasi-static cyclic tests on masonry spandrels». *Earthquake Spectra* vol. 28, n. 3, pp. 907–29.
- Brignola, A., Pampanin, S. and Podestà, S. (2012). “Experimental Evaluation of the In-Plane Stiffness of Timber Diaphragms”. *Earthquake Spectra*, vol. 28, n. 4, pp. 1687-1709.
- CBI (Co-ordinated Building Information). (2012). «GIB Fire Rated Systems» Appraisal No. 289. CBI 5113.
- CEN (European Committee for Standardization) (2009). “Structural timber - Strength classes”. *EN 338*. Brussels, Belgium.
- CSI (Computers and Structures Inc.). (2014). “CSI Analysis Reference Manual, SAP2000 v17”. Berkeley, California.
- Dizhur, D., Ingham, J. M., Moon, L., Griffith, M. Schultz, A., Senaldi, I., Magenes, G., Dickie, J., Lissel, S., Centeno, J., Ventura, C., Leite, J. C., Lourenco, P. B. (2011). «Performance of masonry buildings and churches in the 22 February 2011 Christchurch earthquake». *Bull. N. Z. Soc. Earthquake Eng.* 44 (4): 279–296.
- Dizhur, D., Ingham, J. M., Biggs, D. and Schultz, A. (2016). “Performance of unreinforced masonry and infilled RC buildings during the 2015 Gorkha, Nepal earthquake sequence”. Proceedings, 16th International Brick and Block Masonry Conference, IBMAC 2016, pp 2399-2408.

---

Dogliani, F., (2000). «Handbook (guidelines) for the design of adjustment interventions, seismic strengthening, and renewal of architectural treasures damaged during the Umbria-Marche earthquake in 1997», Official Bulletin of Marche Region, Ancona (in Italian).

Giongo, I., Dizhur, D., Tomasi, R. and Ingham, J. M. (2015). “Field testing of flexible timber diaphragms in an existing vintage URM building”. *Journal of Structural Engineering*, vol. 141, 2015.

Giongo, I., Rizzi E., Ingham, J. M., Dizhur, D. (2018). «Numerical modeling of in-plane behavior of straight sheathed timber diaphragms», *ASCE Journal of Structural Engineering*, vol. 144(10), ISSN: 0733-9445, doi:10.1061/(ASCE)ST.1943-541X.0002148.

Hsiao, J. K., Tezcan, J., (2012), *Seismic Retrofitting for Chord Reinforcement for Unreinforced Masonry Historic Buildings with Flexible Diaphragms*, Practice Periodical on Structural Design and Construction, ASCE, Vol. 17, No. 3, pp. 102-109.

Manie, J., and Kikstra, W. P., (Editors), (2014). "DIANA – Finite Element Analysis. User’s Manual release 9.5" Published by TNO DIANA BV, Delftechpark 19a, 2628 XJ Delft, The Netherlands.

McLain, T. E., (1975). «Curvilinear load-slip relations in laterally-loaded nailed joints», PhD thesis, Colorado state University, Colorado.

NZS (Standards New Zealand). 1993. Timber structures standard. NZS3603:1993. Wellington, New Zealand: NZS.

Pellicane, P. J., Stone, J. L., Vanderbilt, M. D., (1991). «Generalized Model for Lateral Load Slip of nailed Joints», *Journal of Materials in Civil Engineering*, ASCE, Vol. 3, No. 1.

Peralta, D. F., Bracci, J. M., and M. B. Hueste, (2003). «Seismic Performance of Rehabilitated Wood Diaphragms», Texas A&M University, Department of Civil Engineering.

Rinaldin G., Amadio C., Gattesco N., (2017). «Review of experimental cyclic tests on unreinforced and strengthened masonry spandrels and numerical modeling of their cyclic», *Engineering Structures*, vol. 132, pp. 609-623.

Schiro, G., Giongo, I., Ingham, J., Dizhur, D., (2018). «Lateral performance of as-built and retrofitted timber diaphragm fastener connections», *Journal of Materials in Civil Engineering*, vol. 30 (1), ISSN: 0899-1561, [https://doi.org/10.1061/\(ASCE\)MT.1943-5533.0002110](https://doi.org/10.1061/(ASCE)MT.1943-5533.0002110).

Wilkinson, T. L., (1971). «Theoretical lateral resistance of nailed joints», *Journal of the Structural Division. Proceedings of the American Society of Civil Engineers*.

Wilson, A. W., (2012). «Seismic assessment of timber floor diaphragms in unreinforced masonry buildings», Doctoral dissertation, The University of Auckland, New Zealand.

Wilson, A., P. J. H. Quenneville, and J. M. Ingham., (2014). «In-plane orthotropic behavior of timber floor diaphragms in unreinforced masonry buildings.» *J. Struct. Eng.* 140 (1): 04013038. [https://doi.org/10.1061/\(ASCE\)ST.1943-541X.000081](https://doi.org/10.1061/(ASCE)ST.1943-541X.000081)

# 5 MODELING OF TIMBER DIAPHRAGMS RETROFITTED WITH DIAGONAL SHEATHING OVERLAY

## 5.1 INTRODUCTION

Research presented in this chapter was focused on the numerical study of the in-plane behavior of wooden floors retrofitted by means of an additional layer of floorboards oriented at 45 degrees with respect to diaphragm principal directions.

## 5.2 MODELING APPROACHES

The work presented in the following was based on the two modeling approaches presented in Chapter 3, namely M1 model and M2 model.

### 5.2.1 M1 MODELING APPROACH

Refined M1 model based on the software package TNO DIANA [Maine and Kikstra (2014)] was used to provide reliable data for the validation process of the simplified M2 model, developed by means of the software package SAP2000 [CSI (2014)]. M2 model was then implemented for the parametric study. The use of M2 approach facilitates the analysis process allowing to analyze the influence of a wider range of parameters. In addition, being SAP2000 a software package well-known to practitioners, modeling details/issues described herein may prove useful also for non-academic purposes.

M1 model featured linear-elastic *frame* elements representing joists while *curved shell* elements and linear elastic orthotropic material properties were adopted for flooring elements of both straight and diagonal floorboard layers. Floorboard interruptions were included in the model by assigning each floorboard to a separate mesh set. *Line interface*

elements, characterized by *no-tension behavior* (zero stiffness in traction, rigid in compression), were generated at floorboard free edges. *Point interface* elements were implemented to reproduce nailed connections, whose load-slip response was considered as uncoupled for the two principal directions (i.e. parallel and perpendicular to grain of timber elements). Multiple shear plane fasteners (e.g. nails driven from the retrofit layer to the joists and passing through the original sheathing) were modeled by introducing a point interface element at each shear plane.

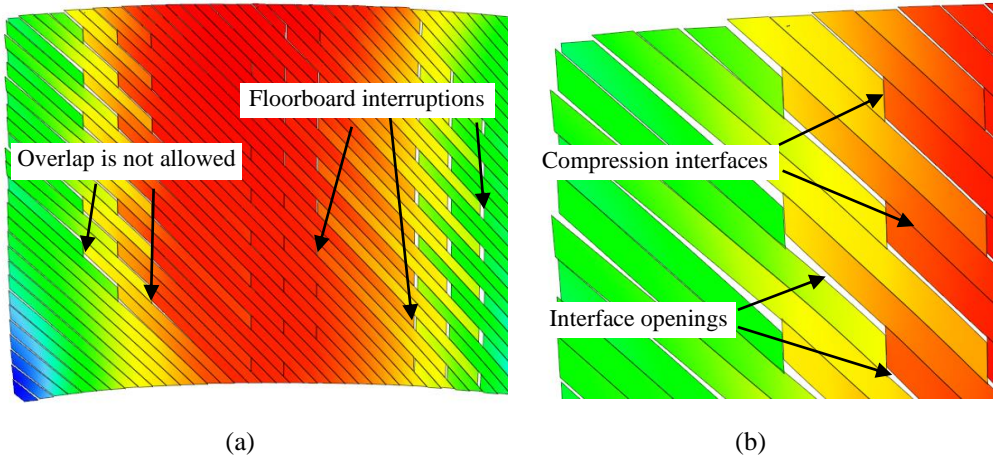


Figure 5.1: M1 model details, deformed shapes: a) Overall deformed shape; b) Diaphragm corner close-up

### 5.2.2 M2 MODELING APPROACH

In M2 model additional floorboards were modeled as linear elastic orthotropic *frame* elements, while linear elastic isotropic *frame* elements were used to represent steel chords. Staggered floorboard layout was reproduced by physically dividing the frame elements. For both straight and diagonal sheathings, contact phenomenon was accounted for by interposing nonlinear *gap-links* between adjacent floorboards and oriented perpendicularly to them. Nailed connections were modeled by means of *non-linear links* with *multilinear elastic* behavior. Due to the uncoupled response of multilinear elastic links, the same backbone curve was assigned to each of the principal shear directions ( $U2$  and  $U3$  Degrees of Freedom, DoFs). Flexural DoFs  $R2$ ,  $R3$  and  $U1$  were fully restrained, while  $R1$  (torsional) DoF was set free. As for M1, nails passing through multiple shear planes were modeled by means of a connector (*multi-linear elastic link*) per each shear plane. Eccentricities between fasteners and floorboard axes were reproduced by means of rigid links (6 DoFs fully restrained) connecting the *multi-linear links* to the *frame* element representing the floorboards (see Figure 5.2).

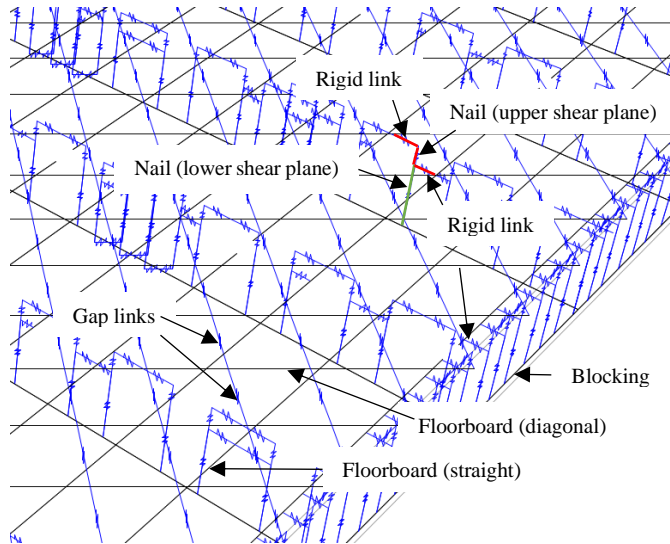


Figure 5.2: M2 model details, for clarity some elements are omitted from view

### 5.2.3 FINITE ELEMENT MODEL VALIDATION

Experimental tests that are available in literature on single diagonal sheathed diaphragms and single straight sheathed diaphragms retrofitted with diagonal board overlay were considered for the validation of each modeling approach (Table 5.1). Specimens “Diaphragm I” and “5x4” were reproduced by means of M1 approach (see Table 5.1). Geometrical and mechanical properties of the components were set consistently with the experimental data reported in [ABK (1981) and Baldessari et al. (2009)]. When available, experimental backbone curves were assigned to the multilinear elastic links representing nailed connections. In case that the experimental curves were not available, the McLain theory [McLain (1975)] as improved by Pellicane et al. (1991) was implemented by considering the actual characteristics of both timber elements and fasteners. Validation results are summarized in Figure 5.3. In each case, comparisons between experimental data and model outputs were found to be satisfactory.

Regarding M2 model, “Diaphragm I”, “5 × 4”, “Wall 1”, “Wall 2” and “6 × 6” specimens were reproduced in the validation phase (see Table 5.1). As for M1, element geometrical properties were set in accordance with the test reports, while mechanical properties of timber were selected according to the wood species as recommended by EN338:2009 [CEN (2009)].

Table 5.1: Model validation process – reference diaphragm specimens

Reference	Specimen ID	Construction type	Load direction
ABK (1981)	Diaphragm I	Single diagonal	Parallel to joists
Baldessari et al. (2009)	5 × 4	Straight + diagonal	Parallel to joists
Ni et al. (2007)	Wall 1	Single diagonal*	---
Ni et al. (2007)	Wall 2	Single diagonal*	---
---	6 × 6	Straight + diagonal **	Parallel to joists

\*Shear wall specimens

\*\*Diaphragm used for the parametric analyses

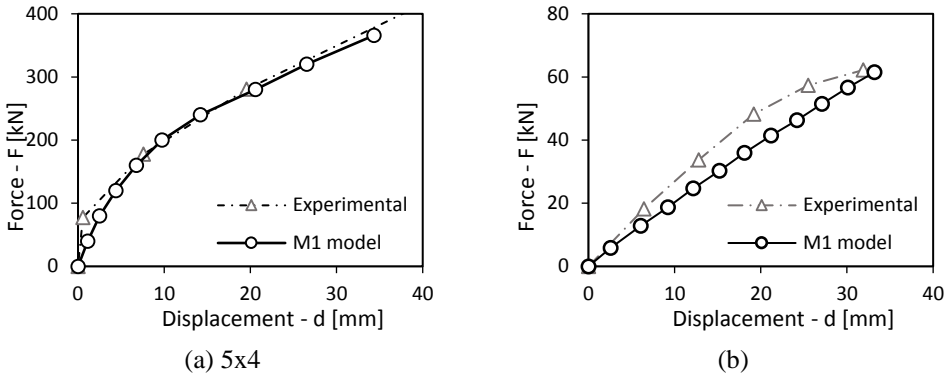


Figure 5.3: M1 model validation: a) 5 × 4; b) Diaphragm I

If available, experimental backbone curves were assigned to *multilinear elastic links* representing nailed connections. If not, the McLain and Pellicane theory was used, as for the M1 modeling approach. In the case of the 6 × 6 diaphragm, the same geometrical and material properties inputs were assigned to both M1 and M2 models. As highlighted in Table 5.4, M2 model outputs were found to be consistent with experimental data and M1 model predictions for 6 × 6 diaphragm.

### 5.3 PARAMETRIC ANALYSES

A series of non-linear static analyses were carried out on a diaphragm selection considered as representative of the European building heritage. Analyzed floors are listed in Table 5.2, where  $L$  refers to joist length,  $B$  is diaphragm dimension in the other direction and  $\alpha=L/B$  is aspect ratio. Diaphragm penetrations were not considered. Geometrical and mechanical properties listed in Table 5.3 were adopted for the components of every floor. The structural layout shown in Figure 5.5 was assumed. Floorboards of the straight sheathing were connected to the joists by means of a nail couple at each floorboard to joist intersection.

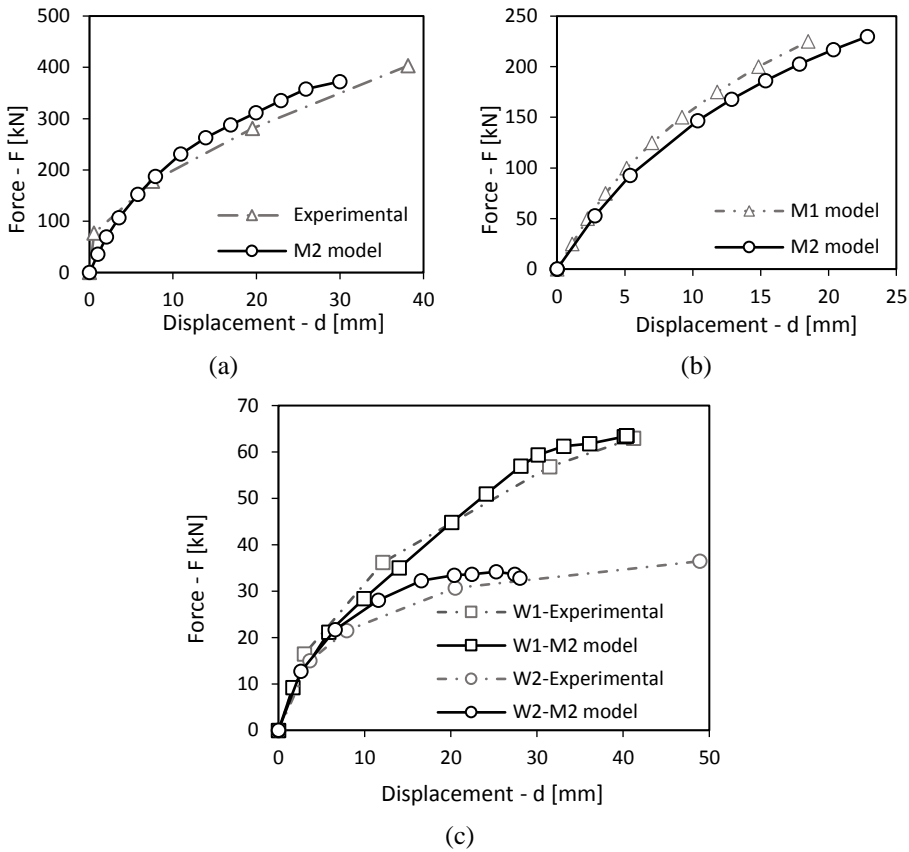


Figure 5.4: M2 model validation: a) 5x4 specimen; b) 6x6 diaphragm, diagonal sheathing over straight sheathing; c) W1 & W2 Walls

Diagonal boards were connected to the underlying joists (through the straight sheathing) by means of a nail couple at each intermediate support, while three nails were used at floorboard end supports. Timber blocking elements were interposed between joists at diaphragm ends. Blocking-to-joist connection was modeled as pinned ( $R2$  and  $R3$  DoFs fully released). Tension stiffness of the joist to blocking element connection was assumed equal to 500 N/mm. Such low stiffness was intended to reproduce the poor behavior expected from in-situ connections. Additional nailing was provided at diaphragm perimeter, connecting each diagonal floorboard to the joist or blocking element below (for the parallel and perpendicular to joists directions respectively). Restraints were assigned at joists level. Global beam-like rotation of diaphragm side ends was allowed. Diaphragm ends perpendicular to the loading direction were restrained in the out of plane direction only.

*Table 5.2: Selected diaphragm geometries*

Diaphragm ID	L [m]	B [m]	$\alpha$
4x4	4	4	1
4x8	4	8	0.5
6x6	6	6	1
6x12	6	12	0.5

*Table 5.3: Common features of FEM models*

Feature	Value
Floorboard section	150 x 20 mm
Joist section	150 x 200 mm
Wood grade	C 24*
Joist spacing	500 mm
Nail couple spacing (diagonal)	130 mm
Nail couple spacing (straight)	100 mm
Seismic mass on diaphragms	230 kg/m <sup>2</sup>
Seismic mass of masonry	2200 kg/m

\*Timber grade according to EN338 [CEN (2009)]

For parallel to joists analyses forces were applied at joist ends and displacements were monitored with reference to the end section of the joist positioned at the diaphragm mid-span. For perpendicular to joists analyses, loads were applied to the side joist and axially rigid rods were added in order to distribute the forces among joists. Displacements were monitored with reference to the mid-span of the side joist. Parabolic load distributions were applied for each load direction, as suggested by ASCE 41-17 [ASCE (2017)]. Experimental backbone curve derived by Schiro et al. (2018) was assigned to each principal shear direction of the non-linear links in order to reproduce an existing connection behavior. Further analyses were carried out by considering different curves (details are discussed in 5.4.2).

## **5.4 ANALYSES RESULTS**

Non-linear static analyses were carried out on diaphragm specimens listed in Table 5.2 by considering both the as-built (single straight sheathing) and the retrofitted configurations (diagonal sheathing overlay over straight sheathing). It was assumed that diaphragms behave as shear beams under parabolic loading (shear deformation only). Thus, results were compared in terms of equivalent shear stiffness values  $G_d$  which,

because of the hypotheses, were evaluated via equation (5.1). It is worth noting that the  $G_d$  values represent the equivalent stiffness of the structural assembly and do not correspond to any specific material property. Analysis results were compared for different levels of the in-plane drift  $dr$ , defined by means of equation (5.2).

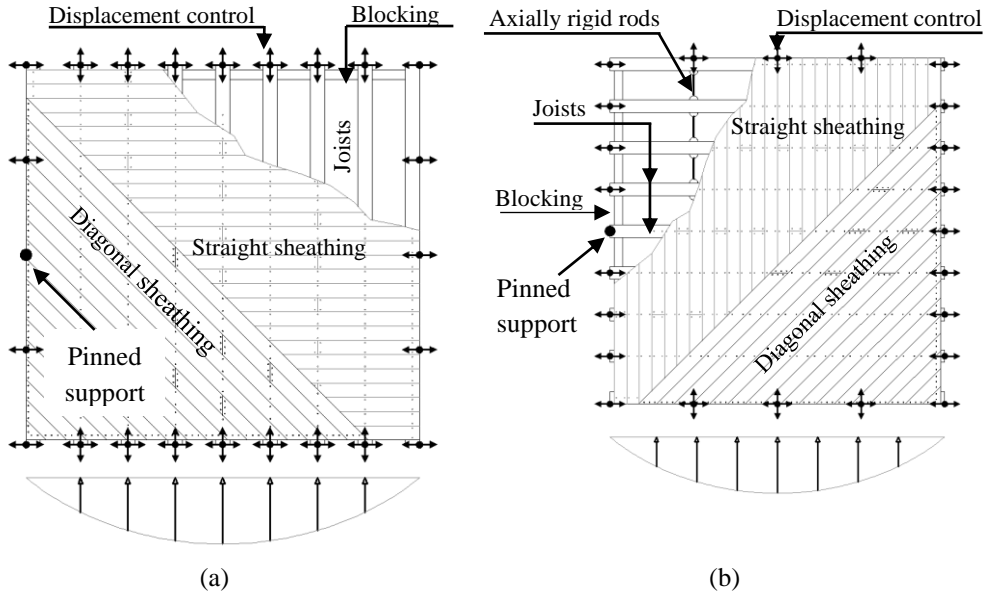


Figure 5.5: Boundary conditions and load profiles: a) Parallel to joists; b) Perpendicular to joists. Arrows represents translational DoFs at the restrained joints

$$G_d = \frac{5 \cdot F \cdot s}{32 \cdot w \cdot \delta} \quad (5.1)$$

$$dr[\%] = 2 \cdot \frac{\delta}{s} (\cdot 100) \quad (5.2)$$

Where:

- $F$  is the total load on the diaphragm;
- $w$  and  $s$  are, respectively, the diaphragm width and the diaphragm span with respect to the loading direction;
- $\delta$  is the diaphragm mid-span displacement under load  $F$ ;

Because no yield points could be clearly identified on the diaphragm backbone curves, it was decided to compare the results by referring to a 0.25% drift value, which is representative of the initial deformation stage.

#### 5.4.1 EFFECTIVENESS OF DIAGONAL SHEATHING OVERLAY

The effectiveness of diagonal sheathing overlays was investigated by comparing equivalent stiffness values of retrofitted units  $G_{d,RF}$  with the ones of as-built diaphragms in the single straight sheathing configuration  $G_{d,AsB}$ . Results, obtained at a 0.25% drift level, are listed in Table 5.4.

Table 5.4: Equivalent stiffness comparison,  $dr = 0.25\%$ , values in kN/m: a) Parallel to joists; b) Perpendicular to joists

	4x4	4x8	6x6	6x12		4x4	4x8	6x6	6x12
$G_{d,AsB}$	224.0	96.4	131.4	63.9	$G_{d,AsB}$	860.5	812.1	403.5	371.1
$G_{d,RF}$	2055.9	2350.2	2446.3	2357.5	$G_{d,RF}$	2616.3	2752.3	2513.3	2627.5
<b>Ratio</b>	<b>9.2</b>	<b>24.4</b>	<b>18.6</b>	<b>36.9</b>	<b>Ratio</b>	<b>3.0</b>	<b>3.4</b>	<b>6.2</b>	<b>7.1</b>

(a)

(b)

It is evident that in each case the retrofit led to an effective stiffness increment. In addition, stiffness values of retrofitted units do not seem to be significantly influenced by diaphragm geometry (e.g. aspect ratio  $\alpha$  and scale factor  $L$ ). Furthermore, retrofitted diaphragms were found to exhibit a substantially isotropic response, while as-built units were characterized by a marked orthotropy. In Table 5.5 ratios between equivalent shear stiffness in perpendicular to joists  $G_{d,90}$  and parallel to joists  $G_{d,0}$  directions are reported.

#### 5.4.2 INFLUENCE OF CONNECTION BACKBONE CURVES

Results summarized in Table 5.4 were obtained by referring to the response of existing nailed connections for all the fasteners. This assumption may lead to stiffness underestimation in cases where existing timber elements are in a good state of preservation. In such a scenario, newly inserted nails would not be affected by timber degradation, responding similarly to new connections. Therefore, further analyses were carried out by modeling the response of newly inserted nails by using different backbone curves. It was decided to adopt the experimental data obtained by Wilson for the New-USA connection specimens [Wilson (2012)], being the mechanical and geometrical features of tested specimens consistent with those adopted for the models (in terms of both timber density, component thickness and type of fasteners).

Table 5.5: Orthotropy ratios  $G_{d,90}/G_{d,0}$ ,  $dr = 0.25\%$

	As-built	Retrofitted
4x4	3.84	1.27
4x8	8.42	1.17
6x6	3.07	1.03
6x12	5.80	1.11

Backbone curves thus determined were then assigned to new nails only, while existing connection (straight sheathing to joists) behavior was not modified. Results summarized in Table 5.6 highlight the influence of such aspect on diaphragm equivalent shear stiffness in terms of ratios between new and vintage nail response assumptions. An average 37% stiffness increase was observed.

Table 5.6: Equivalent shear stiffness ratios, new connections/vintage connections

	$G_{d,0}$	$G_{d,90}$
4x4	1.42	1.36
4x8	1.37	1.38
6x6	1.40	1.38
6x12	1.29	1.33

## 5.5 CONCLUSIONS

The effectiveness of a retrofit intervention based on the use of a layer of floorboards laid diagonally over the existing sheathing and nailed to the sub-structure was investigated by means of a series of non-linear static analyses. Two alternative modeling strategies were proposed and validated against a selection of experimental results found in literature. In-plane stiffness of the retrofitted diaphragms was observed to be significantly higher compared to as-built configuration and the influence of nailed connection behavior was found to be non-negligible.

**NOTE:** Research outcomes presented in this Chapter have been published in:

Rizzi E., Capovilla M., Giongo I., Piazza M. “Numerical study on the in-plane behaviour of existing timber diaphragms strengthened with diagonal sheathing”, proceedings of the 4th International Conference of Structural Health Assessment of Timber Structures, SHATIS’17, 20-22 September 2017, Istanbul, Turkey.

---

## 5.6 REFERENCES

- Agbabian, M. S., Barnes, S. B. and Kariotis, J. C. (ABK) (1981). "Methodology for mitigation of seismic hazards in existing unreinforced masonry buildings. Diaphragm testing." National Science Foundation. El Segundo, California.
- ASCE (American Society of Civil Engineers). (2017). "Seismic Evaluation and Retrofit of Existing Buildings" *ASCE 41-17*, Reston, Virginia.
- Baldessari, C., Piazza, M. and Tomasi, R. (2009). "The refurbishment of timber floors: characterization of the in-plane behavior" Proceedings, PROHITEC International Conference, Taylor and Francis, Rome, Italy, 2009.
- CEN (European Committee for Standardization) (2009). "Structural timber - Strength classes". *EN 338*. Brussels, Belgium.
- CSI (Computers and Structures Inc.). (2014). "CSI Analysis Reference Manual, SAP2000 v17". Berkeley, California.
- Manie, J., and Kikstra, W. P., eds. (2014). DIANA—Finite element analysis. User's manual release 9.5. Delft, Netherlands: TNO DIANA BV.
- McLain, T. E., (1975). «Curvilinear load-slip relations in laterally-loaded nailed joints», PhD thesis, Colorado state University, Colorado.
- Ni, C., Karacabeyli, E. (2007). "Performance of Shear Walls with Diagonal or Transverse Lumber Sheathing" on Journal of Structural Engineering, 2007.
- NZS (Standards New Zealand) (1993). "Timber Structures Standard". *NZS 3603:1993*. Wellington, New Zealand.
- Pellicane, P. J., Stone, J. L., Vanderbilt, M. D., (1991). «Generalized Model for Lateral Load Slip of nailed Joints», Journal of Materials in Civil Engineering, ASCE, Vol. 3, No. 1.
- Schiro, G., Giongo, I., Ingham, J., Dizhur, D., (2018). «Lateral performance of as-built and retrofitted timber diaphragm fastener connections», Journal of Materials in Civil Engineering, vol. 30 (1), ISSN: 0899-1561, [https://doi.org/10.1061/\(ASCE\)MT.1943-5533.0002110](https://doi.org/10.1061/(ASCE)MT.1943-5533.0002110).
- Wilson, A. W., (2012). «Seismic assessment of timber floor diaphragms in unreinforced masonry buildings», Doctoral dissertation, The University of Auckland, New Zealand.
- Wilson, A., Quenneville, P. J. H., Ingham, J. M. (2014). "In-plane orthotropic behavior of timber floor diaphragms in unreinforced masonry buildings", Journal of Structural Engineering 2014;140(1):0401303

# 6 TIMBER DIAPHRAGMS RETROFITTED WITH CLT PANELS

## 6.1 INTRODUCTION

The use of CLT slab panels fixed to the existing joists is recognized as being an effective solution for the improvement of out-of-plane floor behavior [Giongo et al. (2016)]. In this chapter, the effectiveness of such retrofit intervention in strengthening/stiffening diaphragm in-plane behavior is analyzed via numerical nonlinear static modeling.

## 6.2 MODELING APPROACHES

The numerical models employed for the study presented herein were developed consistently with the approaches proposed in Chapter 3. Due to the lack of experimental data regarding the investigated retrofit solution, M1 model was implemented to provide reliable data for the M2 model validation.

In M1 model, floorboards and CLT panels were represented by means of *curved shell* bi-dimensional elements (*Q20SH*). Floorboard-to-joist and panel-to-joist connections were represented by means of *point-interface* elements (*N6IF*). *Line interface* elements (*L16IF*) were interposed between adjacent floorboard elements and at the CLT panel edges to reproduce contact (element overlapping not allowed). Timber was modeled as linear elastic accounting for actual orthotropic behavior. Nailed connection response was set according to experimental results reported in Schiro et al. (2018), while screwed panel-to-joist connections were modeled as linear elastic. Stiffness values provided in EN1995 [CEN (2004)] were considered. The non-linear response of connections between adjacent CLT panels was simulated by assigning a non-linear response in the shear direction. The unit shear force vs. slip curve assigned to the interface elements

---

was obtained by dividing the connector experimental response by the connector tributary area.

In M2 model reinforcement was represented using *shell-thick* bi-dimensional elements for CLT panels. Connections were modeled by means of *multilinear-elastic link* elements ( $U1$ ,  $R2$  and  $R3$  DoFs fully restrained while  $R1$  DoF was set free) positioned at the actual connector locations. Nonlinear load-slip curves were assigned to the shear  $U2$  and  $U3$  DoFs. For panel-to-panel connectors, stiffness in the direction perpendicular to panel edge was evaluated by referring to the theoretical approach proposed by Tomasi et al. (2010) and assigned to the  $U1$  DoF. Timber was modeled as orthotropic linear-elastic material. Nonlinear connector load-slip behavior was assigned to the shear DoFs according to experimental results obtained by Schiro et al. (2018), while panel-to-joist connectors were modeled as linear elastic. Contact between timber elements was simulated by using *gap* links (rigid in compression, no-tension elements).

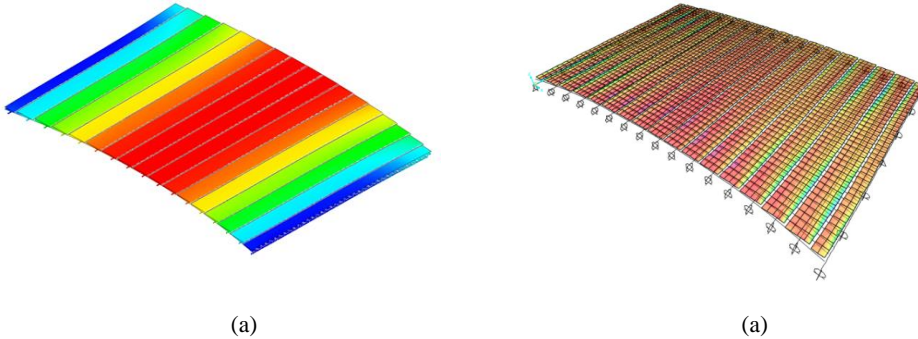


Figure 6.1: FE model views: a) M1 model; b) M2 model

### 6.3 FINITE ELEMENT MODEL VALIDATION

Due to the lack of experimental evidence available in literature for the retrofitted configuration, results obtained from the M2 model were compared to refined M1 model outputs. Consistent geometrical and mechanical properties were assigned to each model. Theoretical formulation by McLain and Pellicane [McLain (1975), Pellicane et al. (1991)] was used to evaluate the connector response. CLT in-plane shear stiffness was evaluated according to the theory proposed by Bogensperger et al. (2010), while for the axial stiffness the influence of timber layers loaded perpendicularly to the grain was neglected. Results of the validation process are reported in Figure 6.2. In each case the M2 model proved to be adequately accurate in reproducing the diaphragm in-plane behavior.

Table 6.1. Model validation process - reference diaphragm specimens

Specimen ID	Construction type	Load direction
6 × 8 PARA	CLT retrofit	Parallel to joists
6 × 8 PERP	CLT retrofit	Perpendicular to joists

## 6.4 PARAMETRIC ANALYSES

### 6.4.1 ANALYSES OVERVIEW

Diaphragm in-plane behavior was evaluated by means of non-linear static analyses. Simulations were carried out on the five full-scale diaphragms listed in Table 6.2, where  $L$  refers to joist length,  $B$  is diaphragm dimension in the perpendicular-to-joist direction and  $AR = L/B$  is the aspect ratio.

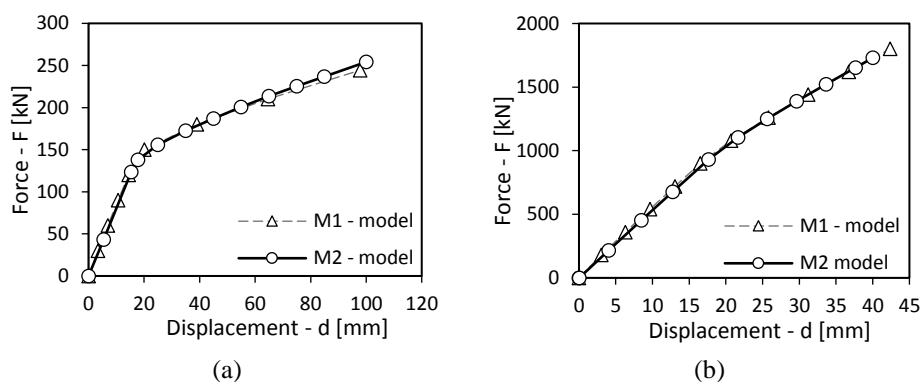


Figure 6.2. M2 - model validation: a) 6x8 – PARA; b) 6x8 – PERP

The material properties, element features and construction details listed in Table 6.3 were adopted as common to every diaphragm specimen. Regarding the as-built configuration, each floorboard was connected to the joists by means of a nail couple at each intersection. Experimental results obtained by Schiro et al. (2018) were used to calibrate the non-linear load-slip behavior of the nails. In all the cases, panels were considered to be laid over joists with the outer layers grain direction parallel to joist axis. Effectiveness of the selected retrofit technique was assessed with respect to several configurations obtained by varying CLT panel width, panel-to-panel connection and diaphragm boundary conditions (e.g. presence of chord elements, in-plane restraint position). Restraints were assigned so as to enable in-plane rotation of the diaphragm ends (see Figure 6.3). For comparison purposes, additional analyses were performed by restraining such rotations and no significant variations were observed. Loads and restraints were applied at joist level.

Table 6.2: Geometrical features of diaphragms

Diaphragm ID	L [m]	B [m]	AR
4 × 4	4.00	4.00	1.0
4 × 8	4.00	8.00	0.5
6 × 6	6.00	6.00	1.0
6 × 8	5.65	8.00	0.7
6 × 12	6.00	12.00	0.5

Parabolic load patterns were considered, as suggested by ASCE 41-17 [ASCE (2017)] and NZSEE 2017 [NZSEE (2017)]. In parallel-to-joists analyses, loads were applied at the joist ends and displacements were monitored with reference to the joist located at diaphragm midspan (unloaded side). In perpendicular-to-joists analyses, loads were applied to the outermost joist. In order to provide load distribution along diaphragm width, axially rigid rods were interposed between joists. In this case, displacements were monitored with reference to the mid-span of the outermost joist (unloaded side, see Figure 6.3). Since the influence of panel-to-joist connection spacing was found to be negligible for the in-plane response, constant spacing was adopted.

Table 6.3: Common properties considered in the analyses

Feature	Value
Floorboard section	150 x 20 mm
Joist cross section	150 x 200 mm
Wood grade	C 24* **
Joist spacing	500 mm
Panel to joist screw diameter	8 mm
Panel to joist crew spacing	150 mm
Nail couple spacing (straight)	100 mm

\*Timber grade according to EN338 [CEN (2004)]

\*\*Also for CLT panels

## 6.4.2 RETROFIT DETAILS

In the study presented herein several retrofit details were considered regarding panel thickness and arrangement, panel-to-panel connection and boundary conditions.

### 6.4.2.1 Panel thickness and arrangement

To account for the influence of panel thickness, analyses were carried out considering two alternative CLT panel construction types listed in Table 6.4. Panel in-plane shear stiffness was evaluated according to the analytical formulation proposed in Bogensperger et al. (2010). In both cases panels composed of C24 timber boards according to EN338 [CEN (2004)] were considered.

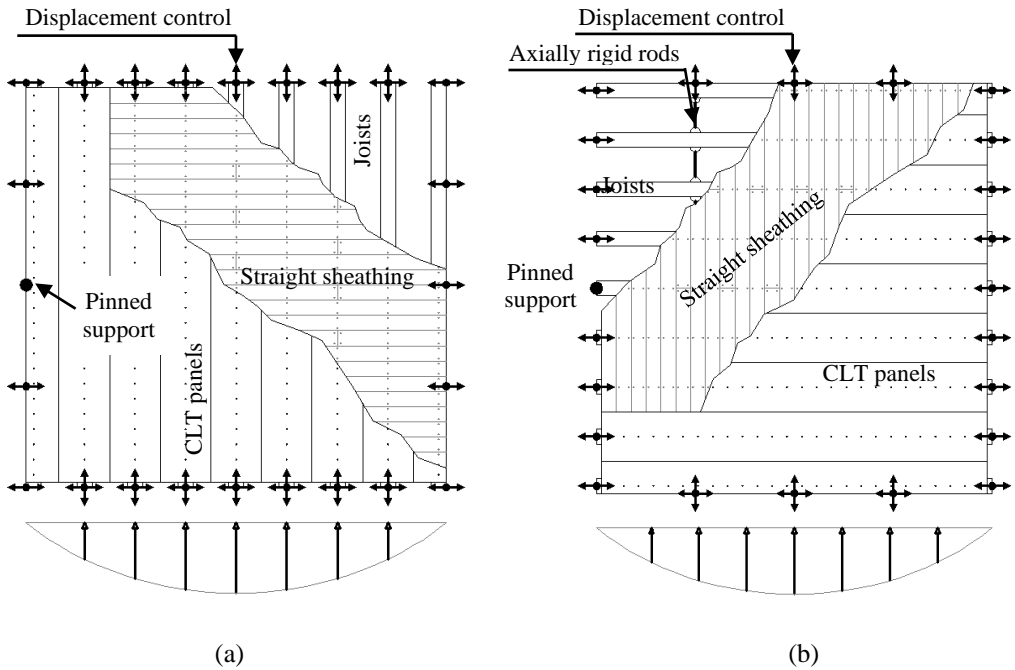


Figure 6.3. Load schemes and boundary conditions: a) Parallel to joists; b) Perpendicular to joists. Arrows represent free in-plane translational DoFs at restrained joints

Table 6.4: CLT panels considered in the parametric study

ID	Thickness	
	[mm]	Layers
P1	60	3
P2	100	5

The effect of panel arrangement was investigated considering two alternative patterns. Pattern *C1* was obtained by laying one panel element over each of the joists. In such arrangement panel width was equal to joist spacing, except for side elements whose width was equal to half joist spacing plus half joist cross-section width. *C2* pattern was based in the use of panels with a maximum width of 1.5 m. *C2* configurations were obtained based on the following principles:

- Panel arrangements were symmetric with respect to diaphragm principal directions;
- CLT elements were arranged so as to concentrate panel-to-panel interfaces where in-plane shear due to parallel-to-joists loading was expected to be minimum.

Based on such assumptions, *C2* configurations were defined as depicted in Figure 6.4 and Figure 6.5. Pattern *C2* was expected to exhibit greater in-plane stiffness while *C1* might be the only possible alternative in the cases where accessibility of diaphragms to be retrofitted is limited.

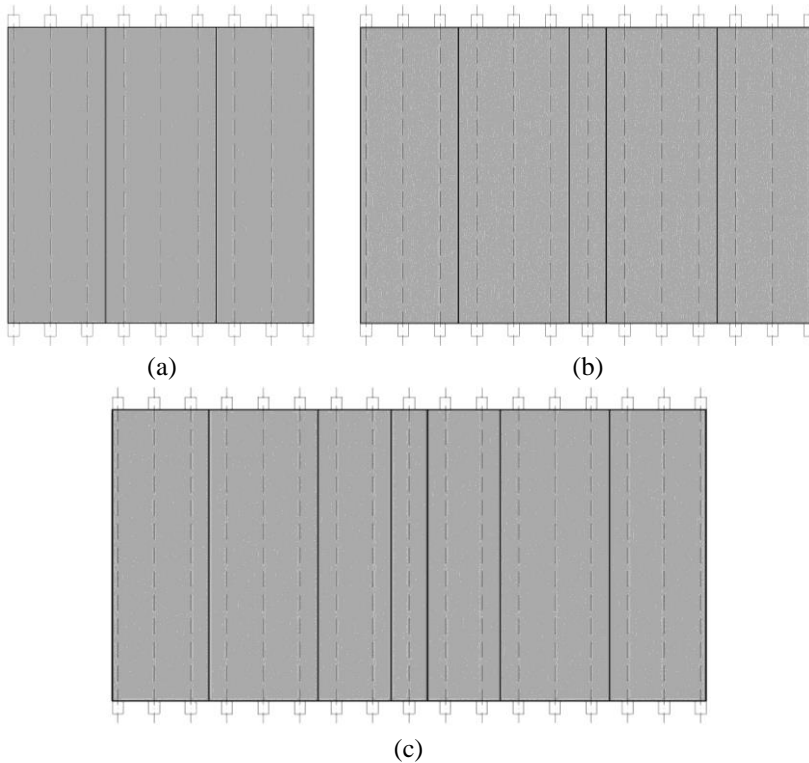


Figure 6.4: *C2* CLT panel arrangements: a) 4x4; b) 4x6; c) 4x8

#### 6.4.2.2 Panel to panel connection

Two types of panel to panel connection were considered in the parametric study. In one case, panels were considered as butt-jointed and connected to each other by means of  $\varnothing$  8 mm self-tapping screws inclined at  $45^\circ$  in the vertical plane (Figure 6.6-b). Such connection type will be referred to by means of the “A” label. Being the screws in such configuration subject to pure shear, their response in the direction parallel to panel interface was represented by referring to the experimental response observed by Gavric et al. (2015) regarding half-lap connections realized by means of  $\varnothing$  8 mm screws (Figure 6.6-a). From Figure 6.6 it is evident that embedment lengths of the tested connection in Gavric et al. (2015) are consistent with those of the selected connection with P1 panel thickness considered in the parametric analyses and mentioned in Table 6.3.

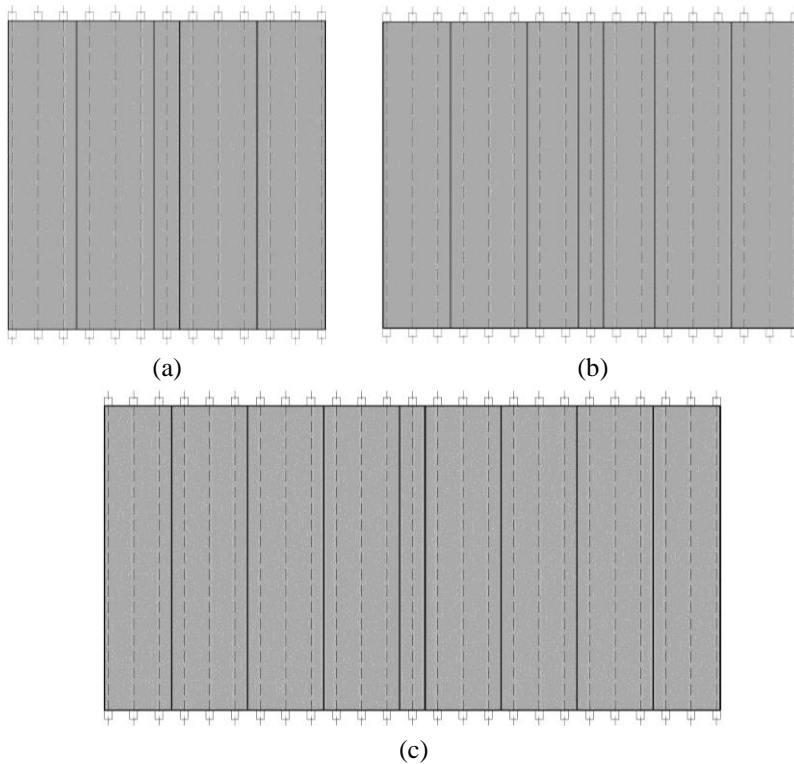


Figure 6.5: C2 CLT panel arrangements: a) 6x6; b) 6x8; c) 6x12

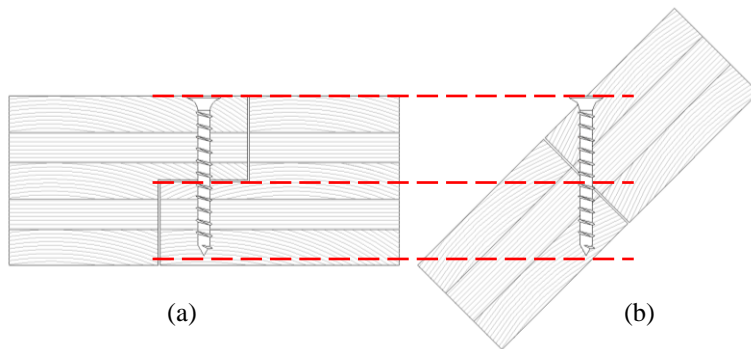


Figure 6.6. Panel-to-panel connections: a) 85mm thick panels as tested in Gavric et al. (2015); b) 60mm thick panel (P1)

On the other hand, double-inclined screws were considered in the case of “B” type connection. According to such connection geometry,  $\text{Ø } 8 \text{ mm}$  screws are inserted with a 45 degrees inclination in the vertical plane and with an additional 45 degrees inclination with respect to the connected panel interfaces (see Figure 6.7). As a result,

each connector will be subject to shear-traction or shear-compression depending on the relative slide direction. In this case, connector load-slip behavior was set according to the experimental results obtained in Hossain et al. (2016) for geometrically and mechanically consistent panel-to-panel connections. Due to the connection geometry reported in Hossain et al. (2016), such scheme was adopted in the case of P2 panels only.

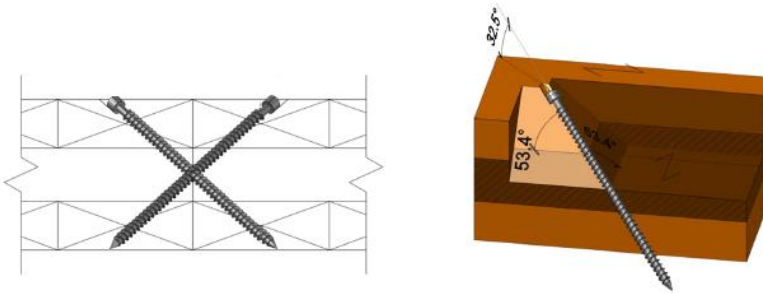


Figure 6.7: Type “B” panel-to-panel connection geometry [Taken from Hossain et al. (2016)]

To account for connector spacing influence, both A-type and B-type connections were implemented considering two alternative spacings, namely 300 mm (A300 and B300) and 150 mm (A150 and B150).

#### 6.4.2.3 Retrofit configurations

Configurations considered in the parametric study, obtained combining the details listed in the previous paragraphs, are listed in Table 6.5.

Table 6.5: Retrofitted configurations considered in the study

ID	CLT panel	Arrangement	Connection
P1-C1-A300	P1	C1	A300
P1-C1-A150	P1	C1	A150
P2-C1-B300	P2	C1	B300
P2-C1-B150	P2	C1	B150
P1-C2-A300	P1	C2	A300

#### 6.4.3 ANALYSES RESULTS

Consistently with previous chapters, results from the nonlinear static analyses were compared in terms of the equivalent shear stiffness  $G_d$  evaluated according to equation (6.1), where  $F$  is total load applied on the diaphragm,  $w$  and  $s$  are respectively the

diaphragm width and the diaphragm span with respect to the loading direction,  $\delta$  is the diaphragm mid-span displacement.

$$G_d = \frac{5 \cdot F \cdot s}{32 \cdot w \cdot \delta} \quad (6.1)$$

Due to the nonlinearity of diaphragm response, stiffness values of different diaphragms were compared at consistent levels of drift ( $dr[\%] = 2 \cdot 100 \cdot \delta/s$ ).

#### 6.4.3.1 Effectiveness of the retrofit intervention

Effectiveness of the retrofit intervention was evaluated comparing the equivalent in-plane stiffness of the floors in the as-built configuration ( $G_{d,AsB}$ ) with the in-plane stiffness of the *P1-C1-A300* retrofitted configuration ( $G_{d,RF}$ ) which was expected to provide the smaller stiffness values among the configurations listed in Table 6.5. Based on stiffness ratios listed in Table 6.6 it is evident that, in each case, the retrofit was observed to be significantly effective in increasing diaphragm in-plane stiffness. Regarding the retrofitted, diaphragm orthotropy ratios  $OR$  were comprised between 1.73 and 2.21 (see Table 6.6, where  $G_{d,PARA}$  and  $G_{d,PERP}$  represent the diaphragm stiffness in parallel and perpendicular to joists directions, respectively).

Table 6.6: Equivalent shear stiffness comparison, *P1-C1-A300* retrofit,  $dr=0.1\%$

Diaphragm	$G_{d,PARA}$ [kN/m]	$G_{d,PERP}$ [kN/m]	*OR	** $R_{PARA}$	** $R_{PERP}$
4x4	1774	3929	2.21	7.62	4.58
4x6	1814	3899	2.15	12.78	4.72
4x8	1772	3880	2.19	18.33	4.79
6x6	1801	3111	1.73	14.06	8.11
6x8	1772	3378	1.91	20.13	7.79
6x12	1703	3127	1.84	26.70	8.48

$$*OR = G_{d,RF,PERP} / G_{d,RF,PARA}$$

$$**R_{PARA(PERP)} = G_{d,RF,PARA(PERP)} / G_{d,AsB,PARA(PERP)}$$

#### 6.4.3.2 Effect of panel thickness and connection type

Analyses on *P2-C1-B300* retrofitted configuration allowed to establish the influence of both panel thickness and connection type on diaphragm in-plane stiffness. Results in terms of stiffness ratio with respect to the standard *P1-C1-A300* configuration ( $R_{PARA}$ ,  $R_{PERP}$ ) are listed in Table 6.7. Stiffness increments were comprised between 52% and 66% under parallel-to-joists loading and between 10% and 24% in perpendicular-to-joists direction.

Table 6.7: Influence of panel type and connection,  $dr = 0.1\%$

Diaphragm	$G_{d,0}$ [kN/m]	$G_{d,90}$ [kN/m]	*OR	**R <sub>PARA</sub>	**R <sub>PERP</sub>
4x4	2704	4333	1,6	1,52	1,10
4x6	2895	4297	1,48	1,60	1,10
4x8	2858	4273	1,5	1,61	1,10
6x6	2933	3848	1,31	1,63	1,24
6x8	2938	4112	1,4	1,66	1,22
6x12	2823	3868	1,37	1,66	1,24

$$*OR = G_{d,RF,PERP} / G_{d,RF,PARA}$$

$$**R_{PARA(PERP)} = G_{d,P2-C1-B150,PARA(PERP)} / G_{d,P1-C1-A300,PARA(PERP)}$$

Stiffness ratios in Table 6.7 are comprehensive of the effects of both panel thickness and panel-to-panel connection type. To isolate the contributions of the two parameters, additional analyses were undertaken on fictitious retrofit configurations listed in Table 6.8. It is worth reminding that such retrofit configurations were labeled as “*fictitious*” since panel-to-panel connection behaviors are not consistent with panel thicknesses due to the reasons reported in paragraph 6.4.2.2.

Table 6.8: Fictitious retrofit configurations

ID	CLT panel	Arrangement	Connection
P1-C1-B150	P1	C1	B150
P2-C1-A300	P2	C1	A300

The influence of panel thickness was evaluated based on stiffness ratios listed in Table 6.9. Panel thickness influence was found to range between 2% and 23% depending on connection type and loading direction. Higher stiffness ratios were observed in the case of the stiffer *B150* panel-to-panel connection. Such trend may be related to the variations in stiffness hierarchy due to variations in panel thickness and connection type. Stiffer connections tend to concentrate strains and stresses into CLT elements making panel thickness more relevant and vice-versa.

#### 6.4.3.3 Influence of panel-to-panel connection spacing

The influence of connection spacing was assessed by halving connection spacing on each of the panel-to-panel interfaces (*P1-C1-A150* and *P2-C1-B150* configurations in Table 6.5). Results related to the 150 mm spacing are listed in Table 6.10 in terms of stiffness ratios referred to the 300 mm spacings for both the *P1-A* and *P2-B* panel type-connection type combinations. In both cases stiffness ratios were observed to be greater

in parallel-to-joists loading direction and in the case of P1-A panel-connection combination.

*Table 6.9: Panel thickness influence,  $dr=0.1\%$*

Diaphragm	A300		B150	
	*R <sub>PARA</sub>	**R <sub>PERP</sub>	*R <sub>PARA</sub>	**R <sub>PERP</sub>
4x4	1,02	1,06	1,18	1,13
4x6	1,03	1,07	1,17	1,12
4x8	1,03	1,09	1,17	1,13
6x6	1,02	1,07	1,23	1,13
6x8	1,03	1,08	1,23	1,14
6x12	1,03	1,09	1,22	1,17

$$*R_{PARA} = G_{d,P2,PARA} / G_{d,P1,PARA}$$

$$**R_{PERP} = G_{d,P2,PERP} / G_{d,P1,PERP}$$

*Table 6.10: Influence of panel-to-panel connection spacing,  $dr = 0.1\%$*

Diaphragm	P1-A		P2-B	
	*R <sub>PARA</sub>	**R <sub>PERP</sub>	*R <sub>PARA</sub>	**R <sub>PERP</sub>
4x4	1,52	1,10	1,42	1,10
4x6	1,60	1,10	1,48	1,10
4x8	1,61	1,10	1,50	1,10
6x6	1,63	1,24	1,52	1,22
6x8	1,66	1,22	1,55	1,20
6x12	1,66	1,24	1,55	1,22

$$*R_{PARA} = G_{d,s150,PARA} / G_{d,s300,PARA}$$

$$**R_{PERP} = G_{d,s150,PERP} / G_{d,s300,PERP}$$

#### 6.4.3.4 Influence of panel arrangement

Due to the stiffness hierarchy, reinforcement strains are concentrated at panel-to-panel interfaces, particularly in the case of parallel-to-joists loading conditions. Therefore, it seems straightforward to affirm that the adoption of wider CLT panel elements will lead to remarkable stiffness increments arising from the reduction in number of panel-to-panel interfaces. To prove such statement, results obtained considering the C2 panel layout were compared with those related to the C1 arrangement. Stiffness ratios related to the P1-A300 configuration are listed in Table 6.11. As expected, C2 arrangement led to significantly higher stiffness values, with parallel-to-joists stiffness being more affected by panel arrangement.

Table 6.11: Influence of CLT panel arrangement, P1 A300 configuration,  $dr=0.1\%$

Diaphragm	*R <sub>PARA</sub>	**R <sub>PERP</sub>	OR
4x4	2,61	1,42	1,21
4x6	3,01	1,38	0,98
4x8	2,47	1,34	1,19
6x6	3,29	1,92	1,01
6x8	3,16	1,77	1,07
6x12	3,12	1,92	1,13

$$*R_{PARA} = G_{d,C2,PARA} / G_{d,C1,PARA}$$

$$**R_{PERP} = G_{d,C2,PERP} / G_{d,C1,PERP}$$

#### 6.4.3.5 Influence of diaphragm boundary conditions

Analyses results discussed in previous paragraphs were obtained by considering the boundary conditions declared in paragraph 6.4.1 (*BC1* in the following). Further analyses were carried out on diaphragms retrofitted according to the *P1-C1-A300* configuration with restraints and loads assigned at reinforcement level (*BC2* in the following). Such configuration can be reproduced in the practice by introducing an L-shaped steel profile running along diaphragm perimeter, screwed to CLT elements and connected to the surrounding masonry. Results listed in Table 6.12 were obtained by neglecting the stiffness of the chord elements (loads and restraints were applied to CLT elements). The influence of such aspect is discussed in the following. Load distributions and control points were placed consistently with the assumptions of paragraph 6.4.1. Results reported in Table 6.12 in terms of stiffness ratios highlight that the influence of boundary conditions was more evident in the case of perpendicular-to-joists direction. Such trend can be justified by considering that, under the assumptions of *BC2* boundary conditions, the existing floor is substantially bypassed by loads which are directly applied to the reinforcement elements. Hence, being the reinforcement stiffer in perpendicular-to-joists direction, the effect of the modified boundary conditions is greater in the corresponding direction.

Table 6.12: Influence of boundary conditions

Diaphragm	*R <sub>PARA</sub>	**R <sub>PERP</sub>
4x4	1,16	1,72
4x6	1,14	1,64
4x8	1,07	1,53
6x6	1,08	1,37
6x8	1,06	1,32
6x12	1,04	1,27

$$*R_{PARA} = G_{d,PARA,BC2} / G_{d,PARA,BC1}$$

$$**R_{PERP} = G_{d,PERP,BC2} / G_{d,PERP,BC1}$$

Further analyses were undertaken to evaluate the influence of chord elements running along diaphragm perimeter. Results were consistent with those discussed in Chapter 3. Chord elements were found to participate to diaphragm in-plane deflection because of their sole in-plane bending stiffness, allowing to rule out for their functioning as actual chords.

#### 6.4.3.6 Remarks on diaphragm in-plane behavior

Typical retrofitted diaphragm load vs. displacement response is depicted in Figure 6.8 for the two principal loading directions. Under parallel-to-joists loading (Figure 6.8-a) load vs displacement response exhibited a first linear stage until the yielding of the most stressed panel-to-panel connection line occurred causing diaphragm stiffness to decrease (point *Y*). Due to the high axial stiffness of panels, connector slip values are consistent on a given interface forcing each connector to yield simultaneously on the most stressed interface line. Stiffness of the post-elastic response depends on panel-to-panel interface locations and connection post-elastic behavior, until diaphragm failure occurs when the most stressed connection line slip equals ultimate connector slip value. When failure criterion of timber panels is disregarded, typical diaphragm response under perpendicular-to-joists loading is depicted in Figure 6.8-b. At small displacements the retrofit behaves as a composite beam in which panels are subjected to a combined in-plane bending plus axial compression/traction state induced by panel-to-panel connections (*A*). As displacement increases, panel-to-panel connections begin to yield making the composite behavior less effective due to the reduced connection post-yield stiffness. For increasing displacements, connections are no longer effective and the sole bending stiffness of the panels is engaged (dashed line in Figure 6.8-b refers to the sum of panel in-plane elastic bending stiffness). Anyway, when failure of CLT panels is accounted for, representative backbones assume the shapes illustrated in Figure 6.9. CLT elements ultimate conditions occur prior to connection yielding, leading to a substantially linear diaphragm response until failure.

Diaphragm backbones for the *PI-C1-A150-BC2* configuration are illustrated in Figure 6.9. Drift and unit shear representative of diaphragm yield ( $dr_y, v_y$ ) and ultimate conditions ( $dr_u, v_u$ ) are listed in Table 6.13 and Table 6.14 for parallel-to-joists loading and perpendicular-to-joists loading respectively. In the case of parallel-to-joists loading, diaphragm backbones in the drift vs. unit shear plane were substantially consistent for each diaphragm, while under perpendicular-to-joists loading, drift vs unit shear plots showed a dependency on joist length. Such trend is due to the fact that, under perpendicular-to-joists loading, diaphragm behavior is governed by CLT panel in-plane bending mechanism.

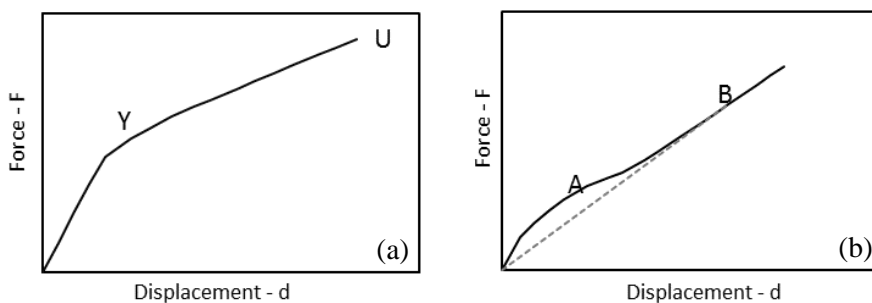


Figure 6.8: Typical retrofitted diaphragm in-plane load vs displacement response: a) Parallel-to-joists loading; b) Perpendicular-to-joists loading

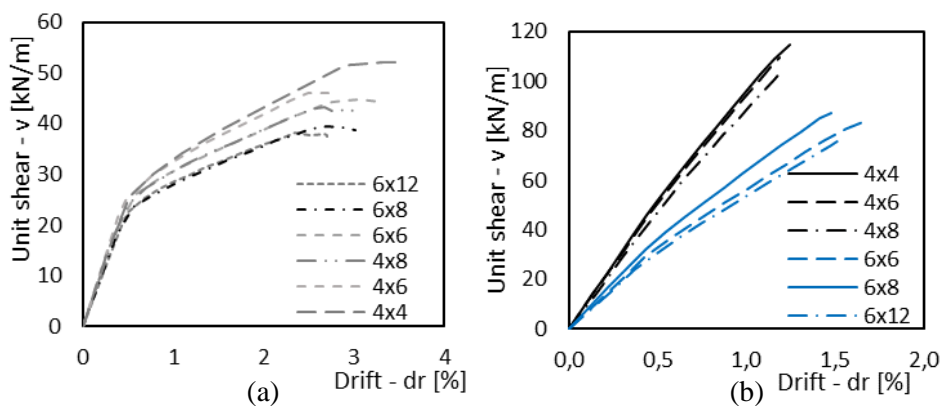


Figure 6.9: P1-C1-A150-BC2 backbones: a) Parallel-to-joists loading; b) Perpendicular-to-joists loading

Table 6.13: P1-C1-A150-BC2 backbone characterization, parallel-to-joists loading

	$dr_y$ [%]	$v_y$ [kN/m]	$dr_u$ [%]	$v_u$ [kN/m]
4x4	0,50	25,70	52,22	3,50
4x6	0,47	24,80	46,08	2,71
4x8	0,50	24,20	43,28	3,01
6x6	0,58	26,00	44,69	3,34
6x8	0,55	23,50	39,47	3,02
6x12	0,50	22,66	38,12	2,70
Mean	0,52	24,48	43,98	3,05
CoV	0,071	0,048	0,105	0,097

Table 6.14: P1-C1-A150-BC2 backbone characterization, perpendicular-to-joists loading

Diaphragm	$d_{r_u}$ [%]	$v_u$ [kN/m]
4x4	126,38	1,20
4x6	124,98	1,22
4x8	118,77	1,24
6x6	101,26	1,72
6x8	104,09	1,51
6x12	89,06	1,50
Mean L=4m	123,38	1,22
CoV	0,027	0,012
Mean L=6m	98,13	1,58
CoV	0,066	0,064

## 6.5 SIMPLIFIED ANALYTICAL MODEL PROPOSAL

In this paragraph a simplified analytical model for predicting diaphragm in-plane stiffness and strength is proposed and calibrated based on numerical results discussed in the previous paragraphs.

### 6.5.1 PARALLEL-TO-JOISTS LOADING DIRECTION

Under parallel-to-joists loading conditions, diaphragm response is governed by panel-to-panel connection behavior and panel in-plane shear strain. Such assumption is closely matched in the case of *BC2* boundary conditions, while the sub-structure significantly contributes to diaphragm flexibility in the case of *BC1* boundary conditions. Referring to the *BC2* configuration, diaphragm behavior can be idealized as depicted in Figure 6.10 in which the sub-structure is disregarded. According to such scheme shear deflection of the single module  $\delta$  can be regarded as the sum of connection slip  $\delta_c$  and panel shear deflection  $\delta_p$ . Such contributions are given by equations (6.2) where  $v$  is shear per unit length,  $i$  is panel width,  $G$  and  $t$  are the shear modulus and thickness of CLT panels respectively and  $k$  is specific stiffness of panel-to-panel connection.

$$\delta = \delta_p + \delta_c = \frac{v \cdot i}{G \cdot t} + \frac{v}{k} \quad (6.2)$$

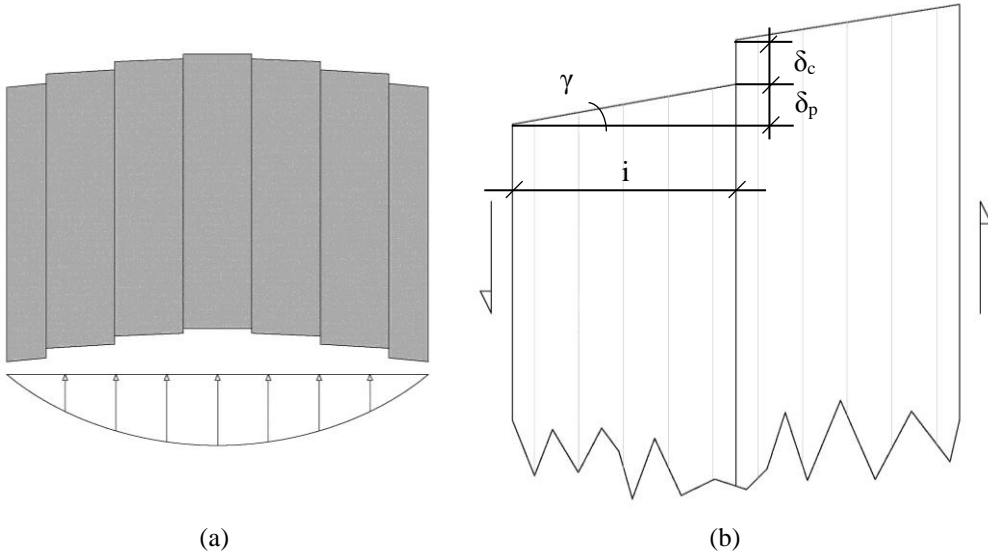


Figure 6.10: Retrofitted diaphragm in-plane behavior idealization, parallel-to-joists loading:  
a) Overall diaphragm deflections; b) Close-up with magnified displacements

According to the definition given in paragraph 6.4.3, diaphragm equivalent shear stiffness  $G_d$  equals the ratio between unit shear  $v$  and shear deflection  $\gamma$  which is, in turn, equal to the ratio between deflection  $\delta$  and panel width  $i$ . Therefore, under such assumptions, diaphragm equivalent shear stiffness is given by equation (6.3).

$$G_{d,BC2} = \frac{v \cdot i}{\delta} = \left[ \frac{1}{G \cdot t} + \frac{1}{k \cdot i} \right]^{-1} \quad (6.3)$$

Errors related to equation (6.3) evaluated according to equation (6.4) are illustrated in Figure 6.11.

$$e = \frac{|G_{d,FEM} - G_{d,eq.(6.3)}|}{G_{d,FEM}} \quad (6.4)$$

In the case of *BCI* boundary conditions values given by equation (6.3) should be reduced to account for sub-structure flexibility. From values listed in Table 6.15 stiffness overestimation ratio related to equation (6.4) was found to be higher for stiffer diaphragms. This aspect might be explained considering that the greater the ratio between reinforcement and substructure stiffness and the greater the sub-structure deflection. Stiffness overestimation ratios listed in Table 6.15 are depicted in Figure 6.12 together with their linear regression function which approximated the value of the stiffness reduction factor. Therefore, in the case of *BCI* boundary conditions, equation (6.5) should be used, in which  $G_{d,BC2}$  is given by equation (6.3).

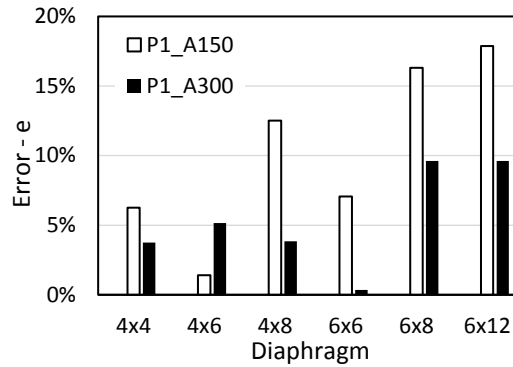


Figure 6.11: Errors related to equation (6.3)

Table 6.15: Diaphragm stiffness in parallel-to-joists direction – stiffness reduction factor calibration

	P1-C1-A300	P1-C1-A150	P2-C1-B300	P2-C1-B150
$G_{d,FEM}$	1773	2858	3120	4700
$G_{d,eq,0}$	1973	3702	4106	7589
$G_{d,FEM}/G_{d,eq,0}$	<b>0,899</b>	<b>0,772</b>	<b>0,760</b>	<b>0,619</b>

$$G_{d,BC1} = G_{d,BC2} \cdot (1 - 5 \cdot 10^{-5} \cdot G_{d,BC2}) \quad (6.5)$$

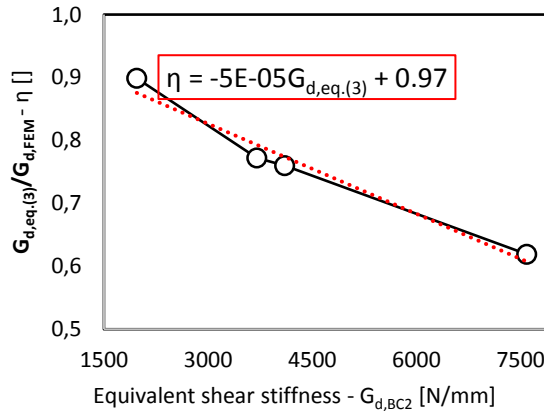


Figure 6.12: Stiffness reduction factor

Under the same assumptions diaphragm strength  $v_u$  should be taken as the minimum value between panel-to-panel connection strength  $S_c$  and panel shear strength  $S_p$ , whose values can be evaluated according to equation (6.6), where:

- $F_{u,c}$  and  $n_c$  are, respectively, shear strength of the individual panel-to-panel connection and the number of connectors on the considered interface;
- $f_v$  is in-plane shear strength of CLT elements;
- $t$  is panel thickness;
- $L$  is panel length in parallel to loading direction.

$$\begin{aligned} S_c &= F_{u,c} \cdot n_c \\ S_p &= f_v \cdot t \cdot L \end{aligned} \quad (6.6)$$

The two failure mechanisms might be checked against different shear actions since shear force acting on the most stressed panel-to-panel interface depends on interface location, while maximum shear force on the most stressed panel is always equal to  $F/2$ , being  $F$  the total load on diaphragm. Hence, checks should be written according to equation (6.7).

$$\begin{aligned} \frac{0.5 \cdot F}{\alpha_c \cdot S_c} &\leq 1 \\ \frac{0.5 \cdot F}{S_p} &\leq 1 \end{aligned} \quad (6.7)$$

Dimensionless  $\alpha_c$  coefficient accounts for the total force on diaphragm  $F$  over in-plane shear acting on the most loaded interface and, for parabolic inertia load distributions, is given by equation(6.8), where  $s=2x_1/B$  (see Figure 6.13).

$$\alpha_c = 2 \cdot [2 + (s - 3) \cdot s^2]^{-1} \quad (6.8)$$

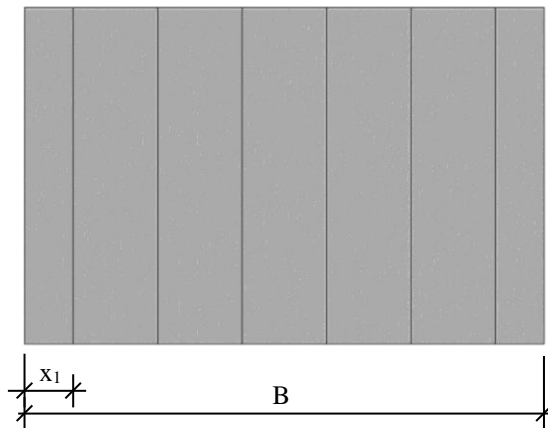


Figure 6.13: In-plane diaphragm check – most loaded interface location

### 6.5.2 PERPENDICULAR-TO-JOISTS LOADING DIRECTION

In perpendicular-to-joists loading direction diaphragm behavior is governed by in-plane panel and joist bending. In the case of *CI* panel arrangement a simplified analytical model can be implemented for estimating diaphragm stiffness and ultimate conditions. In the following the contribution of the substructure and the composite behavior introduced by panel-to-panel connections outlined in paragraph 6.4.3.6 are neglected leading to a stiffness and strength underestimation. If the presence of  $n_j$  joists (and, therefore,  $n_j$  CLT panels) is assumed, the load vs. mid-span displacement relation under a parabolic load profile is given by equation (6.9), Where  $F$  is total in-plane load on diaphragm,  $L$  is joist length (which is assumed to be equal to panel length).  $EJ$  and  $GA$  are bending and shear stiffness of the panels.

$$\delta = F \cdot \left[ \frac{61}{3840} \cdot \frac{L^2}{n_j \cdot EJ} + \frac{5}{32} \cdot \frac{L}{n_j \cdot GA} \right] = F \cdot \eta \quad (6.9)$$

If such relation is substituted into equation (6.1), equivalent diaphragm shear stiffness  $G_d$  is given by equation (6.10), where  $B$  is diaphragm width according to Figure 6.13.

$$G_{d,PERP} = \frac{5 \cdot L}{32 \cdot B} \cdot \frac{1}{\eta} \quad (6.10)$$

Total load on diaphragms  $F$  should be checked with respect to both shear and bending strength of the panels. Under the hypotheses declared in the previous paragraphs, diaphragm shear strength  $F_{R,S}$  and bending strength  $F_{R,B}$  can be evaluated by means of equations (6.11) and (6.12), where  $t$  and  $i$  are panel thickness and width, respectively and  $f_m$  and  $f_v$  are bending and shear strength of the panels, respectively. Diaphragm strength  $F_{max}$  is equal to the smaller of the aforementioned values ( $F_{max} = \min\{F_{R,S}; F_{R,B}\}$ )

$$F_{R,B} = \frac{32}{30} \cdot \frac{t \cdot i^2}{L} \cdot f_m \cdot n_j \approx \frac{t \cdot i^2}{L} \cdot f_m \cdot n_j \quad (6.11)$$

$$F_{R,S} = 2 \cdot t \cdot i \cdot f_v \cdot n_j \quad (6.12)$$

Since timber behavior is assumed to be linear until failure, ultimate displacement can be calculated as the in-plane displacement calculated by substituting  $F_{max}$  into equation (6.9).

---

## 6.6 CONCLUSIONS

A series of non-linear static analyses were performed on a selection of diaphragm geometries in order to evaluate the effects on the in-plane behavior of a retrofit intervention based on the use of CLT panels. Numerical results highlighted a remarkable stiffening of diaphragm in-plane response as a consequence of the retrofit intervention. The influence of a selection of construction details such as panel thickness, panel-to-panel connection, panel arrangement and boundary conditions was analyzed and discussed. Due to the nature of the reinforcement, diaphragm response was observed to be, in general, stiffer under perpendicular-to-joists loading. However, some configurations were found to exhibit a nearly-orthotropic behavior.

**NOTE:** Part of the research outcomes presented in this Chapter have been published in:

Rizzi E., Capovilla M., Giongo I., Piazza M. “In-plane behaviour of timber diaphragms retrofitted with CLT panels”, proceedings of the 11th International Conference on Structural Analysis of Historical Constructions, SAHC 2018, 11-13 September 2018, Cuzco, Peru.

## 6.7 REFERENCES

- Augenti, N. and Parisi, F. (2010). “Learning from Construction Failures due to the 2009 L’Aquila, Italy, Earthquake”. *Journal of Performance of Constructed Facilities*, vol. 24, No. 6.
- ASCE (American Society of Civil Engineers). (2013). “Seismic Evaluation and Retrofit of Existing Buildings” *ASCE 41-13*, Reston, Virginia.
- Baldessari, C., Piazza, M. and Tomasi, R. (2009). “The refurbishment of timber floors: characterization of the in-plane behavior” *Proceedings, PROHITEC International Conference*, Taylor and Francis, Rome, Italy, 2009.
- Bogensperger, T., Moosbrugger, T., Silly, G., (2010) «Verification of CLT-Plates under Loads in plane». In *Proceedings of WCTE 2010 – Word Conference on Timber Engineering*, 2010.
- CEN (European Committee for Standardization) (2004). “Design of Timber Structures”. *EN1995*. Brussels, Belgium.
- CEN (European Committee for Standardization) (2009). “Structural timber - Strength classes”. *EN 338*. Brussels, Belgium.
- CSI (Computers and Structures Inc.). (2014). “CSI Analysis Reference Manual, SAP2000 v17”. Berkeley, California.
- Dizhur, D., Ingham, J. M., Biggs, D. and Schultz, A. (2016). “Performance of unreinforced masonry and infilled RC buildings during the 2015 Gorkha, Nepal earthquake sequence”. *Proceedings, 16th International Brick and Block Masonry Conference, IBMAC 2016*, pp 2399-2408.
- Gavric, I., Fragiaco, M., Ceccotti, A., (2015) «Cyclic Behavior of Typical Screwed Connections for Cross-Laminated (CLT) structures», *European Journal of Wood and Wood Products* volume 73, pages179–191, 2015.
- Giongo I., Schiro, G., Piazza, M., Tomasi, R., (2016) “Long-term out-of-plane testing of timber floors strengthened with innovative timber-to-timber solutions”. *Proceedings of the World Conference on timber Engineering (WCTE)*, Vienna, Austria.
- Hossain, A., Danzig, I., Tannert, T., (2016) «Cross-Laminated Timber Shear Connections with Double-Angle Self-Tapping Screws Assemblies». *Journal of Structural Engineering*, ASCE, ISSN 0733-9445, 2016.
- Manie, J., and Kikstra, W. P., eds. (2014). *DIANA—Finite element analysis. User’s manual release 9.5*. Delft, Netherlands: TNO DIANA BV.
- NZSEE (New Zealand Society for Earthquake Engineering) (2015). “Assessment and improvement of the structural performance of buildings in earthquakes”. *NZSEE 2015*. Wellington, New Zealand.

---

Pellicane, P. J., Stone, J. L., Vanderbilt, M. D., (1991). «Generalized Model for Lateral Load Slip of nailed Joints», *Journal of Materials in Civil Engineering*, ASCE, Vol. 3, No. 1.

Peralta, D. F., Bracci, J. M., and M. B. Hueste, (2003). «Seismic Performance of Rehabilitated Wood Diaphragms», Texas A&M University, Department of Civil Engineering.

Schiro, G., Giongo, I., Ingham, J., Dizhur, D., (2018). «Lateral performance of as-built and retrofitted timber diaphragm fastener connections», *Journal of Materials in Civil Engineering*, vol. 30 (1), ISSN: 0899-1561, [https://doi.org/10.1061/\(ASCE\)MT.1943-5533.0002110](https://doi.org/10.1061/(ASCE)MT.1943-5533.0002110).

Tena-Colunga, A. and Abrams, D. P., (1996). “Seismic Behaviour of Structures with Flexible Diaphragms”, *Journal of Structural Engineering*, vol. 122, no. 4, pp. 439-445.

Tomasi, R., Crosatti, A., Piazza, M., (2010) “Theoretical and Experimental Analysis of Timber-to-Timber Joints Connected with Inclined Screws”, *Construction and Building Materials*, 2010.

Wilson, A. W., Quenneville, P. J. H. and Ingham, J. M., (2014). «In-plane orthotropic behavior of timber floor diaphragms in unreinforced masonry buildings.» *J. Struct. Eng.* 140 (1): 04013038. [https://doi.org/10.1061/\(ASCE\)ST.1943-541X.0000819](https://doi.org/10.1061/(ASCE)ST.1943-541X.0000819).

# 7 NON-LINEAR DYNAMIC MODELING OF DIAPHRAGM IN-PLANE BEHAVIOR

## 7.1 INTRODUCTION

The goal of the study presented in this Chapter was to assess the seismic force and displacement demands on timber diaphragms. The retrofit techniques presented in the previous chapters were observed to be significantly effective in increasing diaphragm in-plane strength and stiffness. Anyway, it is not straightforward to predict the consequences of such interventions on seismic demands. Indeed, with reference to a conventional seismic response spectrum, changes in the structure period (which directly depends on structural mass and stiffness distribution) may have different effects depending on the structural dynamic properties. If the natural period of the structure  $T_I$  is comprised within the constant acceleration part of the spectrum, changes in stiffness may not influence force demands. Conversely, in the case of extremely flexible structures,  $T_I$  may place the structure in the constant displacement section of the spectrum and, in the case, stiffness increments may result ineffective when the objective is the displacement demand mitigation. In the case when  $T_I$  is comprised within the constant velocity part of the spectrum, stiffness increments will, in general, result in smaller displacement and higher force magnitudes. In general, ordinary buildings fall in the first or in the third case, while the constant displacement part of the spectrum is typical of large and flexible structures such as high-rise buildings and suspension bridges. As illustrated in Chapter 2, ASCE 41-17 [ASCE (2017)] and NZSEE 2017 [NZSEE (2017)] suggest to evaluate seismic demands based on diaphragm natural period which, in turn, depends on diaphragm tributary masses and in-plane stiffness. According to such idealization, the flexibility of straight sheathed diaphragms, in conjunction with the relatively large mass due to out-of-plane loaded walls, may lead to fairly high natural periods, so as to put the structure in the constant-velocity part of the spectrum. In such scenario the stiffening of the diaphragms is expected to be an effective

intervention for mitigating displacement demands with the side effect of increasing seismic-induced forces. To investigate such subject without referring to the simplified approach based on response spectra, a series of nonlinear dynamic analyses were undertaken considering the diaphragm configurations presented in the previous Chapters.

## 7.2 FINITE ELEMENT MODEL DETAILS

The numerical study presented in this Chapter was based on the M2 modeling approach proposed in the previous chapters featuring some adaptations for its implementation in dynamic simulations. In detail, timber mechanical properties were set as linear-elastic accounting for material orthotropy, joists and floorboards were modeled as *1D frame* elements while *2D shells* were used to reproduce CLT panels and plywood sheets. Nail and screw connections were modeled by means of *nonlinear-plastic* links placed at actual connector locations, featuring the *Pivot* hysteretic model consistently with what recommended by Wilson (2012). Contact phenomena between adjacent timber elements were modeled according to the M2 *model* proposal whose details are given in Chapter 3.

## 7.3 FINITE ELEMENT MODEL VALIDATION

Accuracy of the selected modeling approach was checked by comparing numerical outputs with a selection of experimental results available in literature related to timber diaphragm in-plane dynamic experimental testing (Table 7.1). Specifically, snap-back tests on century-old straight sheathed diaphragms loaded perpendicularly to the joists [Giongo et al. (2015)] and a ground motion shaking test performed on a newly-constructed straight sheathed diaphragm in the parallel-to-joists direction [ABK (1981)] were considered.

*Table 7.1 Experimental reference data for model validation*

Diaphragm ID	Authors	Test type	L [m]	B [m]
Specimen A	Giongo et al. (2015)	Snap-back	9.60	5.60
Specimen B	Giongo et al. (2015)	Snap-back	9.60	4.70
Diaphragm E	ABK (1981)	Ground motion	6.10	18.30

Actual diaphragm geometries, material properties and test methods were accurately reproduced in the models. For Specimen A and Specimen B actual material properties

experimentally obtained by Giongo et al. (2015) were assigned to the timber elements. Experimental connection backbones reported in Schiro et al. (2018) obtained from laboratory testing of nailed joints extracted from a diaphragm portion adjacent to specimens A and B were assigned to the corresponding nonlinear links. Inter-floorboard friction was considered according to the modeling strategy presented in Chapter 3. In the case of Diaphragm E, timber material properties were selected from NZS 3603:1993 Standard [NZS (1993)] according to timber species declared in ABK (1981). Shear and perpendicular to grain moduli of elasticity were evaluated according to Piazza et al. (2005). Due to the substantial consistency of connection geometry and material properties, experimental backbone obtained by Wilson (2012) for NEW-NZ assemblies was assigned to nonlinear links representative of nailed connections. Snap-back tests were simulated by means on non-linear time history analyses. Initial deformed shape was imposed by applying in-plane loads following a quasi-static force increasing rate. Load distributions and final magnitudes were applied consistently with the experimental procedure reported in Giongo et al. (2015). In-plane mid-span displacements at full load application, representative of snap-back test initial conditions, were found to be consistent with the experimental evidence. To avoid the presence of residual dynamic effects, in-plane loads were kept constant for a reasonable amount of time before simulating the actual snap-back test by suddenly removing the in-plane loads. Numerical and experimental acceleration vs. time plots at mid-span are compared in Figure 7.1. Modal parameters were estimated according to three alternative methods, namely the peak picking (PP), the frequency domain decomposition (FDD) and the enhanced frequency domain decomposition (EFDD). Diaphragm 1<sup>st</sup> mode periods obtained from post-processing of numerical outputs are compared with the experimental evidence in Table 7.2.

*Table 7.2: Model validation on snap-back tests*

		Load	Imposed displacement	1 <sup>st</sup> mode period
		[kN]	[mm]	[s]
Specimen A	Experimental	63.8	152.6	0.41
	Model	63.2	155.0	0.38
Specimen B	Experimental	38.8	157.1	0.45
	Model	38.8	157.8	0.43

Diaphragm E was modeled according to the specifications given in ABK (1981). Specifically, displacement vs. time function recorded at Castaic (CA) in the N69W direction for the 1971 Wasatch Earthquake and amplified by a 1.8 scale factor was applied to the diaphragm specimen.

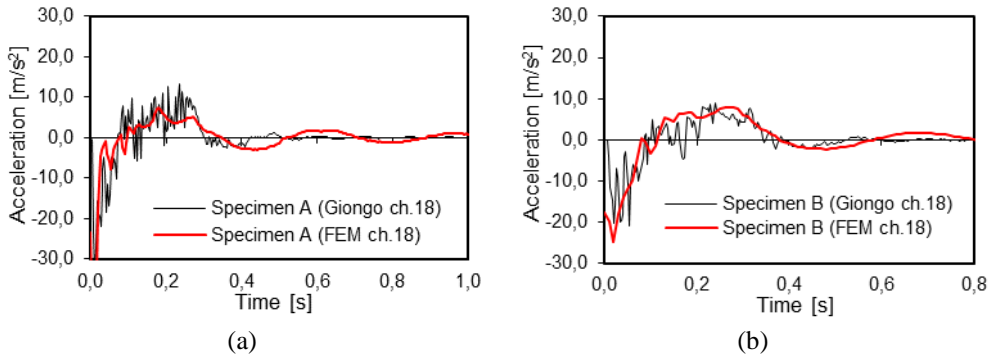


Figure 7.1 Dynamic model validation, snap-back tests [Giongo et al. (2014)]: a) Specimen A; b) Specimen B

Diaphragm tributary mass was represented by 1-ton lead weights connected to diaphragm ends and supported on low-friction rollers. A schematic of the test setup is given in Figure 7.2. For the numerical simulation, displacement vs. time record taken from PEER Ground Motion Database was converted into acceleration vs. time and applied to the model in a nonlinear time history analysis providing in-plane restraints at jack locations. From the comparison in Figure 7.3 it is evident that the model accurately predicted diaphragm response in the midspan displacement vs. force plane and, most importantly, both force and displacement demands were correctly estimated.

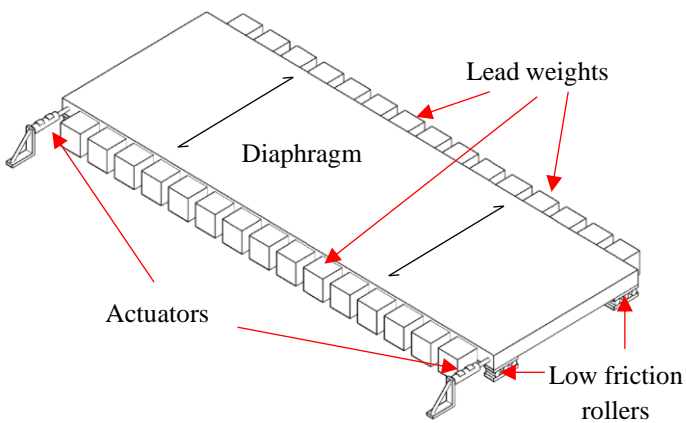


Figure 7.2: Schematic of ground motion test on Diaphragm E [ABK (1981)]

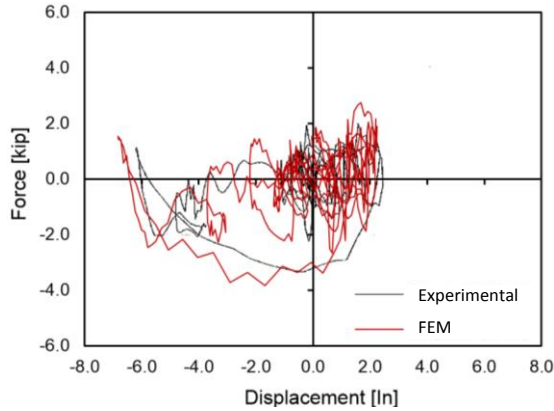


Figure 7.3 Diaphragm E [ABK (1981)]: experimental vs model output

## 7.4 PARAMETRIC STUDY

### 7.4.1 DIAPHRAGM GEOMETRIES

A series of nonlinear-dynamic analyses were undertaken considering the 5 diaphragm geometries listed in Table 7.3, where  $L$  is joist length,  $B$  is diaphragm dimension perpendicular to joist direction and  $AR$  is diaphragm aspect ratio ( $AR=L/B$ ). For each of the configurations, a series of accelerograms were applied to each diaphragm in both principal loading directions separately (namely parallel-to-joists and perpendicular-to-joists).

Table 7.3: Parametric analyses - diaphragm dimensions

ID	L [m]	B [m]	AR
4×4	4.0	4.0	1.0
4×8	4.0	8.0	0.5
6×6	6.0	6.0	1.0
6×8	5.7	8.0	0.7
6×12	6.0	12.0	0.5

### 7.4.2 DIAPHRAGM CONFIGURATIONS

As-built and retrofitted diaphragm configurations were considered in the study. In particular the straight sheathed configuration was assumed as representative of as-built diaphragm while for the retrofitted configuration, techniques presented in the previous chapters were considered.

---

#### 7.4.2.1 As-built straight sheathed diaphragms

Straight sheathed diaphragms were assumed as representative for the as-built configuration. Material properties and element geometries considered in the study are listed in Table 7.4. For comparative purposes, two joist section geometries were considered. Slender joist cross-section (*SL*), featuring an aspect ratio  $h/b=6$ , is representative of diaphragm constructions that can be typically encountered in URM buildings of Northern Europe, North America and Oceania while squat joist type (*SQ*,  $h/b=1.5$ ) is typical of diaphragm constructions in the Mediterranean region. Nonlinear load-slip behavior of floorboard-to-joist connections was set according to the experimental results presented by Schiro et al. (2018) and representative of the shear response of aged timber-to-timber nailed connections. A nail couple was inserted at each floorboard-to-joist intersection. Floorboards were interrupted considering the maximum floorboard length listed in Table 7.3. Floorboards interruptions were staggered according to the directions given in ATC (1981). Floorboard interruptions were always placed at floorboard-to-joist intersection, avoiding the presence of un-supported floorboard ends. In the presence of floorboard interruptions, a nail couple was inserted at each floorboard end. Retrofitted diaphragm configurations were obtained by adding elements to the straight sheathed diaphragm model as described in the following paragraphs. Due to the uncertainties about its presence, inter-floorboard friction was disregarded.

Table 7.4: As-built diaphragms: materials and details

Item	Value
Floorboard section	150 x 20 mm
SL Joist section	50 x 300 mm
SQ Joist section	150 x 200 mm
Timber grade (floorboards & joists)	C 24 <sup>1</sup>
Joist spacing	500 mm
Nail couple spacing <sup>2</sup>	100 mm
Maximum floorboard length	4000 mm

<sup>1</sup> material properties are reported in [CEN (2009)]

<sup>2</sup> nail properties as per vintage nail connections in Schiro et al. (2018)

#### 7.4.2.2 diaphragms with plywood overlays

Retrofit details were selected according to Chapter 4. Plywood sheathing consisted of  $1200 \times 2400 \text{ mm}^2$  9mm-thick F8 grade [AS/NZS (2008)] plywood sheets arranged on the diaphragm surface according to the *PI* layout in which sheet orientation is alternated. Plywood sheets were modeled as linear elastic 2D shell elements accounting

for material orthotropy. Blocking elements were interposed between joists in the perpendicular-to-joists direction and modeled as pinned 1D frame elements. Plywood-to-solidwood connection pattern was assumed consistently with the *E150\_F300* scheme. Namely, sheets were supposed to be screwed to the joists and blocking elements through the floorboards along the diaphragm perimeter with an average 150 mm spacing (screws intersected 2 shear planes, specifically sheet-to-floorboard and floorboard-to-joist/blocking). Except for diaphragm perimeter, sheets were nailed to the straight sheathing underneath without affecting the joists, with a 150 mm spacing along the sheet edges and according to a 300 mm grid pattern on the internal sheet portion. Shear load vs. slip response of the screws along the diaphragm perimeter was assumed consistently with the experimental results reported in Schiro et al. (2018) while nailed plywood-to-solidwood connection response was predicted according to the formulation proposed by McLain (1975) and updated by Pellicane et al. (1991) based on the selected geometries and material properties. Sheet-to-sheet contact phenomenon was modeled by means of *non-linear gap links* interposed between the edges of adjacent plywood sheets.

#### **7.4.2.3 Diaphragms with diagonal sheathing overlays**

Diaphragms retrofitted by means of an additional floorboard layer oriented at 45 degrees with respect to the straight sheathing, were modeled according to Chapter 5. Blocking elements were interposed between the joists at the diaphragm ends and modeled consistently with the description given in the previous paragraph. Cross section, material properties and maximum element length of the additional floorboards were assumed consistently with the corresponding features of the straight sheathing listed in Table 7.4. Diagonal floorboards, represented by means of 1D frame elements, were nailed to the joists and to the blocking elements by means of nail couples at each floorboard-to-joist intersection. Consistently with the assumption related to straight sheathing, interruptions of additional floorboards were always placed in correspondence with the joist elements and were appropriately staggered. Spacing of each nail couple was assumed equal to 130 mm, with the couples aligned with the joist/blocking element underneath (nail couples were inclined  $45^\circ$  with respect to floorboard axis). At each floorboard end (in correspondence with floorboard interruptions and along the diaphragm perimeter) three nails spaced at 65 mm were inserted to connect the floorboard end to the underlying joist/blocking element. The stiffening effect of the additional nails on the existing floorboard-to-joist connection was considered. Non-linear links representative of the additional nails were split into two stretches (one each shear plane). The joint between the two shear planes (placed at existing-flooring level) was connected to the closest floorboard of the straight sheathing by means of a rigid link element.

#### 7.4.2.4 Diaphragms with CLT panel overlays

Such retrofit technique consists in the use of CLT panels laid over the existing diaphragm flooring. The retrofit details were selected consistently with the *PI-CI-A150* configuration analyzed in Chapter 6. The addition of a CLT panel continuously spanning over each underlying joist was assumed. Diaphragms retrofitted with CLT panels were modeled according to Chapter 6. The use of three-layered 60 mm thick CLT panels obtained from C24 timber boards was considered. The panels were modeled as 2D linear-elastic shell elements. Material orthotropy was accounted for by mediating the stiffness of each individual layer over the panel thickness. The in-plane shear stiffness was evaluated according to the analytical formulation proposed by Bogensperger et al. (2010). The panels were laid over the existing flooring so that the external board layers resulted oriented in the parallel-to-joists direction. Adjacent panels were interconnected by means of screws inclined at  $45^\circ$  to the horizontal and perpendicular to the panel edges so that the connector is loaded in shear for shear forces acting parallel to the panel-to-panel interface. Diaphragms with CLT overlays were analyzed in the *SQ* joist configuration only, being *SL* joists not suitable for the insertion of panel-to-joist screws in the practice.

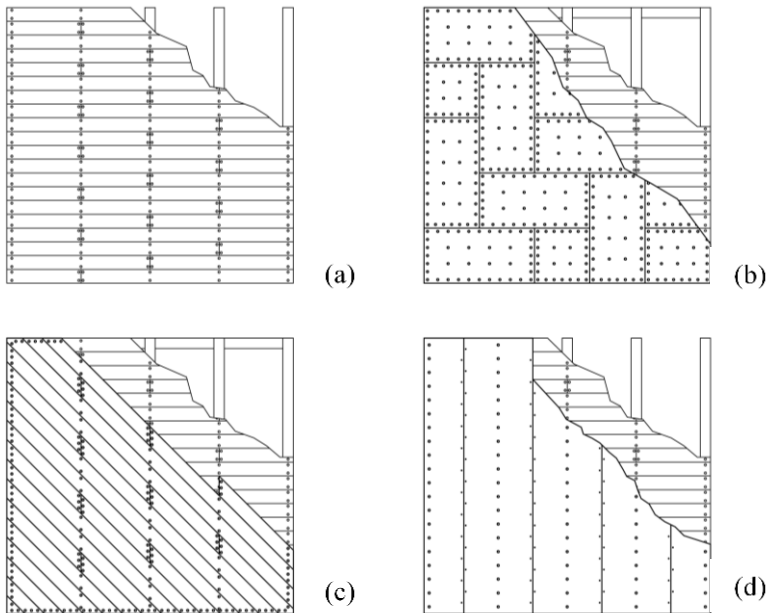


Figure 7.4 Diaphragm constructions: a) Straight sheathing; b) Plywood overlain diaphragms; c) Diagonal sheathing over straight sheathing; d) CLT panels over straight sheathing. For clarity reasons, some dimensions are not in scale

### 7.4.3 DYNAMIC INPUTS

Dynamic inputs consisted of two sets of seven natural accelerograms each, selected from the PEER-GMD (Table 7.5 and Table 7.6). Accelerograms were scaled to spectral-compatibility with two acceleration response spectra defined according to ASCE 7-10 [ASCE (2010)] and representative of two peak ground acceleration levels, namely 0.2g (Sacramento, CA) and 0.4g (Seattle, WA). Response spectra were evaluated considering a Class D (stiff) soil and a 475-years return period [ASCE (2010)]. In both cases, spectral-compatibility of the selected scaled accelerograms was checked within the 0.15s - 3s period range. Deviation between accelerogram set mean accelerations and the selected response spectra was always lower than 10% (see Figure 7.5).

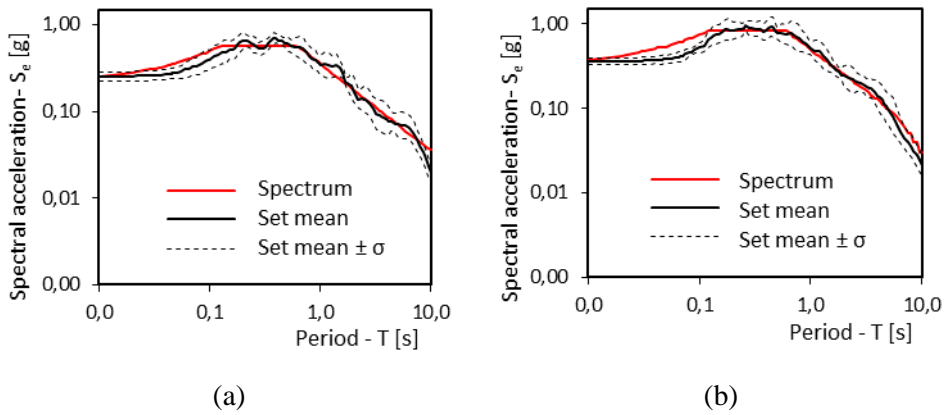


Figure 7.5 Spectral compatibility check: a) 0.2g set vs Sacramento response spectra; b) 0.4g set vs Seattle response spectra

Table 7.5: Ground motion inputs – PGA = 0.2g set

PEER #	Record ID	Year	Magnitude	Scale factor
9	Borrego	1942	6.5	3.44
293	Irpinia	1980	6.9	3.52
323	Coalinga	1983	6.4	4.05
756	Loma Prieta	1989	6.9	2.10
2694	Chi Chi	1999	6.2	1.51
6963	Darfield	2010	7.0	4.49
8057	Christchurch	2011	6.2	5.37

Table 7.6: Ground motion inputs – PGA = 0.4g set

PEER #	Record ID	Year	Magnitude	Scale factor
51	San Fernando	1971	6.6	6.59
578	Taiwan Smart	1986	7.3	1.31
832	Landers	1992	7.3	1.70
1094	Northridge	1994	6.7	4.37
1144	Gulf of Aqaba	1995	7.2	2.87
1791	Hector Mine	1999	7.1	2.74
5793	Iwate	2008	6.9	3.28

#### 7.4.4 BOUNDARY CONDITIONS AND COMMON ASSUMPTIONS

Diaphragm tributary masses due to dead loads and live loads combined according to ASCE 7-10 [ASCE (2010)], were uniformly spread over the diaphragm area at the flooring level. Masses representative of out-of-plane loaded masonry walls, whose stiffness contribution was neglected in the analyses, were applied at a discrete number of joints placed along diaphragm ends. For this purpose, 400 mm thick masonry walls (masonry *s.g.* = 18kN/m<sup>3</sup>) and a 3 m inter-story height were considered. Because mass increments related to the retrofit elements addition are limited when compared to overall mass, the values listed in Table 7.7 were assumed in all the analyses.

Table 7.7: Diaphragm masses

Mass source	Value	Unit
Diaphragm dead loads	2.0	[kN/m <sup>2</sup> ]
Diaphragm live loads	2.0	[kN/m <sup>2</sup> ]
Live loads combination factor	0.3	[---]
Out-of-plane loaded walls	22.0	[kN/m]

Assumed boundary conditions are illustrated in Figure 7.6. In-plane rotation of parallel-to-loading diaphragm ends was allowed so as not to restrain the possible overall diaphragm flexural behavior. Out-of-plane DoFs were restrained along the diaphragm perimeter. In perpendicular-to-joists analyses, axially rigid rods were interposed between the joists to allow inertia force distribution over the diaphragm width. Both in-plane and out-of-plane restraints were applied at the joist level.

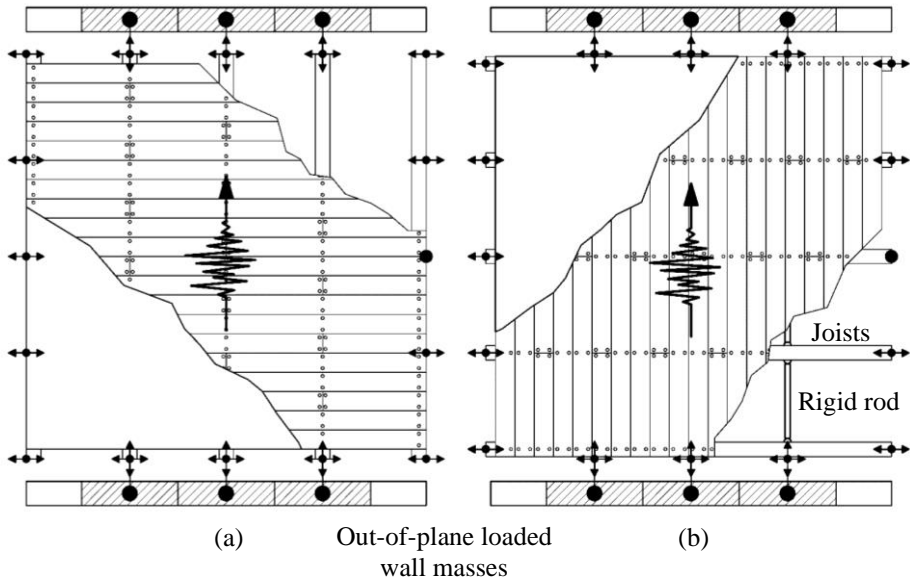


Figure 7.6 Boundary conditions: a) parallel-to-joists analyses; b) perpendicular-to-joists analyses. Arrows are free translational DoFs at restrained joints

## 7.5 RESULTS AND DISCUSSION

Analyses results are compared in terms of diaphragm drift ( $dr$ ) and unit shear ( $v_d$ ) demands. Diaphragm drift is defined as mid-span displacement  $\delta$  over half diaphragm span length according to equation (7.1). Diaphragm span  $s$  is equal to  $B$  (Table 7.3) for parallel-to-joists analyses and is equal to  $L$  for perpendicular-to-joists analyses. Unit shear is defined as half total load on diaphragm ( $F$ ) over diaphragm width ( $w$ ) according to equation (7.2). Diaphragm width is equal to  $L$  (Table 7.3) for parallel-to-joists analyses and is equal to  $B$  for perpendicular-to-joists analyses.

$$dr = \frac{2 \cdot \delta}{s} \quad (7.1)$$

$$v_d = \frac{F}{2 \cdot w} \quad (7.2)$$

For each accelerogram of each set, maximum absolute values of drift and unit shear were extrapolated from the numerical outputs. Demands listed in Table 7.8 and Table 7.9 and illustrated in Figure 7.7 were calculated by mediating such envelope values among each set of accelerograms. For parallel-to-joists analyses results are reported without joist type distinction since its influence was observed to be negligible. Conversely, joist type was observed to significantly affect results when accelerations

were applied in perpendicular-to-joists direction, especially in the case of straight sheathed diaphragms. This finding is in good agreement with the outcomes of nonlinear static simulations presented in the previous chapters which highlighted that perpendicular-to-joists in-plane stiffness of straight sheathed diaphragms is strongly affected by the in-plane bending stiffness of joists. In the case of retrofitted diaphragms, the greater flooring contribution to the in-plane stiffness makes the joist type influence less relevant but still appreciable. Joist influence factors ( $\alpha_j$ ) evaluated according to equation (7.3) are listed in Table 7.10. In equation (7.3)  $x$  is the parameter on which joist influence factor is evaluated.

$$\alpha_j = 100 \cdot \frac{|x_{SQ} - x_{SL}|}{x_{SL}} \quad (7.3)$$

Expectedly, retrofitted diaphragms were observed to be subjected to greater force demands and smaller displacement demands compared to as-built straight sheathed construction.

*Table 7.8: Dynamic demands on diaphragms - parallel-to-joists analyses*

Diaphragm type	0.2g set		0.4g set	
	$v_d$ [kN/m]	$dr$ [%]	$v_d$ [kN/m]	$dr$ [%]
Straight	4.58	2.96	6.88	4.82
PLY	10.58	0.48	13.50	0.90
Diagonal	11.28	0.32	14.78	0.52
CLT	15.58	0.36	20.48	0.52

*Table 7.9: Dynamic demands on diaphragms - perpendicular-to-joists analyses*

Diaphragm type	Joist type	0.2g set		0.4g set	
		$v_d$ [kN/m]	$dr$ [%]	$v_d$ [kN/m]	$dr$ [%]
Straight	SL	4.70	2.66	6.64	3.62
	SQ	10.82	0.74	16.34	1.14
PLY	SL	8.40	0.24	13.28	0.42
	SQ	8.38	0.14	13.20	0.22
Diagonal	SL	9.20	0.16	12.72	0.22
	SQ	9.26	0.10	13.12	0.18
CLT	SQ	9.76	0.08	16.16	0.16

Table 7.10: Influence of joist type on dynamic demands ( $\alpha_j$ )

Diaphragm type	0.2g set		0.4g set	
	$v_d$ [%]	dr [%]	$v_d$ [%]	dr [%]
Straight	130.21	72.18	146.08	68.51
PLY	0.24	41.67	0.60	47.62
Diagonal	0.65	37.50	3.14	18.18

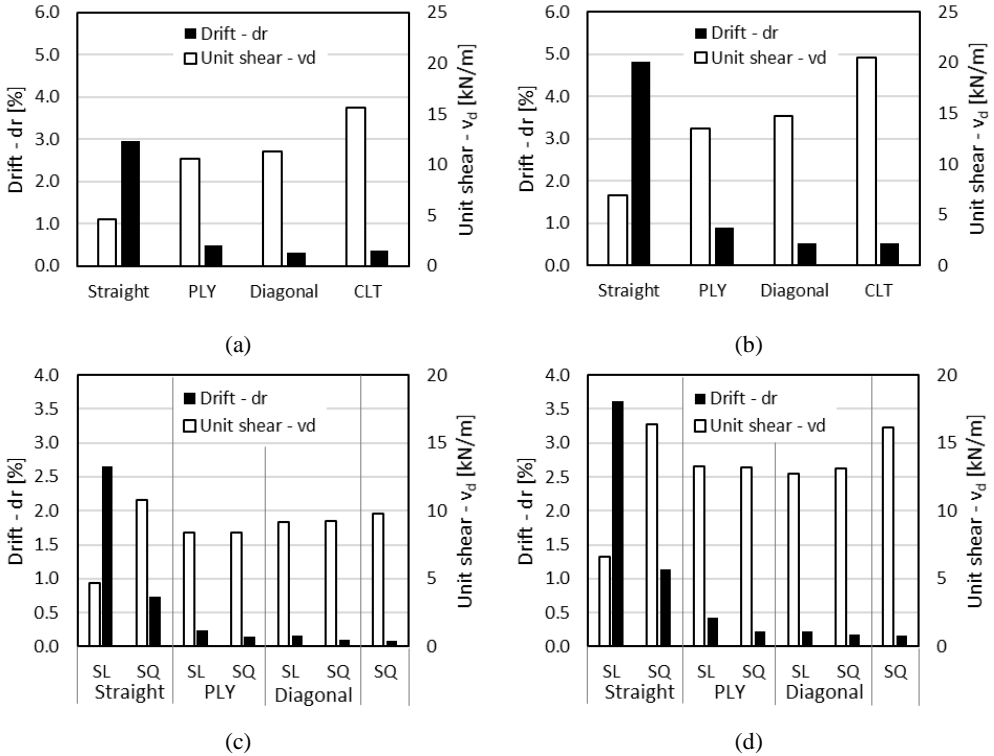


Figure 7.7: Nonlinear dynamic analyses deflection and force demands on diaphragms, mean values: a) Parallel-to-joists, 0.2g set; b) Parallel-to-joists, 0.4g set; c) Perpendicular-to-joists, 0.2g set; d) Perpendicular-to-joists, 0.4g set

Qualitative demand estimation for the  $6 \times 8$  diaphragm, based on the 0.2g PGA acceleration and displacement response spectra, is illustrated in Figure 7.8. Diaphragm in-plane periods were evaluated according to the assessment procedure proposed in NZSEE 2017 [NZSEE (2017)]. In-plane stiffness values evaluated in Chapters 3 to 6 and representative masses listed in Table 7.7 were assigned as inputs. For parallel-to-joists shaking direction (Figure 7.8-a), as-built diaphragm period was comprised within the constant velocity part of the spectrum. Consequently, smaller periods related to

retrofitted configurations implied higher spectral accelerations (and, therefore, higher seismic force demands). In the selected case scenario, each of the retrofitted configurations led to in-plane periods comprised within the constant acceleration part of the spectra for which, according to the spectral shape, the maximum force demands are expected. Similar trends were observed with the diaphragm being subjected to perpendicular-to-joists shaking (Figure 7.8-b), except for the case of the as-built configuration featuring squat joists. In such case, the in-plane period was already comprised within the constant-acceleration part of the spectrum and stiffening interventions resulted in smaller displacement demands without to imply higher force demands. Demand ratios (= retrofitted/AsB) obtained from the numerical outputs were found to be quite consistent with the response spectra-based predictions (Table 7.11).

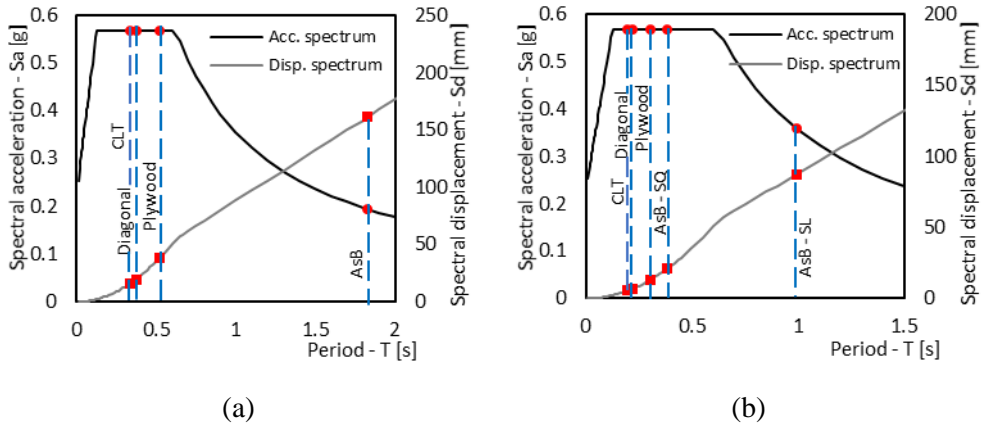


Figure 7.8: 6x8 diaphragm, qualitative demand evaluation: a) Parallel to joists; b) Perpendicular to joists

Table 7.11: 6x8 diaphragm, seismic demand ratios comparison: FEM results vs spectrum predictions

Shaking	Configuration	FEM		Spectrum	
		$F_d$	$\Delta_d$	$F_d$	$\Delta_d$
Parallel to joists	Plywood	2.84	0.16	2.92	0.23
	Diagonal	2.89	0.08	2.92	0.12
	CLT	3.59	0.08	2.92	0.10
Perpendicular to joists	SQ/SL	2.55	0.30	1.58	0.24
	Plywood	1.94	0.07	1.58	0.15
	Diagonal	2.20	0.05	1.58	0.08
	CLT	1.90	0.02	1.58	0.06

## 7.6 STANDARD COMPARISON

Assessment procedures proposed in NZSEE 2017 [NZSEE (2017)] and ASCE 41-17 [ASCE (2017)] and summarized in Chapter 2, were implemented to predict seismic demands on diaphragms. Since the aforementioned Standards refer to slender joist diaphragm construction, the sole *SL* joist configuration was considered in perpendicular-to-joists analyses. Consistency between calculated values and nonlinear dynamic analysis results was evaluated in terms of errors  $e_m$  as per equation (7.4), where  $X$  is the calculated parameter (force or displacement demand), and  $X_{FEM}$  is the corresponding value extrapolated from numerical analyses.

$$e_m = \frac{X - X_{FEM}}{X_{FEM}} \quad (7.4)$$

From mean errors listed in Table 7.12 a substantial overestimation of both force and displacement demands can be appreciated for each of the selected diaphragm typologies. Greater errors were found in the case of as-built diaphragm configurations.

Table 7.12: Standard assessment procedures vs. numerical results - mean errors ( $e_m$ )

Direction	Diaphragm type*	PGA 0.2g			PGA 0.4g		
		ASCE $V_d$	NZSEE 2017 $V_d$	$\Delta_d$	ASCE $V_d$	NZSEE 2017 $V_d$	$\Delta_d$
Parallel to joists	AsB	3.14	1.46	0.09	2.88	2.48	0.01
	Plywood	1.22	0.70	1.08	1.94	1.47	1.40
	Diagonal	1.10	0.58	1.67	1.76	1.30	2.35
Perpendicular to joists	AsB	2.55	1.71	-0.05	2.13	2.86	0.00
	Plywood	1.17	0.45	1.31	0.58	1.13	1.82
	Diagonal	1.01	0.44	1.59	0.61	1.11	2.31

\*AsB = As built; Plywood = Plywood overlain; Diagonal = Diagonal sheathing over straight sheathing

## 7.7 CONCLUSIONS

Effects of diaphragm in-plane stiffness variations on seismic shaking-induced force and displacement demands were investigated by means of nonlinear-dynamic modeling. Diaphragms were analyzed in the as-built and retrofitted configurations selected consistently with the work presented in Chapters 3 to 6. For stiffness over mass ratios representative of the as built configuration and under the seismic inputs considered herein, the retrofit interventions were found to be capable of significantly mitigate the

---

displacement demand with the side effect of increasing force demand. In the case of as-built diaphragms with squat joist-sections, the higher original stiffness led to displacement mitigation without remarkable force increase.

## 7.8 REFERENCES

- Agbabian, M. S., Barnes, S. B. and Kariotis, J. C. (ABK) (1981). "Methodology for mitigation of seismic hazards in existing unreinforced masonry buildings. Diaphragm testing." National Science Foundation. El Segundo, California.
- AS/NZS (Australian/New Zealand Standard). (2008). «Structural Plywood», AS/NZS 2269:2008.
- ASCE (American Society of Civil Engineers). (2017). "Seismic Evaluation and Retrofit of Existing Buildings" *ASCE 41-17*, Reston, Virginia.
- ASCE (American Society of Civil Engineers). (2010). "Minimum design loads for buildings and other structures" *ASCE/SEI 7-10*, Reston, Virginia.
- Applied Technology Council (ATC). (1981). «Guidelines for the design of horizontal wood diaphragms». Berkeley, California.
- Bogensperger, T., Moosbrugger, T., Silly, G., (2010) «Verification of CLT-Plates under Loads in plane». In Proceedings of WCTE 2010 – Word Conference on Timber Engineering, 2010.
- CEN (European Committee for Standardization) (2009). "Structural timber - Strength classes". *EN 338*. Brussels, Belgium.
- Giongo, I., Dizhur, D., Tomasi, R. and Ingham, J. M. (2015). "Field testing of flexible timber diaphragms in an existing vintage URM building". *Journal of Structural Engineering*, vol. 141, 2015.
- McLain, T. E., (1975). «Curvilinear load-slip relations in laterally-loaded nailed joints», PhD thesis, Colorado state University, Colorado.
- NZS (Standards New Zealand) (1993). "Timber Structures Standard". *NZS 3603:1993*. Wellington, New Zealand.
- NZSEE (New Zealand Society for Earthquake Engineering) (2017). "Assessment and improvement of the structural performance of buildings in earthquakes". *NZSEE 2017*. Wellington, New Zealand.
- PEER, "PEER-NGA-West2 Ground Motion Database", Berkeley, California, USA
- Pellicane, P. J., Stone, J. L., Vanderbilt, M. D., (1991). «Generalized Model for Lateral Load Slip of nailed Joints», *Journal of Materials in Civil Engineering*, ASCE, Vol. 3, No. 1.
- Piazza, M., Tomasi, R., Modena, R. (2005) "Strutture in legno", ISBN: 9788820335830, Hoepli ed., Milan, Italy, *in Italian*.

---

Schiro, G., Giongo, I., Ingham, J., Dizhur, D., (2018). «Lateral performance of as-built and retrofitted timber diaphragm fastener connections», *Journal of Materials in Civil Engineering*, vol. 30 (1), ISSN: 0899-1561, [https://doi.org/10.1061/\(ASCE\)MT.1943-5533.0002110](https://doi.org/10.1061/(ASCE)MT.1943-5533.0002110).

Wilson, A. W. (2012). “Seismic assessment of timber floor diaphragms in unreinforced masonry buildings”. Doctoral dissertation, The University of Auckland, Auckland, New Zealand.

---

# **PART 2**



# 8 USE OF TIMBER FOR URM WALL RETROFIT

## 8.1 LITERATURE REVIEW

The seismic vulnerability is recognized as being the most important factor to consider in the design phase of structural strengthening systems for unreinforced masonry (URM) buildings. Recent earthquake events occurred in Italy [Sorrentino et al. (2018), Fiorentino et al. (2018)] have shown that a change of the original use to situations implying higher loads along with improper interventions on historic masonry structures may lead to disproportionate damage levels. Given the importance of the subject, researchers have proposed a wide range of strengthening solutions for URM buildings over the last decades. The literature review reported herein focuses on the research related to timber-based retrofit solutions for URM walls. The research reported by Giongo et al. (2017) was reserved a dedicated paragraph (section 8.2) since it represents the starting point for the research presented in Thesis Part 2.

Sustersic and Duijc (2012) investigated the use of cross laminated timber (CLT) panels as retrofitting solution for reinforced concrete (RC) frames with masonry infills. The Authors modeled a three-story RC building representative of the Southern European construction practice of the early 70's. Nonlinear static simulations were undertaken considering the sole RC frame and the RC frame infilled with alternative CLT panel arrangements as illustrated in Figure 8.1. Panels were connected to the RC frame by means of common steel angle brackets. In terms of maximum allowable PGA, the Authors observed an improvement ranging between 20% and 90% depending on the panel disposition scheme. The Authors also reported for the importance of using ductile connection systems. The thermal insulation and thermal damping features of the system were also investigated highlighting that the proposed solution allows to exploit the

thermal insulation properties of timber, eventually also implementing additional insulation layers.

The Authors furtherly investigated the retrofit system by means of shake table tests of masonry-infilled RC frames as reported in Sustersic and Dujic (2014). A reinforced concrete frame and a masonry-infilled RC frame were tested in both the un-strengthened and strengthened configurations (see Figure 8.2). CLT panels were connected to the structure at floor level by means of the system illustrated in Figure 8.2-d. The retrofit was reported to be effective even when applied to the previously damaged structure restoring its original stiffness and strength. The retrofitted systems underwent 30% smaller inter-story drift levels compared to the as built configuration.

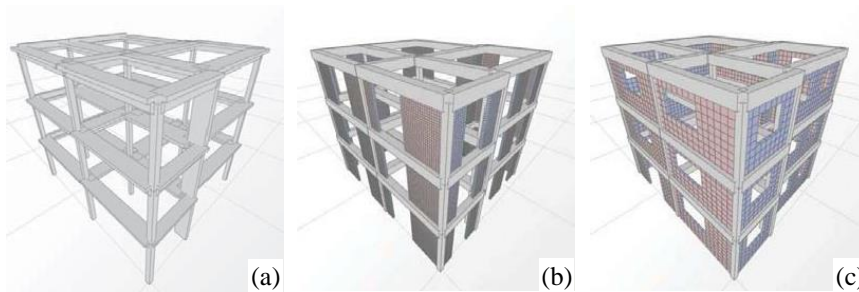


Figure 8.1: FE models considered by Sustersic and Dujic (2012): a) RC frame; b) “Short panels” arrangement; c) “Long panels” arrangement. Reproduced from Sustersic and Dujic (2012)



Figure 8.2: Specimens tested by Sustersic and Dujic (2014): a) RC frame; b) Masonry infilled RC frame; c) Retrofitted specimen; d) Timber to RC frame connection. Reproduced from Sustersic and Dujic (2014)

Lucchini et al. (2014) proposed to insert timber panels in the internal side of the walls, connected through epoxy grouted threaded steel rods in order to preserve the original façade. The proposed technique implied the masonry walls being completely superseded

by the internal CLT skeleton which also provides the masonry elements out-of-plane restraints (see Figure 8.3).



Figure 8.3: Example of façadism intervention. Reproduced from Lucchini et al. (2014).

Dizhur et al. (2017) proposed to connect a timber frame to the inner façade of the building using screw-type fasteners as illustrated in Figure 8.4. The system was tested by means of a series of dynamic out-of-plane shaking tests considering alternative retrofit details. Brick masonry specimens were 3.3 m high  $\times$  1.2 m wide  $\times$  0.23 m thick and were fixed to the shake table at the base and connected to a timber floor portion placed at 3 meters height. The walls also featured a 30 cm high parapet. Retrofitted specimens were observed to resist higher PGA levels experiencing smaller out of plane displacements compared to the sole wall configuration.

Pozza et al (2017) studied the solutions with CLT panels being connected to the external or the internal side of the walls. In the former case the timber panels were fastened to a metallic curb anchored to the wall at the floor level, in the latter case the panels were connected to the floor by means of an L-shaped metallic curb as illustrated in Figure 8.5. Two 1.4 m high  $\times$  0.9 m wide  $\times$  0.12 m thick brick masonry samples were built and tested under cyclic in-plane loading in the as-built and retrofitted configurations. The retrofitted wallet exhibited greater in-plane strength (2.5 times), ductility (2 times) and energy dissipation compared to the as-built. The Authors also performed numerical simulations in the Open Sees framework considering an entire two-story building façade reporting for a significant improvement of the in-plane behavior, whose efficiency depended on retrofit details.

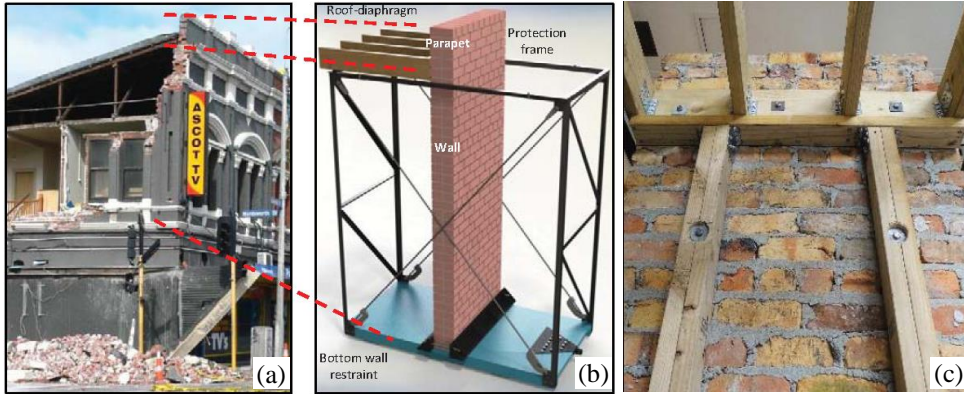


Figure 8.4: Experimental campaign presented in Dizhur et al. (2017): a) b) Test setup; c) Timber frame connected to masonry. Reproduced from Dizhur et al. (2017)

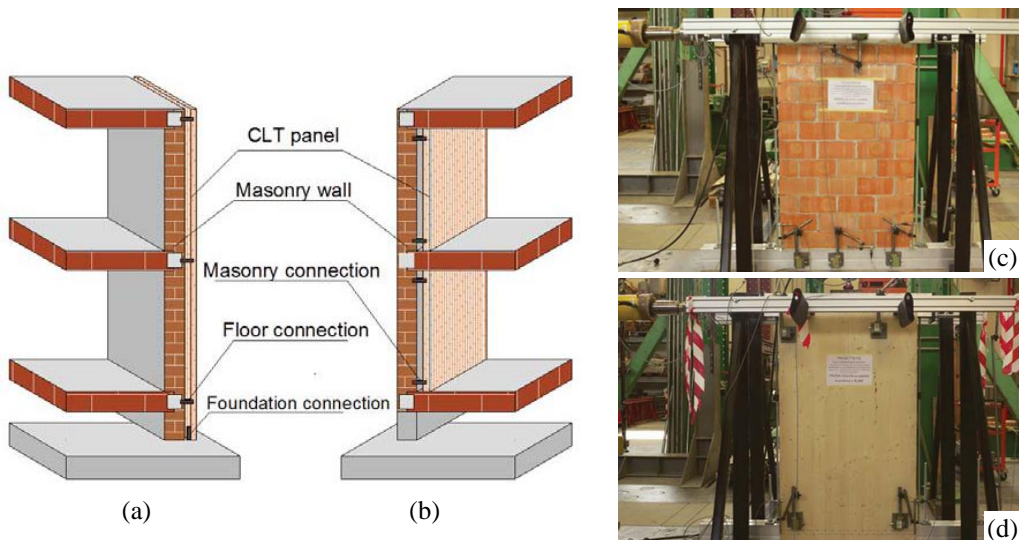


Figure 8.5: Solutions considered in Pozza et al. (2017): a) CLT panels on the outer façade; b) CLT panels on the inner wall face; c) As-built wall specimen; d) Retrofitted wall specimen. Reproduced from Pozza et al. (2017)

Guerrini et al. (2020) tested the effectiveness of a retrofit system based on the use of a timber frame mechanically connected to the masonry and to the floors braced by means of orientated strand board (OSB) panels as illustrated in Figure 8.6. Two purposely built 2.7 m high  $\times$  2.0 m wide  $\times$  0.1 m thick single-wythe masonry piers were subjected to cyclic in-plane loading. One specimen was tested in the as-built configuration while the other was retrofitted prior to testing. The Authors reported that the as built specimen initially developed a flexural-rocking mechanism which subsequently developed to a

sliding shear failure. The shear sliding was inhibited by the timber frame, therefore the retrofitted specimen maintained the flexural behaviour up to the formation of the diagonal cracks which led to failure. The timber frame was also reported to carry almost the entire vertical load at ultimate conditions due to the toe crushing experienced by the masonry. The shear capacity of the retrofitted pier was 1.35 times greater compared to the as-built specimen, while displacement capacity increment related to the retrofit was almost 170%.

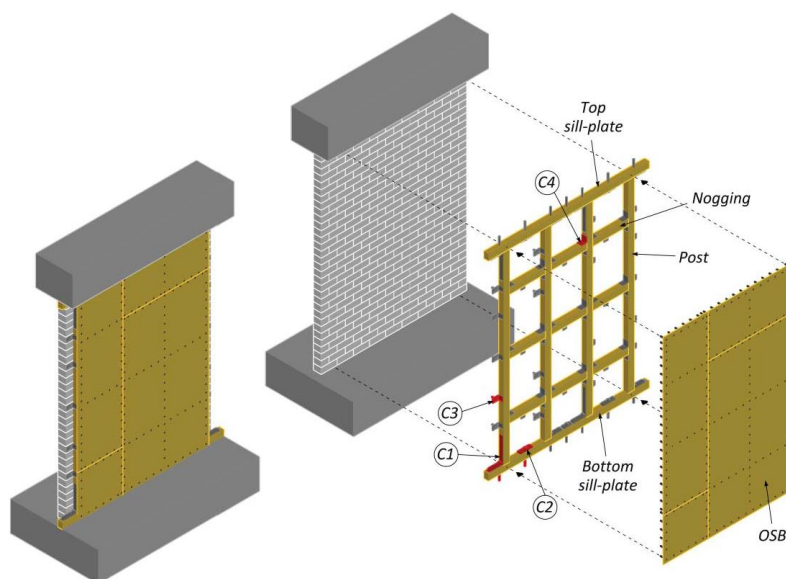


Figure 8.6: Retrofit strategy tested by Guerrini et al. (2020), reproduced from Guerrini et al. (2020)

## 8.2 RESEARCH PRESENTED IN GIONGO ET AL. (2017)

Giongo et al. (2017) proposed to use a timber-based panel connected to the masonry by means of dowel-type fasteners which can be either grouted or screwed in the wall depending on the situation (Figure 8.7 reports a cross-sectional view of the solution). Such work represents the starting point of the research presented in Thesis Part 2, therefore it is reported in detail herein.

The research comprised numerical modeling of masonry piers subjected to in-plane loading in the as built and in the retrofitted configuration. The goal was to investigate the effectiveness of the selected retrofit strategy based on reasonable input data and to identify the influent parameters.



Figure 8.7: Schematic representation of retrofitting technique proposed by Giongo et al. (2017). Reproduced from Giongo et al. (2017)

Models were based on the TNO DIANA finite element software [Manie and Kikstra (2014)]. Masonry walls were modeled by means of *quadratic curved shell* 2D elements featuring a *total strain* constitutive behavior and a *smearred cracking* approach [Manie and Kikstra (2014)]. Masonry peak conditions were implemented according to a *Rankine* failure surface identified by masonry tensile and compressive strength values. Material softening was set as linear in tension and parabolic in compression according to fracture energy values set according to Lourenco (2001) and CEB-FIP (1993). Timber panels were modeled as linear-elastic 2D *quadratic curved shell* elements featuring mechanical properties evaluated according to Bogensperger et al. (2010) and CEN (2009). Timber to masonry connections and hold downs were modeled by means of *point interface* elements while *line interfaces* were used to simulate panel to panel and panel to base contact.

A series of numerical analyses were undertaken to assess the influence of parameters such as masonry wall aspect ratio ( $h_w/l_w = \text{height/length}$ , ranging from 0.7 to 1.1), masonry wall thickness ( $t_w = 250$  mm and  $t_w = 400$  mm), masonry material properties, timber panel thickness ( $t_p = 60$  mm and  $t_p = 99$  mm; 3-layer panels), timber panel length ( $l_p = l_w$ ,  $l_p = l_w/2$  and  $l_p = l_w/3$ ), stiffness ( $k_C$  from 10 kN/mm to 50 kN/mm) and strength ( $r_C$  from 10 kN to 30 kN) of the panel-to-wall connectors, stiffness of tension and shear anchors ( $k_T$ ,  $k_S$  from 50 kN/mm to rigid). Various vertical stress levels on top of the models ( $\sigma_n$ ) were applied to simulate alternative conditions.

Not surprisingly, the Authors observed that for piers showing rocking behavior, the retrofit intervention effectiveness was determined by the effectiveness of the tension

anchors at the base even if the influence of the hold down stiffness was reported to be “very limited” (see Figure 8.8-a, curves W1\_P1\_2T1\_K5 and W1\_P1\_2TR\_K5).

Regarding walls that in the un-strengthened configuration failed in rocking, the Authors reported for capacity increments in the range of 20 – 40%, while the use of distributed connections over the wall surface prevented for the rocking phenomena engaging the wall shear capacity as illustrated in Figure 8.8-b, -c.

The Authors also considered the effects of implementing alternative CLT panel layouts (Figure 8.9-a). Models featuring two shorter panels ( $l_p = l_w/2$ , W1\_P3\_4T1\_K5) led to the same capacity increments related to the adoption of one single panel ( $l_p = l_w$ , W1\_P1\_2T1\_K5).

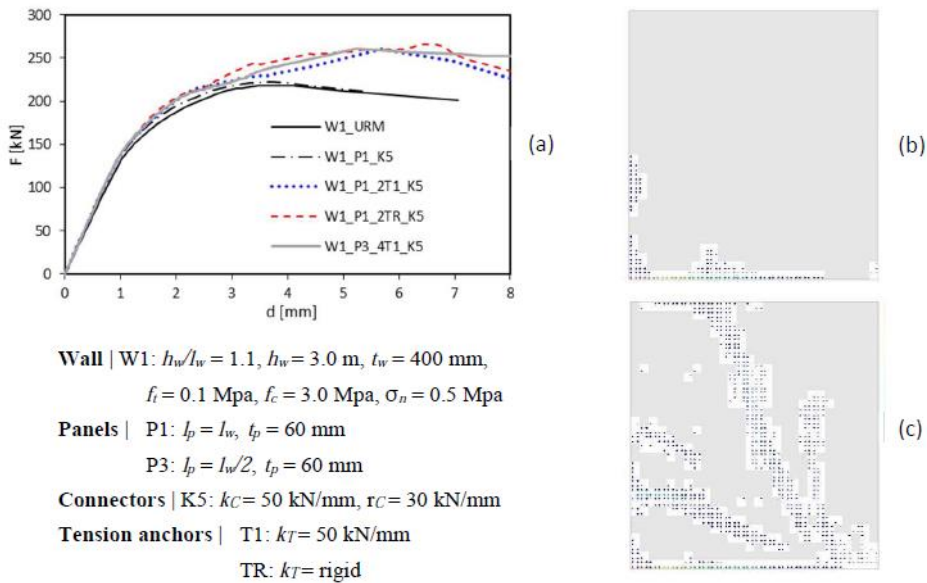


Figure 8.8: Analysis result examples – W1 wall – “Rocking behaviour” - a) capacity curve; b) crack pattern (peak capacity) of the unreinforced wall; c) crack pattern (peak capacity) of the retrofitted wall. Reproduced from Giongo et al. (2017)

For piers that originally failed in shear, a greater capacity increment compared to the “rocking” piers was reported for (capacity increment ranging between 25% and 50%). Models also suggested that the retrofit strategy can prove itself beneficial even without to implement base anchors. This was attributed to “the stitching effect associated with the panel-to-wall connectors, that limited strain concentration and resulted in a more homogeneous crack distribution”.

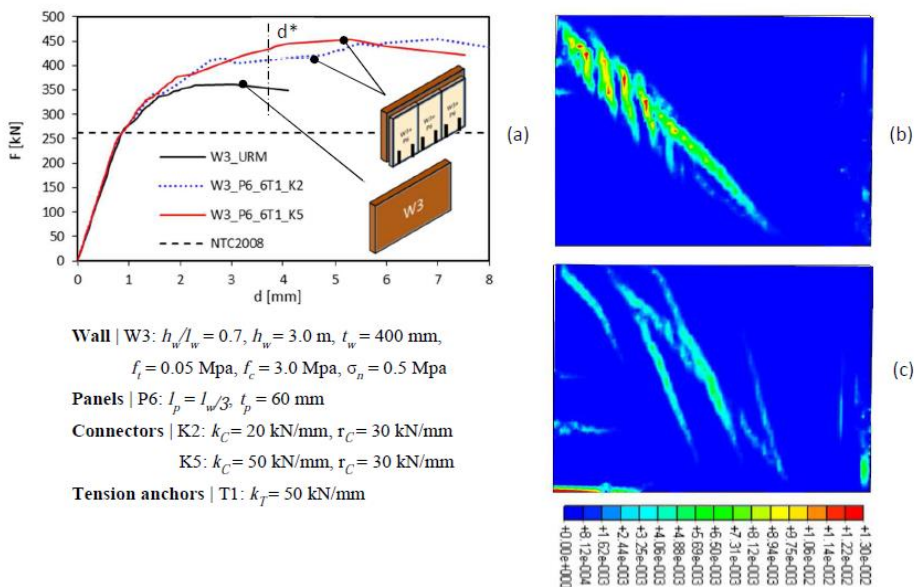


Figure 8.9: Analysis result examples – W1 wall – “Shear cracking behaviour” - a) capacity curve; b) principal tot. strain of the unreinforced wall (at  $d^*$ ); c) principal tot. strain of the retrofitted wall (at  $d^*$ ). Reproduced from Giongo et al. (2017)

### 8.3 CONCLUSIONS

The literature review reported in paragraph 8.1 reflects the growing interest for timber-based retrofit solutions for URM walls. The research presented in Giongo et al. (2017), which represents the starting point of the work presented in Thesis Part 2 consisted in the preliminary evaluation of the effectiveness of the solution presented by the Authors which was extended during the PhD program. The previously reported numerical results highlighted the effectiveness of the selected timber-based retrofit system in improving in-plane behavior of masonry walls. Nonlinear static analyses based on reasonable input parameters regarding the behavior of the timber-masonry connection system highlighted a significant capacity increase ( $\geq 20\%$ ) for URM walls failing both in rocking and diagonal shear. On the other hand, the retrofit was not observed to affect wall stiffness making it suitable to be implemented in cases where a selection of walls must be strengthened without to affect the original horizontal load distribution.

## 8.4 REFERENCES

- Bogensperger, T., Moosbrugger, T., Silly, G., (2010) «Verification of CLT-Plates under Loads in plane». In Proceedings of WCTE 2010 – Word Conference on Timber Engineering, 2010.
- CEB-FIP (Comite Euro-International Du Beton) (1993) “Model Code 90”, Thomas Telford Ltd, 1993.
- CEN (European Committee for Standardization) (2009). “Structural timber - Strength classes”. EN 338. Brussels, Belgium.
- CEN (European Committee for Standardization) (2005). “Eurocode 6: Design of masonry structures – Part 1-1: General rules for reinforced and unreinforced masonry structures” . *EN1996-1-1*. Brussels, Belgium.
- Churilov, S., Dumova-Jovanoska, E. (2011) “Experimental evaluation of in-plane shear behaviour of unreinforced and strengthened brick masonry walls”, in 7th International Conference AMCM 2011, Kraków, Poland, 2011.
- Churilov, S., Dumova-Jovanoska, E. (2012) “Analysis of masonry walls strengthened with RC jackets”, in 15th World Conference on Earthquake Engineering, Lisbon, 2012.
- Dizhur, D., Giaretton, M., Giongo, I., Ingham, J. M. (2017) “Seismic retrofit of masonry walls using timber strong-backs” *Journal of the Structural Engineering Society of New Zealand Inc*, vol. 30, no. 2, pp 30-44, 2017.
- Fiorentino, G., Forte, A., Pagano, E., Sabetta, F., Baggio, C., Lavorato, D., Nuti, C., Santini, S. (2018) “Damage patterns in the town of Amatrice after August 24th 2016 Central Italy earthquakes” *Bulletin of Earthquake Engineering*, 2018.
- Giongo, I. , Schiro, G., Piazza, M. (2017) “On the use of timber-based panels for the seismic retrofit of masonry structures” *Proceedings of the 3rd International Conference on Protection of Historical Constructions (PROHITECH)*, Lisbon, Portugal, 2017.
- Guerrini, G., Damiani, N., Miglietta, M., Graziotti, F. (2020) “Cyclic response of masonry piers retrofitted with timber frames and boards”, *Proceedings of the Institution of Civil Engineers – Structures and Buildings*, ISSN 0965-0911 | E-ISSN 1751-7702.
- Lourenco, P. (2008) “Structural masonry analysis: recent developments and prospects”, in *Proceedings of the 15th International brick & brick masonry conference*, Sydney, Australia; 1341-1356, 17-20 February 2008.
- Lucchini, A., Mazzucchelli, E. S., Mangialardo, S., Persello, M. (2014) “Façadism and CLT technology: An innovative system for masonry construction refurbishment” *Proceedings of the 40th IAHS World Congress on Housing*, Funchal, Portugal, 2014.
- Manie, J., and Kikstra, W. P., eds. (2014). “DIANA—Finite element analysis. User’s manual release 9.5”. Delft, Netherlands: TNO DIANA BV.

---

Newmark, N. M., Siess, C. P., Viest, I. M. (1951) “Test and analyses of composite beams with incomplete interaction” Proceedings of the Society for Experimental Stress Analysis, University of Illinois, Urbana, Illinois, vol. 9 (1), pp. 75-92, 1951.

Pozza, L., Evangelista, F., Scotta, R. (2017) “CLT used as seismic strengthener for existing masonry walls” Proceedings of the 17th Conference ANIDIS - L'ingegneria sismica in Italia, Pistoia, Italy, 2017.

Sustersic, I., Dujic, B. (2012) “Seismic strengthening of existing buildings with cross laminated timber panels” Proceedings of the World Conference on Timber Engineering (WCTE), Auckland, New Zealand, 2012.

Sustersic, I., Dujic, B. (2014) “Seismic shaking table testing of a reinforced concrete frame with masonry infill strengthened with cross laminated timber panels” Proceedings of the World Conference on Timber Engineering (WCTE), Quebec City, Canada, 2014.

Sorrentino, L., Cattari, S., da Porto, F., Magenes, G. and Penna, A. (2018) “Seismic behaviour of ordinary masonry buildings during the 2016 central Italy earthquakes” Bulletin of Earthquake Engineering, 2018.

# 9 EXPERIMENTAL SHEAR TESTING OF TIMBER-MASONRY CONNECTION SYSTEMS

## 9.1 INTRODUCTION

An in-situ experimental campaign investigating the mechanical behavior of several timber-masonry connection systems is reported in this Chapter. Experimental program comprised a series of shear tests under monotonic and reversed cyclic loading conditions. The influence of parameters such as masonry and timber panel type, screw fasteners, and grout formulations was investigated.

## 9.2 TEST CONFIGURATION

This section describes the characteristics of the materials involved in the experimental campaign. For the timber elements and for the fasteners the data are referred to the corresponding technical approval provided by the producers, whereas for masonry preliminary tests were performed on small specimens collected from the building. In addition, the testing protocol and the experimental apparatus are presented.

### 9.2.1 MATERIALS

#### 9.2.1.1 General

Shear tests were carried out on two different types of masonry present in the historic four-story URM building adopted as reference in this study. Regarding dry connection system, a series of tests were performed on four brick masonry walls (Figure 9.1-b) located at the top floor, which date back to a period around 1910-1920, when one additional story was raised on the original structure. The remaining 12 tests were conducted on two rubble masonry walls (Figure 9.1-a) made of coarse stone blocks

(milestone and dolomite) and lime mortar. Due to the material texture and bed-joint condition both brick and stone masonry were considered to be on the lower bound of the respective typology, with expected compressive strength in the range of 1.8-3.0 MPa for the brick masonry and values < 2.0 MPa for the stone rubble masonry, consistently with what recommended by the recently updated Italian Standard [C.S.L.PP (2019)].



Figure 9.1: Tested masonry typologies: stone masonry wall and brick masonry wall: a) Rubblestone masonry; b) Brick masonry

Grouted connections were tested on rubble masonry only Figure 9.1-a). Several small specimens, including mortar, bricks and stone blocks, were gathered from different places of the building and were tested in the laboratory of the University of Trento to check the quality of the masonry and to characterize the principal mechanical properties. In particular, 15 bricks, 5 stone blocks and 30 mortar samples were tested in compression to determine the compressive strength and the modulus of elasticity of the materials. The brick tensile strength was also derived from three-point bending tests [ASTM (2014)]. The results in terms of mean values and coefficients of variation are reported in Table 9.1.

Table 9.1: Mechanical properties of the two tested masonry types according to the preliminary tests

Material characteristic			n° samples	Mean	CoV
Brick compression strength	$f_{bc}$	[N/mm <sup>2</sup> ]	15	14.83	0.32
Brick modulus of elasticity	$E_{bc}$	[N/mm <sup>2</sup> ]	15	1225	0.29
Brick bending tensile strength	$f_{bt}$	[N/mm <sup>2</sup> ]	7	3.70	0.43
Stone compression strength	$f_{sc}$	[N/mm <sup>2</sup> ]	5	64.30	0.33
Stone modulus of elasticity	$E_{sc}$	[N/mm <sup>2</sup> ]	5	7660	0.40
Mortar compression strength	$f_{mc,brick}$	[N/mm <sup>2</sup> ]	13	5.16	0.35
Mortar compression strength	$f_{mc,stone}$	[N/mm <sup>2</sup> ]	46	2.95	0.95

### 9.2.1.2 Dry connection system

Table 9.2 details the main features of the five fastener types chosen for the campaign according to the technical documentation and approval certificates supplied by the producers [ETA-05/0010, ETA-15/0352]. As already stated in the introduction, all the fasteners were developed for the use in concrete as self-tapping screw anchors but are suitable for a whole range of other materials such as natural stone and brick. The assembly process is relatively simple: after drilling a pilot-hole the dust has to be removed and then the anchor can be fixed using a screwdriver or a screw wrench. Fasteners M1 and M2 differ for insertion length in the masonry wall for a given panel thickness. Fasteners M1 and U1 have comparable geometric properties but are produced by two different companies. Anchor U2 has the largest diameter of all (almost 14 mm over 10 mm). Lastly, fastener T is composed by two different threaded parts of equal length, one to be fixed in the masonry wall and the other in the timber panel. A detailed representation of the geometric properties of all the fasteners is provided in Figure 9.2.

*Table 9.2 Geometric and mechanical properties of the fasteners according to the technical assessment given by the producers*

Fastener type			M1	M2	U1	U2	T*
Total length:	$L$	[mm]	180	240	160	150	160
Thread length:	$L_t$	[mm]	100	100	100	100	70 (70)
Thread diameter:	$d_{thread}$	[mm]	12.0	12.0	12.5	16.6	12 (14)
Core diameter:	$d_{core}$	[mm]	9.4	9.4	9.4	13.3	9.4 (9.5)
Shaft diameter:	$d_{shaft}$	[mm]	9.4	9.4	9.9	13.7	-
Head diameter:	$d_{head}$	[mm]	18	18	15	21	16
Washer diameter:	$d_{washer}$	[mm]	43	43	20**	28**	-
Axial resistance:	$N_{Rks}$	[kN]	25	25	55	103	25
Yielding moment:	$M_{yk}$	[Nm]	38	38	95	269	38

\* In brackets the timber thread properties

\*\* Part of the fastener (see Figure 9.2)

Due to the location of the timber panels at the internal side of the wall, their thickness should be kept to a minimum to avoid excessive loss of inner floor space. For this reason, one cross-laminated timber (CLT) and two laminated veneer lumber (LVL) panel types with a thickness respectively of 60 mm and 40 mm were selected for the tests. The tested specimens realized with spruce CLT and LVL material were  $300 \times 300 \text{ mm}^2$  whereas beech LVL specimens were  $300 \times 200 \text{ mm}^2$  (dimension parallel to the loading direction  $\times$  dimension perpendicular to the loading). In both cases the fastener was inserted at the center of the timber specimen. The mechanical properties of the panels are listed in Table 9.3.

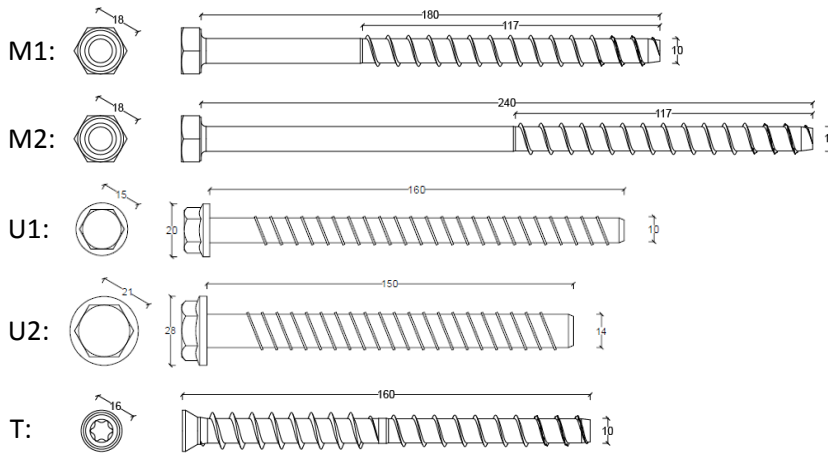


Figure 9.2: Representation of the five tested typologies of screw anchors adopted for the test (measurements in [mm])

Table 9.3: Strength and stiffness properties of the timber elements as declared by manufacturers

Element type			Spruce CLT	Spruce LVL	Beech LVL
			Panel	Panel*	Panel*
Bending:	$f_{m,0,k}$	[N/mm <sup>2</sup> ]	24	32	60
	$f_{m,90,k}$	[N/mm <sup>2</sup> ]	-	8	10
Tension:	$f_{t,0,k}$	[N/mm <sup>2</sup> ]	14.5	18	51
	$f_{t,90,k}$	[N/mm <sup>2</sup> ]	0.12	5	8
Compression:	$f_{c,0,k}$	[N/mm <sup>2</sup> ]	21	30	53.3
	$f_{c,90,k}$	[N/mm <sup>2</sup> ]	2.5	9	19
Shear:	$f_{v,k}$	[N/mm <sup>2</sup> ]	2.3	4.6	7.8
MoE:	$E_{0,mean}$	[N/mm <sup>2</sup> ]	11550	10600	13200
Shear modulus:	$G_{mean}$	[N/mm <sup>2</sup> ]	450	600	820
Density:	$\rho_{mean}$	[kg/m <sup>3</sup> ]	420	530	800
	$\rho_k$	[kg/m <sup>3</sup> ]	350	480	730
Thickness	$t$	[mm]	60	40	40

\* In-plane bending properties

### 9.2.1.3 Grouted connection system

Grouted connections were tested on the rubblestone masonry only. Two types of grout were chosen for the assembly of tested specimens. Namely, a fully-epoxy (EX) resin [ETA-10/0012] and a hybrid (HY) resin featuring an epoxy-vinylestere formulation [ETA-02/0024]. To account for the influence of dowel type and diameter, both threaded 8.8 grade steel bars and B450C steel concrete rebar were used in the diameters of 14

mm and 20 mm. All the specimens were assembled with 60 mm-thick  $250 \times 500 \text{ mm}^2$  three-layered spruce CLT panels whose mechanical properties are listed in Table 9.3. In all the cases loads were applied in the direction parallel to outer layers grain direction. All the possible combinations of the selected materials and geometries were considered, as listed in Table 9.5. Specimens were assembled consistently with the directions provided by the grout technical sheets concerning installation procedures and curing times. A 30 cm-deep hole was drilled perpendicularly to wall surface by means of a hammering drill. Hole diameter was related to dowel diameter. Namely,  $\varnothing 22 \text{ mm}$  holes were drilled to accommodate  $\varnothing 14 \text{ mm}$  dowels and  $\varnothing 30 \text{ mm}$  holes were drilled in the case of  $\varnothing 20 \text{ mm}$  dowels. Due to the weak mechanical properties of the mortar, holes were always drilled starting from a stone element on the interested wall surface. Timber panel portion was perforated and placed in correspondence of the hole previously drilled in the masonry and held in place by means of an auxiliary timber frame visible in Figure 9.3-a. Timber hole diameter matched wall hole diameter. Holes were then cleared from drilling residuals and a containment metallic net with closed front end was put into place (see Figure 9.3-b). Metallic net nominal diameter matched hole diameter, therefore  $\varnothing 22 \text{ mm}$  nets were used in the case of  $\varnothing 14 \text{ mm}$  dowels and  $\varnothing 30 \text{ mm}$  nets were installed in the case of  $\varnothing 20 \text{ mm}$  dowels. Grout was then injected (Figure 9.3-c) so as to completely fill the hole (also comprising panel thickness) and the dowel was finally inserted (see Figure 9.3-d).

## 9.2.2 TEST SET-UP

The details of the experimental apparatus adopted for the campaign are shown in Figure 9.4. Firstly, a rectangular timber reaction frame (dimensions  $2.5 \times 2.2 \text{ m}^2$  composed by four GL75 [ETA-14/0354] beam elements with a cross-section area of  $160 \times 60 \text{ mm}^2$ ) was fixed on the selected masonry wall using the same screw anchors (a minimum of 3 fasteners type T per each post of the reaction frame) of the shear tests. The hydraulic actuator used to apply the shear load was secured to one timber post of the frame by means of a C-shaped steel bracket. The specimen under test was primarily connected to the wall driving the anchor through the pre-drilled pilot hole in the brick/stone block using a 5 mm thick spacer in the back side of the timber panel. The specimen was joined to the actuator through a hinged union interposing a 75 kN load cell. To prevent in-plane and out-of-plane rotations of the specimen during the push phase of the cyclic testing two steel angle brackets were attached to the reaction frame. Strips of polyzene were positioned in the internal side of the steel angle brackets in order to reduce the friction between the steel-to-steel surface. Lastly, a linear variable differential transducer (LVDT) was used to monitor the displacement of the timber specimen with respect to the masonry wall. The base of the LVDT was placed on a sturdy steel support fixed on

the floor; this allowed to disregard the (minimal) reaction frame deformability in the calculation of the fastener stiffness.



*Figure 9.3: Specimen preparation: a) CLT panel in place and metallic net insertion; b) Metallic net closed front-end; c) Grout injection; d) Dowel insertion*

## **9.2.3 TESTING PROCEDURE**

### **9.2.3.1 Dry connections**

With reference to dry connection system, both monotonic and cyclic behaviors were investigated. The load was applied in displacement control up to a maximum displacement of 50 and 30 mm for the monotonic and for the cyclic tests, respectively. In particular, testing protocols of EN 26891 [CEN (1991)] and EN 12512 [CEN (2001)] were adopted. The monotonic tests (EN 26891) provided the yield displacements required to perform the complete procedure of cyclic testing (EN 12512). In addition, the standard ASTM E2126 [ASTM (2011)] was employed to plot the envelope curves starting from the total load-displacement hysteresis loops and, from the envelope curves, to determine the equivalent energy elastic-plastic (EEEP) curves both for tension and compression loads (see Figure 9.5 right).

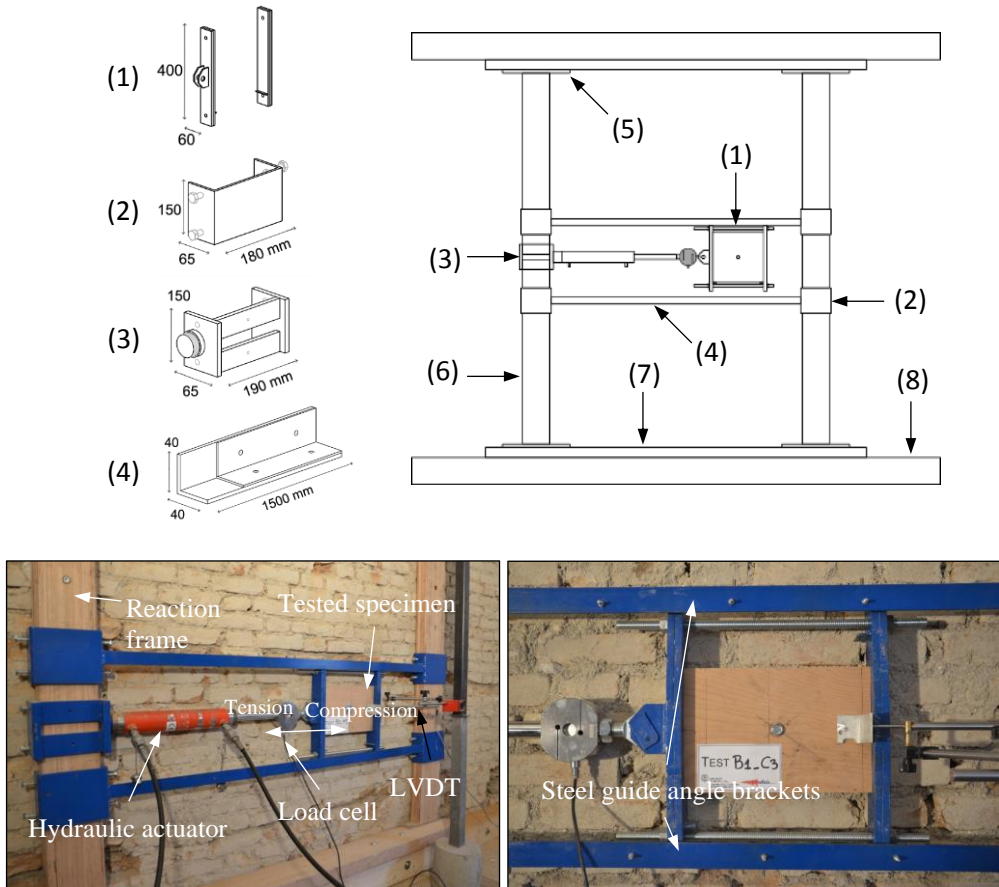


Figure 9.4: Test set-up diagram, details and instruments arrangement

Table 9.4 reports all the tested configurations, selected varying the type of masonry, timber panel and fastener and considering different load-to-grain angles. For all the tests performed with fastener M1 and M2 in combination with softwood panels (either CLT or LVL), a 38 mm wide and 4 mm thick washer was used to enable the formation of the second plastic hinge. In the case of beech LVL panels a first trial monotonic test was executed without using the washer; because no significant timber damage was observed around the fastener head, it was decided to perform all the tests including beech LVL panels without washer. Fasteners U1 and U2 are produced with a built-in washer (Table 9.2 and Figure 9.2); therefore, it was also assumed unnecessary to use an external washer.

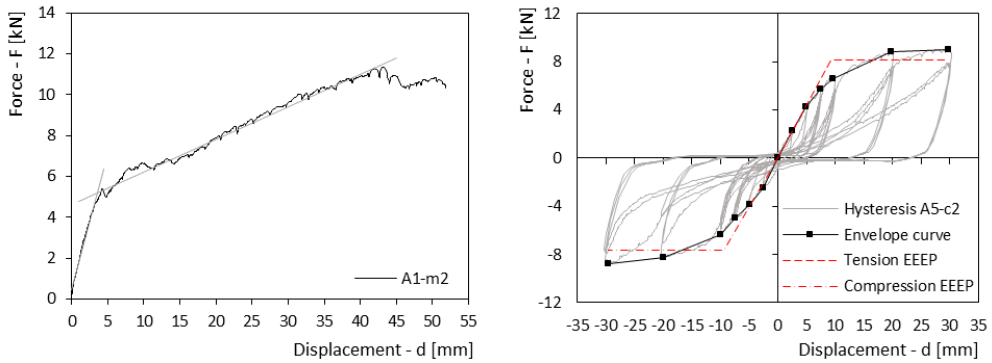


Figure 9.5: Typical load-displacement curves of a monotonic test (left) and of a cyclic test (right)

Table 9.4: Configurations of the 64 shear tests performed

Test ID	n° repetitions		Masonry type	Timber panel		Fastener
	Monotonic	Cyclic		Material	$\alpha^*$ [°]	
A1	1	3	Brick	Spruce CLT	0°	T
A2	1	3	Brick	Spruce CLT	90°	T
A3	1	3	Brick	Spruce CLT	45°	T
A4	2	3	Brick	Spruce CLT	0°	M1+washer
A5	2	3	Brick	Spruce CLT	0°	M2+washer
A8	1	3	Brick	Spruce CLT	0°	U2
A9		3	Brick	Spruce CLT	0°	U1
B1	1	3	Brick	Beech LVL	0°	M1
B2	1	3	Brick	Beech LVL	90°	M1
B3		3	Brick	Beech LVL	0°	U2
D1	2	3	Stone	Spruce CLT	0°	M1+washer
D2		3	Stone	Spruce CLT	0°	T
D3	1	3	Stone	Spruce CLT	0°	U2
E1	1	3	Brick	Spruce LVL	0°	M1+washer
E2	1	3	Brick	Spruce LVL	90°	M1+washer
E3**	1	3	Brick	Spruce LVL	0°	T

\* Load-to-grain angle (grain: maximum number of layers in the fibre direction)

\*\* Panel thickness: 60 mm

### 9.2.3.2 Grouted connections

To mitigate out-of-plane deflections of the specimens triggered by the irregular wall surface, grouted connection shear behavior was investigated by means of hemi-cyclic test sequences. Specifically, the procedure proposed by EN 12512 [CEN (2001)] was modified so as to perform the positive displacement hemi-cycles only.

Table 9.5: Tested grouted connection assemblages

Connection ID	Repetitions	Grout	Dowel type	Dowel diameter
HY 14 TH	6	Hybrid	8.8 grade threaded	14 mm
HY 14 RB	3	Hybrid	B450C rebar	14 mm
HY 20 TH	7	Hybrid	8.8 grade threaded	20 mm
HY 20 RB	3	Hybrid	B450C rebar	20 mm
EX 14 TH	3	Epoxy	8.8 grade threaded	14 mm
EX 14 RB	3	Epoxy	B450C rebar	14 mm
EX 20 TH	4	Epoxy	8.8 grade threaded	20 mm
EX 20 RB	5	Epoxy	B450C rebar	20 mm

## 9.3 RESULTS – DRY CONNECTIONS

### 9.3.1 OBSERVED FAILURE MODES

After the execution of each test (either monotonic or cyclic), the load was returned to zero and the fastener was removed to evaluate the failure modes of the connection. Similar to other tests reported in literature on shear dowels embedded in stone masonry [Giuriani et al. (1993)], partial or total splitting of either bricks and stone blocks was experienced in almost all the tests (Figure 9.6 and Figure 9.7). Only in the case of rubble stone masonry some of the blocks (Test D1-m1, D1-m2, D3-m1 and D3-c2) remained undamaged whereas the surrounding mortar underwent a complete crushing (see Figure 9.7-d). This was probably related to the poor mechanical performance of the lime-mortar (see Table 9.1) and/or to the local excessive thickness of the mortar joints. This phenomenon is reflected in the load-displacement curves of the tests, characterized by a relatively low value of the slip modulus ( $< 0.5$  kN/mm) and an almost linear behavior.

Figure 9.8 presents the graphs of two cyclic tests (test A1-c3 and A3-c1) and a schematic representation of the brick condition during the loading phases. The three principal damage conditions observed for brick masonry tests are represented: brick cracking (tension), crushing (compression) and splitting. When the crack opening began, the response curves showed a sudden, yet limited, capacity loss (Figure 9.8-a) that did not correspond to the actual failure of the connection as the capacity continued to increase. Conversely, when crushing of the brick around the fastener became noticeable (usually accompanied also by timber bearing failure and plastic hinge/hinges formation in the fastener), the load approaches the maximum load carrying capacity of the connection.

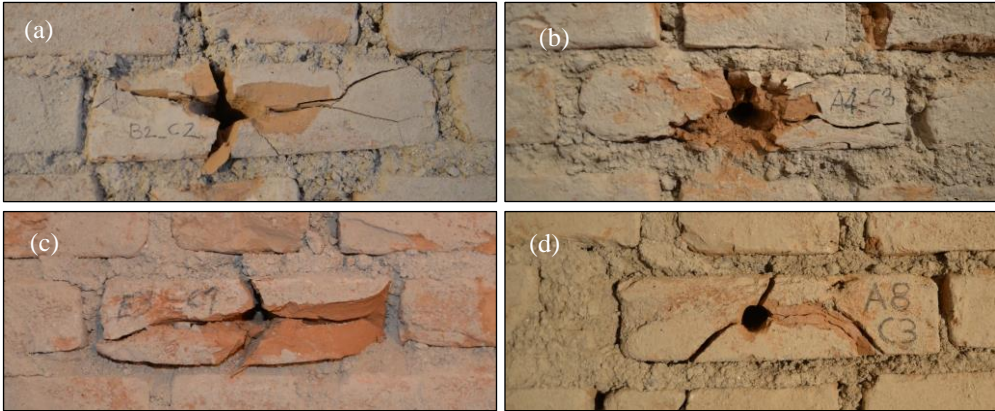


*Figure 9.6: Observed damage for the brick masonry: a) brick tensile cracking; b) local crushing; c) brick splitting; d) early failure due to pre-existing cracks (test interrupted and discarded)*



*Figure 9.7: Observed damage for the rubble stone masonry: a) block tension cracking; b) analogous of a “plug shear” failure; c) block splitting; d) mortar crushing*

The second and more dangerous type of failure is the splitting of the brick, namely the opening of a crack parallel to the load direction. This was experienced only in a few specimens and generally at large displacement values ( $d > 15$  mm). The splitting failure of the brick caused an almost total loss of capacity of the connection since there was no more material opposing the movement of the fastener. The (small) residual capacity

might be due to the compression within the masonry wall which tended to hold the brick portions together after the splitting. It is worth reminding that the risk of splitting is minimum when the predrilled hole is at the center of the brick, while it increases moving towards the edges.

With the exception of the few tests where crushing of the mortar surrounding the stone block was observed and the test configurations involving U2 fasteners (A8, B3 and D3), all the tests developed at least one plastic hinge inside the masonry in the fastener portion closer to the wall surface (Figure 9.9 left). U2 fasteners showed a higher value of characteristic yielding moment ( $M_{y,k} = 269 \text{ Nm}$ , see Table 9.2) compared to the other fasteners with the consequence that the plastic hinges did not activate during the tests. As expected, in single threaded fasteners (M1, M2 and U1) the first plastic hinge originated at the top of the threaded part inserted in the masonry wall; in the case of monotonic loading, also a second plastic hinge, formed in the timber element due to the presence of the washer, was clearly distinguishable from the anchors recovered after the end of the tests. For the cyclic tests the presence of the second plastic hinge was not as evident as for the monotonic tests, probably due to lower maximum displacement value and to the return to the zero values of load and displacement which may have straightened back the fastener shank. Double threaded fasteners (T) formed a single plastic hinge located at the interface between the masonry wall and the timber panel and exhibited marked timber crushing also in correspondence with the fastener head. A brittle tensile rupture of the screw anchor shank was experienced only once, in test D1-c3 (Figure 9.9 right). The maximum load recorded during this test was the highest of the whole campaign ( $F_{max} = 18.29 \text{ kN}$ ). Failure of the screw shank in tension was calculated from the product data sheet as equal to 25.0 kN which is greater than the 10.4 kN determined for the washer pull-through resistance (it is worth noting that no embedment of the washer was observed). This may have been caused by weakening of the fastener due to oligocyclic fatigue.

Due to the irreversible nature of the splitting failure of bricks and stone blocks and of the timber crushing of the wood panels, a significant level of pinching appears from the load-displacement curves of the cyclic tests, particularly for the hysteresis loops at relatively large displacement amplitudes (i.e.  $d = 10 \text{ mm}$ ,  $20 \text{ mm}$  and  $30 \text{ mm}$ ). Therefore, in the second and third cycles the only contribution to energy dissipation is provided by the yielding of the steel fastener. For this reason, connections with fasteners that have a smaller value of yield moment may exhibit less pinching, thanks to the lower energy required to activate the plastic hinge (this was confirmed by the results as shown in Figure 9.10).

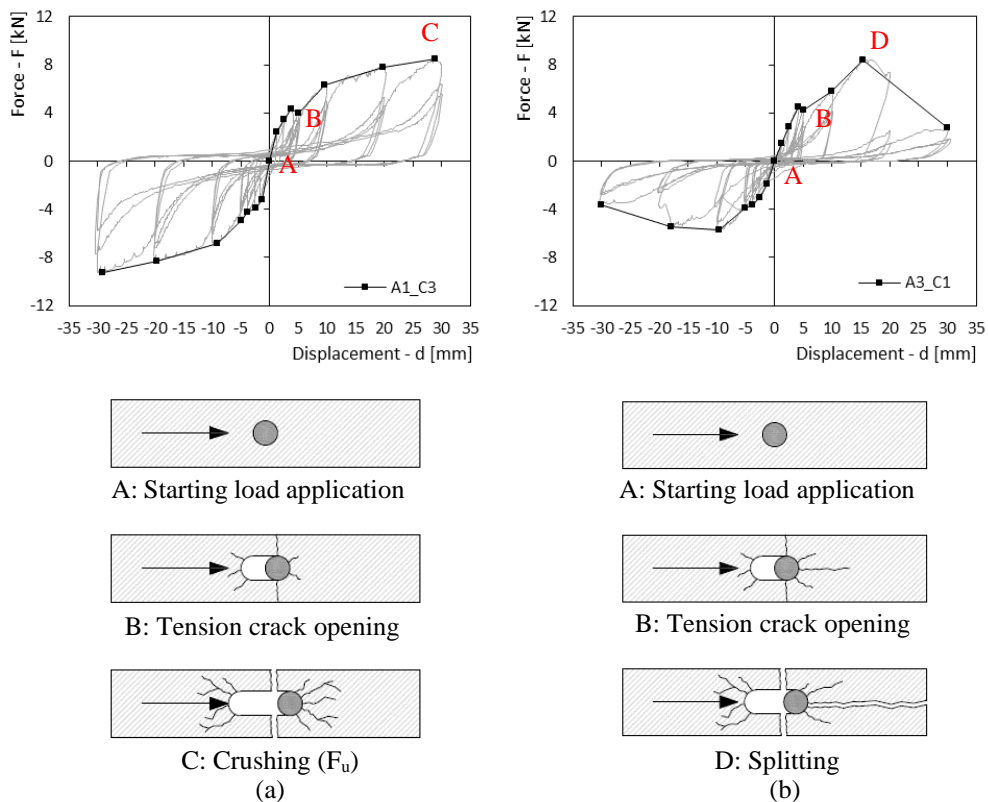


Figure 9.8: Representations of two different failure modes observed for the specimens on brick masonry walls: a) compression crushing; b) splitting

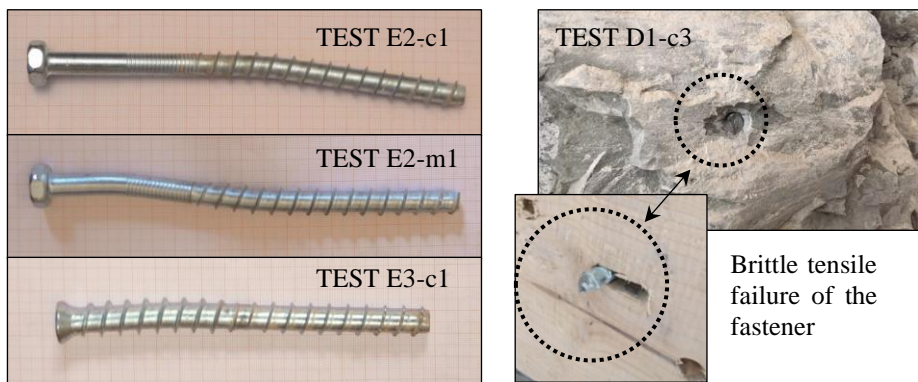


Figure 9.9: Examples of plastic hinges from the fasteners removed after the tests (left) and tensile rupture registered for test D1-c3 inserted in stone masonry (right)

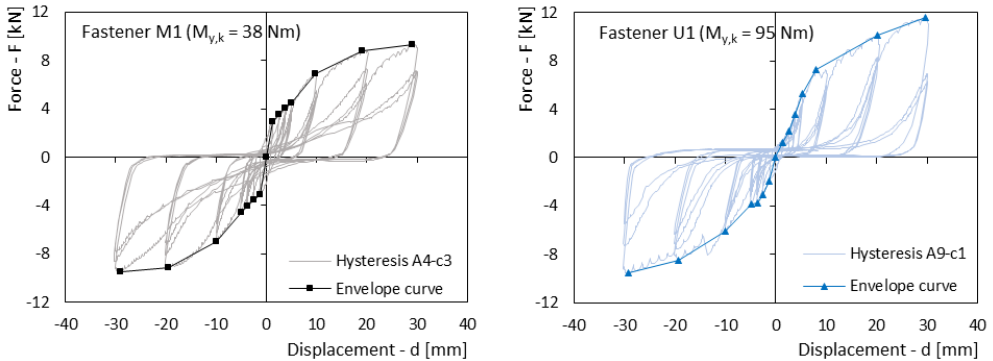


Figure 9.10: Hysteresis loops of test A4-c3 (fastener M1) and test A9-c1 (fastener U1)

Due to the large number of specimens tested on brick masonry, it was not possible to carry out the whole campaign on a single wall. Consequently, three brick masonry walls, located in three different areas of the building, were chosen for the experimental investigation (Table 9.6 details the position of every single cyclic and semi-cyclic test on brick masonry). The connection showed a tendency to strength and stiffness reduction in the tests executed on wall W3. In a visual inspection, several brick blocks in W3 displayed signs of defects and inclusions (e.g. excessive porosity, grains of burnt limestone or grogs). For this reason, it was decided to carry out a complementary non-destructive testing (NDT) campaign on the three selected walls, to supplement the material test results reported in Table 9.1. In particular, the scleroscopic method was adopted, using a Schmidt impact hammer according to EN 12504-2 [CEN (2012)]. This technique had been already applied on brick masonry by other authors [Brozovsky and Zach (2012)] who effectively identified an almost linear relation between the measured rebound number from the NDT test and the compression strength of the block. Twenty-four measurements for each wall were collected on randomly selected intact brick blocks; the frequency distributions of the rebound number are shown in Figure 9.11. It can be observed that wall W3 exhibited lower values of rebound number, a possible sign of decreased mechanical properties.

The poorer quality of masonry construction of wall W3, with respect to the other tested walls, is also confirmed by comparing the outcomes of the scleroscopic tests with the results of the compression tests performed on the mortar samples collected in the same locations. Specifically, it was noticed a direct correlation between the mean values of rebound number registered from the impact hammer tests (20, 27 and 24 respectively for walls W1, W2 and W3) and the mean values of the mortar compression strength

relative to the same wall portions (6.12 MPa, 8.25 MPa and 4.83 MPa for walls W1, W2 and W3).

Table 9.6: Location of each cyclic and semi-cyclic test performed on brick masonry wall

Test ID	Wall	Test ID	Wall	Test ID	Wall
A1-c1	W1	A5-c2	W1	B2-c3	W1
A1-c2	W1	A5-hc3	W3	B3-c1	W2
A1-c3	W1	A8-c1	W1	B3-hc2	W3
A2-c1	W1	A8-c2	W1	B3-hc3	W3
A2-hc2	W3	A8-hc3	W3	E1-c1	W2
A2-h3	W3	A9-c1	W2	E1-c2	W2
A3-h1	W2	A9-hc2	W3	E1-c3	W2
A3-hc2	W3	A9-hc3	W3	E2-c1	W2
A3-hc3	W3	B1-c1	W1	E2-c2	W2
A4-c1	W1	B1-c2	W1	E2-hc3	W3
A4-c2	W1	B1-c3	W1	E3-c1	W2
A4-c3	W1	B2-c1	W1	E3-c2	W2
A5-c1	W1	B2-c2	W1	E3-hc3	W3

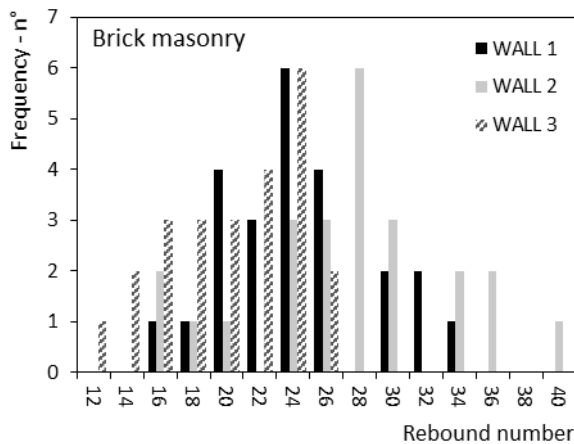


Figure 9.11: Frequency distributions of the rebound number measured via scleroscopic test method on the three tested walls

### 9.3.2 MONOTONIC TESTING

This section reports the results of the monotonic loading tests. As stated before, all the monotonic tests were performed up to a displacement value of 50 mm (except for tests B1-m1 and B2-m1). Figure 9.12 shows the load-displacement curves for the spruce CLT

panel and brick masonry combination, on the left using the fastener T and varying the load-to-grain angle and on the right maintaining the load parallel to the grain of the outer layers of the panel using different types of fastener. The different inclination of the load with respect to the grain direction of the CLT panel seems to have no impact on the mechanical behavior of the connection (this was also confirmed by the corresponding cyclic tests). The graph on the right exhibits, instead, a more pronounced variety of results. It is worth noting that using a steel fastener with larger diameter and higher yielding moment (e.g. fastener U2) leads to poorer mechanical performance of the overall connection. This may be due to failure on the masonry side: a much stiffer steel dowel exerts excessive pressure on the brick leading to preliminary failure, as shown by the early loss of strength of the load-displacement curve. Furthermore, the need of a wider pilot-hole may have contributed to weaken the brick element.

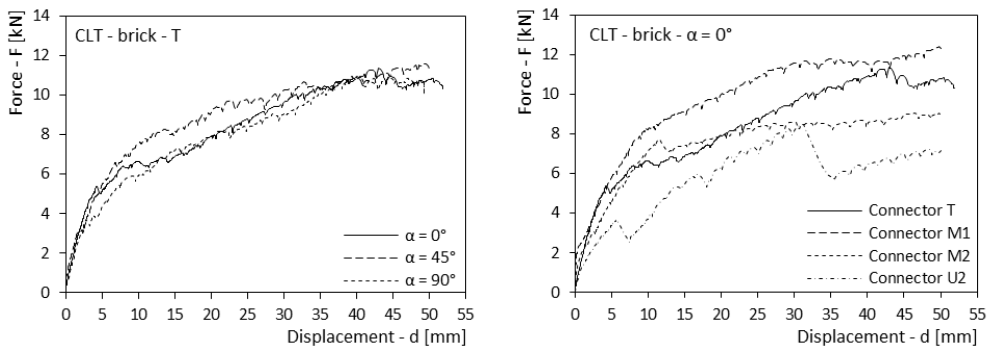


Figure 9.12: Selected load-displacement curves for different load-to-grain angles (left) and for different types of fasteners (right)

Table 9.7 summarizes the results of each monotonic test, in terms of maximum load, yield point and slip modulus. For tests A8-m1, D1-m1, D1-m2, D3-m1 and E3-m1 the yield point was not calculated because of early failure of the masonry due to cracking of the brick and/or block (A8-m1 and E3-m1) or due to crushing of the surrounding mortar (D1-m1, D1-m2 and D3-m1). This latter phenomenon also resulted in relatively low values of slip modulus because the stone blocks were free to translate in the first phase of the monotonic tests. Unlike spruce CLT panels, beech LVL specimens (tests B1-m1 and B2-m1) showed larger sensitivity to testing in different load-to-grain angles. The test perpendicular to the main fiber direction (B2-m1) exhibited a 27.5% decrease in the maximum load and a 71.7% reduction of the slip modulus with respect to test parallel to the main fiber (B1-m1). This behavior may be related to the lower percentage of orthogonal layers in the beech LVL (2 over a total of 14 lamellae for a 40 mm thick panel) compared to spruce CLT. The results for spruce LVL panels tested with different

load-to-grain angle (E1-m1 and E2-m1) were similar to those of beech LVL panels: the test parallel to the grain recorded higher maximum load (+32.2%) and higher slip modulus (+73.5%) with respect to the panel tested orthogonal to the main fibre direction.

Table 9.7: Maximum load, yield point and slip modulus of all the monotonic tests performed

Test ID	Maximum load	Yield point		Slip modulus
	$F_{\max}$ [kN]	$F_y$ [kN]	$d_y$ [mm]	$k_s$ [kN/mm]
A1-m2	11.35	5.18	3.61	1.31
A2-m1	10.94	6.11	7.38	0.75
A3-m1	11.58	7.67	6.70	1.02
A4-m1	12.39	7.56	6.41	0.99
A4-m2	11.94	6.06	6.82	0.74
A5-m1	9.06	7.02	7.80	0.80
A5-m2	8.89	6.81	10.11	0.62
A8-m1	8.46	-	-	0.70
B1-m1*	12.86	7.75	3.75	1.77
B2-m1*	9.32	5.34	9.19	0.50
D1-m1	12.70	-	-	0.24
D1-m2	18.10	-	-	0.33
D3-m1	15.61	-	-	0.42
E1-m1	15.12	6.45	3.54	1.44
E2-m1	11.44	5.41	5.11	0.83
E3-m1	9.72	-	-	0.43

\* Tested up to 30 mm

### 9.3.3 CYCLIC TESTING

The cyclic test protocol was calibrated according to EN 12512 [CEN (2001)]. The yield displacement derived from the monotonic testing was equal to 5 mm for all the configurations with the exception of test A5 (fastener M2) where it was set at 10 mm. The cyclic tests were performed up to a displacement amplitude of 30 mm both in tension and compression loading (in the graphs the tension and compression loads will be reported in the positive and negative axis, respectively). The examined parameters were:

- Type of fastener (different diameter, length, steel and typology);
- Load-to-grain direction ( $0^\circ$ ,  $45^\circ$  and  $90^\circ$ );
- Type of timber panel (spruce CLT, spruce LVL and beech LVL);
- Type of masonry (brick masonry, rubble stone masonry).

Table 9.8 reports the principal parameters that characterize the envelope curves of each considered configuration: peak load, slip modulus (calculated according to EN 26981 [CEN (2001)] and the yielding load of the equivalent energy elastic-plastic curve associated to the envelope curve [ASTM (2011)]. The mean value and coefficient of variation (corresponding to three repetitions for each test) are listed, keeping the tension and compression semi-cycles as separate.

Other important aspects to consider in a cyclic test concern the strength reduction of the connection from the first to the third cycle at the same displacement amplitude, and the energy dissipation of the joint during the hysteresis cycles. Usually, the impairment of strength  $\Delta F$  and equivalent viscous damping ratio  $v_{eq}$  (according to EN 12512) are used to describe such qualities. Table 9.9 and Table 9.10 summarize the  $\Delta F$  data in terms of percentage reduction with respect to the first loop at the same displacement amplitude and the  $v_{eq}$  data (complete cycles comprehending tension and compression loading).

### 9.3.3.1 Influence of the type of fastener

The influence of the type of fastener was investigated by selecting the following wall-panel combination: brick masonry wall and spruce CLT panel loaded parallel to the main grain direction. Fasteners T, M1, M2, U2 and U1 were tested in configurations A1, A4, A5, A8 and A9, respectively. As pointed out in Table 9.8, all the tests exhibited comparable mean values of maximum capacity and different (mean values of the slip modulus (either between different tests or between tension and compression semi-cycles of the same configuration,  $CoV$  of  $F_{max}$  considering all configurations equal to 16.41% and  $CoV$  of  $k_s$  equal to 50.13 %)). The larger scatter observed for the slip moduli may be explained by reminding that the calculation method is based on the secant stiffness values measured at  $0.1 \times F_{max}$  and  $0.4 \times F_{max}$  (EN 26891), which is the force range where the tension cracking of the bricks occurred (for the specimen that exhibited cracking). Therefore, the early loss of strength caused higher variability of the slip modulus, whereas the more stable values of maximum capacity may be correlated to the compression strength of the bricks and to the embedment strength of the timber panels, almost uniform for all the configurations analyzed in this section (see Figure 9.8 left).

The connection capacity and slip modulus of the envelope curves appear governed more by the mechanical properties of the masonry walls and timber panels than by the choice of fastener typology. One exception may be the use of a fastener with large diameter (e.g. fastener U2  $\rightarrow$  test A8) which may cause early failure due to the weakening of the block (net resisting area reduction) affecting the slip modulus (tension cracking) or even the ultimate load (splitting). When looking at the impairment of strength values and equivalent viscous damping ratios (Table 9.9 and Table 9.10) a more marked difference among fasteners stands out. In particular, two groups may be distinguished on the base

of the steel type: zinc plated steel (fasteners T, M1 and M2) and zinc plated hardened carbon steel (fasteners U1 and U2). The latter group exhibited higher strength loss and smaller equivalent viscous damping ratios for displacements greater than 10 mm. This is linked to the more pronounced pinching experienced by hardened carbon steel anchors, with respect to normal steel anchors (see Figure 9.10).

*Table 9.8: Mean value and coefficient of variation of the maximum load, slip modulus and yield load, determined using the EEEP curve according to ASTM (2011), of the envelope curves for each cyclic test configuration*

Test ID	Load	F <sub>max</sub> [kN]		k <sub>s</sub> [kN/mm]		F <sub>y,EEEP</sub> [kN]	
		Mean	CoV	Mean	CoV	Mean	CoV
A1	Tension	7.96	4.6%	1.11	28.6%	6.90	3.3%
	Compression	8.52	11.2%	1.61	12.7%	6.70	15.1%
A2	Tension	7.45	5.6%	0.84	39.0%	6.13	7.2%
	Compression	7.18	0.6%	0.75	13.0%	5.99	1.2%
A3	Tension	7.40	13.9%	0.80	41.8%	5.69	1.2%
	Compression	5.73	-	1.33	-	4.86	-
A4	Tension	8.91	4.0%	0.91	27.6%	7.82	3.2%
	Compression	9.63	4.8%	1.44	41.5%	8.02	7.0%
A5	Tension	8.20	9.8%	0.97	33.6%	6.13	11.9%
	Compression	7.99	9.7%	0.80	1.1%	6.95	10.6%
A8	Tension	9.34	8.7%	1.32	79.2%	8.56	15.4%
	Compression	9.87	5.9%	0.60	12.1%	8.44	3.3%
A9	Tension	8.38	38.1%	1.06	5.5%	7.08	36.0%
	Compression	9.57	-	0.86	-	7.97	-
B1	Tension	10.25	1.7%	3.94	33.2%	8.85	4.1%
	Compression	12.30	10.0%	1.38	14.0%	9.92	14.5%
B2	Tension	8.10	7.9%	1.08	28.8%	7.27	8.9%
	Compression	8.99	19.2%	0.51	15.2%	7.72	20.2%
B3	Tension	12.64	7.3%	1.28	12.3%	10.95	9.1%
	Compression	11.71	-	0.85	-	10.93	-
D1	Tension	12.64	14.4%	1.18	45.0%	11.13	14.5%
	Compression	14.98	20.9%	1.54	21.3%	12.30	27.5%
D2	Tension	6.57	8.4%	0.84	41.0%	5.74	13.4%
	Compression	5.52	0.3%	0.35	16.4%	4.89	9.0%
D3	Tension	9.80	11.1%	2.30	60.5%	8.75	2.6%
	Compression	11.95	37.2%	0.80	49.6%	10.59	36.6%
E1	Tension	9.29	12.8%	1.42	31.2%	7.51	15.3%
	Compression	9.41	5.8%	2.10	61.5%	7.69	6.3%
E2	Tension	7.85	18.5%	1.33	67.4%	6.54	15.1%
	Compression	7.73	22.2%	0.93	47.6%	6.42	23.8%
E3	Tension	8.26	6.3%	0.86	30.8%	6.73	10.2%
	Compression	7.50	17.6%	1.28	41.6%	6.36	22.8%

The higher yield moment of hardened carbon steel anchors ( $M_{yk} = 95$  Nm and  $M_{yk} = 269$  Nm for fasteners U1 and U2 with respect to  $M_{yk} = 38$  Nm for fasteners T, M1 and M2) delayed or even inhibited the formation of the plastic hinge on the fastener, reducing the amount of energy dissipation of the second and third loops for the cyclic loading conditions.

Table 9.9: Cyclic tests: mean values and coefficients of variation of the impairment of strength  $\Delta F$  at increasing levels of displacement

Test ID	$\Delta F$ [%]	0.75 $d_y$ *	1 $d_y$ *	2 $d_y$ *	4 $d_y$ *	6 $d_y$ *
Total loop n°		5	8	11	14	17
A1	Mean	20%	18%	24%	28%	31%
	CoV	0.43	0.38	0.16	0.34	0.22
A2	Mean	20%	14%	21%	27%	35%
	CoV	0.18	0.86	0.50	0.21	0.28
A3	Mean	37%	26%	31%	58%	32%
	CoV	0.32	0.29	0.13	0.32	0.11
A4	Mean	18%	16%	23%	22%	22%
	CoV	0.29	0.30	0.23	0.27	0.27
A5**	Mean	27%	22%	30%	17%	0%
	CoV	0.47	0.42	0.31	0.34	0.00
A8	Mean	28%	23%	15%	30%	38%
	CoV	0.36	0.39	0.52	0.42	0.40
A9	Mean	15%	21%	21%	30%	39%
	CoV	0.57	0.30	0.22	0.28	0.19
B1	Mean	22%	20%	22%	26%	39%
	CoV	0.47	0.43	0.38	0.37	0.16
B2	Mean	15%	22%	20%	24%	29%
	CoV	0.55	0.39	0.39	0.25	0.23
B3	Mean	28%	34%	27%	37%	41%
	CoV	0.10	0.25	0.25	0.25	0.20
D1	Mean	20%	20%	35%	34%	37%
	CoV	0.61	0.33	0.39	0.21	0.54
D2	Mean	10%	8%	16%	20%	21%
	CoV	0.40	0.63	0.76	0.74	0.65
D3	Mean	14%	18%	28%	48%	47%
	CoV	0.61	0.40	0.44	0.25	0.32
E1	Mean	22%	30%	32%	29%	32%
	CoV	0.08	0.39	0.12	0.19	0.38
E2	Mean	21%	19%	25%	34%	25%
	CoV	0.30	0.41	0.44	0.33	0.55
E3	Mean	26%	29%	26%	42%	32%
	CoV	0.63	0.80	0.44	0.33	0.25

\* Relative to the third loop

\*\* Different yield displacement ( $d_y=10$  mm instead of 5 mm)

Table 9.10: Cyclic tests: mean values and coefficients of variation of the equivalent viscous damping ratios  $v_{eq}$  at increasing levels of displacement

Test ID	$v_{eq}$ [%]	0.25 $d_y$	0.50 $d_y$	0.75 $d_y^*$	1 $d_y^*$	2 $d_y^*$	4 $d_y^*$	6 $d_y^*$
Total loop n°		1	2	5	8	11	14	17
A1	Mean	22.3%	18.3%	9.8%	7.5%	6.2%	7.3%	8.5%
	CoV	0.16	0.11	0.30	0.23	0.24	0.21	0.32
A2	Mean	12.9%	10.7%	6.2%	4.9%	3.7%	4.8%	4.3%
	CoV	0.18	0.19	0.24	0.22	0.59	0.13	0.15
A3	Mean	18.5%	11.8%	8.5%	8.0%	10.2%	5.0%	5.3%
	CoV	0.22	0.15	0.09	0.38	0.67	0.48	0.54
A4	Mean	33.1%	24.1%	10.7%	7.3%	5.3%	7.1%	10.0%
	CoV	0.14	0.14	0.10	0.09	0.15	0.20	0.09
A5**	Mean	19.4%	13.4%	6.0%	5.1%	5.1%	6.9%	0.0%
	CoV	0.11	0.10	0.20	0.33	0.51	0.45	0.00
A8	Mean	32.6%	22.4%	13.2%	10.1%	6.0%	5.1%	6.6%
	CoV	0.08	0.11	0.55	0.60	0.37	0.33	0.46
A9	Mean	24.4%	18.8%	9.8%	8.3%	4.1%	4.8%	4.7%
	CoV	0.14	0.07	0.14	0.24	0.16	0.16	0.34
B1	Mean	30.2%	21.4%	11.1%	8.0%	7.2%	9.8%	12.0%
	CoV	0.07	0.06	0.30	0.23	0.33	0.19	0.13
B2	Mean	21.1%	19.2%	9.9%	8.4%	5.8%	8.1%	9.9%
	CoV	0.27	0.17	0.20	0.18	0.27	0.37	0.25
B3	Mean	24.8%	15.1%	4.7%	3.6%	2.5%	2.1%	4.6%
	CoV	0.29	0.23	0.32	0.26	0.00	0.33	0.69
D1	Mean	24.2%	19.7%	12.6%	11.0%	9.3%	9.5%	8.8%
	CoV	0.16	0.22	0.36	0.32	0.10	0.09	0.28
D2	Mean	19.9%	14.0%	9.5%	8.2%	7.8%	9.0%	6.9%
	CoV	0.24	0.18	0.12	0.13	0.24	0.40	0.31
D3	Mean	21.2%	18.4%	12.4%	10.5%	9.0%	7.7%	9.9%
	CoV	0.31	0.26	0.05	0.23	0.16	0.38	0.17
E1	Mean	32.2%	21.4%	8.8%	6.1%	4.7%	5.0%	5.3%
	CoV	0.12	0.03	0.11	0.18	0.21	0.29	0.16
E2	Mean	27.4%	22.0%	11.8%	8.1%	5.6%	5.8%	5.0%
	CoV	0.02	0.18	0.31	0.29	0.19	0.44	0.37
E3	Mean	19.2%	13.6%	8.9%	8.8%	5.4%	5.0%	5.9%
	CoV	0.09	0.14	0.20	0.18	0.28	0.47	0.60

\* Relative to the third loop

\*\* Different yielding displacement ( $d_y=10$  mm instead of 5 mm)

### 9.3.3.2 Influence of the load-to-grain direction

The considered load-to-grain direction angles were:

- 0°, 45° and 90° for softwood CLT panel, brick masonry wall and fastener T (test configuration A1, A2 and A3 respectively);
- 0° and 90° for hardwood LVL panel, brick masonry wall and fastener M1 (test configuration B1 and B2 respectively);
- 0° and 90° for softwood LVL panel, brick masonry wall and fastener M1 (test configuration E1 and E2 respectively);

As already observed in the monotonic loading tests (section 9.3.2), CLT panels manifested quite consistent mechanical behavior in terms of maximum load and slip modulus, independently from the loading direction. Nonetheless, the best performance was usually obtained for load parallel to the main grain direction of the panel ( $\alpha = 0^\circ$ ). The smaller maximum capacity obtained for the 45° configuration (test A3) was due to the splitting of the block and was not linked to the load-to-grain direction. On the contrary, LVL panels (either realized with beech or spruce lumber) exhibited a clearer distinction between specimens loaded parallel or perpendicular to the main fiber direction of the panels ( $\approx 20\%$  capacity variation). As for the monotonic tests, the 90° load-to grain angle configurations presented the lowest ultimate strength and slip modulus values. The different response between CLT and LVL panels seems to be attributable to the smaller percentage of orthogonal layers in the LVL panels with respect to the whole panel thickness (14% for hardwood LVL, 14% and 20% for softwood LVL panels with thickness of 40 mm and 60 mm, respectively, and 33% for spruce CLT) which is directly related to the embedment strength.

### 9.3.3.3 Influence of the type of timber panel

Figure 9.13 presents the comparison among different timber panels while maintaining constant the other connection parameters. The figure reports on the left the results for the tests performed with fastener M1 (test configuration A4, B1 and E1 for softwood CLT, hardwood LVL and softwood LVL panels) and on the right the results for the tests performed with fastener T (test configuration A1 and E3 for softwood CLT and softwood LVL panels). Also tests with fastener U2 were carried out on brick masonry using both softwood CLT panels and beech LVL panels (test configurations A8 and B3), but the graphs are not reported here for sake of brevity (for the outcomes discussion refer to Table 9.8, Table 9.9 and Table 9.10). Typically, specimens realized with softwood CLT or softwood LVL showed similar performances whereas connections assembled using beech LVL panels exhibited an increase both in maximum load capacity and slip modulus value (despite of the minor thickness of beech LVL panels).

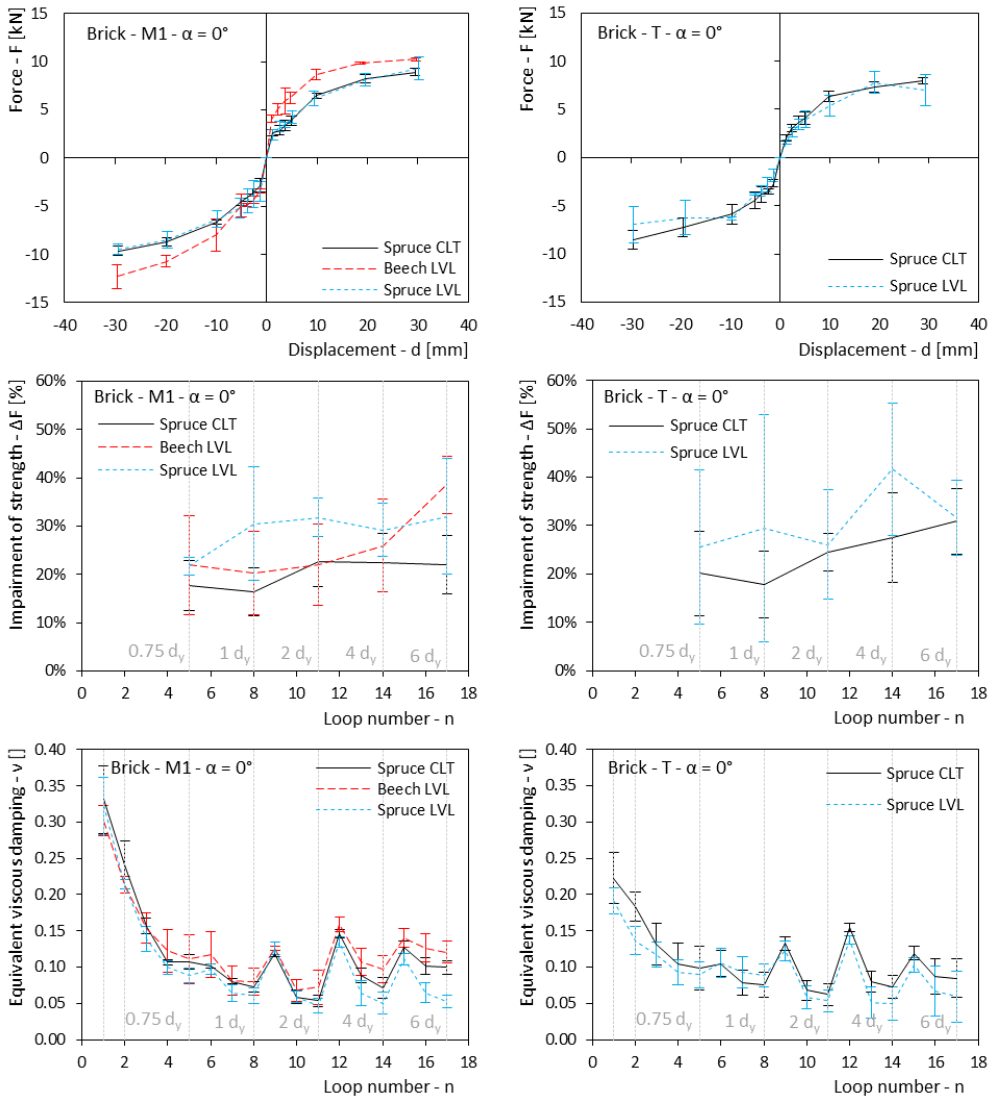


Figure 9.13: Mean envelope curves, impairment of strength and equivalent viscous damping (including standard deviations: error bars) of fasteners M1 (left) and T (right) for brick masonry and  $\alpha$  equal to  $0^\circ$  varying the type of timber panel

This seems to confirm the hypothesis that the governing property on the timber side is the embedment strength of the wood, which depends mainly on the density of the material. Being softwood CLT and softwood LVL panels both obtained from the same wood species, they have comparable values of embedment strength ( $\approx 40$  MPa), whereas the higher density of beech hardwood is reflected by a higher value of the embedment strength ( $> 60$  MPa).

#### **9.3.3.4 Influence of the type of masonry**

To compare the results related to the two masonry typologies, the test configuration couples A4-D1, A1-D2 and A8-D3 can be examined (corresponding, respectively, to fasteners M1, T and U2 connecting spruce CLT panels with brick and stone masonry walls). Not surprisingly, tests performed on the stone masonry (i.e. D1, D2 and D3 configurations) exhibited higher load capacity and stiffness than tests performed on brick masonry (i.e. A1, A4 and A8 configurations). However, they displayed also more scattered results due to the higher variability of the rubble stone masonry pattern (block dimensions, thickness of mortar joints, etc.). In addition, a preferential crack propagation direction was observed in the failure modes on stone masonry (see Figure 9.7). This phenomenon may be due to the sedimentary nature of most of the rocks composing the masonry walls. The stratigraphy of various superimposed layers of sediments determines an orthotropic behavior of the final material (rock) with smaller tensile strength in the direction perpendicular to the layers. Focusing on the hysteretic properties at small displacement levels, stone masonry manifested lower equivalent viscous damping ratios than brick masonry (Figure 9.14, last two graphs). A possible explanation can be found in the higher hardness of the stone blocks compared to clay bricks. At small displacements, the larger deformation of the softer brick and the early cracking allow for greater energy dissipation. As the displacement increases, the dissipation property of the connection is more dependent on the fastener typology, therefore the divergence of the equivalent viscous damping ratio between stone and brick masonry tends to decrease. Finally, even though the masonry typology has a great impact on the performance of the connection, there may be a threshold beyond which a further enhancement of the masonry material properties does not influence the connection behavior. In particular, if the tensile strength of the stone block is relatively large (e.g. granite stone has tensile strength values in the range of  $\approx 7 \div 25$  MPa) and the mortar bed-joint conditions are sound, then the capacity of the connection is mainly governed by the timber panel and fastener properties (e.g. in test D1-c3 where the stone block remained intact).

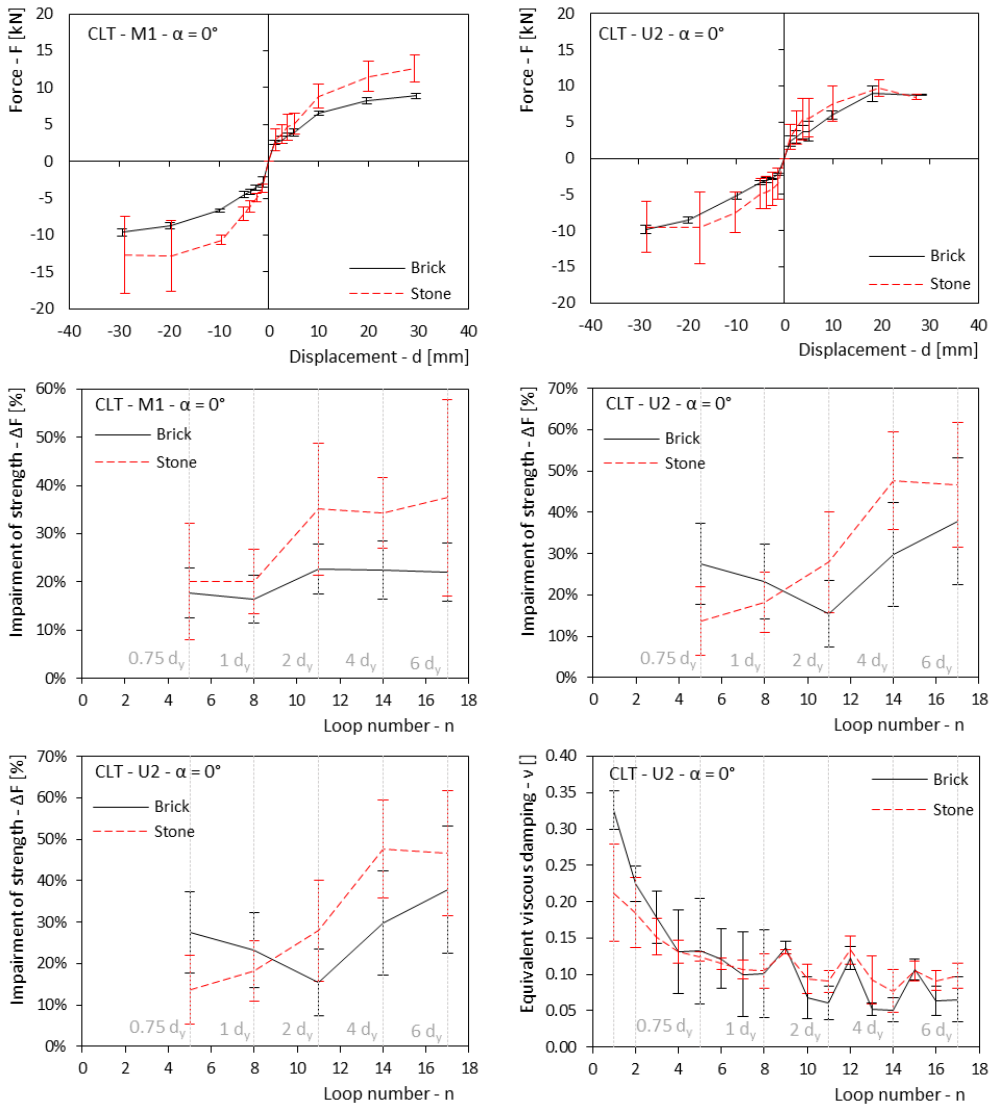


Figure 9.14: Mean envelope curves, impairment of strength and equivalent viscous damping (plus standard deviations: error bars) of fasteners M1 (left) and U2 (right) for CLT timber panels and  $\alpha$  equal to  $0^\circ$  varying the masonry type

### 9.3.3.5 General remarks

For all the cyclic and semi-cyclic tests, the maximum connection capacity was limited by the local failure of the masonry (with the exception of test D1-c3 where a brittle failure of the steel anchor shank was experienced). Depending on the type of masonry failure (tension, splitting, compression crushing, mortar crushing, etc.) the maximum load and the slip modulus were subjected to consistent variation. For such reason, in

order to determine upper bound and lower bound limits for both the capacity and the stiffness of dry timber-masonry connections, a statistical analysis of the maximum load values and the slip moduli was carried out. However, it is worth reminding that this is a preliminary study and the validity range must be limited to masonry material with mechanical properties comparable to those of the presented campaign (see Table 9.1). Firstly, the frequency distributions of the maximum load and of the slip modulus were calculated separating the tension and compression semi-cycles and assuming discrete intervals of 0.5 kN and 0.25 kN/mm for the maximum load and slip modulus respectively (Figure 9.15).

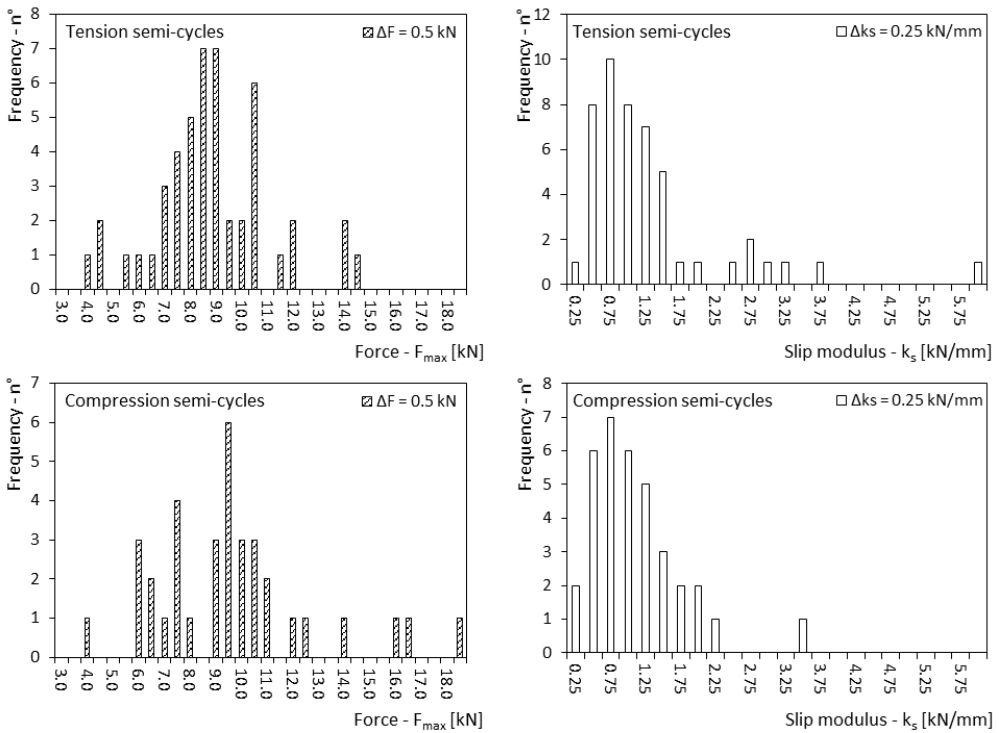


Figure 9.15: Statistical frequency analysis of all the 48 cyclic tests performed (divided in tension and compression semi-cycles) of the maximum load ( $\Delta F = 0.5$  kN) and of the slip modulus ( $\Delta k_s = 0.25$  kN/mm)

Table 9.11 lists the statistical moments of all the cyclic tests from the first moment, namely the expected value or mean of the sample, to the fourth standardized moment, specifically the kurtosis of the sample (also the excess kurtosis is reported). The third standardized moment (skewness) and the fourth standardized moment (kurtosis) are generally considered as shape indicator of the sample distribution. Both the maximum load and the slip modulus distribution exhibit positive values for the skewness, meaning

that the distributions are skewed to the right. Also the excess kurtosis presents positive values. The distributions with positive excess kurtosis, called leptokurtic, have heavier tails with respect to the normal distribution. However, these two moments might be considered only as rough indicators of the true shape distribution of the population due to the limited size of the sample.

*Table 9.11: Statistical moments of the tension semi-cycles, compression semi-cycles*

Moment		Tension semi-cycles		Compression semi-cycles		Total	
		$F_{\max}$ [kN]	$k_s$ [kN/mm]	$F_{\max}$ [kN]	$k_s$ [kN/mm]	$F_{\max}$ [kN]	$k_s$ [kN/mm]
Expected value	$\mu_1$	8.60	1.22	9.38	0.99	8.93	1.12
Variance	$m_2$	4.94	1.04	9.72	0.41	7.10	0.79
Skewness	$m_3$	0.29	2.39	0.92	1.59	0.86	2.51
Excess kurtosis	$m_4$	0.62	7.61	1.28	4.26	1.75	9.07

Figure 9.16 shows the distribution fitting for the maximum load (right) and slip modulus (left) in terms of both probability density function and cumulative probability function. The fitting is performed using the method of moments and selecting a lognormal distribution due to the right skewed and leptokurtic nature of the experimental data. The method of moments approach simply adopts the sample mean and variance of the sample as estimators of the population mean and variance; from this equivalence the parameters of the selected distribution can be determined.

As an estimation of the goodness of fit the Shapiro-Wilk expanded test for log-normality was implemented. The null-hypothesis of the test is that the population is log-normally distributed. If that is the case, then the p-values are expected to be greater than the selected cutoff (or significance level)  $\alpha$ . The calculated p-values are 0.102 and 0.837 for the maximum load and the slip modulus distribution. Therefore, assuming a significance  $\alpha$  level equal to 0.05, the null-hypothesis cannot be rejected with a confidence of 10.2% and 83.7% respectively. In addition, the quantile-quantile (Q-Q) plots are reported in Figure 9.17 for a graphical validation of the goodness of fit of the chosen distributions.

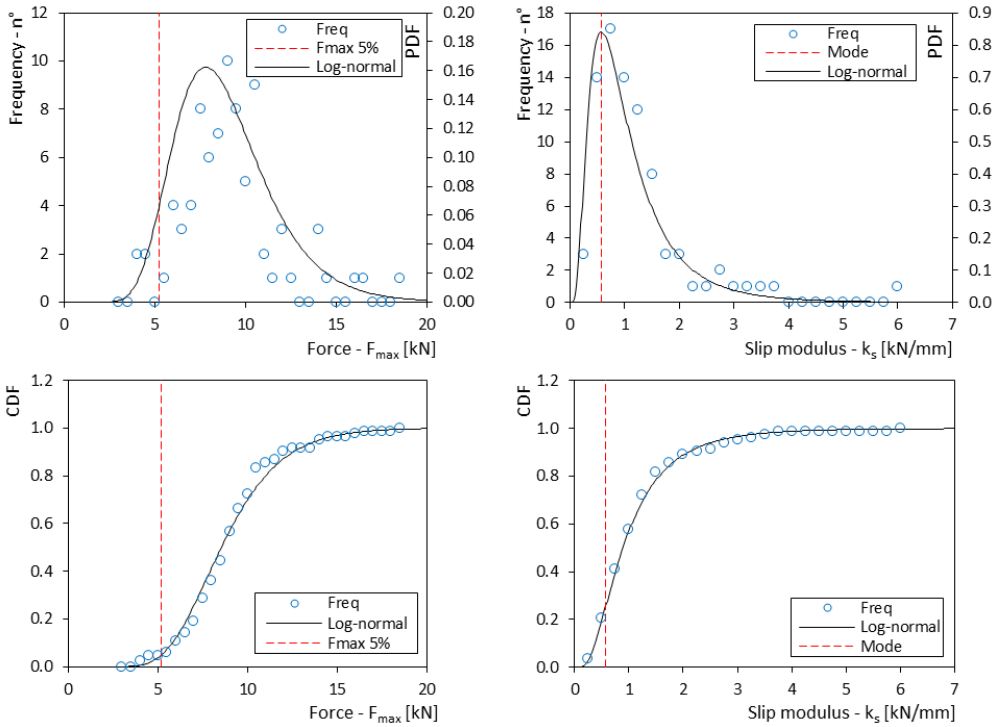


Figure 9.16: Lognormal distribution fitted to the data (both for tension and compression semi-cycles) of load  $F_{max}$  (left) and slip modulus  $k_s$  (right) and representation of load characteristic value (5%) and slip modulus mode value

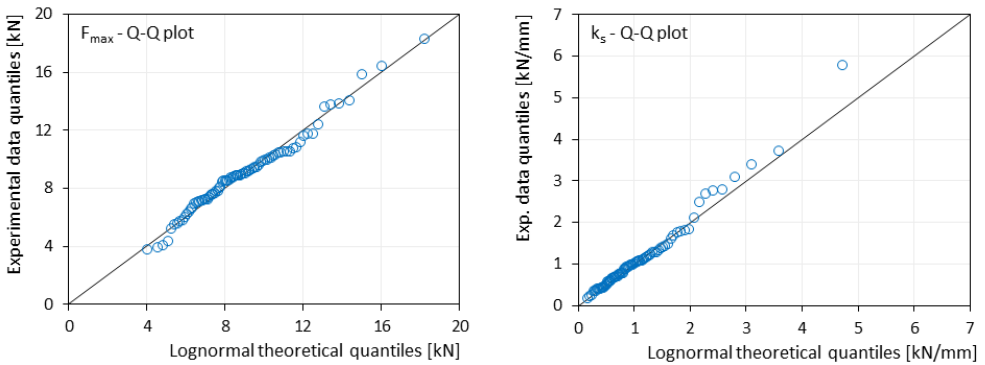


Figure 9.17: Quantile-Quantile plot of load  $F_{max}$  (left) and slip modulus  $k_s$  (right) fitted to a lognormal distribution

## 9.4 RESULTS – GROUTED CONNECTIONS

### 9.4.1 OBSERVED FAILURE MECHANISMS

After testing procedure was completed the panel was removed and connection components were inspected. It is worth noting that connections retained a residual withdrawal strength, even after the whole loading sequence was completed. In all the cases dowels remained strongly fixed to the support and it was not possible to extract them from the masonry. Based on the observed failure mechanism, two types of connection behavior were observed. In the case of weak stone blocks, tension cracking occurred prior to dowel yielding, leading to the behavior of Figure 9.18-a. If the case, after a sudden loss of force due to crack opening, additional displacements forced the dowel against the compression side of the cracked block and the pre-cracking load value was restored. Due to the modified restraint imposed by the stone block, dowel yielding occurred for greater displacements. In other cases, failure mechanism involved dowel yielding without to engage stone ultimate cracking resistance (Figure 9.18-b).

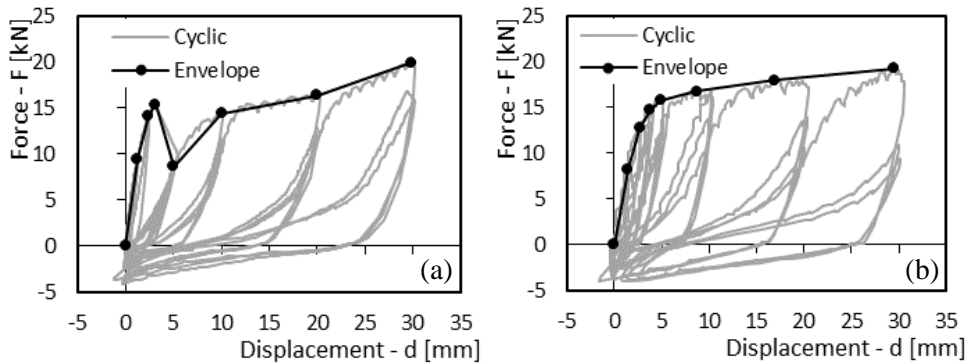


Figure 9.18: Typical Force vs displacement plots: a) HY 14 TH – stone tension cracking; b) EX 14 TH – Dowel yielding w/o stone tension cracking

Observed failure mechanisms always involved stone tension cracking (Figure 9.19-a,-b,-c) and the formation of a plastic hinge in the dowel at the masonry-to-timber interface (Figure 9.19-d). Similarly to the case of dry connections, crack orientation was related to the principal directions of the stone elements dictated by the sedimentation process. Limited cracking was observed in the grout between the dowel and the timber element (Figure 9.19-e) coupled with limited timber borer.



Figure 9.19 Observed failure mechanisms: a, b, c) Tension cracking of stone elements; d) Residual deformation of threaded steel rod; e) Grout embedment; f) Residual grout at timber-masonry interface

#### 9.4.2 ENVELOPE BACKBONE CHARACTERIZATION

Mean values of connection strength and stiffness are listed in Table 9.12. Stiffness values are intended as 1<sup>st</sup> cycle secant stiffness and  $F_{max}$  refers to the maximum load recorded in the test. The irregular masonry texture (variability in stone element dimensions and shape, anisotropy of stone blocks, possible micro-cracking induced by drilling procedure) led to scattered results as highlighted by the relatively high values of the  $CoVs$ , especially regarding the stiffness parameter  $k_I$ . Despite this it was possible to estimate the influence of selected parameters (dowel diameter and type, grout formulation) on connection behavior.

With reference to mean values:

- The influence of dowel diameter was observed to be relevant on both connection strength and stiffness values, especially in the case of hybrid grout (HY) type (see Figure 9.20);
- Specimens assembled with epoxy (EX) exhibited greater stiffness and strength compared to those assembled with hybrid (HY) grout;
- Both stiffness and strength were observed to be slightly affected by dowel type and no clear tendencies can be reported.

Table 9.12: Observed mean strength and stiffness values for the tested connections

Connection ID	$F_{max}$		$k_1$	
	[kN]	CoV	[kN/mm]	CoV
HY 14 TH	15.84	0.23	3.01	0.71
HY 14 RB	15.77	0.28	2.43	0.14
HY 20 TH	27.62	0.08	4.75	0.44
HY 20 RB	28.83	0.15	5.90	0.26
EX 14 TH	25.97	0.23	8.97	0.29
EX 14 RB	22.88	0.16	8.56	0.47
EX 20 TH	35.90	0.20	8.39	0.41
EX 20 RB	34.51	0.16	10.26	0.64

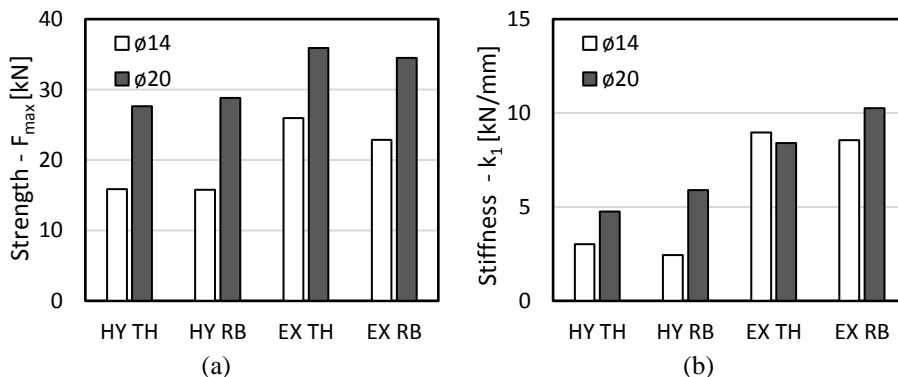


Figure 9.20: Influence of dowel diameter: a) Connection strength  $F_{max}$ ; b) 1<sup>st</sup> cycle secant stiffness  $k_1$

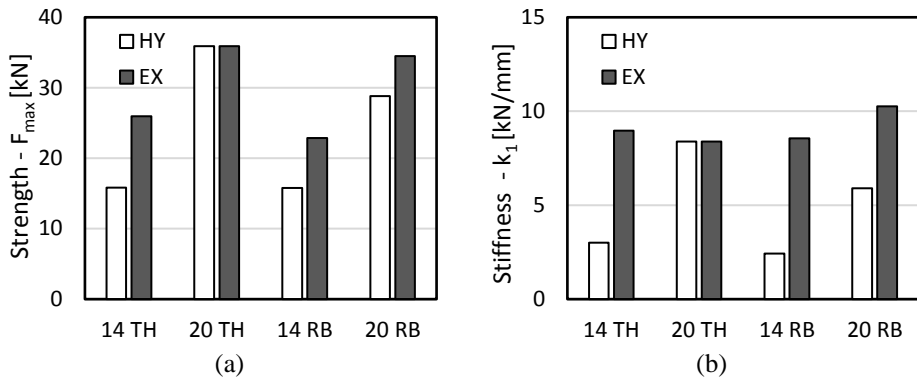


Figure 9.21: Influence of grout formulation: a) Connection strength  $F_{max}$ ; b) 1<sup>st</sup> cycle secant stiffness  $k_1$

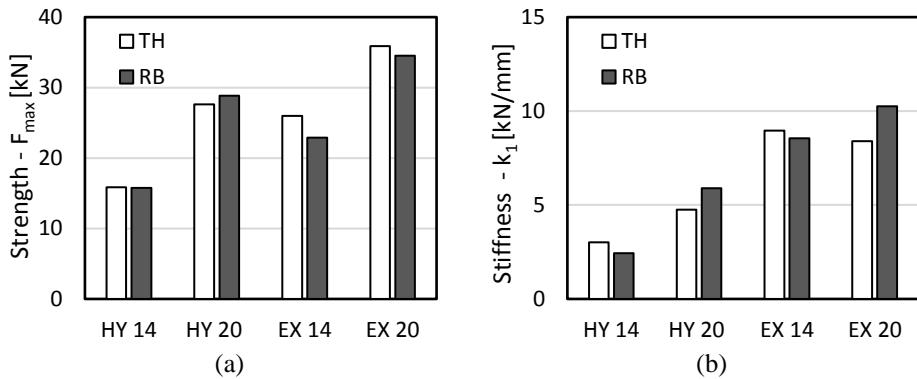


Figure 9.22: Influence of grout formulation: a) Connection strength  $F_{max}$ ; b) 1<sup>st</sup> cycle secant stiffness  $k_1$

### 9.4.3 CYCLIC BEHAVIOR

Values representative of connection behavior under repeated cyclic loading are reported in Table 9.13 regarding the third cycle impairment of strength and in Table 9.14 and Table 9.15 concerning the equivalent viscous damping ratios.

Table 9.13: Mean values and coefficients of variation of the third loop impairment of strength  $\Delta F$  at increasing levels of displacement

Test ID	$\Delta F$ [%]	0.75 d <sub>y</sub>	1 d <sub>y</sub>	2 d <sub>y</sub>	4 d <sub>y</sub>	6 d <sub>y</sub>
Total loop n°		5	8	11	14	17
EX 20 TH	Mean	16%	20%	31%	36%	42%
	CoV	0,58	0,65	0,23	0,35	0,32
EX 20 RB	Mean	26%	43%	41%	68%	41%
	CoV	0,76	0,64	0,32	0,35	0,37
EX 14 TH	Mean	19%	22%	22%	30%	41%
	CoV	0,34	0,15	0,81	0,26	0,29
EX 14 RB	Mean	23%	15%	15%	38%	35%
	CoV	0,41	0,68	0,26	0,44	0,14
HY 14 TH	Mean	47%	19%	24%	35%	35%
	CoV	0,38	0,41	0,22	0,29	0,25
HY14 RB	Mean	22%	14%	21%	37%	36%
	CoV	0,49	1,04	0,17	0,09	0,19
HY 20 TH	Mean	20%	17%	19%	43%	45%
	CoV	0,28	0,37	0,66	0,68	0,55
HY 20 RB	Mean	24%	16%	20%	31%	22%
	CoV	0,40	0,17	0,25	0,43	0,10

Table 9.14: Mean values and coefficients of variation of the equivalent viscous damping ratios  $v_{eq}$  at increasing levels of displacement, first loop cycle

Test ID	$v_{eq}$ [%]	0.25 d <sub>y</sub>	0.50 d <sub>y</sub>	0.75 d <sub>y</sub>	1 d <sub>y</sub>	2 d <sub>y</sub>	4 d <sub>y</sub>	6 d <sub>y</sub>
Total loop n°		1	2	3	6	9	12	15
EX 20 TH	Mean	13%	10%	9%	8%	13%	15%	12%
	CoV	0,57	0,30	0,35	0,26	0,05	0,12	0,11
EX 20 RB	Mean	17%	13%	11%	11%	15%	15%	8%
	CoV	0,50	0,38	0,28	0,24	0,32	0,21	0,43
EX 14 TH	Mean	16%	13%	9%	9%	16%	17%	12%
	CoV	0,35	0,17	0,18	0,28	0,07	0,05	0,05
EX 14 RB	Mean	11%	13%	9%	9%	15%	17%	11%
	CoV	0,42	0,22	0,08	0,14	0,14	0,02	0,14
HY 14 TH	Mean	16%	13%	7%	7%	13%	13%	10%
	CoV	0,25	0,22	0,34	0,25	0,15	0,14	0,17
HY14 RB	Mean	13%	11%	7%	7%	11%	15%	12%
	CoV	0,26	0,15	0,30	0,31	0,06	0,13	0,02
HY 20 TH	Mean	18%	13%	6%	6%	10%	10%	10%
	CoV	0,19	0,24	0,39	0,36	0,20	0,32	0,21
HY 20 RB	Mean	13%	10%	6%	6%	12%	16%	12%
	CoV	0,04	0,14	0,25	0,13	0,20	0,17	0,23

Table 9.15: Mean values and coefficients of variation of the equivalent viscous damping ratios  $v_{eq}$  at increasing levels of displacement, third loop cycle

Test ID	$v_{eq}$ [%]	0.75 $d_y$	1 $d_y$	2 $d_y$	4 $d_y$	6 $d_y$
Total loop n°		5	8	11	14	17
EX 20 TH	Mean	5%	5%	4%	4%	3%
	CoV	0,40	0,34	0,37	0,66	0,82
EX 20 RB	Mean	6%	6%	5%	5%	3%
	CoV	0,52	0,34	0,58	0,67	0,86
EX 14 TH	Mean	4%	4%	6%	5%	6%
	CoV	0,43	0,58	0,57	0,52	0,74
EX 14 RB	Mean	5%	5%	5%	4%	5%
	CoV	0,27	0,21	0,47	0,15	0,44
HY 14 TH	Mean	6%	6%	3%	3%	4%
	CoV	0,29	0,31	0,51	0,32	0,35
HY14 RB	Mean	5%	5%	4%	4%	4%
	CoV	0,40	0,45	0,28	0,07	0,03
HY 20 TH	Mean	4%	4%	3%	4%	3%
	CoV	0,51	0,50	0,63	0,73	0,53
HY 20 RB	Mean	4%	4%	4%	5%	3%
	CoV	0,47	0,21	0,36	0,47	0,26

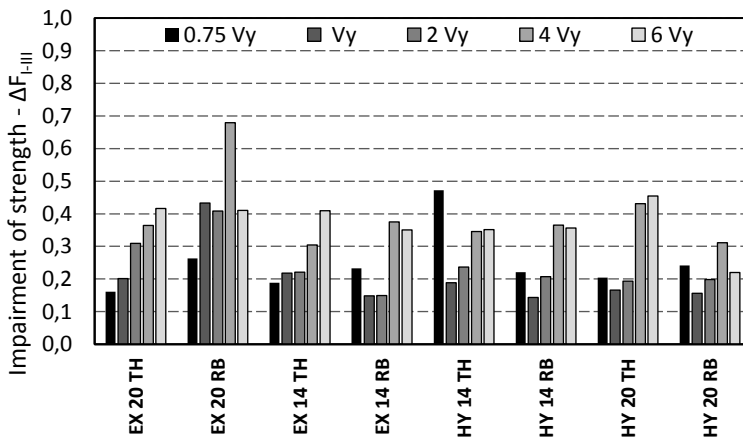


Figure 9.23: Third loop impairment of strength - mean values

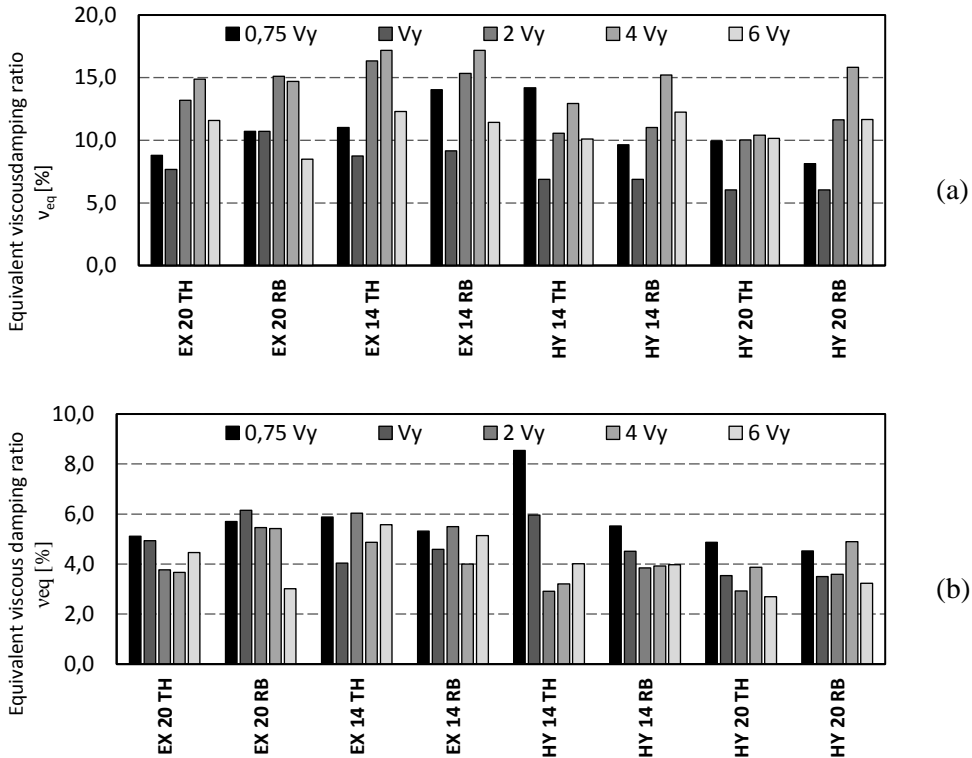


Figure 9.24: Equivalent viscous damping ratios –  $v_{eq}$ : a) First loop cycle; b) Third loop cycle

## 9.5 COMPARISONS BETWEEN CONNECTION TYPES

Results in terms of connection strength  $F_{max}$  and 1<sup>st</sup> cycle secant stiffness  $k_I$  (mean values) are listed in Table 9.16 and depicted in Figure 9.25. For consistency, only results obtained on rubble stone masonry are reported (grouted connections plus D-type dry connections). In general, grouted connections exhibited higher values for both connection strength and stiffness.

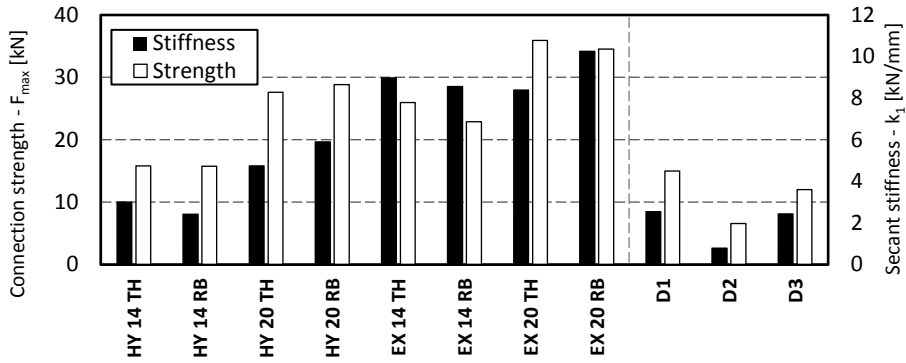


Figure 9.25: Connection properties comparison

Table 9.16: Connection strength  $F_{max}$  and 1<sup>st</sup> cycle secant stiffness  $k_1$  – mean values among connection types

Connection ID	$F_{max}$ [kN]	$k_1$ [kN/mm]
HY 14 TH	15.84	3.01
HY 14 RB	15.77	2.43
HY 20 TH	27.62	4.75
HY 20 RB	28.83	5.90
EX 14 TH	25.97	8.97
EX 14 RB	22.88	8.56
EX 20 TH	35.90	8.39
EX 20 RB	34.51	10.26
D1	14.98	2.54
D2	6.57	0.79
D3	12.00	2.44

## 9.6 SIMPLIFIED ANALYTICAL MODEL

In this paragraph a simplified model for predicting connection strength based on the attained results and the observed failure modes is proposed. The formulations were derived according to the theoretical approach implemented in the EN 1995 Standard [CEN (2014)] for steel-timber connections with dowel-type fasteners. In particular, rigid-plastic constitutive laws are assumed for both timber panels and steel dowels. According to experimental evidences the relevant failure mechanisms are those identified by the activation of one (mode I) or two (mode II) plastic hinges in the dowels as depicted in Figure 9.26. In the following  $M_y$  is dowel yielding moment and  $p$  is equal to the embedment strength of the CLT panel multiplied by the hole diameter  $d_H$ .

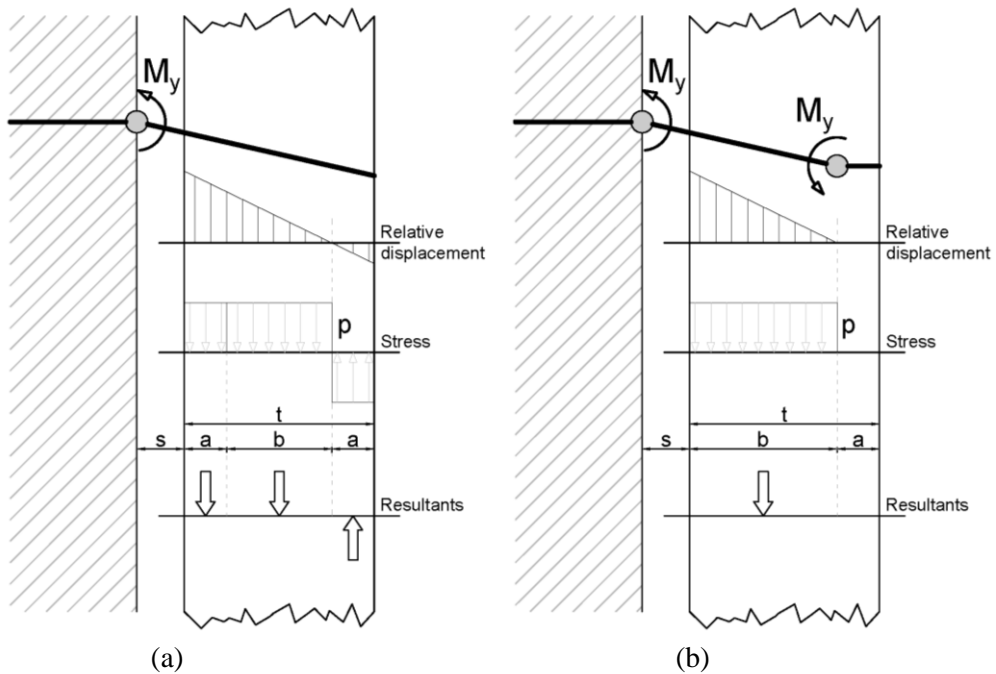


Figure 9.26: Failure modes for timber-masonry connection systems: a) Mode I; b) Mode II.

To account for the possible gap between the masonry and the CLT element the parameter  $s$  was introduced in the calculations. For failure mode I rotation equilibrium with respect to the plastic hinge is given by equation (9.1).

$$M_y + pa(t - a) - pbs + \frac{t}{2} = 0 \quad (9.1)$$

Solution of equation (9.1) with respect to  $b$  allows to calculate connection strength  $F_{RI}$  according to equation (9.2).

$$F_{RI} = pb = p \left[ -2s - t + \frac{\sqrt{2} \sqrt{p[2M_y + p(2s^2 + 2st + t^2)]}}{p} \right] \quad (9.2)$$

In the same way for mode II, rotation equilibrium condition with respect to the hinge in the masonry is given by equation (9.3), whose solution with respect to  $b$  leads to the calculation of the connection strength  $F_{RII}$  which is given by equation (9.4).

$$2M_y - pb \left( s + \frac{b}{2} \right) = 0 \quad (9.3)$$

$$F_{RII} = pb = p \left[ \frac{\sqrt{p \cdot (4M_y + ps^2)}}{p} - s \right] \quad (9.4)$$

Since failure mechanism is not known *a priori*, connection strength  $F_R$  should be taken as the lower of  $F_{RI}$  and  $F_{RII}$ .

The proposed formulation was validated considering experimental results presented in this chapter. For screw-type fasteners features listed in Table 9.2 were considered, otherwise yielding moment was calculated according to nominal dowel geometrical and mechanical features. Timber panel embedment strength was calculated according to Austrian version of EN1995 [ÖNORM (2019)] and unit length pressure  $p$  was calculated based on timber hole diameter, which is equal to dowel diameter for screw-type fasteners and is equal to 22 mm and 30 mm for Ø 14 mm and Ø 20 mm dowels respectively in the case of grouted connections. Results obtained for a zero timber-masonry gap ( $s = 0$ ) are compared to experimental connection yielding strength values  $F_y$  in Table 9.17.

Table 9.17: Analytical model vs. experimental results comparisons: a) Dry connections; b) Grouted connections

ID	$F_R$ [kN]	$F_y$ [kN]	err	ID	$F_R$ [kN]	$F_{y,HY}$ [kN]	$F_{y,EX}$ [kN]	err <sub>HY</sub>	err <sub>EX</sub>
A1	6,27	5,18	21%	14 TH	15,60	11,87	23,51	31%	-34%
A2	5,98	6,11	-2%	14 RB	14,48	14,23	19,8	2%	-27%
A3	6,12	7,67	-20%	20 TH	23,72	22,8	32,1	4%	-26%
A4	6,27	6,81	-8%	20 RB	20,80	25,4	26,1	-18%	-20%
A5	6,27	6,92	-9%						

(a)

(b)

---

According to the analytical model each of the dry connection types failed according to mode II (double plastic hinge), while for grouted connections failure mode I was predicted. Error values listed in Table 9.17 were calculated according to equation (9.5).

$$err = \frac{F_R - F_y}{F_y} \quad (9.5)$$

Results listed in Table 9.17 appear to be satisfactory except for the inability of the model to account for grout type, while failure modes were predicted consistently with experimental evidences.

The model was also implemented considering a 10 mm-wide timber-masonry gap  $s$  leading to strength reductions of approximately 30% for dry connections and 20% in the case of grouted connections. In such case failure modes were predicted to be consistent with those previously observed, except for 14 RB connection type which was foreseen to fail according to mode II.

## 9.7 CONCLUSIONS

An extensive experimental investigation on timber panel to masonry wall connections was undertaken to evaluate the mechanical performance of the connections under static and seismic shear loading conditions. The tests were performed in an existing URM building, which dates back to the late 1800s, adopting monotonic, cyclic and semi-cyclic loading protocols. Two different masonry typologies (brick masonry and rubble stone masonry) and three different timber panels (spruce CLT, spruce LVL and beech LVL) were selected for the campaign. The majority of the tests were carried out with a load-to-grain angle of  $0^\circ$  (load parallel to the main grain direction of the wood panel); nevertheless, also the  $45^\circ$  and the  $90^\circ$  load-to-grain directions were examined in the case of dry connections and for the three types of timber panels. For dry connection system, five different screw anchor fasteners were used, with variable geometry (diameter, length, threaded parts, etc.) and material (mild steel and hardened carbon steel). Grouted connections were assembled with threaded 8.8 class steel dowels in two diameters and using two types of grout. In summary, the main outcomes of the study can be listed as follows:

- Dry connections on stone masonry walls exhibited higher mean values of maximum capacity and slip modulus with respect to the corresponding configuration on brick masonry walls, but also higher variability in the failure modes linked to the irregular masonry texture.
- From the timber point of view, the identified key property in determining the dry connection capacity and stiffness, not surprisingly, was the embedment strength of

the material. Therefore, the use of hardwood LVL increases both the capacity and the stiffness of the connection compared to softwood-based material. Specimens realized with softwood CLT and softwood LVL showed similar performance, indicating that the product type has less influence on the mechanical properties of the connection with respect to the timber species or grade.

- The tests performed with different load-to-grain angles ( $\alpha = 0^\circ, 45^\circ$  and  $90^\circ$ ) suggest that the connections built with CLT panels are less sensible to the force direction. On the contrary, the specimens realized with LVL panels (either using spruce or beech wood) manifested a non-negligible reduction in both maximum load capacity and slip modulus. This distinction may be a consequence of the smaller percentage of lamellae and/or veneers in the perpendicular direction for the LVL compensated panel compared to the CLT panel (respectively equal to 14% and 33% of the whole thickness of the element).
- The choice of fastener typology seems to have lower impact on the strength and stiffness parameters of the dry connection in comparison with the selection of timber panel products or masonry wall elements. It is worth reminding that higher strength values of the masonry constituents might determine a stronger engagement of the fastener properties and result in an increased influence of the fastener typology. It is, however, advisable to use mild steel fasteners on brick masonry walls due to the increased energy dissipation of the connection under cyclic loading (earlier formation of the plastic hinge). On the other hand, for stone masonry walls the adoption of hardened carbon steel fasteners can reduce the risk of brittle tensile failure.
- As indicative reference values for estimating the shear performance of screw anchors connecting timber-based panels to masonry walls, a capacity of 9.0 kN on average and a mean slip modulus equal to 1.1 kN/mm may be assumed. If required, different percentile values may be calculated from the proposed probability distribution used for fitting the reported experimental data. A tentative value of 1.5 for the resistance partial factor  $\gamma_R$ , derived according to EN 1990 [CEN (2006)] by assuming a reliability index  $\beta = 3.8$  and a sensitivity factor  $\alpha_R = 0.8$ , is recommended to be used in Ultimate Limit State calculations with Load and Resistance Factor Design (LRFD) methods. However, the validity range of the above-mentioned values is limited to masonry support with characteristics comparable to those of the case study presented herein (see Table 9.1).
- Regarding grouted connections, the irregular masonry texture led to a significant variability in the attained results. It was nevertheless possible to estimate the influence of the selected parameters on connection behavior.

- 
- Failure mechanisms always involved dowel yielding. In most of the cases also stone cracking and mortar crushing phenomena were observed. Limited signs of borer were observed in timber elements.
  - Steel dowel type was not observed to be clearly influent on connection behavior, unlike dowel diameter which significantly affected both connection strength and stiffness.
  - Grout type was observed to have a noticeable influence on connection shear behavior with particular reference to stiffness.

Dry screw anchors and grouted connections appear to be a viable solution for connecting timber panels and brick masonry walls. However, in the case of random rubble stone masonry with thick and irregular mortar bed joints, “wet” alternatives based on the use of adhesives were observed to provide stiffer and stronger connections. In such case the experimentation on an irregular masonry texture allowed to highlight the influence that may be introduced by such parameter which was observed to be, in some cases, greater than the influence of the single connection parameters. Regarding dry connections also the steel grade of the fastener may be selected in the design phase of the intervention to favor either energy dissipation or strength. As regards the timber panel design selection, CLT panels constitute a solid option thanks to consistent mechanical properties for various *load-to-main grain* angles and to comparable performance in terms of maximum load and slip modulus with respect to LVL material. On the other hand, LVL panels may be used to minimize the thickness of the reinforcing solution and the resultant loss of inside living space. However, the differences in performance parallel and perpendicular to the main grain direction must be taken into consideration for the design analysis.

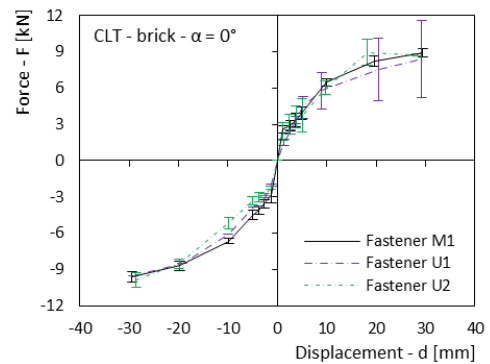
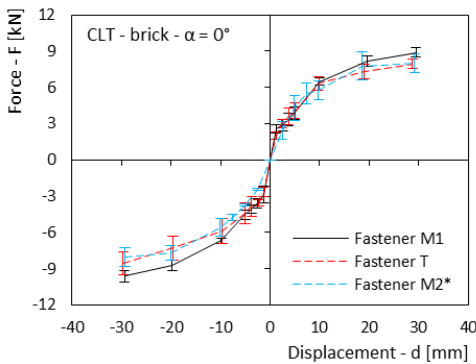
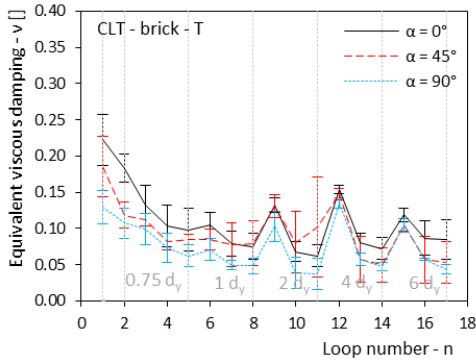
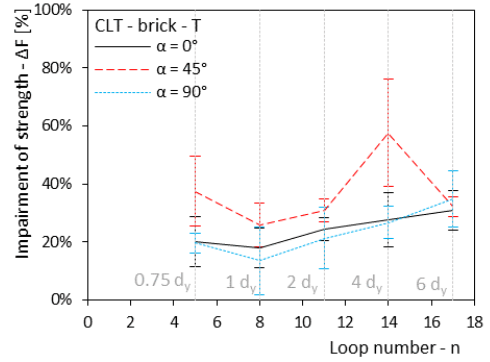
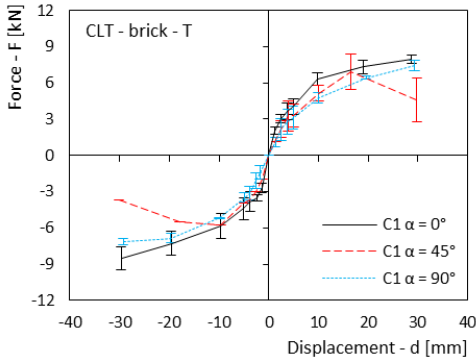
Although the experimental work here presented herein was carried out bearing in mind the final goal of in-plane strengthening of URM walls, the outcomes can prove useful also for different applications, whenever coupling of timber and masonry is requested (e.g. temporary shoring in the post-earthquake emergency when speed and reversibility of the intervention can be critical aspects).

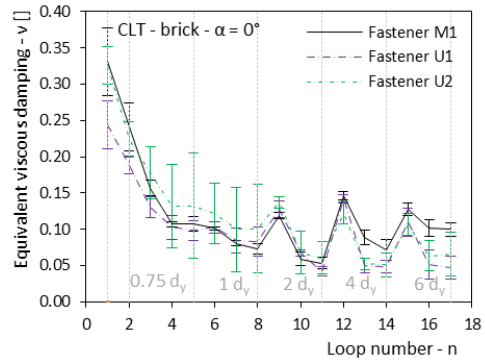
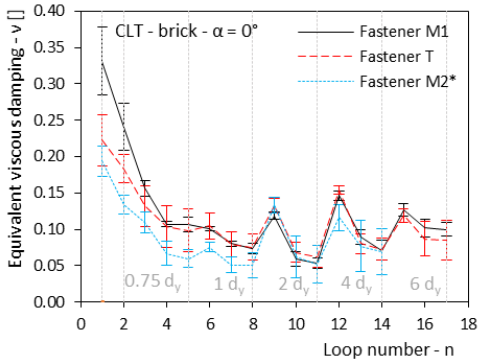
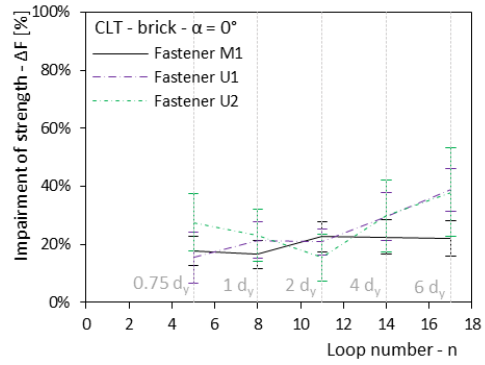
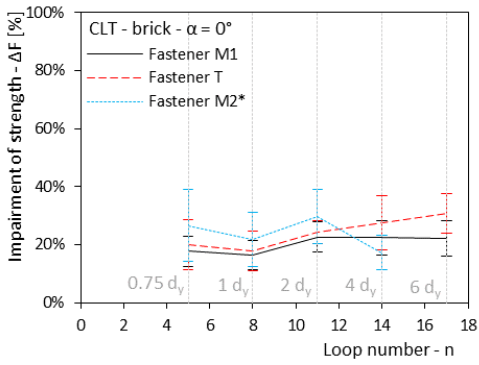
**NOTE:** Part of the research outcomes presented in this Chapter have been published in:

Riccadonna D., Giongo I., Schiro G., Rizzi E., Parisi M. A. “Experimental shear testing of timber-masonry dry connections for the seismic retrofit of unreinforced masonry shear walls” *Construction and Building Materials*, vol. 211, pp. 52-72, 2019.

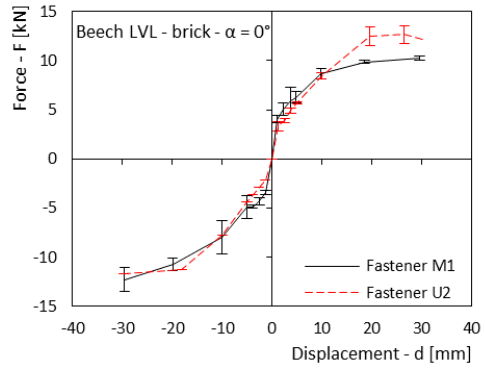
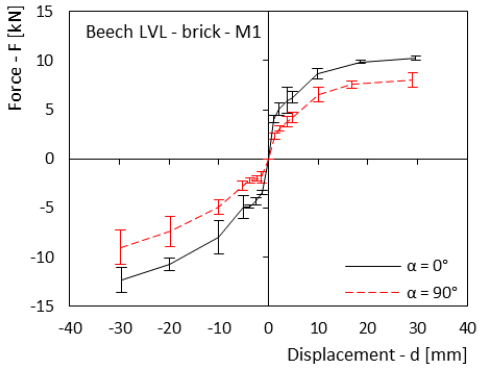
## 9.8 ANNEX

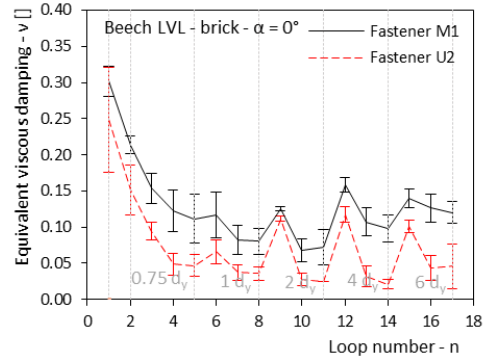
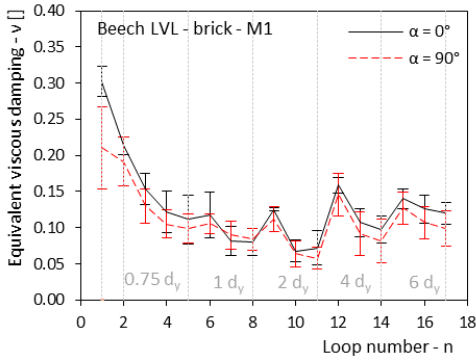
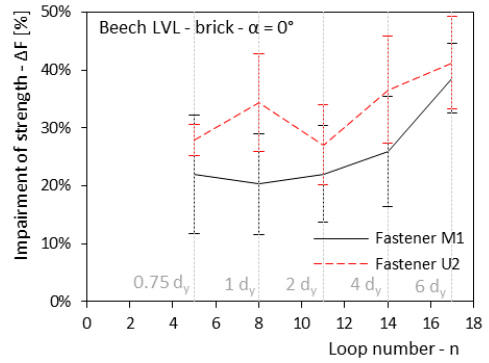
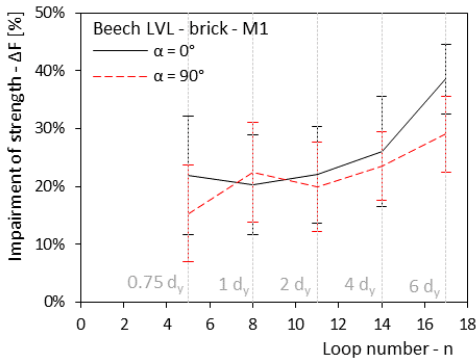
### Test configuration A (brick masonry wall – spruce CLT panel)



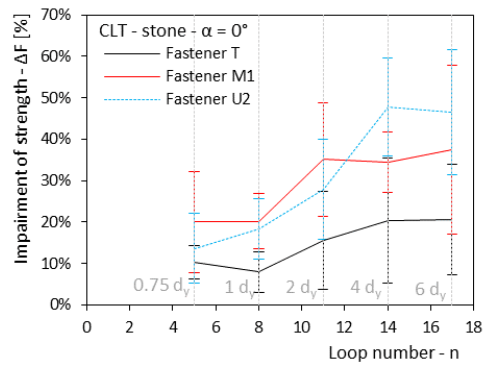
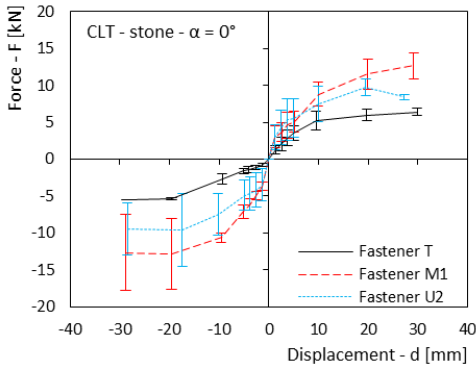


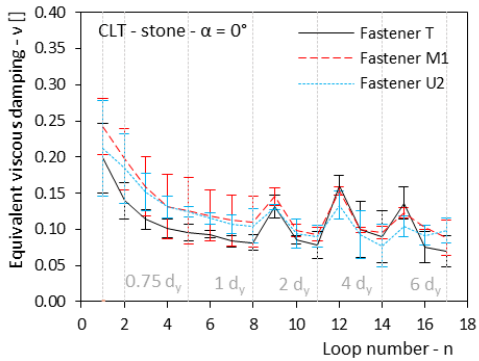
### Test configuration B (brick masonry wall – beech LVL panel)



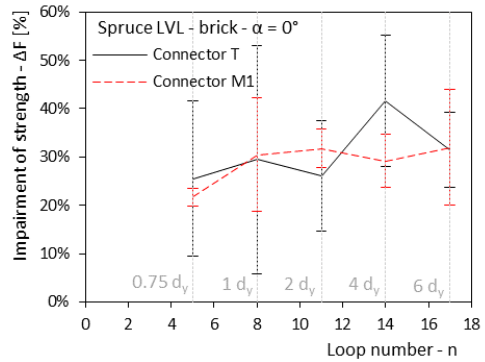
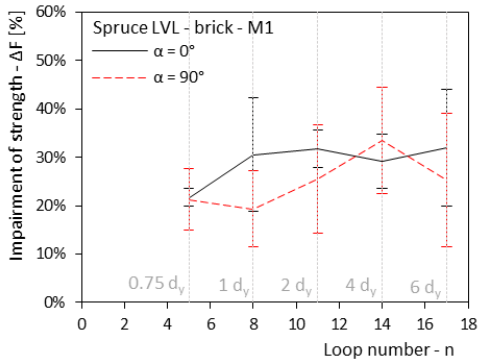
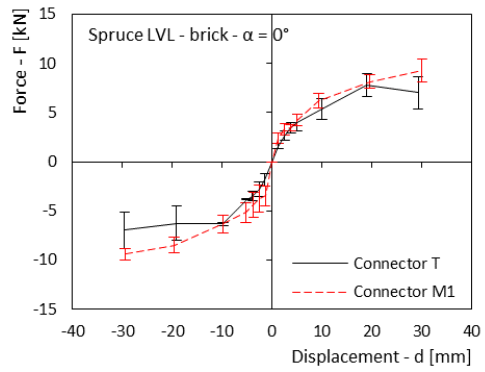
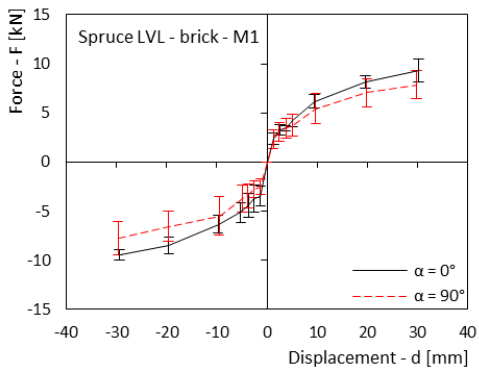


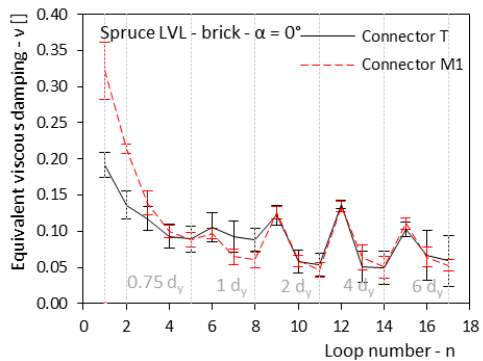
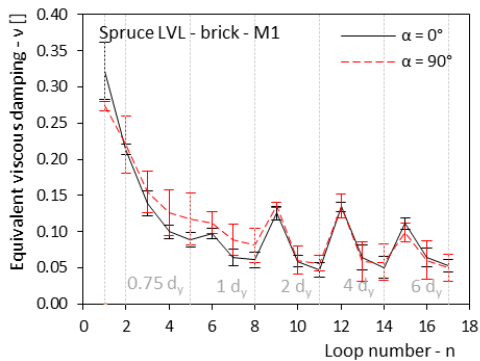
Test configuration D (stone masonry wall – spruce CLT panel)





Test configuration E (brick masonry wall – spruce LVL panel)





---

## 9.9 REFERENCES

ASTM (American Society for Testing and Materials International) (2011) “Standard test methods for cyclic (reversed) load test for shear resistance of vertical elements of the lateral force resisting systems for buildings” *ASTM E2126-11*, West Conshohocken, Pennsylvania, United States.

ASTM (American Society for Testing and Materials International) (2014) “Standard test method for sampling and testing brick and structural clay tile” *ASTM C67-14*, West Conshohocken, Pennsylvania, United States.

Brozovsky J., and Zach, J. (2012). “Evaluation of technical condition of masonry structures” Proceedings of the 15<sup>th</sup> International Brick and Block Masonry Conference, Florianopolis, Brazil, 2012.

CEN (European Committee for Standardization) (2001). “Timber structures – Test methods – Cyclic testing of Joints made with mechanical fasteners”. *EN 26891*. Brussels, Belgium.

CEN (European Committee for Standardization) (2004). “Eurocode 5 – Design of timber structures, Part 1-1: General - common rules and rules for buildings”. *EN 1995-1-1*. Brussels, Belgium.

CEN (European Committee for Standardization) (2006). “Eurocode – Basis of structural design”. *EN 1990*. Brussels, Belgium.

CEN (European Committee for Standardization) (2009). “Timber structures – Joints made with mechanical fasteners – General principles for the determination of strength and deformation characteristics”. *EN 26891*. Brussels, Belgium.

CEN (European Committee for Standardization) (2012). “Testing concrete in structures – Part 2: Non-destructive testing – Determination of rebound number”. *EN 12504-2*. Brussels, Belgium.

CIRCOLARE 21 gennaio 2019, n. 7 C.S.LL.PP. Ministero delle Infrastrutture dei Trasporti, *Istruzioni per l'applicazione dell'«Aggiornamento delle “Norme tecniche per le costruzioni”» di cui al decreto ministeriale 17 gennaio 2018.*, 11 febbraio 2019, G.U. n. 35 del 11 febbraio 2019 - Suppl. Ordinario n. 5. In Italian.

European Technical Assessment ETA-05/0010, HECO MULTI-MONTI MMS Concrete screw for use in concrete, 2015.

European Technical Assessment ETA-15/0352, Fischer concrete screw ULTRACUT FBS II Adjustable concrete screw, 2016.

European Technical Assessment ETA-14/0354, Beam BauBuche GL75 - Glued laminated timber made of hardwood – Structural laminated veneer lumber made of beech, 2018.

Giuriani, E., Gattesco, N. and Del Piccolo, N. (1993) “Experimental tests on the shear behavior of dowels connecting concrete slabs to stone masonry walls” *Materials and Structures*, vol. 26, pp 293-301, 1993.

ÖNORM (Austrian Standards) (2019) “Eurocode 5: Design of timber structures - Part 1-1: General - Common rules and rules for buildings - Consolidated version with national specifications, national comments and national supplements for the implementation” *ÖNORM EN 1995-1-1*. Wien, Austria.



---

# **10 ONSITE TESTING OF MASONRY SHEAR WALLS STRENGTHENED WITH TIMBER PANELS**

## **10.1 INTRODUCTION**

The on-site experimental campaign was extended to real-scale testing of masonry walls retrofitted with the refurbishment technique presented in Chapter 8. Three full-scale brick masonry wall specimens isolated from the skeleton of a century-old building were subjected to in-plane semi-cyclic loading. Two of the specimens were tested before (as-built configuration) and after (repaired configuration) applying the reinforcement panel to the wall, while the third specimen was tested with the timber panel connected to the undamaged wall (retrofitted configuration).

## **10.2 EXPERIMENTAL PROGRAM**

The effectiveness of the proposed retrofit/repair technique was evaluated experimentally via in-situ testing. Three masonry wall specimens were isolated from the structure of a decommissioned hotel located in northern Italy within the Comano Terme bath area. The building, currently scheduled for demolition, was constructed in the second half of the XIX century as a three-story stone masonry building to which was later added an extra clay-brick story on top. Specimens 1 and 2 were tested at first in the as-built condition (AsB-1 and AsB-2) and then retested after being repaired (RP-1 and RP-2). Differently, Specimen 3 was tested only once, with the reinforcement being applied to the undamaged and “never before tested” specimen (R-3).

---

## 10.2.1 MATERIALS

The masonry specimens were isolated from the walls of the vertical addition constructed in the 1920s. The walls consisted of three-leaves masonry built with clay bricks ( $\approx 200 \text{ mm} \times 100 \text{ mm} \times 50 \text{ mm}$ ) and lime mortar with an average thickness of 340 mm. Thickness of horizontal mortar bed joints ranged between 8 and 20 mm while vertical joints thickness ranged between 5 and 10 mm. The mechanical properties of the masonry constituents are reported in Table 1. Irregular mortar samples and entire brick units were extracted from the masonry surrounding the selected specimens and tested in the laboratory. Sampling procedures were carefully executed by means of manual tools paying attention at minimizing the manipulation-induced mechanical alterations. Bricks were tested according to ASTM C67 2017 [ASTM (2017)] procedures. Mortar samples were roughly regularized by means of cutting machines and a thin layer of high strength dental plaster was applied on the loaded faces to improve compressive load distribution. Mortar specimen dimensions were limited by the bed joint thickness and by the extraction procedures, ranging between 15 and 20 mm in the direction of joint thickness and from 15 to 50 mm in plan. Compression forces were always applied parallel to the smaller specimen dimension, therefore height over length (width) ratios were always smaller than the unit. Recorded compressive strength values were corrected accounting for specimen aspect ratio as proposed by Lumantarna (2011). Mortar MoE reported in Table 10.1 was estimated from the experimental load vs. displacement relations considering the actual specimen height (net of dental plaster layer thickness).

*Table 10.1: Brick masonry mechanical properties from preliminary tests*

Material characteristic			n° samples	Mean	CoV
Brick compression strength	$f_{bc}$	[N/mm <sup>2</sup> ]	15	14.83	0.32
Brick modulus of elasticity	$E_{bc}$	[N/mm <sup>2</sup> ]	15	1225	0.29
Brick bending tensile strength	$f_{bt}$	[N/mm <sup>2</sup> ]	7	3.70	0.43
Mortar compression strength	$f_{mc}$	[N/mm <sup>2</sup> ]	15	4.59	0.50

For the tests on repaired and retrofitted walls, three-layer 60 mm thick CLT panels were used. The mechanical properties of the timber panels as provided by the product technical assessment document [ETA-18/0303] are given in Table 10.2.

The distributed timber panel-to-masonry wall connection was realized with two different types of timber-masonry (T-M) screw fasteners (Figure 10.1). Type A fastener is a partially threaded screw intended to be used in concrete and masonry, while Type B fastener features two threaded parts: a longer front thread to be inserted into masonry and a shorter rear thread to be inserted into timber.

Table 10.2: Spruce CLT panel mechanical properties

Bending	$f_{m,0,k}$	[N/mm <sup>2</sup> ]	24
	$f_{m,90,k}$	[N/mm <sup>2</sup> ]	-
Tension	$f_{t,0,k}$	[N/mm <sup>2</sup> ]	14.5
	$f_{t,90,k}$	[N/mm <sup>2</sup> ]	0.12
Compression	$f_{c,0,k}$	[N/mm <sup>2</sup> ]	21
	$f_{c,90,k}$	[N/mm <sup>2</sup> ]	2.5
Shear	$f_{v,k}$	[N/mm <sup>2</sup> ]	2.3
MoE	$E_{0,mean}$	[N/mm <sup>2</sup> ]	11550
Shear modulus	$G_{mean}$	[N/mm <sup>2</sup> ]	450
Density	$\rho_{mean}$	[kg/m <sup>3</sup> ]	420
	$\rho_k$	[kg/m <sup>3</sup> ]	350

To increase the contact surface between the screw head and the panel, type A fasteners were installed with  $\varnothing 43$  mm washers. Fastener characteristics are listed in Table 10.3. Mechanical properties of Type A fasteners were taken from the available product standard [ETA-05/0010], while for Type B fasteners the properties were obtained experimentally [EN ISO 6892-1]. An 8 mm thick steel bracket fixed to the timber panel by using 13 screws ( $\varnothing 8$  mm) inserted at  $45^\circ$  was used as hold-down to prevent the panel uplift and connect the CLT panel to the floor structure. The bracket capacity was designed to provide sufficient over-strength so as to exclude hold-down failure during testing.

Table 10.3: Properties of timber-masonry fasteners

Fastener type			A	B
Total length:	L	[mm]	180	230
Thread length:	$L_t$	[mm]	100	160 (70)
Thread diameter:	$d_{thread}$	[mm]	12.0	10.0 (12.0)
Core diameter:	$d_{core}$	[mm]	9.4	7.5
Shaft diameter:	$d_{shaft}$	[mm]	9.4	-
Hole diameter:	$d_{hole}$	[mm]	10	8
Axial resistance:	$N_{Rks}$	[kN]	25	58

In brackets the timber thread properties

## 10.2.2 SPECIMEN PREPARATION

After removal of the original plaster, three wall portions of  $1.8 \times 1.8$  m<sup>2</sup> were isolated from the surrounding masonry by thru cutting the walls with a circular steel blade with diamond segments (Figure 10.2-a). Weight of the roof, of the uppermost floor and of

masonry above the horizontal cuts was supported on provisional steel props to guarantee safety. The vertical stress required to activate masonry shear failure was applied to the specimens by using a loading rig that will be described in the next section (Figure 10.2-b). A 30 mm thick (on average) layer of M5 strength-class lime mortar was laid on top of the specimen surface to provide adequate load spreading.

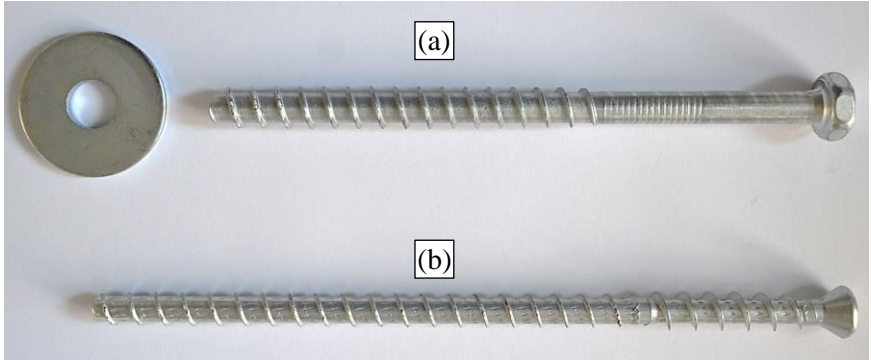


Figure 10.1: TM fasteners: a) Type A + washer; b) Type B

To prevent local crushing of the masonry due to force concentration in the area surrounding the hydraulic jack, a  $250 \times 250 \times 15 \text{ mm}^3$  steel plate was placed on top of a 20 mm thick layer of high-strength mortar. The reinforcement was installed by drilling calibrated holes through both the CLT panel and the masonry with a regular pattern according to the spacing values listed in Table 10.4. Regularity of the pattern was partially altered to avoid the cracks originated from the testing of the specimens in the as-built condition. Attention was also paid to drill the holes in correspondence with the bricks so as not to install the fasteners into the bed joints and reduce their effectiveness. Holes were cleared from dust and debris prior to the fastener insertion with an impact screwdriver. CLT panels were installed with the grain direction of the external board layers oriented vertically (Figure 10.2-c).

Table 10.4: Specimen IDs and description

Test ID	Configuration	T-M Fastener	Fastener spacing [mm]	Reinforcement side
AsB-1	As-built	--	--	--
RP-1	Repaired	A	400	R
AsB-2	As-built	--	--	--
RP-2	Repaired	B	400	L
R-3	Retrofitted	B	300	R



Figure 10.2: Specimen preparation: a) Specimen after removal of the plaster and creation of the thru cuts; b) AsB-1 specimen prior to testing; c) R-1 specimen prior to testing

### 10.2.3 TEST SETUP AND INSTRUMENTATION

Vertical compression was applied to the top surface of the specimen by means of 3  $\emptyset$  14 mm steel wire ropes. The wire ropes were anchored to reinforced concrete ring beams located at the first floor-level and purposely built for this testing campaign (Figure 10.3-c). Ribbed steel plates with specifically designed rounded rails to guide the wires, were positioned on top of the specimen to allow the force transfer from the wire ropes to the masonry. The horizontal load was applied by a single-effect hydraulic jack positioned approximately at 1.6 m from the base of the specimen as illustrated in Figure 10.3-a. The reaction to the lateral loading was provided by a horizontal steel I-beam connected to two timber frames, one on each side of the masonry wall. The reaction frames were built using solid-wood beams and were anchored to the existing floor structure (Figure 10.3-b). The magnitude of the lateral force was measured by a 300 kN load cell provided with a spherical articulation for an optimal force transfer. It is worth stressing that in all the tests, the horizontal force simulating the earthquake action was applied to the

masonry with no direct load-transfer between the actuator and the CLT panel (when present).

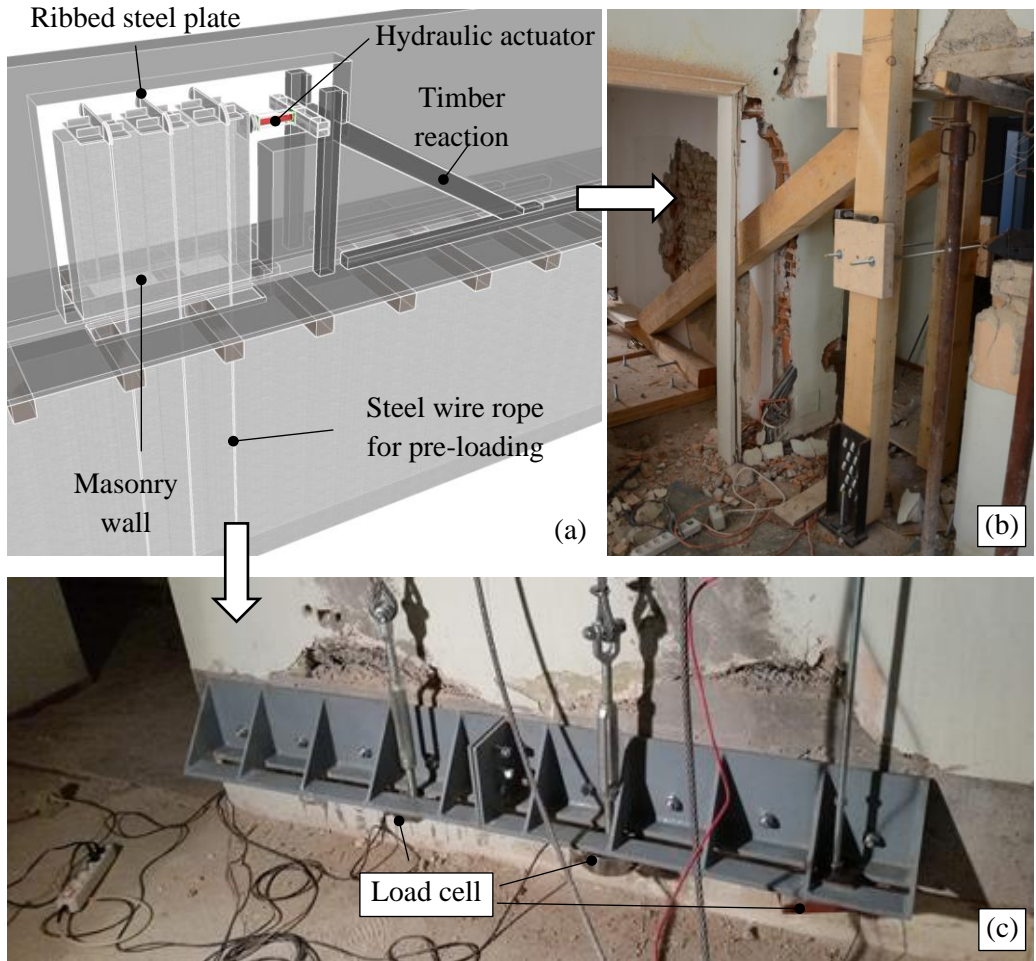


Figure 10.3: Test setup: a) setup schematic; b) close up of the timber reaction frame; c) detail of the anchoring system for the steel wire ropes

Deformations were measured by a total of 8 wire transducers, 4 on each side of the wall (measuring the two diagonals and the vertical tension and compression edges). Instruments were identified by means of a letter (*V* for vertical and *D* for diagonal), a number (*1* for instruments expected to read elongations and *2* for shortening) and an additional letter identifying the side of the specimen, with respect to the loading direction (see Figure 10.4). Absolute horizontal displacements were measured by means of an LVDT positioned at the actuator location and a couple of wire transducers installed

at the front end of the specimen as illustrated in Figure 10.4. Out-of-plane displacements were monitored by means of two LVDTs placed at the front end (*DISP\_OF*) and at the rear end (*DISP\_OB*) of the specimen.

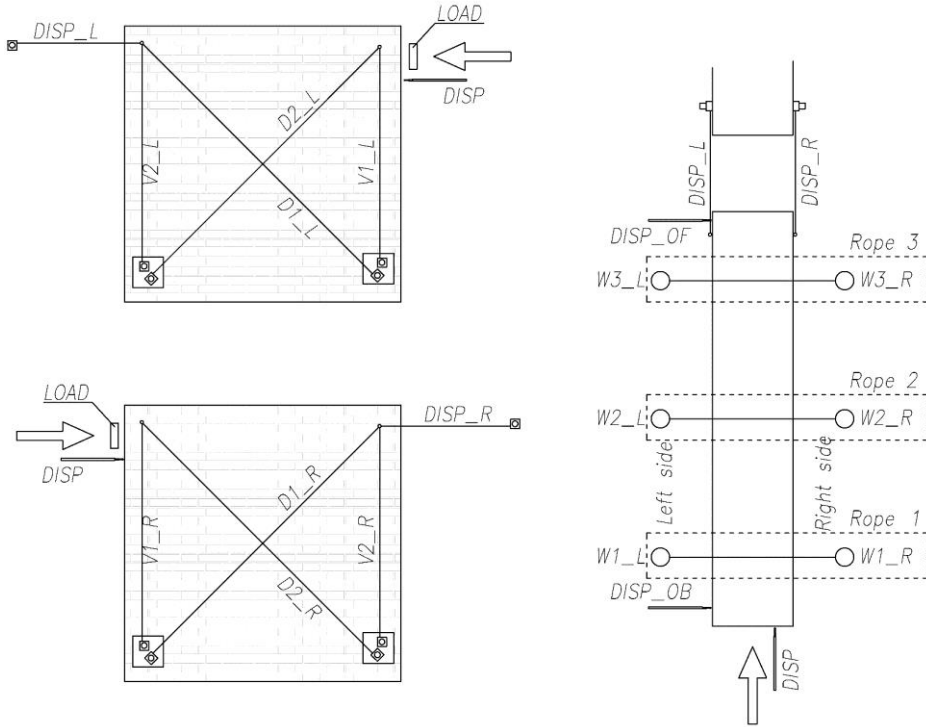


Figure 10.4: Instrument layout

On the reinforced side of repaired/retrofitted specimens wire sensors were applied to the CLT panel to measure timber in-plane deformations and absolute horizontal displacements in the direction of loading, while the above-mentioned instruments recording the out-of-plane deformations were always placed on the un-reinforced side of the wall. In the case of repaired/retrofitted specimens, vertical tension force on the hold-down was measured by means of a ring load cell, while the panel uplift was measured by an additional linear displacement transducer (LDT). Tension forces acting on the wire ropes were monitored by means of six load cells positioned at the rope anchoring points visible in Figure 10.3-c.

---

## 10.2.4 TEST PROTOCOL

Vertical forces were introduced by increasingly stressing the wire ropes up to  $\approx 23$  kN each, introducing a uniform compression stress over the specimen top surface of  $\approx 0.23$  MPa. The wire ropes were tensioned by steps of 5 kN load increments starting from the central rope at every step. During the application of the vertical load, data from the instruments were continuously recorded. Once the wire ropes had been tightened, shear testing began by applying load semi-cycles with the jack acting in compression only. To allow the specimens to be effectively repaired after testing, loading sequences on as-built specimens were terminated at the formation of the shear stair-stepped diagonal crack, without reaching the ultimate displacement capacity. Repaired and retrofitted specimens were first subjected to force-controlled load cycles similarly to the as-built specimens. When the applied load approached the specimen in-plane shear capacity, load application switched to displacement-control and additional cycles were performed with increasing displacement amplitudes. Further details on the test sequence are provided in the results section. The actuator was driven by a manual hydraulic pump by maintaining a displacement velocity of approximately 0.2 mm/s.

## 10.2.5 RESULTS AND DISCUSSION

The uniform vertical stress magnitudes  $\sigma_0$  applied to the specimens are listed in Table 10.5 along with the estimation of the masonry elastic modulus  $E$  obtained from the data collected during the vertical loading phase.

*Table 10.5: Applied vertical stresses and elastic modulus of the masonry wall specimens*

Test ID	$\sigma_0$ [MPa]	$E$ [MPa]
AsB-1	0.22	381.6
RP-1	0.22	
AsB-2	0.22	239.9
RP-2	0.23	
R-3	0.21	301.0

### 10.2.5.1 Specimen 1

Subsequent to the application of the vertical stress up to 0.22 MPa, Specimen 1 was first tested in the unreinforced condition (AsB-1). The horizontal loading was applied in semi-cycles following a stepwise procedure of 5 kN load increments up to 30 kN, after which the step size was increased to 10 kN until the maximum load ( $F_{max} = 69.3$  kN)

was reached. Figure 10.5 shows the load-displacement curves obtained from AsB-1 test plotted with respect to displacements measured by  $DISP\_R$  and  $DISP\_L$  transducers.

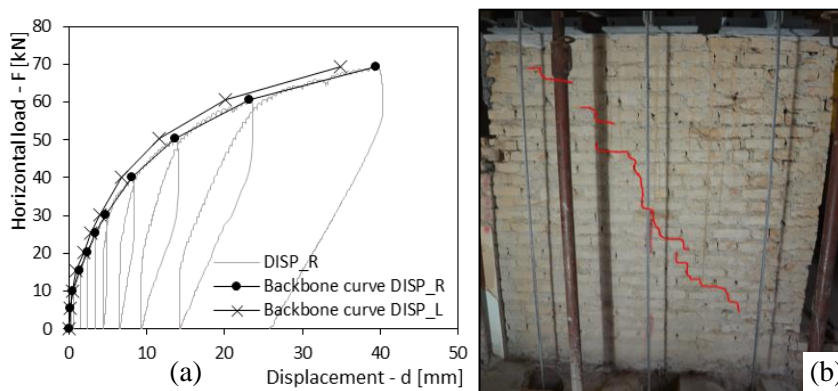


Figure 10.5: AsB-1 test: a) Load-displacement curve; b) Cracking pattern

After the formation of the diagonal crack (sign of the reach of the maximum shear capacity of the unreinforced masonry specimen) the test was ended. A 60 mm thick CLT panel was then connected to the tested specimen by means of 17 type A fasteners. 16 fasteners ( $\approx 5$  fasteners per square meter of wall surface area) were arranged on four rows maintaining a minimum distance from the panel edge of approximately 300 mm and an approximate spacing of 400 mm between the fasteners (Table 10.4). An additional fastener was inserted near the edge of the wall to prevent the premature collapse (with consequent possible damages of the instrumentation) of a small portion of the wall isolated by the cracks from previous testing in the unreinforced condition. The load-displacement curves observed for the masonry pier and the CLT panel are reported in Figure 10.6. Dissipated energy was evaluated as the difference between the input energy and the energy returned by the specimen when unloading as the integral of applied force multiplied by displacement increments. Load-displacement curves and dissipated energy for specimen 1 are compared in Figure 10.7. Thanks to the reinforcement, the lateral stiffness of the repaired specimen was found to be consistent with the stiffness of the undamaged wall ( $-1.4\%$  variation of the secant stiffness  $K_s$  at  $0.4 \times F_{max}$  and  $0.1 \times F_{max}$ ) while the shear capacity increased significantly ( $+37.1\%$  variation of maximum load  $F_{max}$ ) as well as the energy dissipation capacity ( $+86.1\%$  of maximum dissipated energy  $E_d$  at the end of the last unloading semi-cycle). Dissipated energy for the repaired configuration was evaluated based on the displacements of the un-reinforced side of the specimen only. Energy dissipation capacity increment was evaluated for the cycle unloading condition (dashed lines in Figure 10.7) with respect to the last cycle unloading displacement experienced by the as-built specimen

(corresponding  $E_d$  value for the repaired specimen was interpolated, based on the unreinforced side displacement only). Details about the parameters derived from the experimental curves are given in Table 10.6.

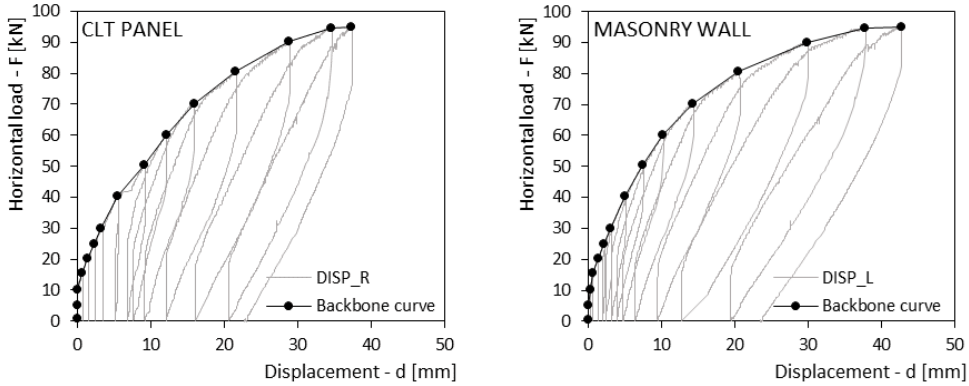


Figure 10.6: Specimen 1 repaired (RP-1) load-displacement curves: a) timber panel side; b) masonry wall side

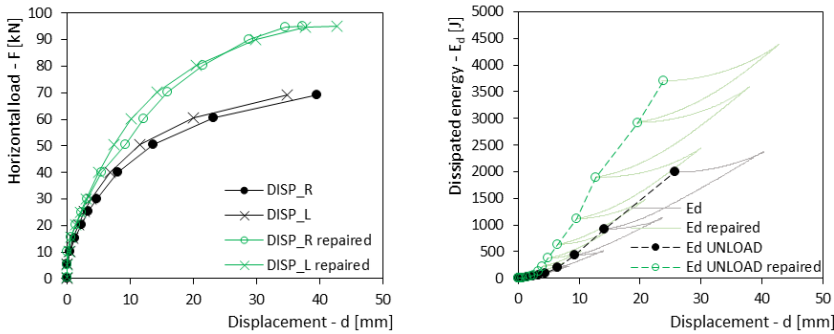


Figure 10.7: Specimen 1: comparison of as built and repaired configuration

### 10.2.5.2 Specimen 2

AsB-2 test was carried out by following the same loading procedure as for AsB-1 test. 5 kN steps up to 30 kN and then 10 kN steps up to the maximum load. Differently from the AsB-1 test, an extra load cycle was performed after the formation of the diagonal shear failure mechanism (for a shear load of approximately 70 kN, consistently with AsB-1 test) pushing the specimen up to a net displacement of 50 mm at the top (Figure 10.8).

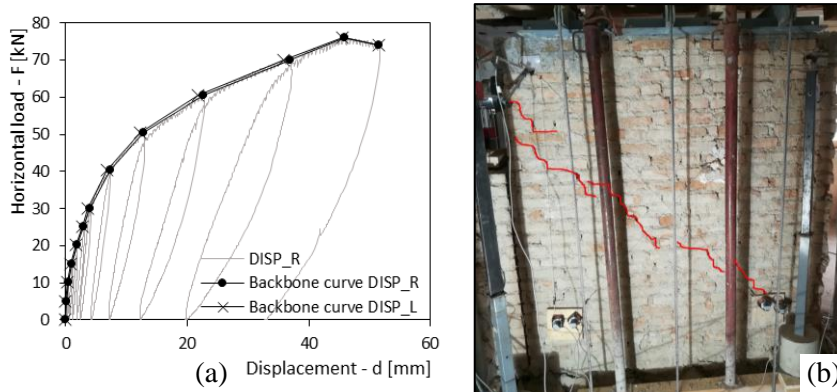


Figure 10.8: Specimen 2 as-built (AsB-2): a) Load-displacement curve; b) Cracking pattern

The masonry pier was then reinforced with a 60 mm thick CLT panel connected to the masonry using 16 type B fasteners. Edge distances and fastener spacings were kept similar to those adopted for RP-1 test, within the geometric limitations of the brick courses, by arranging the fasteners in four rows of four connectors. After repair, a 20% increase in the maximum capacity  $F_{max}$  of Specimen 2 was observed (test RP-2), with a clear “pseudo-ductile” post-yield response. However, due to safety reasons (e.g. cracking of the masonry spandrel adjacent to the specimen base and increasing out-of-plane displacements), it was not possible to reach the actual ultimate condition. It is worth noting that the 44.7 mm displacement reached during RP-2 test by instrument *DISP\_R* corresponds to a drift ratio  $dr = 2.5\%$  ( $dr = displacement / wall height$ ) which largely exceeds the acceptance criteria for ultimate limit states recommended for masonry piers by relevant standards [e.g. ASCE (2017), NZSEE (2017), C.S.LL.PP. (2019)]. It is also important to note that a residual deformation from AsB-2 (characterized by a residual displacement of approximately 33 mm at the top of the wall) was present when test RP-2 was commenced. If such residual deformation was included in the calculation of the drift ratio, the  $dr$  value would be 4.3%.

Due to the extensive damage experienced by specimen 2 when tested in the unreinforced condition, a reduced initial stiffness was observed for the repaired configuration if compared to the as-built condition (-24.2% variation of secant stiffness  $K_s$ ). The increase in maximum capacity  $F_{max}$  (+20%) and energy dissipation  $E_d$  (+62.5%) was smaller than that observed for specimen 1 but nonetheless considerable. In the comparison, dissipated energy for the as-built configuration was evaluated at the last unloading displacement experienced by the repaired using interpolation on the black dashed line in Figure 10.10.

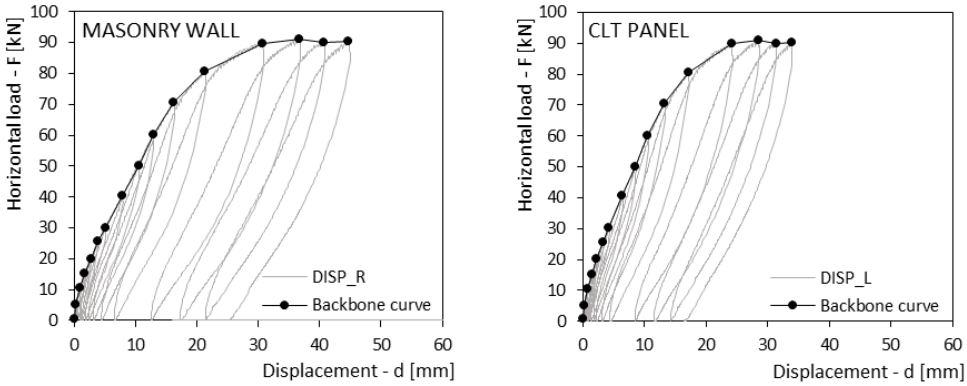


Figure 10.9: Specimen 2 (repaired) load-displacement curves

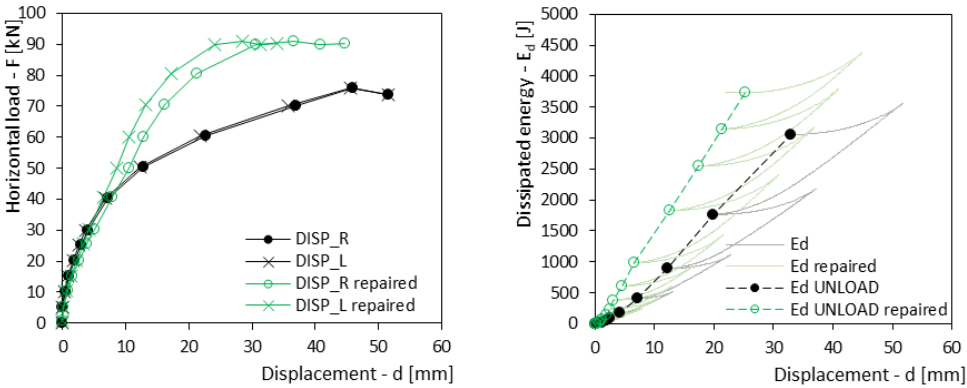


Figure 10.10: Specimen 2: comparison of as built (AsB-2) and repaired (RP-2) configurations; a) backbone curves; b) energy dissipation

### 10.2.5.3 Specimen 3

For the last test, the reinforcement panel was applied to a wall specimen that had not been tested before in order to assess the effectiveness of the strengthening solution in a scenario without pre-existing damage. A total of 25 type B fasteners ( $\approx 8$  fasteners per square meter of wall surface area) were inserted to connect the CLT panel to the masonry wall disposed in five rows using a 300 mm spacing in either vertical and horizontal directions and maintaining a 300 mm distance from the panel edges. Figure 10.11-a reports the loading cycles and the envelope curve plotted with respect to the masonry displacements. After reaching the maximum load capacity of the system at 106 kN of lateral force with the formation of a clear shear failure mechanism, illustrated in Figure 10.11-b, additional displacement-controlled cycles with 10 mm amplitude increments were performed. As visible from Figure 10.11-a, test R-3 exhibited a

softening behavior with a 10% capacity loss after two cycle-sets in displacement control (maximum wall displacement = 80.3 mm). Similarly to specimen 2, also specimen 3 was not pushed to the actual ultimate conditions due to safety concerns. However, the observed experimental drift capacity  $dr$  was equal to 4.5%, denoting a remarkable deformation capacity of the strengthened system (for reference on the deformation capacity of unreinforced brick walls see Morandi et al. (2018)).

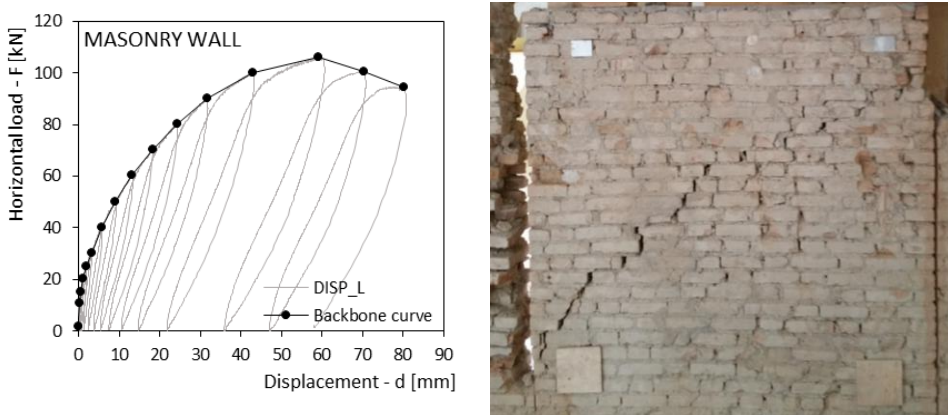


Figure 10.11: Specimen 3 (R-3, retrofitted): a) Load-displacement curve; b) Cracking pattern

### 10.3 GENERAL REMARKS

Load-displacement and energy dissipation curves from all the tests are compared in Figure 10.12. To allow for a direct comparison between as-built and repaired/retrofitted configurations, the displacement values are taken from the instruments fixed to the masonry. A remarkable consistency can be observed between the responses of tests AsB-1 and AsB-2, making it plausible to assume that also specimen 3 would have shown a similar behavior if tested in the as-built condition. Consequently, it appears reasonable to affirm that, thanks to the strengthening intervention, the wall capacity of specimen 3 (test R-3) was increased by 40%. When used to repair previously damaged walls (tests RP-1 and RP-2), the proposed technique not only permitted to restore the original wall capacity, but it also resulted in a noticeable capacity increase (i.e.  $\geq 20\%$ ). As visible from the data reported in Table 10.6, all the tested configurations (as-built, repaired and retrofitted) exhibited comparable stiffness values. The lack of any noticeable stiffness increase due to the strengthening presence (compare R-3 with AsB-1 and AsB-2), together with the capacity increase shown by the repaired specimens (RP-1 and RP-2), seem to confirm the findings from previous numerical study reported in Giongo et al. (2017), which suggests that the retrofit system is effectively engaged only after the cracking of the wall. Such negligible impact over the wall stiffness could prove

beneficial in the case of selective interventions in which only a few walls must be retrofitted without to induce major changes in the force distribution within the building, as opposed to alternative and popular strengthening techniques such as jacketing of the walls with shotcrete.

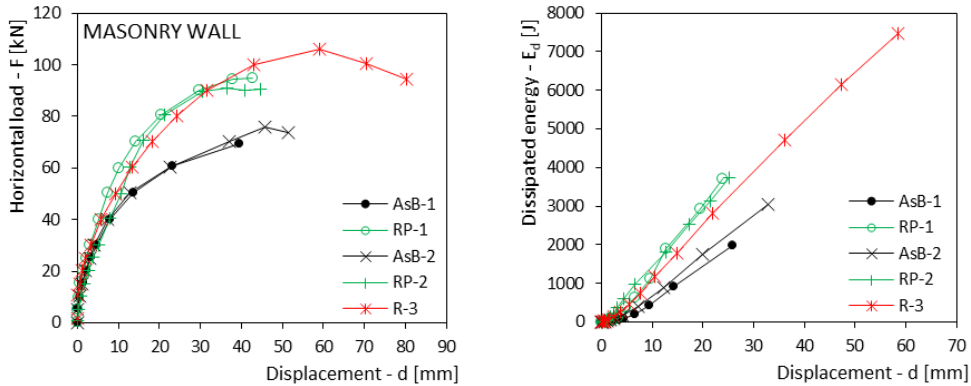


Figure 10.12: Comparison of the load-displacement backbone curves and the total energy dissipation for every test performed

Table 10.6 gives also the maximum force ( $F_{max,HD}$ ) and the stiffness ( $K_{HD}$ ) registered for the hold-downs used to anchor the timber panels to the floor. The different hold-down stiffness exhibited by the three specimens reflects different anchoring conditions. The higher value measured for specimen 1 was due to the nearby presence of a reinforced concrete floor that allowed for a stiffer connection, whereas for the other two specimens the hold-down was anchored to wood joists as the closest floor structure was a timber floor. It is worth stressing that the hold-down performance that is required from the data shown in Table 10.6, appears to be comparable with the capacity and the stiffness of devices already available on the market [Acler et al. (2011); Tomasi and Sartori (2013); Gavric et al. (2015)].

Figure 10.13 shows the backbone curves with reference to the measurements taken on the timber panels (Figure 10.13-a) and the slip values measured at the masonry-to-timber interface at the top of the specimen (Figure 10.13-b). When the lateral load approached the specimen peak-capacity, the wall-panel slip increased, indicating progressive yielding of the fasteners (approximately at slip values between 5 and 10 mm in accordance with previous work presented in Chapter 9). This is particularly evident for specimen 3 where the reinforced wall was tested up to a maximum displacement of 80 mm while the CLT panel experienced only half the displacement.

Table 10.6: Summary of the experimental outcomes in terms of maximum load, stiffness and dissipated energy

Specimen ID	Fasteners		$F_{\max}$ [kN]	$K_{s \text{ UR}}$ [kN/mm]	$E_{d \max}$ [J]	$dr_{\max}^*$ [%]	$F_{\max \text{ HD}}$ [kN]	$K_{\text{HD}}$ [kN/mm]
	Type	n°						
AsB-1	--	--	69.3	6.62	1990		--	--
RP-1	A	17	95.0	6.53	3703		39.9	4.75
AsB-2	--	--	75.9	5.94	3057		--	--
RP-2	B	16	91.1	4.50	3732	2.5	32.4	3.54
R-3	B	25	106.0	5.28	7484	4.5	53.0	2.63

\* the values refer to the maximum deformation reached during testing and might underestimate the specimen deformation capacity.

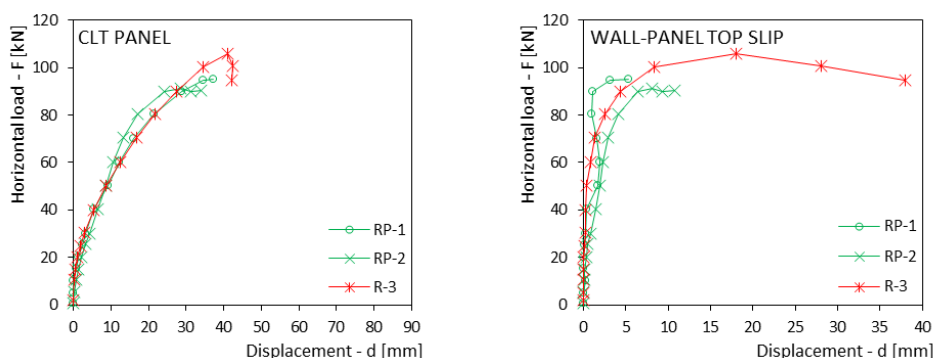


Figure 10.13: a) Comparison of the backbone curves obtained from CLT panel readings; b) masonry wall - CLT panel slip measured at the top of the specimen.

## 10.4 CONCLUSIONS

The outcomes of an in situ experimental campaign investigating the effectiveness of a technique for repairing and retrofitting URM walls by using CLT panels were presented herein. The main results are summarized in the following:

- Damaged specimens showed capacities greater than the original wall capacity ( $\geq +20\%$ ) after being repaired with CLT panels connected to the masonry through a minimum of  $\approx 5$  screw fasteners per square meter of wall surface. Specimen performance showed limited correlation to the typology and diameter of the screw fasteners.
- In case of retrofit, the specimen capacity was observed to be 40% higher than the capacity of the unreinforced specimens, thanks to  $\approx 8$  screw fasteners per square meter of wall surface. Pronounced yielding of the fasteners was observed after wall cracking.

- 
- Although it was not possible to reach specimen ultimate displacements, the displacement capacity shown by both repaired and retrofitted specimens was significantly larger than the values recommended by current standards for ULS. In particular, retrofitted test R3 showed a notable drift capacity of 4.5%.
  - Reinforced wall specimens tested in either repaired and retrofitted configurations showed energy dissipation levels significantly higher than those observed for the specimens tested as-built.
  - Test results showed a negligible impact of the reinforcement over the wall lateral stiffness, confirming that the reinforcement system is effectively engaged only after the wall cracking. Because of this aspect, selective wall strengthening can be applied without significant alterations of the force distribution among the resisting walls of the building.
  - The good performance shown by repaired and retrofitted specimens were obtained with the CLT panels anchored to the ground via hold-downs that inhibited the rocking of the panel. Strength demand and stiffness demand on the hold-down were found to be compatible with the performance of the devices commonly used in the timber construction field.

**NOTE:** Research outcomes presented in this Chapter have been submitted to the Journal “Proceedings of the Institution of Civil Engineers – Structures and Buildings”

## 10.5 REFERENCES

- Acler E, Piazza M, Tomasi R, Webber M (2011) “Experimental investigation of the behaviour of different types of connections between the XLAM panels and the concrete slab”. In: Proceeding of the Structural Engineering World Congress SEWC 2011, Como, Italy.
- ASTM (American Society for Testing and Materials International) (2017) “Standard Test Methods for Sampling and Testing Brick and Structural Clay Tile” *ASTM C67*. West Conshohocken, PA, USA, 2015.
- C.S.LL.PP. n°7 (2019). “Istruzioni per l’applicazione dell’”Aggiornamento delle “Norme tecniche per le costruzioni” di cui al decreto ministeriale 17 gennaio 2018”. Ministero delle Infrastrutture e dei Trasporti. Ministry of Infrastructure and Transport (in Italian).
- Deutsches Institut für Bautechnik (DIBt) – “European Technical Assessment ETA-05/0010, HECO MULTI-MONTI MMS Concrete screw for use in concrete”, 2015.
- CEN (European Committee for Standardization) (2018). “Metallic materials - Tensile testing - Part 1: Method of test at room temperature”. *EN ISO 6892-1*. Brussels, Belgium.
- European Technical Assessment “ETA-18/0303, Rubner XLAM – Rubner CL. Solid wood slab elements to be used as structural elements in buildings”, 2018.
- European Technical Assessment “ETA-05/0010, HECO MULTI-MONTI MMS Concrete screw for use in concrete”, 2015.
- Gavric I, Fragiaco M, Ceccotti A (2015) “Cyclic behaviour of typical metal connectors for cross-laminated (CLT) structures”. *Mater Struct*, 48:1841–1857. doi:10.1617/s11527-014-0278-7.
- Giongo I, Schiro G and Piazza M (2017) “On the use of timber-based panels for the seismic retrofit of masonry structures”. In Proceedings of the 3rd International Conference on Protection of Historical Constructions (Editors: Mazzolani F.M., Lamas A., Calado L., Proenca J.M., Faggiano B.) Lisbon, Portugal.
- Lumantarna, R. (2011) “Material characterisation of New Zealand’s clay brick unreinforced masonry buildings”. Thesis Dissertation, The University of Auckland, Auckland, New Zealand.
- NZSEE (New Zealand Society for Earthquake Engineering) (2017). “Assessment and improvement of the structural performance of buildings in earthquakes”. *NZSEE 2017*. Wellington, New Zealand.
- Morandi P, Albanesi L, Graziotti F et al. (2018) “Development of a dataset on the in-plane experimental response of URM piers with bricks and blocks”. *Construction and Building Materials – 190*: 593-611. doi.org/10.1016/j.conbuildmat.2018.09.070.

---

Tomasi R, Sartori T (2013) “Mechanical behaviour of connections between wood framed shear walls and foundations under monotonic and cyclic load”. *Constr Build Mater* 44(13):682–690. doi:10.1016/j.conbuildmat.2013.02.055.

# 11 SHEAR TESTING OF RETROFITTED MASONRY WALLETS

## 11.1 INTRODUCTION

In this Chapter an experimental campaign investigating the effectiveness of the timber-based retrofit system on rubble masonry wallets is reported. To provide a comparison benchmark the retrofitted configurations also comprised a hydraulic lime based composite system (CRM). A series of 16 diagonal tension (shear) tests were carried out as per ASTM E519-15 [ASTM (2015)] on twelve masonry specimens which were assigned to three groups of four. Group 1 specimens were tested in the as-built configuration at first (AsB), then reinforced by means of the CRM system and re-tested in the repaired configuration (labeled as RP). Specimens assigned to group 2 were tested in the CRM retrofitted configuration only (labeled as R). Group 3 wall specimens were tested after being retrofitted by means of the CLT-based system. Adopted IDs and tested configurations are summarized in Table 11.1.

*Table 11.1: Test IDs and configurations*

ID	Group	Walls	Configuration	Reinforcement
AsB	1	1, 2, 3, 4	As Built	---
RP	1	1, 2, 3, 4	Repaired	CRM
R	2	5, 6, 7, 8	Retrofitted	CRM
RC	3	9, 10, 11, 12	Retrofitted	CLT

## 11.2 MATERIALS

Masonry wall specimens were built with roughly squared dolomite stone elements and nominal M2.5 strength class hydraulic lime mortar (hereafter referred to as M1). For the CRM reinforcement system, nominal M10 strength class hydraulic lime mortar (hereafter referred to as M2) was used together with a glass fiber net whose features are listed in Table 11.2. To improve plaster to masonry adhesion,  $\varnothing$  8 mm helix steel bars were grouted to masonry by means of hydraulic lime grout and embedded in the M2 plaster. M1 and M2 mortar samples were tested according to EN 1015-11 [CEN (2019)]. Experimental results in terms of mean mortar compressive strength  $f_c$  and mean flexural strength  $f_b$  are listed in Table 11.3.

Table 11.2: Glass fiber net – mechanical properties

Feature	Unit	Value
Field mesh dimensions	[mm <sup>2</sup> ]	20 × 20
Tensile strength dir. 1	[kN/m]	63.5
Tensile strength dir. 2	[kN/m]	68.5
MoE dir.1	[MPa]	66750
MoE dir.2	[MPa]	61680

Table 11.3: Mortar mechanical properties as per EN 1015-11 [CEN (2019)]

	$f_c$ [MPa]	samples n <sup>o</sup>	CoV	$f_b$ [MPa]	samples n <sup>o</sup>	CoV
M1	5.4	12	0.067	2.0	6	0.260
M2	14.0	12	0.080	3.4	6	0.155

Table 11.4: CLT panels - mechanical properties

Bending:	$f_{m,0,k}$	[N/mm <sup>2</sup> ]	24
	$f_{m,90,k}$	[N/mm <sup>2</sup> ]	-
Tension:	$f_{t,0,k}$	[N/mm <sup>2</sup> ]	14.5
	$f_{t,90,k}$	[N/mm <sup>2</sup> ]	0.12
Compression:	$f_{c,0,k}$	[N/mm <sup>2</sup> ]	21
	$f_{c,90,k}$	[N/mm <sup>2</sup> ]	2.5
Shear:	$f_{v,k}$	[N/mm <sup>2</sup> ]	2.3
MoE:	$E_{0,mean}$	[N/mm <sup>2</sup> ]	11550
Shear modulus:	$G_{mean}$	[N/mm <sup>2</sup> ]	450
Density:	$\rho_{mean}$	[kg/m <sup>3</sup> ]	420
	$\rho_k$	[kg/m <sup>3</sup> ]	350
Thickness	$t$	[mm]	60

For the CLT-based retrofit system, 60 mm-thick three-layered panels (Table 11.4) were used. Timber-to-masonry connection was realized by means of 8.8 steel grade  $\text{Ø}$  14 mm threaded dowels grouted to the masonry by means of epoxy grout consistently with EX 14 TH connection type tested in Chapter 9.

### 11.3 SPECIMEN PREPARATION

Twelve  $120 \times 120 \text{ cm}^2$  40 cm-thick masonry wall portions were built from dolomite stone elements and M1 hydraulic lime mortar. Stones were roughly squared and arranged to form a double-leaf masonry with irregular bond pattern (Figure 11.1-a). To allow for their handling and to facilitate setup positioning, wallets were built on wooden pallets with one of the lower corners being laid on a provisional support to be removed prior to testing (Figure 11.1-b). The construction of the twelve specimens took approximately one week and every wallet of the three groups was built according to the same specifications. Testing was undertaken after the prescribed mortar curing time was elapsed.



Figure 11.1: As-built wall specimen preparation: a) Building phase; b) Completed specimen

To accommodate the helix bars used for the plaster-to-masonry connection, 30 cm-deep  $\text{Ø}$  20 mm holes were drilled inclined at approximately  $30^\circ$  with respect to horizontal (Figure 11.2-a). The connectors were located at specimen corners (minimum distance from specimen ends  $> 20$  cm) plus one in the middle, for a total of 5 connectors per specimen ( $\approx 3.5$  connectors/ $\text{m}^2$ ). Hydraulic lime grout was then injected (Figure 11.2-b) and helix bars were inserted in the holes. A first coating layer of M2 mortar was then applied prior to positioning of the glass-fiber net (Figure 11.2-c). The helix bars were then bent before applying the finishing M2 mortar layer (Figure 11.2-d). The total reinforcement thickness was equal to approximately 20 mm. CRM system application procedure was identical for both retrofitted (R) and repaired (RP) configurations. For

the CLT-based retrofit system  $110 \times 110 \text{ cm}^2$  wood panel elements were connected to the masonry by means of 5 grouted connectors per wall, according to the same scheme adopted in the case of the CRM reinforcement system. The connection type (i.e. adhesive connection) was consistent with the EX 14 TH system tested in Chapter 9. 30 cm deep  $\text{Ø} 22 \text{ mm}$  holes were drilled in the masonry perpendicularly to the wallet face. CLT elements were perforated so as to match holes in the masonry and positioned alongside the masonry specimen. Containment metallic nets were then inserted prior to grout injection filling the volume in the masonry and the panel thickness. Threaded steel dowels were then slowly inserted by rotating them about their axis to prevent the inclusion of air bubbles.



*Figure 11.2: CRM reinforcement: a) Hole drilling; b) Hydraulic lime grout injection; c) Positioning of the net; d) Reinforcement completed*

## 11.4 SETUP AND INSTRUMENTATION

An auto-equilibrated test setup based on the ASTM E519-15 [ASTM (2015)] standard was designed. Such system allowed for diagonal compression loads to be applied without the need of rotating the specimens. Setup comprised: a) two steel beams, each one obtained by welding together two UPN 180 profiles, b) two welded steel shoes, c)

a 600 kN single-effect hydraulic jack and d) two  $\text{Ø } 36 \text{ mm}$  10.9 steel grade threaded rods. All carpentry elements were of S275 steel grade. To accommodate the steel shoes and to provide a uniform force distribution, an approximately 20 mm-thick M15 strength class mortar layer was applied to loaded corners. The steel shoes transferred the compression loads to the masonry only, without engaging the reinforcing elements (timber panel and reinforced plaster) directly. The jack was driven by means of a manual hydraulic pump. The specimens were instrumented by means of 4 100 mm wire displacement transducers located at the two diagonals on each side and a 600 kN load cell interposed between the jack and the upper steel beam.

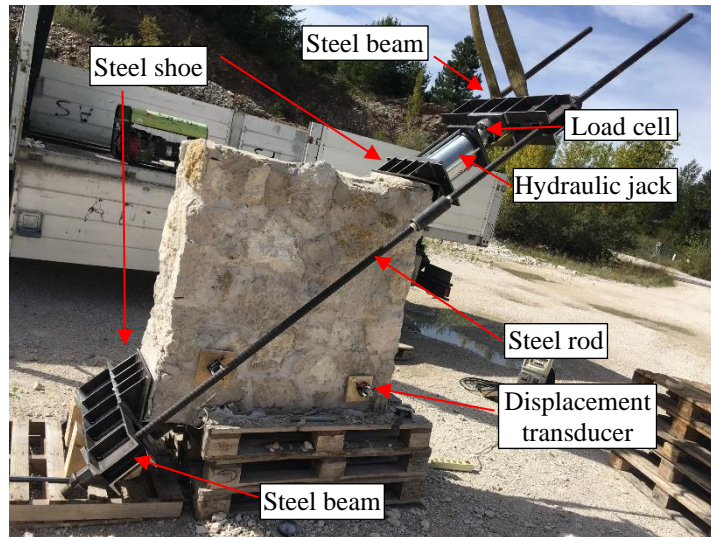


Figure 11.3: Test setup and instrumentation

## 11.5 TEST PROTOCOL

A first 25 kN adjustment cycle was performed to get the steel shoes in contact with specimen corners. Diagonal loads were then applied according to a hemi-cyclic force-controlled protocol (compression only). Hemi cycle amplitudes were gradually increased by 50 kN load steps up to the specimen capacity  $F_{max}$ . In the case of as-built configuration, the test procedure was stopped immediately after the maximum load was reached (according to the real-time load vs. diagonal shortening curve). For retrofitted and repaired specimens, the test procedure continued with additional displacement-controlled hemi-cycles until the applied force fell below  $0.8 \times F_{max}$ . To preserve test setup and instrumentation, the specimens were never pushed to the actual ultimate

condition and, for the same reason, in few cases test sequence was stopped prior to the reach of the  $0.8 \times F_{max}$  residual strength (see 11.6.5).

## 11.6 TEST RESULTS

### 11.6.1 FAILURE MECHANISMS

Each specimen exhibited diagonal cracking failure. Diagonal cracks formed along the parallel-to-loading direction as a result of the diagonal tensile stress in the perpendicular-to-loading direction. Crack opening almost always interested mortar joints except for few cases where also the stone elements were involved in the cracking mechanism.



Figure 11.4: Retrofitted specimens: a) CRM reinforcement after testing; b) CRM unreinforced side after testing; c), d) RC\_4 specimen during testing

Even at large diagonal strains, CRM retrofitted (R) and repaired (RP) specimens never exhibited plaster detachment. Reinforced side underwent light diagonal cracking in the parallel-to-loading direction while the crack width on the unreinforced side reached remarkable amplitudes. Unreinforced side of CLT retrofitted (RC) specimens exhibited

cracks comparable with those of R and RP specimens (unreinforced side). CLT panels exhibited visible out-of-plane deflections after masonry cracking occurred, without experiencing damage.

### 11.6.2 SHEAR STRENGTH

Test results in terms of shear strength  $s_s$  derived from peak diagonal force according to ASTM E519 [ASTM (2015)] are listed in Table 11.5.

*Table 11.5: Shear strength -  $s_s$  as per ASTM E519-15 [ASTM (2015)]*

Configuration	$s_s$ [MPa]	CoV	$s_s/s_{s,AsB}$ [--]
AsB	0,309	0,094	---
RP	0,299	0,080	0,979
R	0,408	0,120	1,322
RC	0,351	0,112	1,136

In terms of mean values, after being damaged and repaired, the shear strength of as-built Group 1 specimens was substantially restored. Values of shear strength ratios  $RP/AsB$  ( $RP/AsB = s_{s,RP}/s_{s,AsB}$ ) recorded for the Group 1 specimens are listed in Table 11.6. Both CRM and CLT retrofit systems applied on un-damaged specimens allowed to obtain an appreciable increase in shear strength compared to AsB specimens.

*Table 11.6: Repaired specimens, RP/AsB shear strength ratios*

Specimen	1	2	3	4	Mean
RP/AsB	1,00	0,75	1,12	1,06	0,98

### 11.6.3 OUT OF PLANE BEHAVIOR

Recordings from diagonal displacement transducers placed on the two opposite wall faces allowed to estimate the degree of asymmetry introduced by the retrofit systems. Since CLT panels were observed to remain substantially un-deformed during testing, RC specimens are not discussed in this paragraph. Response symmetry was evaluated according to the symmetry index  $s_i$  given by equation (11.1), where  $\varepsilon_{2,R}$  and  $\varepsilon_{2,L}$  are right hand side and left hand side values of compressed diagonal strains.

$$s_i = 1000 \cdot \left| \varepsilon_{2,R} - \varepsilon_{2,L} \right| \quad (11.1)$$

Typical evolutions of the symmetry index are plotted in Figure 11.5. Due to the irregular masonry texture, even in the case of as-built specimens, response was not symmetrical. Symmetry index growth was observed to be approximately linear with respect to mean diagonal strain. For R and RP specimens, symmetry index over  $\varepsilon_2$  rate was instead greater after the peak diagonal force was reached. Such phenomenon was attributed to the asymmetry introduced by the masonry cracking which increased the engagement of the reinforcement. Symmetry index values recorded at peak force are listed in Table 11.7.

Table 11.7: Symmetry index values at peak force

Configuration	$S_{i,mean}$ [%]	CoV
AsB	0,841	0,503
RP	1,748	0,486
R	0,887	0,533

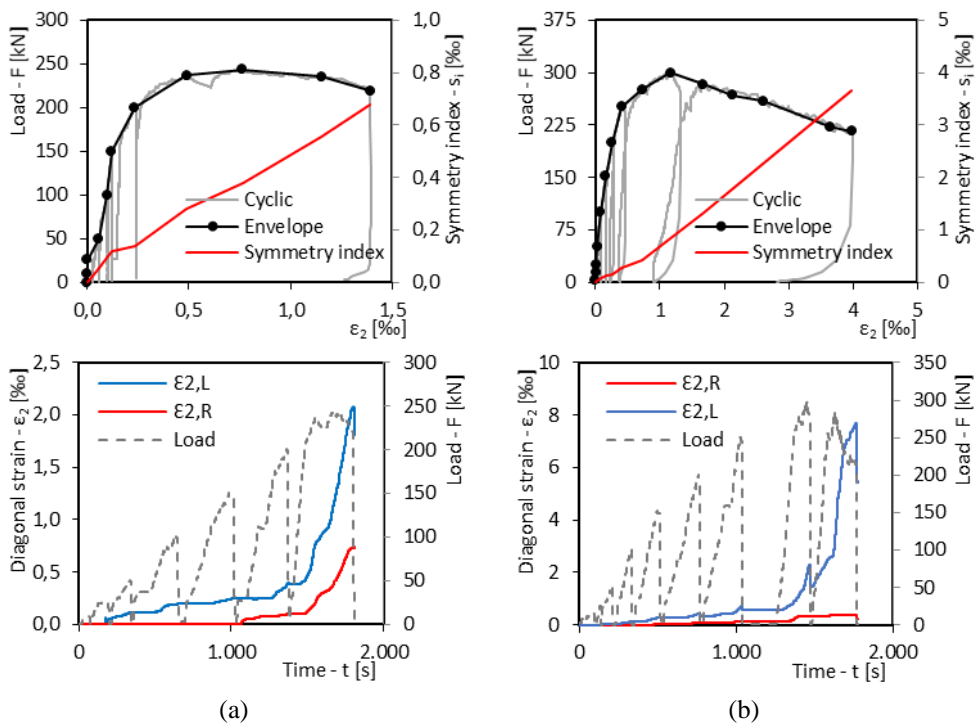


Figure 11.5: Strain asymmetry – typical plots: a) AsB specimens; b) RP & R specimens

From results listed in Table 11.7 the CRM retrofit system was not observed to introduce evident asymmetry in specimen behavior when applied to undamaged masonry. In the case of RP specimens, the previously cracked masonry shifted the center of stiffness to the reinforced side, even for small load values.

#### 11.6.4 BACKBONE CURVE IDEALIZATION

For each test, envelope curves were extrapolated from the cyclic load-displacement hysteresis loops according to ASTM E2126 [ASTM (2011)] and used to define the equivalent energy elastic-plastic (EEEE) backbone curves. The procedure was implemented considering the mean diagonal strains and, in the case of retrofitted / repaired specimens, the curves were also plotted with respect to the strains of the unreinforced side (UR label). Typical envelope curves and corresponding EEEP backbones are illustrated in Figure 11.6. Representative parameters in terms of diagonal strain  $\varepsilon_2$  and diagonal shear stress ( $s = 0.707 \times F_{max}/A$ ) are listed in Table 11.8 in terms of diagonal strain and diagonal shear at yield  $\varepsilon_y, s_y$ .

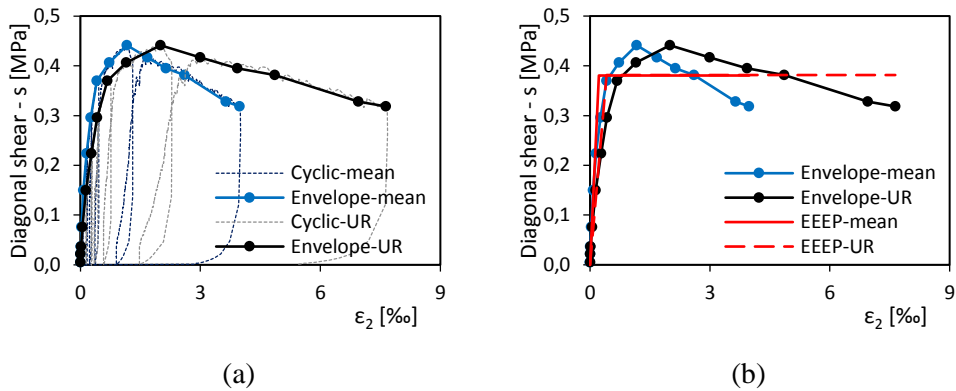


Figure 11.6: Cyclic envelopes and EEEP backbones according to [ASTM (2011)]

#### 11.6.5 COMMENTS ON POST-PEAK BEHAVIOR

Post-peak behavior of R and RC specimens is illustrated in Figure 11.7 based on dimensionless diagonal shear  $s/s_s$  vs. relative diagonal strain  $\varepsilon/\varepsilon(s_s)$  relations. Since ultimate conditions were never reached during testing, relative strain capacity was conventionally estimated as the strain value corresponding to an 80% residual strength. According to such idealization, with respect to mean curves in Figure 11.7, relative strain capacity of RC specimens was observed to be approximately 2.5 times greater compared to R specimens.

Table 11.8: EEEP backbones parameters

Test ID	Mean		UR side	
	$\epsilon_y$ [‰]	$S_y$ [MPa]	$\epsilon_y$ [‰]	$S_y$ [MPa]
AsB_1	0,152	0,24	---	---
AsB_2	0,226	0,34	---	---
AsB_3	0,055	0,28	---	---
AsB_4	0,255	0,27	---	---
RP_1	0,356	0,26	0,639	0,26
RP_2	0,322	0,25	0,473	0,26
RP_3	0,283	0,29	0,345	0,29
RP_4	0,194	0,27	0,319	0,28
R_1	0,124	0,29	0,091	0,29
R_2	0,140	0,37	0,258	0,37
R_3	0,221	0,38	0,411	0,38
R_4	0,100	0,35	0,188	0,35
RC_1	0,007	0,39	0,011	0,39
RC_2	0,020	0,25	0,028	0,25
RC_3	0,095	0,30	0,162	0,30
RC_4	0,001	0,24	0,002	0,23

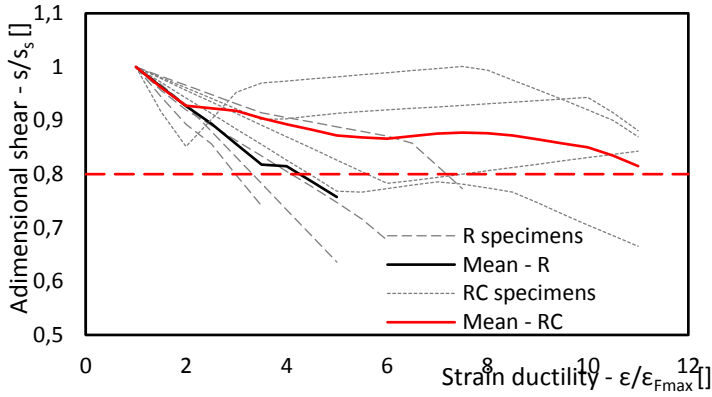


Figure 11.7: Post-peak behavior, CRM retrofit (R) vs CLT retrofit (RC)

## 11.7 CONCLUSIONS

The tested retrofit solutions were found to have a beneficial effect on shear strength of the masonry assemblages. The timber based retrofit system led to smaller retrofitted over as built shear strength ratios compared to the more invasive and less sustainable CRM solution (1.14 vs. 1.3). On the other hand, strain capacity of specimens retrofitted by means of the CLT based technique was observed to be 2.5 times greater compared to the CRM solution. In both cases the use of retrofit techniques based on relatively flexible materials applied on a single face of the wallets allowed to mitigate the side effects related to the asymmetric configurations.

---

## 11.8 REFERENCES

ASTM (American Society for Testing and Materials International) (2015) “Standart test method for diagonal tension (shear) in masonry assemblages” *ASTM E519-15/E519M-15*. West Conshohocken, PA, USA, 2015.

ASTM (American Society for Testing and Materials International) (2011) “Standard test methods for cyclic (reversed) load test for shear resistance of vertical elements of the lateral force resisting systems for buildings” *ASTM E2126*. West Conshohocken, PA, USA, 2011.

CEN (European Committee for Standardization) (2019). “Methods of test for mortar for masonry – Part 11: Determination of flexural and compressive strength of hardened mortar”. *EN1015-11*. Brussels, Belgium.

# CONCLUSIONS

The research work presented in the Thesis focused on the role of timber in the seismic resilience of existing URM buildings. Specifically, the behavior of timber assemblages typically present in traditional URM buildings, such as the wood diaphragms, was carefully assessed. Then, the possible use of timber as retrofit material for the timber diaphragms and also for the masonry piers was investigated.

In-plane behavior of existing timber diaphragms was investigated by means of an extensive numerical study. Two modeling approaches with different levels of refinement were employed to assess the influence of certain parameters (i.e. diaphragm aspect ratio, scale factor, diaphragm size, board-to-board contact and friction) that are generally disregarded by assessment procedures and previously reported numerical studies. Such aspects were observed to be, in general, non-negligible in the assessment of diaphragm in-plane behavior.

Numerical analyses were then extended to the case of timber diaphragms retrofitted by means of reversible and easy to be implemented timber-based solutions, which also allowed for minimizing of the mass increments. Each of the selected retrofit systems was observed to be effective in improving diaphragm in-plane strength and stiffness. The influence of several retrofit details regarding both geometrical and mechanical features was investigated leading to the definition of useful parameters to be considered in design procedures.

A series of nonlinear-dynamic analyses were performed to evaluate the effects of in-plane stiffness variations on the diaphragm seismic demand (regarding both force and displacement) considering two seismic input intensity levels. As a consequence of diaphragm stiffening, in-plane displacements were significantly reduced at the cost of higher force demands.

Effectiveness of a timber-based retrofit system for URM walls was investigated by means of an extensive in-situ experimental campaign. The first stage of the campaign

---

comprised a series of monotonic and reversed cyclic shear tests on timber-masonry connection systems. Several configurations were considered and the influence of various parameters such as the type of connection (dry or grouted), fastener, masonry, and timber element was assessed with respect to monotonic (strength and stiffness) and cyclic (impairment of strength and energy dissipation) properties.

The experimental program was subsequently extended to full-scale testing of masonry piers retrofitted/repared by means of the selected timber-based system. Three masonry wall specimens were isolated from the skeleton of a century-old building and tested in the as-built, repaired and retrofitted configurations. Compared to as-built, both repaired and retrofitted specimens exhibited greater shear and displacement capacities, while consistent stiffness values were observed among the three configurations. Further experimental testing was undertaken on newly-constructed rubble masonry specimens. In this case, the selected timber-based retrofit was tested alongside a benchmark CRM system based on natural hydraulic lime mortar and glass fibre nets. The latter exhibited higher shear strength values compared to the first, while post-peak behaviour of timber-based system showed higher strain capacity.

# ACKNOWLEDGEMENTS

I would like to gratefully thank my supervisors Prof. Maurizio Piazza and Dr. Ivan Giongo for the precious support they provided me during the three years of the PhD program.

I am sincerely thankful to the members of the Timber & Masonry Research Group of the University of Trento: Stefano Bezzi, Davide Cassol, Andrea Gaspari, Daniele Riccadonna, Gianni Schiro and Francesco Smioldo.

I am thankful to the former undergraduate students Mirko Capovilla, Marco Carlet, Davide Galvanin, Elisa Paulazzo, Stefano Segatta and Giovanni Sommacal for their precious help.

The author sincerely acknowledges the technicians of the LPMS laboratory of the University of Trento Ivan Brandolise, Tiziano Dallatorre, Luca Corradini, Dr. Marco Molinari and Alfredo Pojer for their precious support during the experimental activities undertaken in these three years.

Part of the research work presented in the Thesis was carried out within the framework of the 2019-2021 ReLUIS-DPC network (Italian University Network of Seismic Engineering Laboratories and Italian Civil Protection Agency).

The author gratefully thanks Terme di Comano (IT) thermal consortium for kindly providing access to the building and for allowing the experimental campaigns to be undertaken.

Terremoto Ltd., Rubner Holzbau S.r.l., HECO Italia EFG S.r.l., Miniera San Romedio S.r.l. and Fischer Italia are thankfully acknowledged for supplying the materials used in the experimental campaigns.